
# UNIVERSITA' DEGLI STUDI DI PARMA

DOTTORATO DI RICERCA IN
SCIENZA E TECNOLOGIA DEI MATERIALI

CICLO XXX

# Molecular Strategies for Functional Materials: Soft Mechanochemistry and Surface Functionalization

Coordinatore:
Prof. Enrico Dalcanale

Tutore:
Prof. Enrico Dalcanale

Dottoranda: Martina Torelli

Anni 2014/2017

*Alla mia famiglia e,*

*soprattutto, alle mie nonne*

*Quando la natura finisce di produrre le proprie specie,*

*l'uomo incomincia a creare, usando cose naturali*

*e con l'aiuto della natura, un'infinità di specie.*

Leonardo da Vinci

# Contents

CHAPTER 1

# TUNING OF A VERTICAL SPIN VALVE WITH A MONOLAYER OF SINGLE MOLECULE MAGNETS*

* Part of this chapter has been published in Advanced Functional Materials (doi 10.1002/adfm.201703600): G. Cucinotta, L. Poggini, A. Pedrini, F. Bertani, N. Cristiani, M. Torelli, P. Graziosi, I. Cimatti, B. Cortigiani, E. Otero, P. Ohresser, P. Sainctavit, A. Dediu, E. Dalcanale, R. Sessoli, M. Mannini.

## 1.1 Introduction

### 1.1.1 Nanotechnology

The term 'Nanotechnology' etymologically derives from the greek word νὰνος (nànos) which stands for 'dwarf'; in its scientific acceptation this prefix denotes a $10^{-9}$ factor and therefore it is used to describe a relatively new discipline which investigates systems of a few nanometres size either in one-, two- or three-dimensions. Traditionally, the first concepts that seeded the idea of nanotechnology are traced back to the famous lecture given by Richard Feynman at the California Institute of Technology in December 1959, titled "There's Plenty of Room at the Bottom", where he pioneeringly explored the possibility of direct manipulation of matter at the atomic scale. Nowadays, nanotechnology can be defined as the ability to engineer functional systems at the molecular scale through a *bottom-up* approach. The most fascinating aspects about this discipline are related to the commingling of classical and quantum mechanical features: thus, handling with objects smaller than a critical size results in a dramatic change in the properties of the resulting materials and the appearance of novel effects. Finally, one of the key features of nanotechnology is that of going beyond the borders of classical disciplines providing a common research field. Among the different areas on which nanotechnology extends, Nanomagnetism, intended as the investigation of the magnetic properties of nano-objects, is one of the most important and fascinating.

### 1.1.2 Molecular magnetism

Molecular magnetism can be defined as a highly interdisciplinary area where the techniques of molecular chemistry are exploited in the design, synthesis and characterization of new classes of magnetic materials based on molecular lattices, unlike the continuous lattices of classical magnets.[1] Interestingly, molecular magnetic materials show, on the one side, magnetic hysteresis comparable to ordinary magnets but, on the other side, are small enough to present quantum effects. Besides being attractive from the theoretical point of view, this combination of classical and quantum aspects can be interesting for several technological applications, such as high density data storage or quantum computation, justifying the increasing research interest towards miniaturization. Nevertheless, not all phenomena are scalable towards miniaturization; in magnetism, for instance, hysteresis loop, observed in

systems with different size, origins from very different physical phenomena[2] as schematized in Figure 1.1.

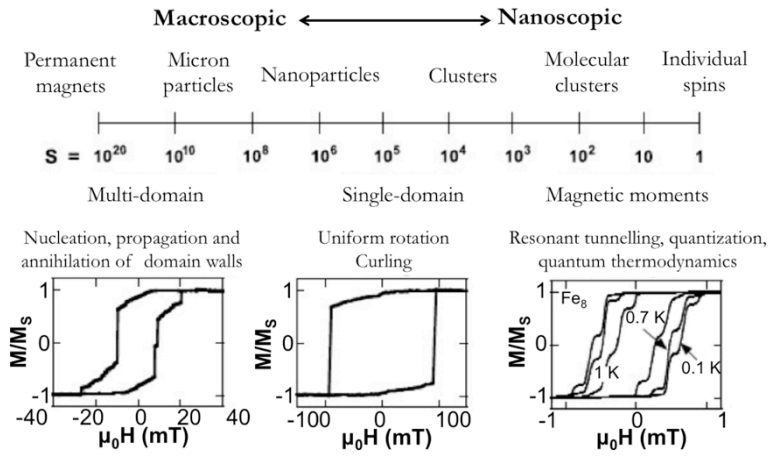


**Figure 1.1** *Transition from macroscopic to microscopic magnetism; the observed hysteresis loop origins from different phenomena.*

In fact, ideally working in a *top-down* approach and progressively decreasing the size of a bulk material, a breakdown of the classical multi-domain model occurs when particle radius becomes comparable with the size of the domain walls.[3] At this point, a single-domain model has to be used and the magnetization generally presents a preferred orientation, which can be reversed by overcoming a barrier depending on the magnetic anisotropy (left part in Figure 1.1). A further decrease in the particles size leads to an inconsistency of the single-domain model; now the energy barrier between the two magnetization states results comparable to the thermal energy, as evidenced by the free fluctuation of the magnetization. This is the so-called *superparamagnetic regime* (central part in Figure 1.1).

A diametrically opposite approach is the use of a bottom-up strategy based on single molecules, large enough to behave as bulk magnets.[4] For these molecules, discovered in the '90s by Caneschi and co-workers[5] and named Single Molecule Magnets (SMMs),[6] the origin of magnetism lies in a slow relaxation of the magnetization, meaning that it is due to the inner chemical structure of the molecular unit without any cooperative effect (right part in Figure 1.1).

### 1.1.3 Single Molecule Magnets

A Single Molecule Magnet (SMM) is a molecule that shows a slow magnetization relaxation of purely molecular origin. Unlike conventional magnets, where a collective long-range order of the magnetic moments is necessary, in SMMs each molecule represents a single magnetic domain and exhibits a hysteresis at liquid-helium temperatures. This peculiar behaviour was reported for the first time by Gatteschi and co-workers in dodecanuclear mixed-valent III/IV manganese oxide cluster $Mn_{12}O_{12}(O_2CCH_3)_{16}(H_2O)_4$.[7] Since the report of this polymetallic cage, a great variety of SMMs has been developed and studied.[8] So far, two major drawbacks restrain the concrete application of SMMs-based technology: first, the fact that their unique properties are accessible only at cryogenic temperatures; second, depositing and addressing individual molecules of SMMs on surfaces while preserving their magnetic properties is still challenging. To better understand how to overcome these limitations, it is convenient to define the main parameters that qualify the performances of molecular magnets. Magnetic blocking temperature ($T_B$), defined as the highest temperature at which a molecular magnet displays hysteresis in magnetization ($M$) *vs*. magnetic field ($H$) plots, is often used to evaluate SMM behaviour. Its value, however, is strongly affected by the sweep rate of the magnetic field and by the technique used for the measurement. The most used parameter in SMM studies is by far the effective energy barrier for the reversal of magnetization ($U_{eff}$), also called anisotropy barrier, which can be seen as the energy required to convert a SMM back into a simple paramagnet. In *3d*-SMMs the barrier $U_{eff}$ scales with the square of the total spin of the molecule ($S$) and linearly with the axial zero-field splitting parameter ($D$):

$$U_{eff} = |D|S^2$$

Therefore, in order to improve SMMs magnetic properties, larger $S$ values and appreciable negative $D$ values must be achieved. In the attempt to pursue this goal, a great number of SMMs based on various transition metal clusters have been reported.[9] In 2003 Ishikawa and co-workers introduced a new class of SMMs, composed by lanthanide organometallic compounds.[10] In particular they reported that lanthanide phthalocyanine double-deckers ($LnPc_2$), sandwich-type complexes made of a lanthanide(III) ion complexed by two phthalocyanines, present a SMM behaviour. Phthalocyaninato ligands are able to coordinate a wide range of metal ions: with large metal centres that support octacoordination, as in the case of rare earths, a square antiprismatic geometry (Figure 1.2) with a $D_{4d}$-symmetry is observed for the complex.

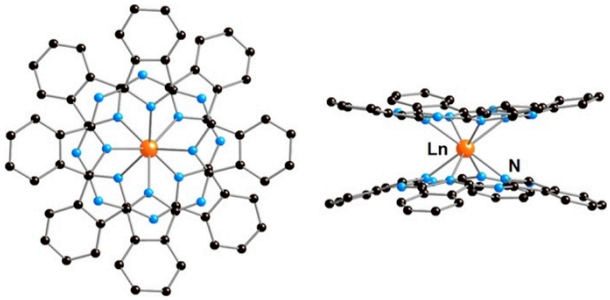


**Figure 1.2** *Structure of the complex anion* $[LnPc_2]^-$. *Color scheme: Ln, orange; N, blue.*

Since the ligands can be either oxidized or reduced, $LnPc_2$ complexes present three different oxidation states. In the anionic form, $[LnPc_2]^-$, the trivalent ion (+3) is coordinated by two Pc ligands formally bearing a -2 charge each. Neutral $[LnPc_2]^0$ and cationic $[LnPc_2]^+$ can be easily achieved by a reversible one- or two-electrons oxidation with mild oxidizing reagents or *via* electrochemistry. The square-antiprism coordination geometry leads to a significantly high magnetic anisotropy, which origins from different mechanisms than those of *3d* metal clusters. In lanthanide-based SMMs, anisotropy is given by the ligand field (LF) in which the lanthanide ion is placed,[11] while in 3*d* metal clusters the easy axis-type magnetic anisotropy is caused by the magnetic interactions among high-spin 3*d* metal ions in the molecule. In $LnPc_2$ the energy terms, determined by strong coupling between the spin (*S)* and orbital angular (*L)* momenta of the lanthanide ions that give rise to a total angular momentum (*J*), are further split by crystal-field effects. Moreover $LnPc_2$ structural simplicity and the possibility to finely tune the anisotropic barrier by a proper selection of the metal ion or the ligand field justify the increasing interest for these systems. In particular, among lanthanide ions, terbium-based phthalocyanine double-deckers ($TbPc_2$) allowed the achievement of energy barriers, $U_{eff}$, one order of magnitude higher than those observed for *3d*-SMMs. The superior magnetic properties are due to the peculiar *4f* electron density distribution of terbium(III), which has a distinct oblate shape in the ground state and a prolate shape in the lowest excited state. Thus, considering a purely electrostatic model, the complex is strongly stabilized by an axial geometry of the ligands in the ground state, while extremely destabilized in the lowest excited state for the same sandwich-type geometry. The resulting large separation between the two states matches the requisite for strong single-molecule magnet behaviour and explains $TbPc_2$ superior magnetic properties among $LnPc_2$.[12]

Set terbium(III) as central ion, further efforts to increase the anisotropy barrier turned to the perturbation of the ligand field through proper functionalization of phthalocyanine ligands in α and β positions. Introduction of functional groups on peripheral portions of one or both ligands is a straightforward strategy to reach higher $U_{eff}$. Torres and co-workers obtained a record anisotropy barrier for peripherally functionalized $TbPc_2$ with $OC_6H_4$-*p*-$^t$Bu substituents.[13] In our group we recently investigated the magnetic properties of $TbPc_2$ bearing iodine moieties in β position.[14] Considering their amorphous state, they revealed anisotropy barriers (915 K for the homoleptic and 864 K for the heteroleptic complex) slightly higher than amorphous pristine $TbPc_2$ (856 K), but lower than its crystalline form (965 K).[15] Peripheral functionalization on $TbPc_2$, beyond being a powerful tool for investigating the correlation between structure and SMM properties, also offers some hints to overcome the fundamental issue of developing new strategies to properly assemble and integrate these materials into functional devices, not only preserving their properties but possibly even enhancing them. Indeed, thanks to their outstanding magnetic properties, SMMs appeared as promising candidates for several applications, which range from high-density magnetic storage[16] to quantum computing[17] and spintronics.[18] However, before such applications will become a reality, the definition of experimental approaches to evolve from bulk crystals to molecules suitable to be grafted on surfaces is necessary.

### 1.1.4 SMMs on surface

Transferring the magnetic properties from bulk material to the surface is far from trivial: molecule-surface interactions may induce hardly predictable perturbations from chemical modification (redox processes, chemical decomposition,…), that completely alters the magnetic properties of the molecule, to molecular deformations. Considering the impact that even a fine modulation of the ligand field has on the anisotropic barrier, deformations, though not so drastic as a chemical decomposition, can induce a modification of the magnetic exchange pathway or simply alter the easy-magnetization axes, and, as a consequence, the magnetization relaxation mechanisms and barriers. Thus surface effects, as well as interaction with the substrate, can strongly affect the SMM behaviour, either increasing or completely removing the magnetic anisotropy. Physisorption is the easiest and, in theory, least chemically demanding method to produce surface arrays. It has been widely used in conjunction with relatively simple monometallic systems such as $LnPc_2$, which

resist thermal evaporation in Ultra-High Vacuum (UHV). Unfortunately, $LnPc_2$ magnetic behaviour was found to be altered or even suppressed by the deposition process, suggesting that the loss of crystalline packing upon sublimation is likely responsible for affecting the magnetization dynamics. Sessoli and co-workers[15] extensively investigated $TbPc_2$ behaviour in different phases (Figure 1.3); pristine $TbPc_2$ was evaporated in UHV at 400 °C and deposited on Kapton.

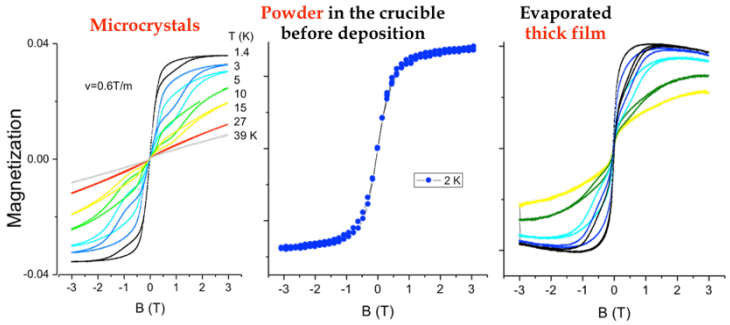


**Figure 1.3** *$TbPc_2$ hysteresis loop in a) microcrystalline sample; b) heated powder before deposition and c) sublimated film on Kapton.*

Interestingly, the mycrocristalline sample showed the typical magnetic profile of terbium double-deckers, with an opening of the hysteresis loop at 15 K (Figure 1.3a), while in the evaporated thick film hysteresis was observed at lower temperature (10 K) (Figure 1.3c). Although the qualitative behaviour remained unaltered, to further understand the origin of this difference, a fraction of the heated sample, extracted from the crucible before evaporation, was magnetically characterized and showed no measurable hysteresis over the whole investigated temperature range (Figure 1.3b). The disappearance of hysteresis in the heated powder and subsequent reappearance once the film was formed proves, on the one hand, the intactness of the complex and, on the other hand, is still intriguing and basically unclear. A likely explanation could be that the harsh thermal treatment causes deformations of the two phthalocyaninato rings from the perfectly staggered situation (45°) (Figure 1.4) observed in the crystal packing, leading to a particularly high efficiency for relaxation mechanisms *via* tunnelling.

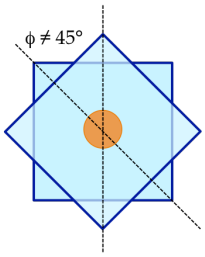


**Figure 1.4** *Distorsions from $D_{4d}$ symmetry induced by intermolecular interactions.*

Peripheral functionalization with proper anchoring group offers an effective alternative to assemble $LnPc_2$ on surface through covalent grafting. Thanks to the formation of more robust bonds, this approach is preferable than the simple physisorption for the realization of durable devices. Furthermore, covalent grafting provides more control over the orientation on surface and coverage density. In our recent communication,[19] we reported an enhancement of magnetic bistability for $TbPc_2$ covalently grafted on silicon wafer compared to evaporated monolayers on noble and ferromagnetic metals. Photoelectron spectroscopy investigations on the robust monolayer, obtained by hydrosilylation of ω-alkenes functionalized double-deckers, suggested a non-innocent role played by the substrate. XPS analysis showed for N*1s* signal an energy shift ascribable either to the stabilization of the cationic specie of $TbPc_2$ formed during the grafting protocol either to an electron depletion of the molecular system due to surface interaction. Although the significant advantages of robustness and enhanced magnetic bistability, covalent approach suffers of poor control over the deposited $TbPc_2$ morphology and limited versatility in the choice of the substrate. Considering these restraints, we proposed a novel protocol for the reversible self-assembly of $TbPc_2$ on surface *via* multiple H-bonding;[20] anchoring is ensured by the strong association of 2-ureido-4[1H]-pyrimidinone (UPy)–2,7-diamido-1,8-naphthyridine (NaPy) complex, respectively present as double-decker peripheral functionalization and as surface decoration. Although not being the only strategy that exploits a non-covalent anchoring, the proposed approach, compared to other reported strategies based on π-π interactions[21] or S-Au bonds,[22] guarantees a long-term stability related to the H-bond architecture, coupled with reversibility through external stimuli (e.g. temperature, solvent…). Furthermore, *ad hoc* functionalization of the NaPy counterpart ideally may give access to the introduction of $TbPc_2$ on all types of surfaces.

Interestingly, quantum effects, which derive from the attainment of the nanometre scale in double deckers systems, may be exploited in molecular

spintronics devices.[23] Thus, besides the choice of the more convenient grafting strategy, addressing technologically relevant substrates would be an attractive goal. In this chapter we present the design of a properly functionalized $TbPc_2$ suitable for the covalent grafting on lanthanum strontium manganite (LSMO); the choice of the surface relies on its wide use as ferromagnetic substrate in organic spin valve devices. Derivatization of the LSMO was achieved through the introduction of phosphonate moieties on the $TbPc_2$ core.

### 1.1.5 Spintronics

The discovery of giant magnetoresistance effect (GMR), independently observed by Grünberg[24] and Fert[25] (Nobel Prize 2007), traditionally marks the birth of spintronics. This quantum mechanical effect, found in multilayered devices composed of alternating ferromagnetic and non-magnetic conductive layers, implies a significant change in the electrical resistance, when an external magnetic field is applied, according to the magnetization alignment of the ferromagnetic portions. The revolutionary idea introduced by this discovery was that electronic spin, as well as electronic charge, could be seen as an "information carrier" in electronic applications. Thus spintronics, portmanteau of the terms *'spin electronics'*, represents the union of electronics and magnetism, committing the binary encoding to electron spin instead of the modulation of electric charge. Expanding the parallelism with electronic charge, indeed, information can be encoded in spins, thanks to their quantized nature, and persists even when the device is switched off. The contemporary exploitation of electronic and spin degrees of freedom appeared particularly promising both at fundamental and applied level, justifying the industrial mass production of spintronics-based devices. Studies on generation, manipulation and detection of spin-polarized electrical current made possible entirely new classes of spin-based sensors, memory and logic devices. In a few years, the new field of "molecular spintronics" emerged, aiming at the creation of molecular devices using magnetic molecules. These devices are generally composed of a semiconductor organic film, which stands between two ferromagnetic electrodes; the first component acts as tunnelling barrier or as spin carrier, while the latter as a spin injector and a spin analyser. Their performances are strongly affected by the nature of boundary region between the organic and inorganic phases.[26] Most important achievements have been hitherto obtained by interfacing organic materials with complex ferromagnetic metal oxides, in particular with Lanthanum Strontium Manganite Oxide (LSMO), whose large

spin polarisation of the surface (nominally 100% at 0 K) and good stability under different conditions may represent a significant advantage with respect to the use of *3d* ferromagnetic thin films. Furthermore, the use of molecules as building blocks allows introducing new functionalities due to the almost infinite combinations offered by the synthesis of complex and tunable molecular objects. Among possible approaches, the introduction of monolayers of magnetic molecules is attracting broad interest; in particular self-assembled monolayer (SAM)-based protocols are among the most used techniques to achieve a bidimensional organization of molecules adsorbed on surface. It is easy to understand why, in this context, the wet chemistry-based deposition of a monolayer of SMMs has attracted growing interest for playing an active role in organic spintronic devices. Quite recently, Urdampilleta and co-workers[27] reported an interesting example of the use of $TbPc_2$ complexes in the preparation of a supramolecular spin valve device. They showed that pyrene functionalized $TbPc_2$, coupled through van der Waals interactions with SWCNT contacted with non-magnetic electrodes, had an influence on the current passing through the molecular quantum dot, thus allowing the readout of the molecular magnetic state by traditional conductance measurements. Their localized magnetic moments led to a magnetic field dependence of the electrical transport through the SWCNT, resulting in magnetoresistance ratios up to 300% at temperatures less than 1 K. This result paved the way to the design of molecular spintronic devices, projecting the implementation of new electrical functionalities and proposing an alternative strategy to expensive lithographic techniques.

Inspired by the described approach, in this Chapter we present the synthesis, chemisorption and magnetic characterization of a $TbPc_2$ complex, specially designed for the functionalization of LSMO, one of the most widely used ferromagnetic substrates in molecular spintronics. Since the aim of the present work has been to perform the optimization and scale-up of a synthesis previously reported in a PhD thesis by our group (Dr. Federico Bertani's PhD thesis, *"Multifunctional Nanomaterials: Theranostic Nanoparticles and SMM-decorated Surfaces"*), we'll rapidly go through the synthetic aspects, then focusing on the grafting protocol and the subsequent magnetic measurements. A diethyl phosphonate moiety has been selected as anchoring group, being compatible with the chemistry of the $TbPc_2$ core structure. This modified hybrid spin injecting electrode has been then used to realize a vertical organic spin valve comprising Gaq3 as organic semiconductor and Cobalt as the second magnetic electrode. The performances of this type of devices have been compared with those of a similar one obtained by replacing the double decker

layer with diamagnetic molecules, diethyl(11-iodoundecyl)phosphonate, bearing the same anchoring group for the chemisorption. The comparison allows disentangling the effect of the chemical functionalization of the manganite from the more specific effect due to the presence of a layer of magnetic molecules forming an additional spinterface for the spin injection into the organic semiconductor.

## 1.2 Results

### 1.2.1 Synthesis and bulk characterization of the LSMO-graftable Tb double decker

In order to promote the covalent grafting on LSMO, a homoleptic $TbPc_2$ bearing two diethyl phosphonate groups ($Tb[Pc(PO_3Et_2)]_2$) as peripheral functionalization on the Pc rings was designed (Figure 1.5). Phosphonic esters are known to ensure the formation of a robust monolayer *via* strong P-O metal linkages.[28]

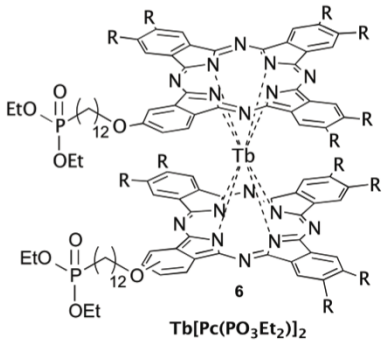


**Figure 1.5** *Chemical structure of the designed target molecule* ***Tb[Pc(PO$_3$Et$_2$)]$_2$ (6)***

Considering the harsh reaction conditions required for both phthalocyanine and $TbPc_2$ formation, post-functionalization of pre-formed $TbPc_2$ complex was needed. The preparation of the dihydroxy-functionalized double decker $Tb[Pc(OH)]_2$ was achieved in two steps starting from the asymmetric $A_3B$-type phthalocyanine Pc(OPMB), modifying a protocol reported by Pushkarev and co-workers.[29] Phthalocyanine formation was performed through a statistical Linstead cyclization of the two monomers **1** and **2**. *P*-methoxybenzyl (PMB), used for protecting the hydroxyl group during the statistical macrocyclisation and the subsequent ligand exchange reaction, allows not only the

discrimination between differently substituted Pcs, but also the introduction of the phosphonate moiety.
Instead, *p-tert*-butylphenoxyl substituents on Pc's residual positions were chosen to increase the solubility, hampering at the same time the formation of *J*-aggregates by steric repulsion. Phthalonitrile **1** was obtained starting from commercially available 4-hydroxy-phthalonitrile in DMF under basic conditions (Scheme 1.1). Functionalized phthalonitrile **2** was synthesized, according to a reported procedure,[30] from 4,5-dichlorophthalonitrile *via* nucleophilic aromatic substitution with 4-*tert*-butyl phenol in DMSO in presence of potassium carbonate (Scheme 1.1).

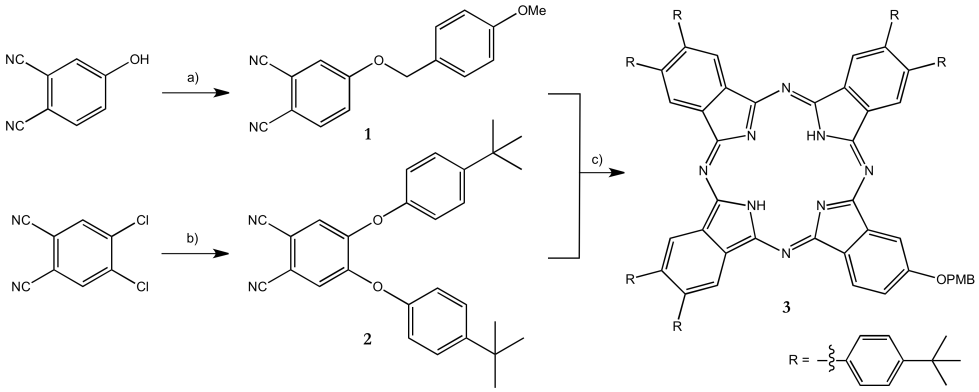


**Scheme 1.1** *Synthesis of $A_3B$ type phthalocyanine* ***3****: a) 4-methoxybenzylchloride, NaH, DMF, 65 °C 4 h, 86%; b) 4-tert-butylphenol, $K_2CO_3$, DMSO, 90 °C, 2 h, 81%; c) Lithium, 1-pentanol, reflux, 3 h, 17%.*

Linstead cyclization of the two functionalized precursors, occurred in presence of *in situ* generated lithium pentanolate, afforded the asymmetric phthalocyanine **3** (Scheme 1.1). Because of the minor reactivity of **1**, a non-stoichiometric ratio (**1**/**2** of 1:2 instead of 1:3) was used.
Complex formation was performed reacting the phthalocyaninato ligand Pc(OPMB) with terbium (III) acetyl-acetonate hydrate in 1-hexadecanol at 180 °C in presence of lithium methoxide (Scheme 1.2). $Tb[Pc(OPMB)]_2$ was obtained as a mixture of constitutional isomers in 35% yield and characterized by UV-Vis spectroscopy and high-resolution matrix-assisted laser desorption ionization time-of-flight mass spectrometry (MALDI-TOF). Deprotection of the two hydroxyl functionalities with trifluoroacetic acid (TFA) in $CH_2Cl_2$ at room temperature afforded $Tb[Pc(OH)]_2$ in quantitative yield. The introduction of the phosphonate groups was realized *via* nucleophilic substitution of diethyl 12-

bromododecylphosphonate (DBDP), previously obtained by microwave-assisted Arbuzov reaction between 1,12-dibromododecane and a sub-stoichiometric amount of triethyl phosphite.

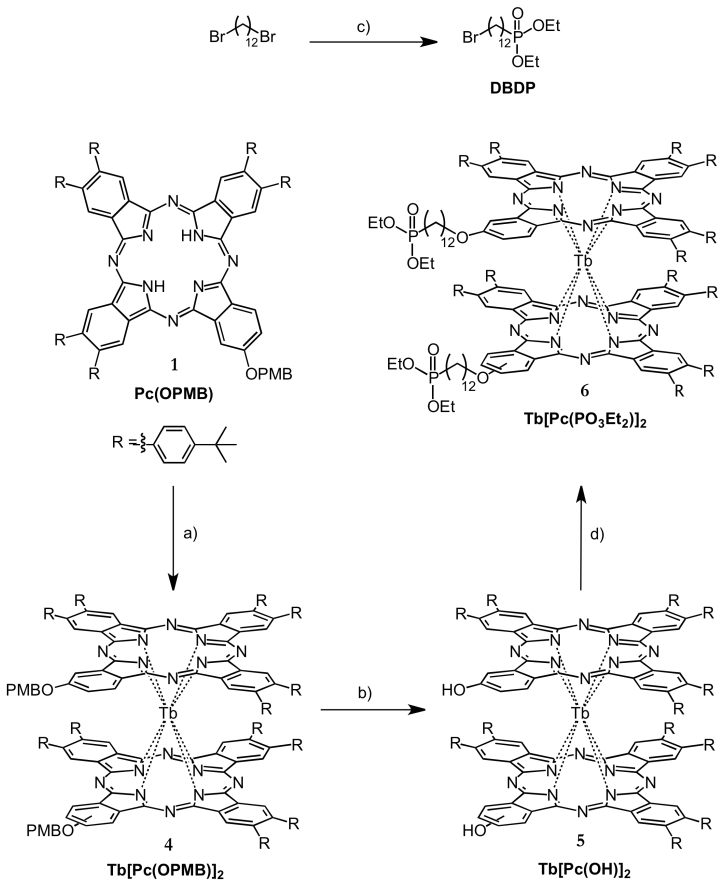


**Scheme 1.2** *Synthesis of* ***Tb[Pc(PO$_3$Et$_2$)]$_2$****: a) Tb(acac)$_3$ · xH$_2$O, MeOLi, 1-hexadecanol, 180 °C, 1 h, 35%; b) TFA, CH$_2$Cl$_2$, 5 h, r.t., quantitative; c) P(OEt)$_3$, 5 min, mw, 220 °C, 90%; d)* ***DBDP****, K$_2$CO$_3$, DMF, 16 h, 90 °C, 48%.*

As demonstrated in our recent works, [20,31] long aliphatic spacers are required to preserve the reactivity of peripheral functionalities in the following steps. Tb[Pc(OH)]$_2$ was reacted with DBDP in N,N-dimethylformamide (DMF) at 90 °C in presence of potassium carbonate. Tb[Pc(PO$_3$Et$_2$)]$_2$ was obtained in 48% yield after column chromatography and was characterized by NMR and UV-

Vis spectroscopies (see SI, Fig. S1-S3) and MALDI-TOF. In particular, MALDI-TOF spectrum (Figure 1.6) reveals the presence of the molecular peak, with an isotopic distribution pattern in agreement with the theoretical one.

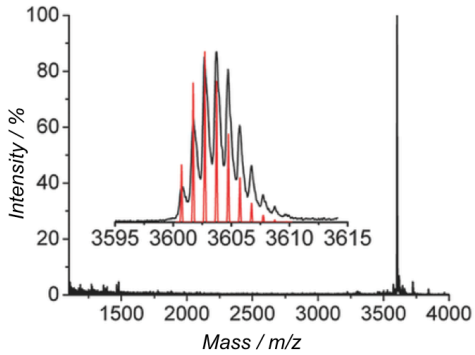


**Figure 1.6** *High resolution MALDI-TOF spectrum of* ***Tb[Pc(PO$_3$Et$_2$)]$_2$****; in the inset experimental (black line) vs. theoretical (red line).*

The characterization carried out with traditional DC and AC magnetometry allows a complete evaluation of the magnetic properties of the complex in the bulk phase. As already observed for other $TbPc_2$ complexes,[15,32] the hysteresis in the magnetization curves is visible below 15 K, thus indicating that the functionalization does not alter significantly the SMM behaviour of the double decker system (Figure 1.7 a).

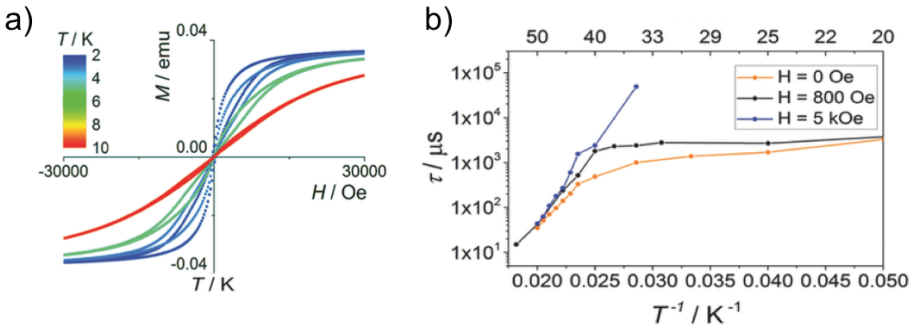


**Figure 1.7** *a) Magnetization vs. field measurements for* ***Tb[Pc(PO$_3$Et$_2$)]$_2$*** *in a temperature range between 2 K and 10 K (colour scale in the inset) and scanning the field between 30 kOe and -30 kOe at 50 Oe s$^{-1}$; b) relaxation times of* ***Tb[Pc(PO$_3$Et$_2$)]$_2$*** *vs. inverse temperature (range 20 – 55 K) at three different static magnetic fields (0 Oe, 800 Oe, 5kOe).*

Zero static field AC susceptibility measurements as a function of temperature are shown in Fig. S4 and, in the out-of-phase component, a frequency dependent peak occurring at relatively high temperatures is visible. The extended Debye model, adopted to analyse these data in the range 0.5 Hz – 10 kHz, allows to extract the relaxation time, $\tau$, of this system for different temperatures (Figure 1.7 b). In the high temperature regime, T > 40 K, the characteristic magnetization dynamic parameters for the system have been extracted on the basis of an Arrhenius model, i.e. $\tau = \tau_0 \exp(\Delta E/k_B T)$. The estimated energy barrier in the thermally activated process, DE = 614(11) K, is smaller than that found for the crystalline phase of $TbPc_2$ (965 K),[13] but in line with the value observed in similar conditions for amorphous non-functionalized $TbPc_2$ systems, in agreement with the amorphous character of $Tb[Pc_2(PO_3Et_2)]_2$ sample. The extracted pre-exponential factor is $\tau_0 = 17(4) \cdot 10^{-11}$ s. Below 40 K, relaxation becomes temperature independent, indicating the onset of a tunnel mechanism of inversion of magnetization, with a significant increase of the width in the distribution of the relaxation times (see SI). The application of a static field (Fig. S5 and S6) leaves unaltered the high temperature behaviour as shown in Fig. 1.7 b, but significantly affects the magnetic relaxation below 40 K, suppressing the tunnelling mechanism with $\tau$ exceeding the accessible timescale of the AC susceptometry. A narrower distribution of $\tau$ is observed in static field, in analogy to what previously found for other functionalized and non-functionalized $TbPc_2$ complexes.[22] This can be explained with the fact that, when tunneling is not suppressed by the external field, the distorsions from idealized $D_{4d}$ strongly affect the tunneling efficiency.

### 1.2.2 Chemisorption of the Tb double-decker on LSMO

The deposition of $Tb[Pc(PO_3Et_2)]_2$ on LSMO has been achieved by implementing the same procedure previously described for the self-assembly of nitronyl nitroxide radicals functionalized with the diethyl-phosphonate group.[33] In parallel, also the deposition of a ω-iodo alkyl-phosphonate, diethyl(11-iodoundecyl)phosphonate, has been performed to obtain a reference diamagnetic layer (see SI for details). Chemisorption of these molecular layers (see Methods for details and SI) has been verified by XPS. Focusing on the grafting of $Tb[Pc(PO_3Et_2)]_2$, this spectroscopic characterization (See Fig. S8) confirms the intactness of the molecular layer. Due to the presence of interfering signals, only the Tb$3d_{3/2}$ (at 1277.7 eV and a shake-up at 1282.7 eV)

and N*1s* signals have been used for this analysis. The N/Tb ratio is 16.7 ± 1.0, perfectly in line with the expected value (16); additionally, the N*1s* peak fitting reveals two components at 398.5 eV and at 400.2 eV. The first peak is directly attributable to a nitrogen in the bulk $TbPc_2$,[34] while the one at higher energy (400.2 eV) suggests that part of the chemisorbed molecules are influenced by the substrate, in analogy to what observed for similar complexes chemisorbed on Si. To characterize the magnetic behaviour of the hybrid system, an X-ray absorption spectroscopy (XAS)-based study using circularly polarized light has been performed to extract the XMCD contribution and its magnetic field dependence at low temperature (2.2 + 0.2 K) for both substrate and molecular layer.

Absorption and dichroic spectra measured at the $L_{2,3}$ edges of Mn (Fig. S6) exhibit the standard LSMO features in perfect agreement with previous reports.[35] Analogously, the XAS and XMCD investigations at Tb $M_{4,5}$ edges, reported in Fig. 1.8, show the expected $TbPc_2$ spectral features[32] and the "edge jump" analysis[36] of the derived isotropic spectrum confirms the formation of a deposit of the order of 0.8 monolayer if compared to a monolayer deposit of $TbPc_2$ sublimated on LSMO.[37] The magnetization curves extracted for the $L_3$ edge of Mn (Fig. S9) show the typical angular dependence of LSMO thin films with in-plane magnetic anisotropy.

On the other hand, the magnetization curves obtained at the Tb $M_5$ edge (Figure 1.8 c) do not follow the behaviour of the LSMO substrate excluding the presence of a strong magnetic coupling between the molecular layer and the ferromagnetic substrate in contrast to what found in other hybrid $TbPc_2$-based assemblies.[38] The presence of a small hysteresis, even if much narrower than the one recorded either by conventional magnetometry (Figure 1.7 a) or XMCD (Figure S10) on the bulk phase, confirms the persistence of the SMM behaviour. Similar observations have been previously reported[32,39] and can be partially justified with the distortion of the molecular structure induced by the chemisorption on the LSMO substrate, as well as some alteration of the electronic structure of the coordinating ligands that could be in line with the features observed in N*1s* XPS spectrum.

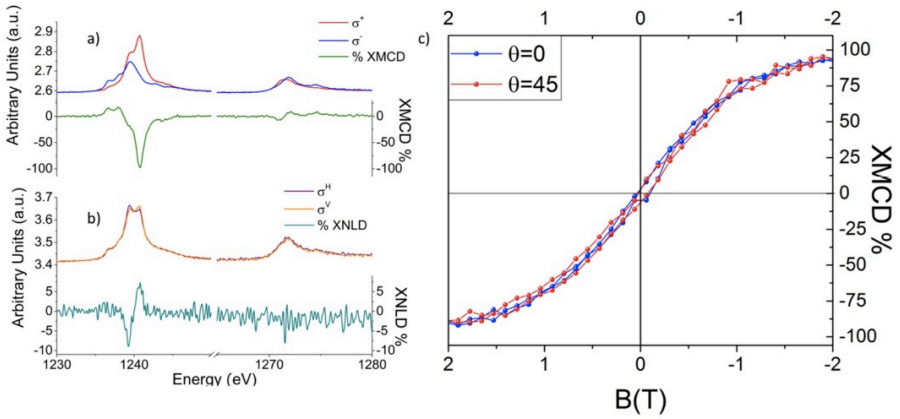


**Figure 1.8** *a) XMCD measurements at 2.2 ± 0.2 K under a 30 kOe magnetic polarized light; green line is obtained from the difference between the left (σ+, red line) and right (σ-, blue line) polarized light; b) XNLD measurements for $TbPc_2$@LSMO performed at 2.2 + 0.2 K under a 30 kOe magnetic field to enhance TEY sensitivity. XNLD (dark green line) is obtained from the difference between the horizontally (σH, purple line) and vertically (σV, orange line) polarized light; c) Field dependence of the XMCD signal measured at the maximum of the dichroic signal at the M5 edge for $TbPc_2$@LSMO. The curves are reported at two angles, q, between the magnetic field and the surface normal (q = 0° and q = 45°).*

Linearly polarized light was also used in order to get information about the orientation of the molecules with respect to the surface. The derived X-ray Natural Linear Dichroism (XNLD) spectrum measured at q = 45° (Figure 1.8 b) shows a small dichroic contribution indicative of a slightly preferential molecular orientation with the phthalocyanine rings parallel to the plane of the LSMO surface. We notice the opposite trend with respect to non-functionalized $TbPc_2$ molecules deposited by sublimation on LSMO, that tend to assemble with a standing configuration.[38]

### 1.2.3 Device preparation and characterization

The effects induced by the SMM layer on the spin injection process were investigated by the direct comparison of two specially designed organic spin valve devices (OSV) differing only by the presence or the absence of the $TbPc_2$, while keeping similar all the other parameters. Vertical cross-bar geometry was employed with LSMO as bottom and Co as top electrodes, 40 nm of tris(8-hydroxyquinoline) Gallium(III) (Gaq3) as charge/spin transport layer, and an Aluminium oxide buffer layer between the Gaq3 and Co.[40] The two

ferromagnetic electrodes are characterized by different coercive field values, allowing the achievement of parallel and antiparallel relative orientations of their magnetic moments and enabling the spin valve functionality.[37] In both sets the LSMO electrode was functionalized by chemisorbing a single layer of alkyl-phosphonate molecules. The first set contained the ω-iodo alkyl-phosphonate to chemically tailor the bottom injecting interface, while the second set was additionally characterized by the presence of SMM centres.

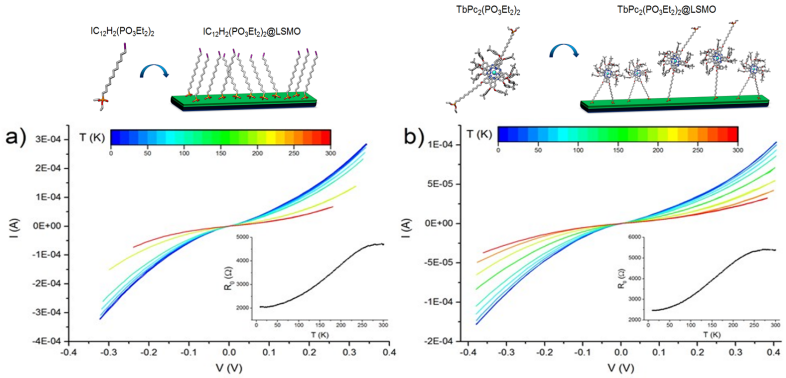


**Figure 1.9** *a) I-V characteristics for OSV functionalized with ω-iodo alkyl-phosphonate and b) with Tb[Pc(PO$_3$Et$_2$)]$_2$ at different temperatures. In the insets: values of resistance (measured at I = 0.5 μA and with no applied magnetic field) as function of temperature in the range 3 – 300 K. On top of I-V curves: chemisorption on LSMO of the two molecules.*

Figure 1.9 reports the I-V characteristics measured at different temperatures in the range 3 – 300 K for the devices bearing respectively the ω-iodo alkyl-phosphonate and Tb[Pc(PO$_3$Et$_2$)]$_2$. The two different functionalizations sketched in Figure 1.9 do not induce qualitative modifications: both sets show typical trends for this geometry and electrodes[41] and can be tentatively described by transport *via* both the LUMO (or HOMO) level[42] or the impurity band model. The observed increase in the resistivity values when Tb[Pc(PO$_3$Et$_2$)]$_2$ is present could be reasonably attributed to an increased thickness of the chemisorbed layer or to a different transport efficiency of the embedded system.

The magnetoresistance (MR) detected for the two sets of devices for the 5 – 200 K temperature interval is presented in Fig. 1.10. The in-plane magnetic field was swept from -1 T to +1 T and *viceversa,* while measuring the device resistance in a four-point probes configuration at a fixed 0.5 μA applied current. Both types feature inverse spin-valve effect, i.e. the lower resistance

corresponds to antiparallel Co and LSMO magnetizations (see arrows in Fig. 1.10). This behaviour is typical for OSV devices based on LSMO-quinolines-Co systems and was confirmed for a number of spin valve devices.[33,37,41-43] It is generally accepted that the fundamental contribution to this inversion comes from the interfacial hybridization between one or both magnetic electrodes and the organic molecules (the so-called spinterface effect).[44] We thus note that the performed functionalization does not induce qualitative changes to this generally established picture.

We also observe a fine structure for the antiparallel resistive section detected at low temperatures for the ω-iodo alkyl-phosphonate set of measurements. Such features are quite typical for OSV and even inorganic devices and are basically attributed to local imperfections of electrodes.

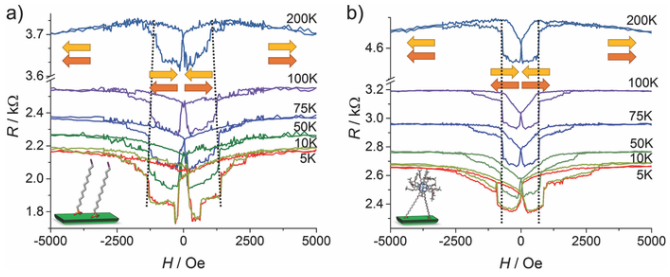


**Figure 1.10** *Inverse spin-valve effect measured sourcing a constant current I = 0.5 μA for a) ω-iodo alkyl-phosphonate and b) Tb[Pc(PO$_3$Et$_2$)]$_2$-based OSV in the temperature range 5 – 200 K; the high and low resistance states correspond to parallel and antiparallel configurations respectively (see arrows). Dotted lines are guides to the eyes to follow the temperature dependence of high switching fields.*

In order to unveil the contribution of the SMM layer to the interfacial effects, a quantitative analysis of data has to be employed. The first statistically relevant difference between the two sets is noticeable for the switching fields. The low switching fields in both types of devices closely correspond to the coercive fields of Co electrodes (see SI, Fig. S11).

Conversely, the high switching fields significantly exceed those of the manganite electrodes (see SI, Fig. S12), and can be tentatively attributed to the hybrid LSMO-PO$_3$Et$_2$ bilayers, similarly to previously reported chemisorbed interfaces,[45] resulting as the most sensitive region of the field scan to the alterations we operated. In fact these external (high) switching fields feature a remarkably different behaviour: when the LSMO is functionalized with the alkylphosphonate layer, the external switching fields increase by decreasing the temperature, as expected for ferromagnetic thin films (see Figure 1.10 a). On the

other hand, when the $TbPc_2$ molecule is integrated at the interface, the standard magnetic behaviour is no longer detected for LSMO based electrode: the switching fields surprisingly become temperature independent above 50 K (see Figure 1.10 b). The same temperature of about 50 K separates two different regimes also for the strength of magnetoresistance as function of temperature. Fig. 1.11 shows the square root of the MR *vs.* T. The MR½(T) plot is linear in standard LSMO based spin valves (without additional functionalization), whose temperature dependence is mainly governed by LSMO surface spin polarization.[33] While the ω-iodo alkyl-phosphonate set generally obeys this standard temperature dependence (red dots in Figure 1.11), a clear deviation from linear behaviour for T < 50 K is visible for samples with LSMO electrodes functionalized with the $TbPc_2$ (blue dots).

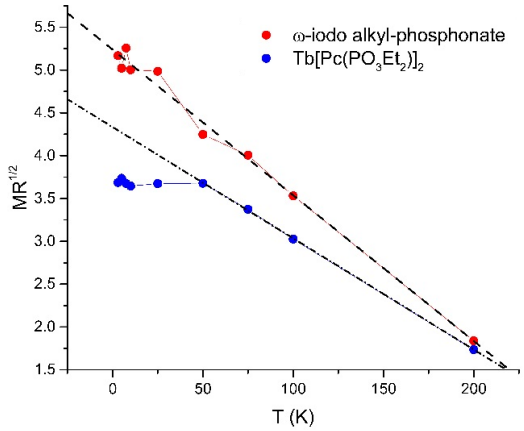


**Figure 1.11** *Square root of the MR as function of temperature for representative devices from the two sets. Red circles represent the LSMO-based OSV functionalized with ω-iodo alkylphosphonate, while blue circles the ones functionalized with $Tb[Pc(PO_3Et_2)]_2$. The black lines are guides to the eye.*

A pictorial comprehensive representation of the OSV behaviour is proposed in Fig. 1.12 as a useful approach to describe the temperature dependence of the magneto-transport character of the devices. Here we show the maps of the absolute value of normalized differences between the MR measurements obtained sweeping the magnetic field from negative to positive values and those obtained in the way back, for two representative devices from the two batches. The device with the monolayer of ω-iodo alkyl-phosphonate is characterized by a temperature dependent hysteresis (with coercive fields that vary linearly from 1400 Oe at 3 K to 1000 Oe at 250 K). On the opposite, $TbPc_2$ based OSV, above 50 K, shows a narrower and temperature independent

hysteretic behaviour (coercive field is 700 Oe in almost the entire temperature range covered). This confirms the evidence from Fig. 1.10 and represents an alternative way to figure out the information. Although in Fig. 1.12 we cannot see each singular MR measurement, we can grasp at a glance the comprehensive trend. We reckon this is a useful pictorial device oriented representation.

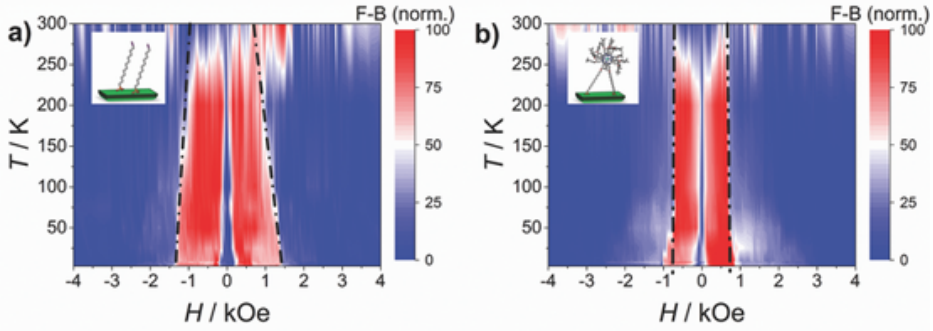


**Figure 1.12** *Colormap of the normalized (to 100) difference between the MR measurements obtained by sweeping the magnetic field forward and backward in the temperature range 3 - 300 K for the OSV functionalized with ω-iodo alkyl-phosphonate (a) and with* $Tb[Pc(PO_3Et_2)]_2$ *(b). The dashed and dotted black lines are guides to the eye for following the coercive fields.*

## 1.3 Discussion

Analysing the coercive fields and magnetoresistance trends in temperature, it becomes clear that the former parameter is mainly altered above 50 K, while the latter below this temperature. This indicates a conceptually different contribution of Tb double decker on the two different parameters. To understand these effects it is necessary to analyse the process of the spin injection, which governs the magnetoresistance and related measurable parameters and, on the other hand, to consider the magnetic properties of the added molecule. Starting from the MR, we can limit our analysis to the case when LSMO injects carriers and spins; inverting the current, i.e. collecting spins with LSMO, does not change the physical picture. The charge-spin injecting interface represents a complex system, where the injecting surface is composed of the last metallic layer strongly hybridised with the first molecular layer; this is followed by partly modified second molecular layer and further by the three-dimensional van der Waals molecular solid.[46] It is widely agreed that the injection of carriers proceeds via a two-step process: the tunnelling event from

the injecting surface into the first non-hybridised layer and the subsequent diffusion of carriers (polarons) into the bulk of molecular solid.[47] There the transport proceeds *via* hopping processes, where the carriers "jump back and forth" gradually moving the polaron to the neighbouring site.[49] In our case the injecting surface is represented by the LSMO-alkylphosphonate bilayer, while the first non-hybridised molecular layer is the $TbPc_2$, with its strong paramagnetic behaviour at these temperatures. The last injecting step is then represented by the diffusion from the double decker to the bulk of $Gaq_3$. It is clear that, as far as the spin transfer is concerned, the injection process can be strongly affected by the paramagnetic scattering. The decrease of the MR with respect to the expected temperature trend may be explained by an additional spin scattering induced by $TbPc_2$ molecules. This scattering is supposed to proceed *via* a partial transfer of the magnetic momentum from incoming charges and localised impurities, like in doped inorganic semiconductors. The scattering is thus expected to depend on the interaction with these magnetic centres and their magnetic dynamics. On the basis of earlier descriptions of the $TbPc_2$ electronic structure,[50] we can exclude a direct involvement of the localized *4f* orbitals of $Tb^{3+}$ ion in the transport process. More probably, charge transfer can occur here through the singly occupied molecular orbital (SOMO) delocalized on the phthalocyaninato ligands. Carriers can feel the magnetic moment of the SMM through space (dipolar interaction) or through a weak, bond-mediated, exchange interaction.[51] We remind that the $TbPc_2$ system has its own intrinsic dynamics defined by its characteristic relaxation time $\tau$. At 50 K the relaxation time value, even in presence of magnetic fields like those experienced in the device, is of the order of 10 μs (see Figure 1.7 b) and this parameter is extraordinary close to the carrier diffusion time ($\tau_d$) in $Gaq_3$. Indeed, the mobility in the quinolines is notably in the interval of $10^{-4}$ – $10^{-5}$ $cm^2/Vs$ with corresponding diffusion times between 1 μs and 10 μs respectively, as evaluated from the Einstein equation. From the model of charge injection described above, it is clear that the diffusion inside $Gaq_3$ represents the "escape channel" (or the "arrival gate", according to the polarity) for carriers localized in the frontier orbitals of $TbPc_2$. This diffusion process defines the time along which the injected spins (or the collected ones) are exposed to the magnetic scattering interaction. The sizeable reduction of the magnetoresistance with respect to the case without the SMM monolayer (Fig. 1.11) can thus be attributed to an additional scattering. Although a description of the microscopic mechanisms of such scattering is still lacking, some possible general trends can be figured out from the involved time scales and their

temperature dependences by considering two limit cases, namely $\tau_d << \tau$ and $\tau_d >> \tau$. In the first case, the magnetic dynamics of the $TbPc_2$ molecule is slower than the charge diffusion process through the $Gaq_3$: this means that its magnetic moment may be considered fixed with respect to the moving carrier. The latter will thus experience, each time it interacts during its diffusive walk with a $TbPc_2$ molecule, the molecular magnetic moment as an additional local static field, the precession around which will partially modify its spin, inducing an additional decrease of magnetoresistance (Figure 1.11). In the opposite case, $\tau_d >> \tau$, the dynamics of $TbPc_2$ is faster than the charge carrier diffusion time and the spin scattering channel cannot be established: the MR is again fully governed by the manganite spin polarisation. This model allows to describe the MR(T) behaviour observed in the OSVs studied: when T > 50 K, we are in the $\tau_d >> \tau$ case (see Fig. 1.7 b) and MR(T) follows the surface magnetization of the LSMO electrode being linearized in the $MR^{½}$ vs T plot.[41] Once temperature is lower than 50 K, the system enters in the $\tau_d << \tau$ regime: a new scattering channel is present which constitutes a bottleneck for spin polarized currents leading to the plateau observed in MR(T) curves of OSV comprising $TbPc_2$ molecules. Devices functionalized with ω-iodo alkyl-phosphonate are instead not affected by this additional magnetic scattering channel and their MR(T) is indeed determined only by manganite spin polarization. Considering the coercive fields and their trend with temperature, we note that this parameter is strongly modified, in contrast to MR, above 50 K, which is in the pure paramagnetic regime of $TbPc_2$. The coercive field $H_C$ represents the applied field value for which half of the magnetic volume has switched its magnetization direction and is strongly related to the dynamics of the domain wall motion. In a magnetoresistance experiment the sensing probe is the spin of the charge carriers, i.e. these magnetic processes are seen from the carriers' perspective. The coercive fields ascribed to the LSMO interface are higher than those measured directly on manganite films. This is a typical scenario in OSVs and can be ascribed to the modification of the surface magnetism of LSMO (or other electrode) *via* the hybridisation with grafting molecules of the SAM.[46b] It is reasonable to assume that a layer of fast relaxing $TbPc_2$ magnetic moments, in contact with this hybridised interfacial layer, may modify the magnetic dynamics of the latter. We can suppose that considering separately the spinterface, i.e. the bilayer formed by the surface of LSMO and the alkyl-phosphonate, is not sufficient to describe the magnetic reversal process because of the additional dipolar interaction of this ultrathin layer with the magnetic molecules. Nevertheless, to the best of our knowledge there are no available

models able to treat these effects. The presence of a strong magnetic layer in the vicinity of the spin injecting surface may represent a powerful tool for the investigation of the magnetic dynamics and other key magnetic parameters and we believe that understanding this from both experimental and theoretical point of view is crucially important.

## 1.4 Conclusions

A new derivative of $TbPc_2$ engineered for the LSMO functionalization has been prepared and used to create an additional spinterface in a vertical organic spin valve. The behaviour of this hybrid spin valve has been compared with that of a similar device fabricated by the chemisorption of a diamagnetic alkyl-phosphonate system in order to disentangle the role of the chemisorbing agent from the additional effects due to the introduction of an almost decoupled SMM which behaviour has been preliminarily evaluated by XAS-based techniques. The crafted spinterface plays an active role establishing an additional spin-scattering layer able to control directly the MR strength. This regime is active below a threshold temperature that can be correlated to the characteristic timescale of the dynamics of the SMMs. Above this critical temperature an unusual effect of freezing the coercive fields of the vicinal SMM magnetic electrode was detected. The observed results open novel perspectives on the use of these molecular layers with a controlled magnetism for a functional tailoring of the spinterface, although a deeper understanding of the interaction between the carriers' spins and single molecule magnets is strongly required.

## 1.5 Acknowledgments

Financial support from the COST Action CA15128 –MOLSPIN and the Italian MIUR through the Research through the PRIN project QCNaMos N. 2015HYFSRT. Special thanks to Dr. Alessandro Pedrini and Dr. Federico Bertani from the University of Parma. Thanks to Dr. Gianluca Paredi of SITEIA, University of Parma, for high-resolution MALDI-TOF MS analyses and Centro Intefacoltà di Misure "G. Casnati" of the University of Parma for the use of NMR facilities. Particular acknowledgments to Prof. Roberta Sessoli, Dr. Matteo Mannini and Dr. Nicola Cristiani from the department of Chemistry, University of Firenze, for magnetic measurements. Thanks to SOLEIL for provision of

synchrotron radiation facilities (project 20150429) and all the staff for assistance in using DEIMOS beamline. Giuseppe Cucinotta and Lorenzo Poggini contributed equally to this work.

## 1.6 Experimental section

Phthalocyanine **Pc(OPMB)** was prepared according to modified published procedures.[21]

**Diethyl 12-bromododecylphosphonate (DBDP)**
A mixture of 1,12-dibromododecane (2.0 g, 6.1 mmol) and triethylphosphite (0.35 mL, 2.0 mmol) was stirred at 220 °C under microwave irradiation for 5 minutes. The resulting solution was dried under vacuum and the residue was purified by flash column chromatography (ethyl acetate/hexane 7:3) to give **DBDP** (0.7 g, 1.8 mmol, 90%) as a colourless oil.
$^{1}$H NMR (400 MHz, $CDCl_3$): δ (ppm) = 4.08 (q, 4H, *J* = 6.1 Hz, POC**H$_2$**), 3.39 (t, 2H, *J* = 6.7 Hz, BrC**H$_2$**), 1.83 (q, 2H, *J* = 6.9 Hz, C**H$_2$**), 1.70 (m, 2H, C**H$_2$**P=O), 1.57 (m, 2H, C**H$_2$**), 1.42-1.25 (m, 22H, C**H$_2$** + C**H$_3$**).
$^{31}$P{$^{1}$H} NMR (162 MHz, $CDCl_3$): δ (ppm) = 32.7 (s, P=O). ESI-MS m/z: 385.2 $[M+H]^+$, 407.4 $[M+Na]^+$, 425.1 $[M+K]^+$.

**Tb[Pc(OPMB)]$_2$ (4)**
To a dispersion of **Pc(OPMB)** (0.127 g, 0.08 mmol) in 0.8 g of 1-hexadecanol, $[Tb(acac)_3] \cdot xH_2O$ (0.018 g, 0.04 mmol) and MeOLi (0.009 g, 0.24 mmol) were added. The resulting mixture was stirred at 180 °C for 1 h. The dark-green residue was dissolved in $CHCl_3$, 2,3-dichloro-5,6-dicyano-*p*-benzoquinone (DDQ, 0.009 g, 0.04 mmol) was added, and the reaction was stirred at room temperature for 0.5 h. The solvent was removed under reduced pressure and the solid was purified by flash column chromatography ($CH_2Cl_2$/hexane 6:4) to give **Tb[Pc(OPMB)]$_2$** as a green solid (0.046 g, 0.014 mmol, 35%).
UV-Vis ($CHCl_3$): $\lambda_{max}$ = 921, 682, 615, 479, 360, 331.
MALDI-TOF *m/z*: $[M]^+$ calcd for $C_{200}H_{192}N_{16}O_{16}Tb$, 3232.396; found, 3232.352.

**Tb[Pc(OH)]$_2$ (5)**
Trifluoroacetic acid (3 mL) was added to a solution of **Tb[Pc(OPMB)]$_2$** (0.046 g, 0.014 mmol) in 10 mL of $CH_2Cl_2$. The reaction mixture was stirred at room temperature for 5 h. The solvent was evaporated to yield **Tb[Pc(OH)]$_2$** (0.043 g,

0.014 mmol, quant.), that was used without further purification for the next step.
UV-Vis ($CHCl_3$): $\lambda_{max}$ = 918, 681, 613, 491, 363, 330.
MALDI-TOF *m/z*: $[M]^+$ calcd for $C_{184}H_{176}N_{16}O_{14}Tb$, 2992.281; found, 2992.250.

**Tb[Pc($PO_3Et_2$)]$_2$ (6)**
To a solution of **Tb[Pc(OH)]$_2$** (0.035 g, 0.012 mmol) in 10 mL of DMF, **DBDP** (0.018 g, 0.048 mmol) and $K_2CO_3$ (0.017 g, 0.12 mmol) were added. The reaction mixture was stirred overnight at 90 °C. The solvent was removed under reduced pressure and the crude was purified by flash column chromatography ($CHCl_3$/MeOH 98:2) to give **Tb[Pc($PO_3Et_2$)]$_2$** as a green solid (0.021 g, 0.005 mmol, 48%).
$^{31}P\{^1H\}$ NMR (162 MHz, $CDCl_3$): δ (ppm) = 31.5 (s, P=O).
UV-Vis ($CHCl_3$): $\lambda_{max}$ = 926, 680, 615, 469, 360, 330.
MALDI-TOF *m/z*: $[M]^+$ calcd for $C_{216}H_{242}N_{16}O_{20}P_2Tb$, 3600.714; found, 3600.705.

**LSMO preparation and functionalization**
The LSMO films have been grown on Neodymium-Gallium Oxide (NGO) single crystals by using the channel spark ablation (CSA) technique.[52] Morphology of the electrodes has been evaluated by Atomic Force Microscopy (See Fig S13) prior functionalization. These surfaces have been cleaned using a protocol described elsewhere[53] and incubated at about 60 °C for 20 h in a 2 mM solution of Tb[Pc($PO_3Et_2$)]$_2$ or diethyl(11-iodoundecyl)phosphonate in a mixture 3:1 of MeOH/$CH_2Cl_2$. Slides were rinsed several times with pure solvents, sonicated in the solvents solution for 30 minutes, rinsed a second time and dried under nitrogen flux in order to assure the removal of the molecules not directly interacting with the LSMO.

**XPS characterization**
In order to minimize air exposure and atmospheric contamination, samples were mounted on sample holder under dry nitrogen environment in a portable glove bag, which was then connected to the fast-entry lock system of the XPS chamber. Spectral analysis consisted in a linear background subtraction and deconvolution using a mixed Gaussian and Lorentzian lineshapes for each spectral component (See SI for further details)

**Synchrotron characterization**
The XAS/XMCD experiments have been performed on monolayer samples at the DEIMOS beamline[54] of the SOLEIL Synchrotron facility. The density of

photon from the X-ray beam has been reduced to prevent any radiation damage. None have been observed. A magnetic field up to 30 kOe was applied along the photon propagation at variable angle with the normal to the surface. The reported XAS spectra have been acquired at the $L_{2,3}$ edges of Mn and $M_{4,5}$ edges of Tb edges under 30 kOe of magnetic field (applied parallel to the X-ray propagation vector) and using the two circular polarization (left, s+ and right, s-) at normal incidence (q = 0°) and rotating the sample plane q = 45° respect to the X-ray propagation vector. XMCD is extracted as the difference $s^- - s^+$. The XNLD spectrum is the difference between vertically and horizontally polarized light absorption, both measured at q = 45°. All the spectra have been normalized following the procedures described in earlier reports.[32,55] The field dependence of the XMCD signal for both the Tb $M_5$ edge and Mn $L_3$ edge were recorded at q = 0° and 45°.

**Spin-valve preparation**

The typical vertical devices were realized following the procedure described on earlier reports[26b,33] using the LSMO electrodes patterned over a STO substrate and functionalized with monolayers of $Tb[Pc(PO_3Et_2)]_2$ with alkyl-phosphonate or ω-iodo alkyl-phosphonate. Subsequently, a 40 nm thick molecular film of $Gaq_3$ was thermally evaporated on the functionalized LSMO surface. A cobalt electrode was then deposited together with an additional tunnelling barrier constituted by a 2 nm thick $AlO_x$ layer at the $Gaq_3$/Co interface in order to avoid cobalt inter-diffusion inside the OSC, which could led to pinholes creation between the two electrodes. Using this strategy we prepared three identical devices with an active area of 1 mm x 0.1 mm.

## 1.7 Supporting Information

### NMR characterization of $Tb[Pc_2(PO_3Et_2)]_2$

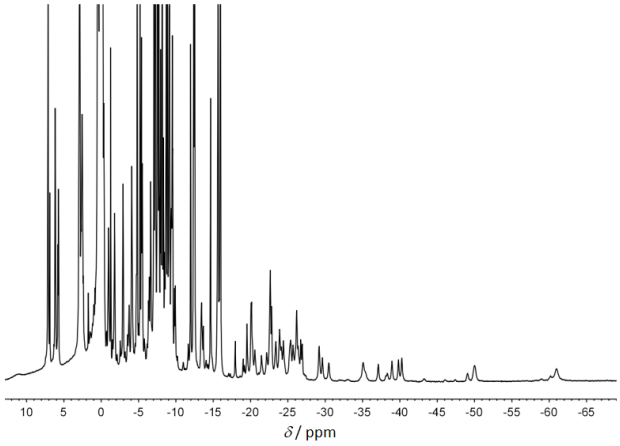


**Figure S1** *$^{1}H$ NMR spectrum (400 MHz, $CDCl_3$, 298 K) of $Tb[Pc(PO_3Et_2)]_2$.*

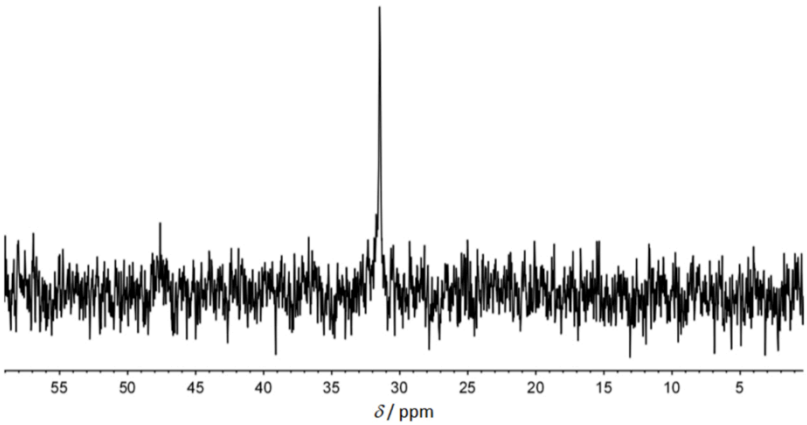


**Figure S2** *$^{31}P$ NMR spectrum (162 MHz, $CDCl_3$, 298 K) of $Tb[Pc(PO_3Et_2)]_2$.*

### UV-Visible absorption characterization of $Tb[Pc_2(PO_3Et_2)]_2$

In the UV-Vis spectrum of $Tb[Pc(PO_3Et_2)]_2$ solution in chloroform, it was possible to notice the promotion of an electron from the first semi-occupied molecular orbital (SOMO) to the second LUMO and from the second fully occupied HOMO to the first LUMO with the Q band at 680 nm. At 330 nm and 360 nm the spectrum shows a typical split Soret band, resulting from the electronic transitions from the third occupied HOMO to the first LUMO. At 469 nm and 926 nm were found the two weak π-radical bands due to electronic transitions from the SOMO orbital to the degenerate LUMO. [S1]

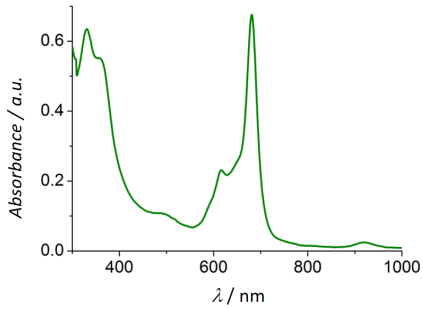


**Figure S3** *UV-Vis absorption spectrum of $Tb[Pc(PO_3Et_2)]_2$ complex in $CHCl_3$.*

### AC magnetic characterization of bulk $Tb[Pc(PO_3Et_2)]_2$

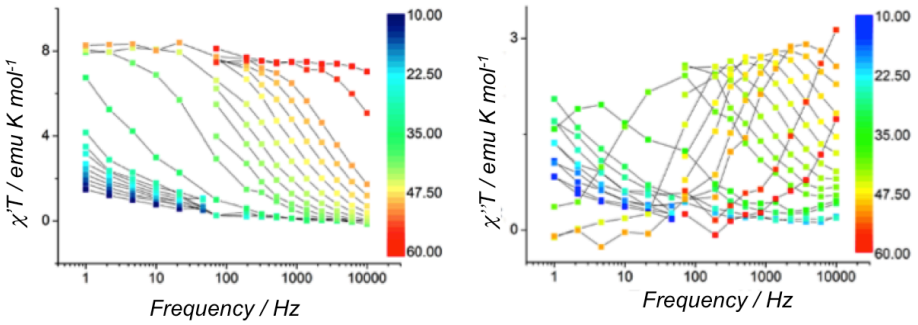


**Figure S4** *Frequency dependence of the χ'T product and χ''T product (left and right, respectively) as a function of temperature in zero static field.*

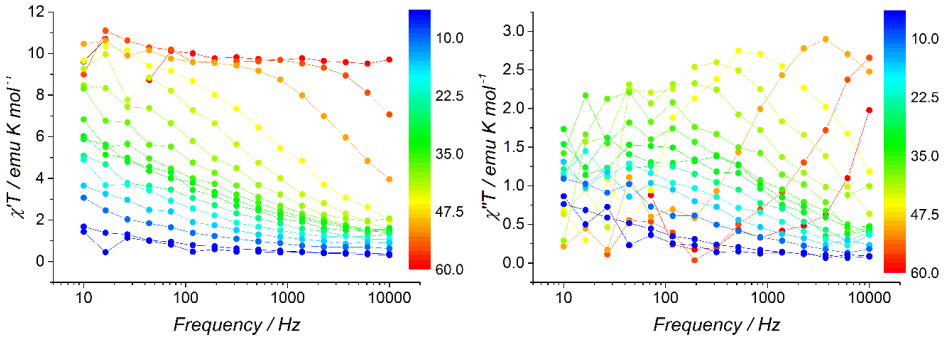


**Figure S5** *Frequency dependence of the χ'T product and χ''T product (left and right, respectively) as a function of temperature at 800 Oe static field.*

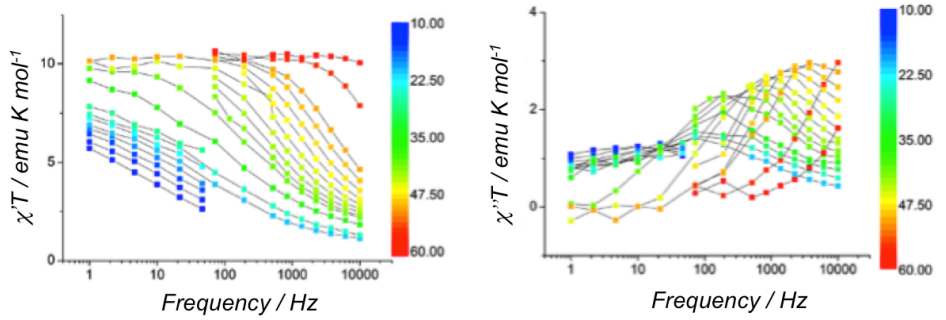


**Figure S6** *Frequency dependence of the χ'T product and χ''T product (left and right, respectively) as a function of temperature at 5000 Oe static field.*

### Chemisorption of ω-iodo undecyl–phosphonate

ω-iodo undecyl-phosphonate has been specifically selected as a simple commercial functionalizing agent. The choice of iodine functionalization has been done in order to provide an internal marker that can be used to easily confirm the presence of the molecular layer through the XPS investigations. This aspect is very important because the XPS P2*p* peak at ca. 132.9 eV,[S2] that could indicate the chemisorption of the molecule, is hidden by the Sr3*d* peak at ca. 133.5 eV[S2] present in the LSMO substrate, making almost impossible the phosphorous identification. On the contrary the I3*d* peak, not overlapping to other signals, can be used to estimate the molecular content at the surface, even if no direct indication can be inferred on the occurrence of a real chemisorption.

This reference signal has been used here also to optimise the deposition protocol, including the cleaning phase carried out by sonication; this treatment is fundamental for removing physisorbed molecules and leaving on surface only those strongly interacting with the LSMO substrate. The XPS characterisation, performed before and after sonication, is reported in Figure S7.

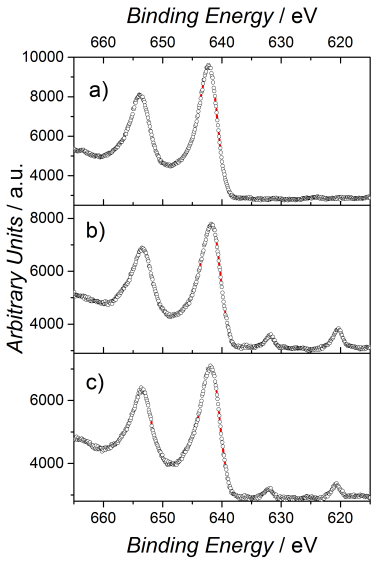


**Figure S7** *XPS spectra in the Mn2p and I3d region on the pristine LSMO (a), before (b) and after (c) treatment in ultrasonic bath for the ω-iodo undecyl-phosphonate functionalised surface.*

The decrease in the intensity of I3*d* peaks after the sonication confirms the initial presence of physisorbed molecules removed with the sonication treatment. In order to have an estimation of the trend of desorption, the ratio between areas of Mn2*p* and I3*d* regions was employed. A decrease of ca. 50% of molecules initially present on LSMO surface can be estimated with this analysis, thus demonstrating that the sonication is a fundamental step to remove the excess of molecular layer present on the surface. Removal of ethyl groups protecting the phosphonate linker head is promoted by the LSMO catalytic properties[S3] leading to the formation of a bond with the oxide surface and the subsequent elimination of ethanol.[28b,34,S5]

**XPS characterization of $Tb[Pc(PO_3Et_2)]_2$ in bulk and monolayer samples**

The elemental ratio between Terbium and Nitrogen was evaluated by estimating the integrated area of each component, this value was corrected by the corresponding photoelectron cross-section for the atomic orbital of interest (Tb*3d* and N*1s*) and further corrected extracting empirical atomic sensitivity ratio for these elements on an non-functionalized $TbPc_2$ system sublimated in UHV on HOPG freshly cleaved surface and directly measured *in situ* using the same experimental conditions (see experimental section for details). The $TbPc_2$/HOPG system was selected in order to reproduce similar chemisorption geometry to the one observed by XNLD on $TbPc_2(PO_3Et_2)_2$ complex chemisorbed on LSMO.[S6,S7] The intensity of the signal for each element corresponds to the area of the respective peak, calculated by standard deconvolution using a mixed Gaussian (G) and Lorentzian (L) line-shapes (ratio G = 70% L = 30%) and subtracting the inelastic background by means of the linear background.

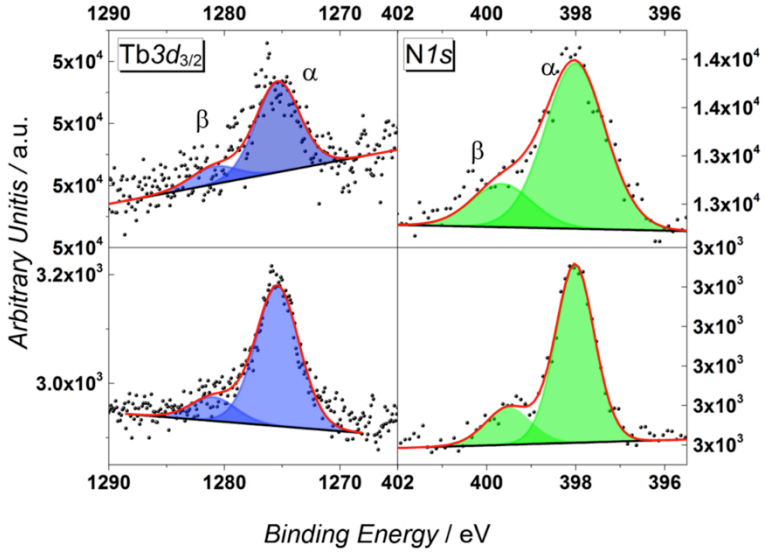


**Figure S8** *XPS spectra in the Tb3d$_{3/2}$ (left) and N1s (right) regions for Tb[Pc(PO$_3$Et$_2$)]$_2$ and TbPc$_2$ (top and bottom respectively).*

| | Tb | | | | | | N | | | | | |
|---|---|---|---|---|---|---|---|---|---|---|---|---|
| | α | | | β | | | α | | | β | | |
| | B.E. (eV ) | % | HMW (eV) | B.E. (eV ) | % | FHMW (eV) | B.E. (eV ) | % | FHMW (eV) | B.E. (eV ) | % | FHMW (eV) |
| $TbPc_2$ | 1275.4 | 5.0 | 4.4 | 1280.9 | 0.9 | 4.6 | 398 | 77.2 | 1.1 | 399.5 | 16.8 | 1.2 |
| | **5.9** | | | | | | **94.1** | | | | | |
| $Tb[Pc(PO_3Et_2)]_2$ | 1275.5 | 4.8 | 4.5 | 1281.0 | 1 | 4.8 | 398 | 74.6 | 1.5 | 399.6 | 19.4 | 1.8 |
| | **5.8** | | | | | | **94.2** | | | | | |
| Theoretical | **5.9** | | | | | | **94.1** | | | | | |

**Table S1** *Detail of curve fitting of $Tb3d_{3/2}$ and N1s with relative percentage for each component and element.*

## XAS/XMCD characterization of the pristine LSMO film

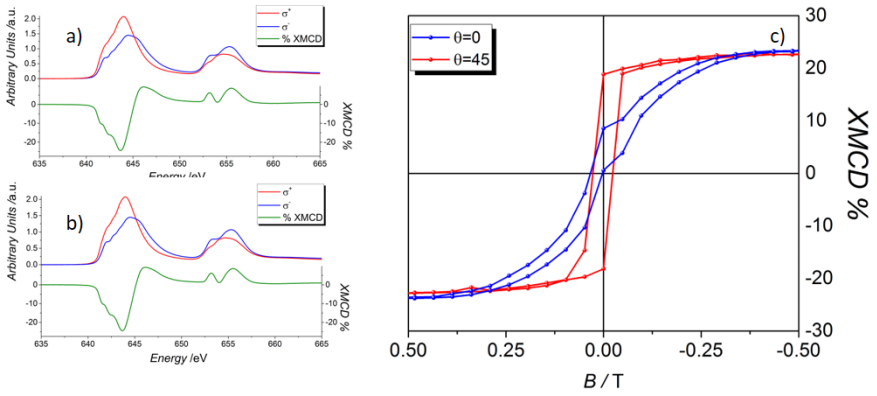


**Figure S9** *XAS, XMCD spectra at the Mn $L_{2,3}$ edges measured at T = 2 K, B = 3 T at q = 0° and q = 45° (a and b respectively) and field dependence (c) of the XMCD signal measured at the maximum of the dichroic Mn edge after chemical grafting.*

## XAS/XMCD characterization of bulk $Tb[Pc(PO_3Et_2)]_2$

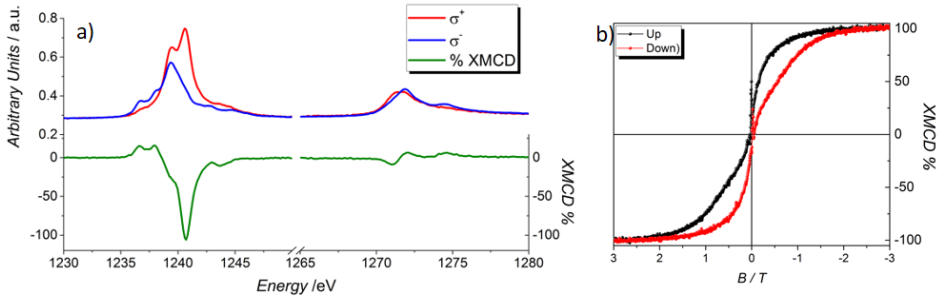


**Figure S10** *XAS, XMCD spectra at the Tb $M_{4,5}$ edges measured at T = 2 K, B = 3 T at q = 0° (a) and field dependence of the XMCD signal measured at the maximum of the dichroic Tb edge (b).*

## Co and LSMO coercive field

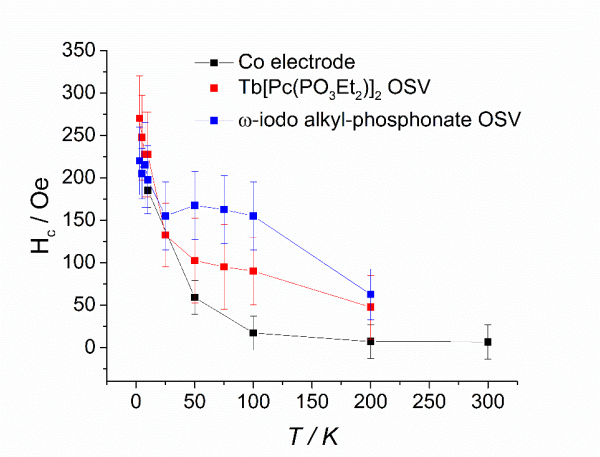


**Figure S11** *Comparison between temperature dependence of coercive fields of cobalt electrode and low-switching fields of OSV with $TbPc_2$ film and iodo alkyl-phosphonate.*

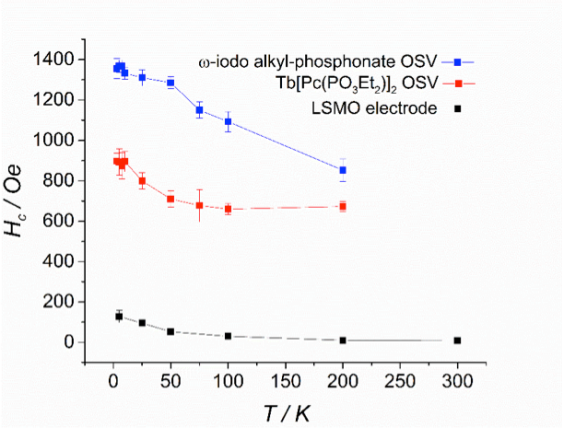


**Figure S12** *Comparison between temperature dependence of coercive fields of LSMO electrode and high-switching fields of OSV with $TbPc_2$ film and iodo alkyl-phosphonate.*

### Atomic Force Microscopy characterization of the LSMO electrode

An NT-MDT P47-pro room temperature setup equipped with NSC36 Micromasch tips has been used to characterize the morphology of the LSMO electrodes revealing a moderate roughness that however hampers to discriminate the presence of the chemisorbed molecular layer.

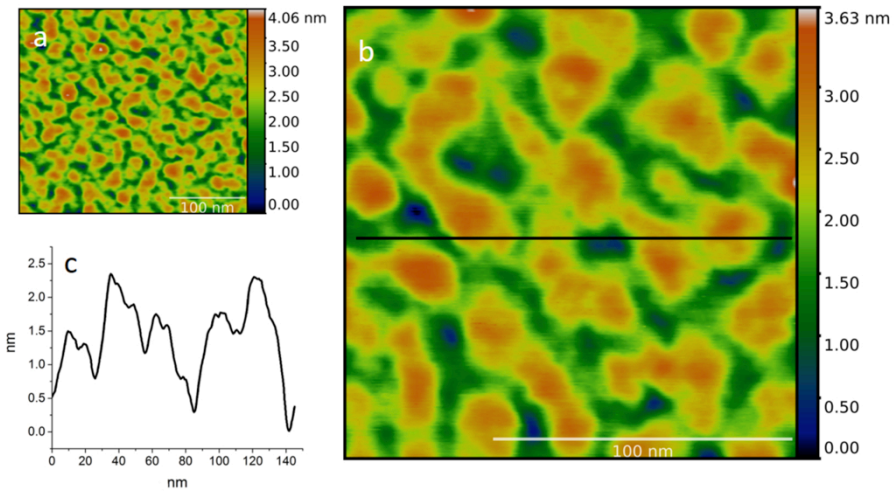


**Figure S13** *AFM characterization of the LSMO electrodes: a) large view of a 300 x 300 nm² area evidencing the absence of relevant inhomogeneity; b) 150 x 150 nm² zoom from which has been extracted the profile line evidencing a roughness of the order of 2 nm.*

## 1.8 References


[1] D. Gatteschi, R. Sessoli, *J. Magn. Magn. Mater*. **2004**, 272-276, 1030-1036.

[2] W. Wernsdorfer, *Adv. Chem. Phys*. **2001**, *118*, 99-190.

[3] A. H. Morrish, *The physical principles of magnetism* **1966**, John Wiley & Sons Inc., New York.

[4] D. Gatteschi, R. Sessoli. J. Villain, *Molecular Nanomagnets* **2006**, Oxford University Press, Oxford.

[5] R. Sessoli, D. Gatteschi, A. Caneschi, M. A. Novak, *Nature* **1993**, *365*, 141-143.

[6] S. M. J. Aubin, M. W. Wemple, D. M. Adams, H. L. Tsai, G. Christou, D. N. Hendrickson, *J. Am. Chem. Soc.* **1996**, *118*, 7746-7754.

[7] A. Caneschi, D. Gatteschi, R. Sessoli, A. L. Barra, L. C. Brunel, M. Guillot, *J. Am. Chem. Soc.* **1991**, *113*, 5873-5874.

[8] R. A. Layfield, *Organometallics* **2014**, *33*, 1084-1099.

[9] a) W. Wernsdorfer, T. Ohm, C. Sangregorio, R. Sessoli, D. Mailly, C. Paulsen, *Phys. Rev. Lett.* **1999**, *82*, 3903-3906; b) A. J. Tasiopoulos, A. Vinslava, W. Wernsdorfer, K. A. Abboud, G. Christou, *Angew. Chem. Int. Ed.* **2004**, *43*, 2117–2121; c) S. Wang, J. L. Zuo, S. Gao, Y. Song, H. C. Zhou, Y. Z. Zhang, X. Z. You, *J. Am. Chem. Soc.* **2004**, *126*, 8900-8901; d) E. Pardo, R. Ruiz-Garcia, F. Lloret, J. Faus, M. Julve, Y. Journaux, F. Delgado, C. Ruiz-Pérez, *Adv. Mater.* **2004**, *16*, 1507-1600; e) Y. Song, P. Zhang, X. M. Ren, X. F. Shen, Y. Z. Li, X. Zeng You, *J. Am. Chem. Soc.* **2005**, *127*, 3708-3709; f) T. Kajiwara, M. Nakano, Y. Kaneko, S. Takaishi, T. Ito, M. Yamashita, A. Igashira-Kamiyama, H. Nojiri, Y. Ono, N. Kojima, *J. Am. Chem. Soc.* **2005**, *127*, 10150-10151.

[10] N. Ishikawa, M. Sugita, T. Ishikawa, S. Koshihara, Y. Kaizu, *J. Am. Chem. Soc.* **2003**, *125*, 8694-8695.

[11] N. Ishikawa, *Functional Phthalocyanine Molecular Materials Structure and Bonding* **2010**, Springer Berlin Heidelberg, *135*, 211-228.

[12] J. D. Rinehart, J. R. Long, *Chem. Sci.* **2011**, *2*, 2078-2085.

[13] C. R. Ganivet, B. Ballesteros, G. de la Torre, J. M. Clemente-Juan, E. Coronado, T. Torres, *Chem. Eur. J.* **2013**, *19*, 1457-1465.

[14] F. Bertani, N. Cristiani, M. Mannini, R. Pinalli, R. Sessoli, E. Dalcanale, *Eur. J. Org. Chem.* **2015**, 7036-7042.

[15] L. Malavolti, M. Mannini, P. Car, G. Campo, F. Pineider, R. Sessoli, *J. Mater. Chem. C* **2013**, *1*, 2935–2942.

[16] L. Krusin-Elbaum, T. Shibauchi, B. Argyle, L. Gignac, D. Weller, *Nature* **2001**, *410*, 444-446.

[17] M. N. Leuenberger, D. Loss, *Nature* **2001**, *410*, 789-793.

[18] J. Camarero, E. Coronado, *J. Mater. Chem.* **2009**, *19*, 1678-1684.

[19] M. Mannini, F. Bertani, C. Tudisco, L. Malavolti, L. Poggini, K. Misztal, D. Menozzi, A. Motta, E. Otero, P. Ohresser, P. Sainctavit, G. G. Condorelli, E. Dalcanale, R. Sessoli *Nat. Comm.* **2014**, *5*, article number: 4582.

[20] A. Pedrini, L. Poggini, C. Tudisco, M. Torelli, A. E. Giuffrida, F. Bertani, I. Cimatti, E. Otero, P. Ohresser, P. Sainctavit, M. Suman, G. G. Condorelli, M. Mannini, E. Dalcanale *Small,* **2017**, in press.

[21] a) M. Lopes, A. Candini, M. Urdampilleta, A. Reserbat-Plantey, V. Bellini, S. Klyatskaya, L. Marty, M. Ruben, M. Affronte, W. Wernsdorfer, N. Bendiab, *ACS Nano* **2010**, *4*, 7531-7537; b) A. Candini, S. Klyastskaya, M. Ruben, W. Wernsdorfer, M. Affronte *Nano Lett.* **2011**, *11*, 2634-2639.

[22] U. Glebe, T. Weidner, J. E. Baio, D. Schach, C. Bruhn, A. Buchholz W. Plass, S. Walleck, T. Glaser, U. Siemling, *ChemPlusChem* **2012**, *77*, 889-897.

[23] M. Mannini, F. Pineider, C. Danieli, F. Totti, L. Sorace, P. Sainctavit, M. A. Arrio, E. Otero, L. Joly, J. C. Cesar, A. Cornia, R. Sessoli, *Nature* **2010**, *468*, 417-421.

[24] P. Grünberg, R. Schreiber, Y. Pang, M. B. Brodsky, H. Sowers, *Phys. Rev. Lett.* **1986**, *57*, 2442-2445.

[25] M. N. Baibich, J. M. Broto, A. Fert, F. Nguyen Van Dau, F. Petroff, P. Etienne, G. Creuzet, A. Friederich, J. Chazelas, *Phys. Rev. Lett.* **1988**, *61*, 2472-2475.

[26] a) I. Bergenti, V. Dediu, M. Prezioso, A. Riminucci, *Philos. Trans. R. Soc. Mathematical Phys. Eng. Sci.* **2011**, *369*, 3054-3068; b) M. Prezioso, A. Riminucci, I. Bergenti, P. Graziosi, D. Brunel, V. A. Dediu, *Adv. Mater.* **2011**, *23*, 1371-1375.

[27] M. Urdampilleta, S. Klyatskaya, J-P. Cleuziou, M. Ruben, W. Wernsdorfer *Nature Mater.* **2011**, *10*, 502-506.

[28] a) S. P. Pujari, L. Scheres, A. T. M. Marcelis, H. Zuilhof, *Angew. Chemie Int. Ed.* **2014**, *53*, 6322-6356; b) C. Queffélec, M. Petit, P. Janvier, D. A. Knight, B. Bujoli, *Chem. Rev*. **2012**, *112*, 3777-3807**.**

[29] V. E. Pushkarev, A. Y. Tolbin, N. E. Borisova, S. A. Trashin, L. G. Tomilova, *Eur. J. Inorg. Chem*. **2010**, 5254-5262.

[30] S. E. Maree, T. Nyokong, *J. Porphyrins Phthalocyanines* **2001**, *5*, 782-792.

[31] A. Pedrini, M. Perfetti, M. Mannini, E. Dalcanale, *ACS Omega* **2017**, *2*, 517-521.

[32] L. Margheriti, D. Chiappe, M. Mannini, P. E. Car, P. Sainctavit, M. A. Arrio, F. B. De Mongeot, J. C. Cezar, F. M. Piras, A. Magnani, E. Otero, A. Caneschi, R. Sessoli, *Adv. Mater*. **2010**, *22*, 5488-5493.

[33] L. Poggini, G. Cucinotta, A. M. Pradipto, M. Scarrozza, P. Barone, A. Caneschi, P. Graziosi, M. R. Cecchini, V. A. Dediu, S. Picozzi, M. Mannini, R. Sessoli, *Adv. Mater. Interfaces* **2016**, *3*, 1500855.

[34] L. Lozzi, L. Ottaviano, S. Santucci, *Surf. Sci.* **2001**, *470*, 265-274.

[35] a) S. Stadler, Y. U. Idzerda, Z. Chen, S. B. Ogale, T. Venkatesan, *Appl. Phys. Lett.* **1999**, *75*, 3384-3386; b) F. Li, Y. Zhan, T. H. Lee, X. Liu, A. Chikamatsu, T. F. Guo, H. J. Lin, J. C. A. Huang, M. Fahlman, *J. Phys. Chem. C* **2011**, *115*, 16947-16953.

[36] P. Totaro, L. Poggini, A. Favre, M. Mannini, P. Sainctavit, A. Cornia, A. Magnani, R. Sessoli, *Langmuir* **2014**, *30*, 8645-8649.

[37] I. Žutić, J. Fabian, S. Das Sarma, *Rev. Mod. Phys*. **2004**, *76*, 323-410.

[38] a) A. Lodi Rizzini, C. Krull, T. Balashov, A. Mugarza, C. Nistor, F. Yakhou, V. Sessi, S. Klyatskaya, M. Ruben, S. Stepanow, P. Gambardella, *Nano Lett*. **2012**, *12*, 5703-5707; b) A. Lodi Rizzini, C. Krull, T. Balashov, J. J. Kavich, A. Mugarza,

P. S. Miedema, P. K. Thakur, V. Sessi, S. Klyatskaya, M. Ruben, S. Stepanow, P. Gambardella, *Phys. Rev. Lett.* **2011**, *107*, 177205(5); c) D. Klar, S. Klyatskaya, A. Candini, B. Krumme, K. Kummer, P. Ohresser, V. Corradini, V. de Renzi, R. Biagi, L. Joly, J. P. Kappler, U. Del Pennino, M. Affronte, H. Wende, M. Ruben, *Beilstein J. Nanotechnol.* **2013**, *4*, 320-324.

[39] L. Malavolti, L. Poggini, L. Margheriti, D. Chiappe, P. Graziosi, B. Cortigiani, V. Lanzilotto, F. Buatier de Mongeot, P. Ohresser, E. Otero, F. Choueikani, P. Sainctavit, I. Bergenti, V. A. Dediu, M. Mannini, R. Sessoli, *Chem. Commun*. **2013**, *49*, 11506-11508.

[40] a) Y. Q. Zhan, X. J. Liu, E. Carlegrim, F. H. Li, I. Bergenti, P. Graziosi, V. Dediu, M. Fahlman, *Appl. Phys. Lett*. **2009**, *94*, 053301(2); b) A. A. Sidorenko, C. Pernechele, P. Lupo, M. Ghidini, M. Solzi, R. De Renzi, I. Bergenti, P. Graziosi, V. Dediu, L. Hueso, A. T. Hindmarch, *Appl. Phys. Lett*. **2010**, *97,* 162509(3).

[41] a) Z. H. Xiong, D. Wu, Z. Valy Vardeny, J. Shi, *Nature* **2004**, *427*, 821-824; b) V. Dediu, L. E. Hueso, I. Bergenti, A. Riminucci, F. Borgatti, P. Graziosi, C. Newby, F. Casoli, M. P. De Jong, C. Taliani, Y. Zhan, *Phys. Rev. B* **2008**, *78(10)*, 115203(6).

[42] J. P. Prieto-Ruiz, S. G. Miralles, H. Prima-García, A. A. Riminucci, P. Graziosi, M. Cinchetti, M. Aeschlimann, V. A. Dediu, E. Coronado, Z. G. Yu, *Nat. Commun.* **2014**, *5*, 4842-4848.

[43] V. A. Dediu, L. E. Hueso, I. Bergenti, C. Taliani, *Nat. Mater*. **2009**, *8*, 707-716.

[44] C. Barraud, P. Seneor, R. Mattana, S. Fusil, K. Bouzehouane, C. Deranlot, P. Graziosi, L. Hueso, I. Bergenti, V. Dediu, F. Petroff, A. Fert, *Nat. Phys*. **2010**, *6*, 615-620.

[45] a) K. V Raman, A. M. Kamerbeek, A. Mukherjee, N. Atodiresei, T. K. Sen, P. Lazić, V. Caciuc, R. Michel, D. Stalke, S. K. Mandal, S. Blügel, M. Münzenberg, J. S. Moodera, *Nature* **2013**, *493*, 509-513; b) K. Bairagi, A. Bellec, V. Repain, C. Chacon, Y. Girard, Y. Garreau, J. Lagoute, S. Rousset, R. Breitwieser, Y. C. Hu, Y. C. Chao, W. W. Pai, D. Li, A. Smogunov, C. Barreteau, *Phys. Rev. Lett*. **2015**, *114*, 247203(5).

[46] M. Cinchetti, V. A. Dediu, L. E. Hueso, *Nat. Mater.* **2017**, *16*, 507-515.

[48] V. I. Arkhipov, E. V. Emelianova, Y. H. Tak, H. Bässler, *J. Appl. Phys*. **1998**, *84*, 848-856.

[49] J. T. Devreese, A. S. Alexandrov, *Reports Prog. Phys.* **2009**, *72*, 66501(52).

[50] L. Vitali, S. Fabris, A. M. Conte, S. Brink, M. Ruben, S. Baroni, K. Kern, *Nano Lett.* **2008**, *8*, 3364-3368.

[51] a) R. Vincent, S. Klyatskaya, M. Ruben, W. Wernsdorfer, F. Balestro, *Nature* **2012**, *488*, 357-360; b) I. V. Krainov, J. Klier, A. P. Dmitriev, S. Klyatskaya, M. Ruben, W. Wernsdorfer, I. V. Gornyi, *ACS Nano* **2017**, *11*, 6868-6880.

[52] P. Graziosi, M. Prezioso, A. Gambardella, C. Kitts, R. K. Rakshit, A. Riminucci, I. Bergenti, F. Borgatti, C. Pernechele, M. Solzi, D. Pullini, D. Busquets-Mataix, V. A. Dediu, *Thin Solid Films* **2013**, *534*, 83-89.

[53] L. Poggini, S. Ninova, P. Graziosi, M. Mannini, V. Lanzilotto, B. Cortigiani, L. Malavolti, F. Borgatti, U. Bardi, F. Totti, I. Bergenti, V. A. Dediu, R. Sessoli, *J. Phys. Chem. C* **2014**, *118*, 13631-13637.

[54] P. Ohresser, E. Otero, F. Choueikani, K. Chen, S. Stanescu, F. Deschamps, T. Moreno, F. Polack, B. Lagarde, J.-P. Daguerre, F. Marteau, F. Scheurer, L. Joly, J.-P. Kappler, B. Muller, O. Bunau, P. Sainctavit, *Rev. Sci. Instrum.* **2014**, *85*, 13106-13114.

[55] M. Perfetti, M. Serri, L. Poggini, M. Mannini, D. Rovai, P. Sainctavit, S. Heutz, R. Sessoli, *Adv. Mater.* **2016**, *28*, 6946-6951.

### 1.9 Additional References

[S1] J. Jiang, D. K. P. Ng, *Acc. Chem. Res.* **2009**, *42*, 79-88.

[S2] J. Chastain, J. Moulder, Handbook of X-Ray Photoelectron Spectroscopy: A Reference Book of Standard Spectra for Identification and Interpretation of XPS Data, **1995**.

[S3] C. Resini, F. Catania, S. Berardinelli, O. Paladino, G. Busca, *Appl. Catal. B Environ*. **2008**, *84*, 678-683.

[S4] P. G. Mingalyov, G. V Lisichkin, *Russ. Chem. Rev*. **2006**, *75*, 541-557.

[S5] D. Klar, A. Candini, L. Joly, S. Klyatskaya, B. Krumme, P. Ohresser, J. -P. Kappler, M. Ruben, H. Wende, *Dalt. Trans.* **2014**, *43*, 10686-10689.

[S7] M. Gonidec, R. Biagi, V. Corradini, F. Moro, V. De Renzi, U. del Pennino, D. Summa, L. Muccioli, C. Zannoni, D. B. Amabilino, J. Veciana, *J. Am. Chem. Soc.* **2011**, *133*, 6603-6612.

CHAPTER 2

# SOFT MECHANOCHEMISTRY ON TETRAQUINOXALINE CAVITANDS

## 2.1 Introduction

### 2.1.1 Mechanoresponsive polymers

Synthetic polymers, thanks to their availability, processability, low density and wide range of mechanical properties, are now ubiquitous for engineering applications and are evolving into multifunctional systems with highly sophisticated behaviour.[1] These emergent materials are commonly referred to as "smart", whereby "intelligence" is rooted in a specific response elicited from a particular stimulus. Since their chain-like character make them suitable for transiently accumulating mechanical energy along the backbone, it is not surprising if, among widespread light-, pH-, heat- or redox responsive polymers, mechanoresponsive materials are gaining a steadily rising attention. As the name suggests, chemical transformations are attained harnessing mechanical forces applied to the resulting material; therefore, in respect to more conventional stimuli, this kind of macroscopic solicitation differs for being directional, thus paving the way to novel possibilities of responsiveness and innovative properties for the resulting 'smart polymer'. Among the wide range of methods by which forces can be applied to a small molecule (e. g. ball milling, atomic force microscopy, turbulent flow…),[1,2] the specific attachment of polymer chains to a molecular scaffold results the most convenient for the controlled application of exogenous stress. In this field, ultrasonication has proven to be capable of generating efficient tensile stresses within solvated polymer chains.[3] Indeed, dilute polymer solutions under acoustic fields experience solvodynamic shear forces due to solvent cavitation. Basically, the elongation of the polymer backbone is due to gradients created by the higher velocities with which polymer chain ends, proximal to a collapsing bubble, are pulled towards the resulting void volume in respect to distal ones; this results in a tensile stress near the midpoint of the chain. The very first reports on responsiveness upon mechanical stress were published by Staudinger, who observed a decrease in the molecular weight of polymers after mastication due to homolytic C-C bond cleavage.[4] These results found a theoretical consolidation in Kauzmann and Eyring's calculations, which predicted that the stretching of specific bonds within a molecule could end up in lowering the activation barrier of homolytic dissociation by altering the potential energy shape of a reaction coordinate.[5] In 1980 Encina and co-workers[6] demonstrated

how cleavage can occur more easily for certain chemical bonds with respect to others; in particular they showed a ten times faster degradation for ultrasonic chain scission of poly(vinylpirrolidone) with randomly incorporated peroxide linkages compared to the neat polymer.

Thus, early publications in the field of polymer mechanochemistry clearly appear focused on investigating the effects of mechanically induced chemical changes in terms of materials degradation and failure. Interestingly, in recent years, perspective moved from a "destructive" to a "constructive" approach;[7] the novel point of view is marked by the introduction of the concept of "mechanophore", defined as a molecule which undergoes a predictable chemical modification triggered by mechanical force. Most of the mechanophores reported so far (Figure 2.1) are characterized by the presence of strategically weakened bonds, strained rings or isomerizable bonds, prone to react once mechanical forces are transferred to them from the polymer chains. Activation of labile bonds can be achieved both in solution and in the bulk. Over the past few years, thanks to the sizable progress in mechanophore design, a broad range of mechanically-triggered transformations has been attained, such as colour/fluorescence change,[8] accessing symmetry-forbidden electrocyclic ring-opening reactions *via* "non conventional" reaction pathways,[9] isomerizations,[10] release of small molecules[11] and activation of latent transition metal catalysts.[12] A benchmark in this field is represented by Jeffrey Moore's work, whose observation of the site-specific cleavage of an azo moiety placed near the centre of a poly(ethylene glycol)[13] chain led, for the first time, to the idea of a rationally designed molecular unit suitable to undergo a mechanochemical change. Besides, Moore and co-workers exploited the potential of polymer mechanochemistry, by making possible reaction pathways typically not accessible *via* purely thermal or photochemical activation. This is the case of the symmetry-forbidden electrocyclic ring-opening of benzocyclobutane,[9] where the directional nature of mechanical forces associated with ultrasound treatment yielded to a novel reaction control by altering the shape of potential energy surfaces; thus an otherwise forbidden process can occur under mild conditions.

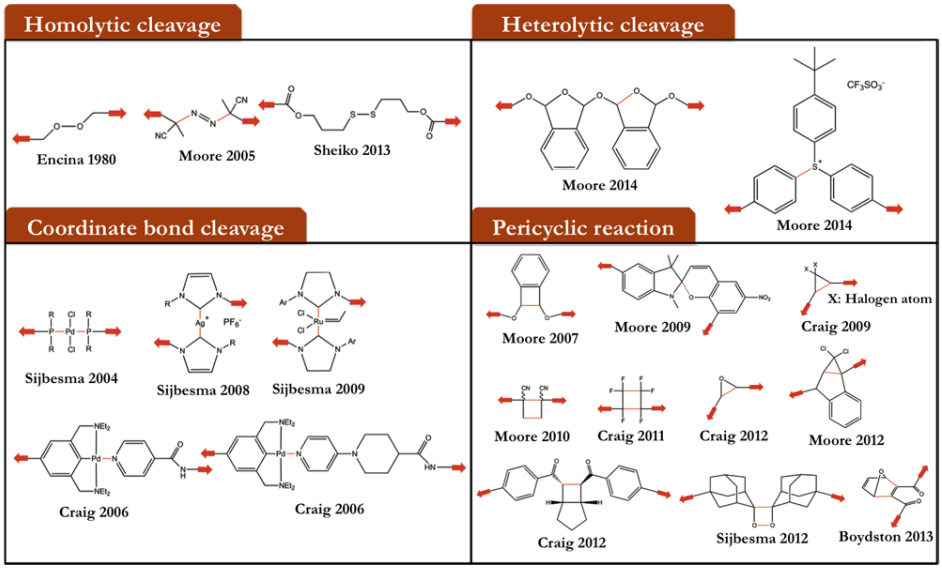


**Figure 2.1** *Overview of the mechanophore structures reported so far; mechanochemically active bond is marked in red.*[7]

Obviously, the possibility to induce macroscopic response in a material upon mechanical stress appears particularly attractive for the development of damage-sensing or self-diagnostic materials. In 2009, research teams from the University of Illinois investigated a spiropyran-based (SP) mechanophore; light-induced opening of the SP ring is known since 1964,[14] but its introduction within the chain of a high molecular weight polymer allowed, for the first time, the stress-induced cleavage of the spiro C-O bond. Remarkably, reversible conversion from the colourless SP into the purple merocyanine (MC) form allowed direct visualization of the force-induced 6$\pi$-electron electrocyclic ring-opening[8a,15] on the "dog bone" specimen (Figure 2.2).

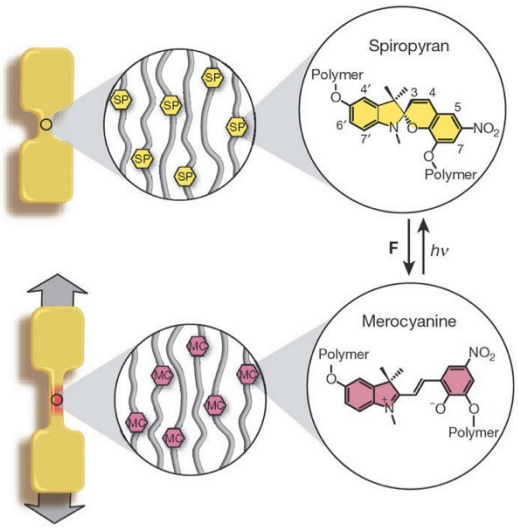


**Figure 2.2** *Schematic representation of 'dog bone' specimens; upon application of tensile force conversion between the colourless SP and coloured MC forms of the mechanophore occurs. Exposure to visible light reverses the conversion back to the original SP form.*[8a]

Simple mechanical models highlighted how a crucial point for an effective transmission of the applied force across the junction relies on the position of the attachment points to the polymer chain. In particular, attachment on the opposite sides of the spiro-junction (5′ or 6′ positions on the indole and 7 or 8 positions on the benzopyran) preferentially stresses the spiro C-O bond over the spiro C-C bond. Being such a highly effective colour-generating mechanophore, SP is probably the most employed stress-sensitive unit reported so far; the correlation between the nature of the polymeric matrix and the activation degree has been investigated by different groups in order to exploit its potential for visible detection and mapping of mechanical stress in bulk polymers. SP stress-induced activation has been firstly reported in a poly(methylacrylate) (PMA) matrix upon ultrasonication in solution. SP bis-functionalized with α-bromo-α-methylpropionyloxy moiety was employed as initiator for a copper(0)-catalysed single electron transfer living radical polymerization (SET-LRP), yielding to a high molecular weight macromolecule (170 kDa) with a relatively narrow polydispersity index (1.2). The convenience of this approach relies on the possibility to place the stress-sensitive unit roughly near the centre of the polymer chain, where mechanical solicitation is higher. SP activation in PMA matrix has been reported also in the bulk state

upon mechanical stretching of the 'dog bone' specimens outlined in Fig. 2.2. Interestingly, the same mechanophore unit showed stress responsiveness also in a compressive loading configuration; conversion to the coloured merocyanine form was indeed observed in glassy mechanophore-crosslinked poly(methyl methacrylate) (PMMA) beads.[8a] In this case, the application of compressive solicitations, which develop in the bead parallel to the loading direction, induces significant tensile stresses in the perpendicular direction, leading to the expected ring opening (Figure 2.3). Maximum tensile stress develops in the centre of the bead, reaching a value of 0.6 of the magnitude of the applied compressive stress ($\sigma_0$). In this specimen geometry, mechanochemical activation was monitored through the relative change in RGB intensity during loading. The evolution of a mechanochemically-induced colour change in the active cross-linked PMMA-4 bead for a representative compression test is shown in Fig. 2.3a. According to elastic predictions, colour changes emerge in the centre of the bead at a strain level just beyond the yield point, while no detectable variations were observed for the monofunctional control PMMA-5 beads. Colour evolution in active cross-linked bead corresponds to a reduction of the relative green channel intensity (Figure 2.3b).

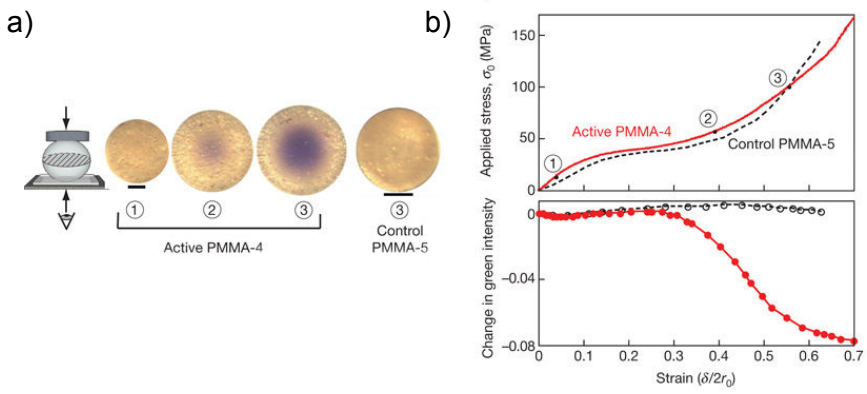


**Figure 2.3** *Mechanochemical activation of glassy SP-crosslinked PMMA beads: a) polymer beads imaged from the bottom at progressively increasing compressive stress (1,2,3) for active difunctional PMMA-4 and monofunctional control PMMA-5; b) compressive stress ($\sigma_0$) and relative change in green intensity vs. applied compressive strain for PMMA-4 (in red) and control PMMA-5 (in black).*[8a]

Sottos *et al*.[16] studied the correlation between mechanophore orientation in bulk polymers and activation degree; this investigation, performed *via* fluorescence anisotropy measurements, relies on the rise of an intense emission, roughly polarized across the long axis of MC species, upon interconversion of the SP form (Figure 2.4). Hence an order parameter, estimating the orientation of MC species relative to the tensile force, was calculated. Upon stretching of previously UV-exposed samples, an increase of the order parameter up to approximately 0.5 was observed, while significantly higher values were obtained for purely mechanically activated specimens. This result underlines a preferential mechanochemical activation for species oriented along the tensile direction.

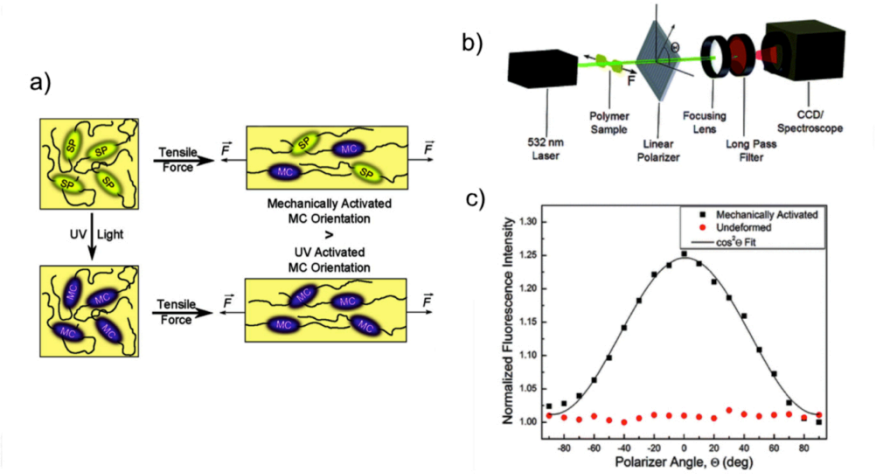


**Figure 2.4** *a) Sketch of the role of mechanophore orientation in bulk matrix; b) Experimental setup for fluorescence anisotropy measurements; c) Normalized fluorescence intensity vs. polarization angle θ for mechanically activated (black line) and undeformed thermally activated SP-linked PMMA (orange line).*[16]

Unfortunately PMA and PMMA matrices do not appear amenable for concrete applications, being respectively too soft, resulting in mechanical activation only at strains close to material failure, or too glassy, leading to SP⇆MC conversion that cannot be investigated at room temperature; thus SP activation has been demonstrated in a polyurethane (PU) platform obtained *via* step growth polymerization (Figure 2.5).[17] The choice of such a versatile matrix, able to conjugate mechanical toughness and elasticity, allowed for investigation of the kinetics of the stress-induced response; furthermore, because of the low glass

transition temperature ($T_g \approx$ -60 °C) of the polymer, equilibrium between SP and MC forms is reached in experimentally accessible times at room temperature.

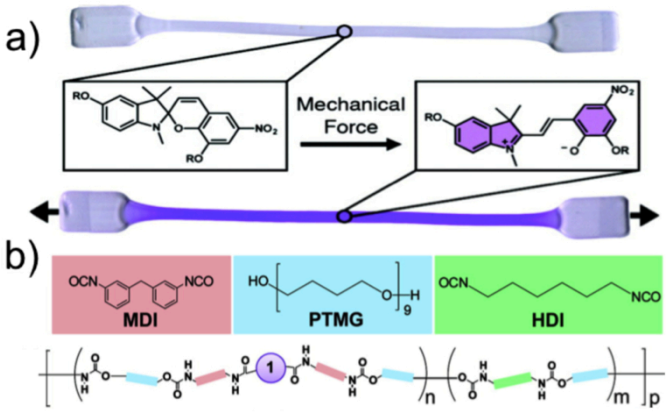


**Figure 2.5** *a) Optical images of pre-stretched dog bone specimen containing 0.03% w/w of SP before (top) and after (bottom) being stretched up to a stretch ratio (final length/ initial length) of 2.0; b) Sketch of the co-monomers and incorporation of mechanophore* ***1*** *into PU via step growth polymerization where m>>n.*[17]

Recently Craig and co-workers[18] reported the covalent incorporation of SP in elastomeric poly(dimethylsiloxane) (PDMS), where, for the first time, mechanophore activation takes place at strains from which a fully elastic recovery of the initial shape of specimens is possible (Figure 2.6). Recovery of the initial colourless state, by contrast, was possible only by illuminating the sample for 1 min with bright white light. PDMS matrix, conjugating a relatively high stretchability with good mechanical strength, optical transparency and wide functional groups tolerance, is quite employed for microfluidics devices and electrolithographic or biomedical applications. Hence, the possibility to obtain full shape recovery, in concert with covalent mechanochemical activation, might pave the way for integrating an already functional material with novel responsiveness.

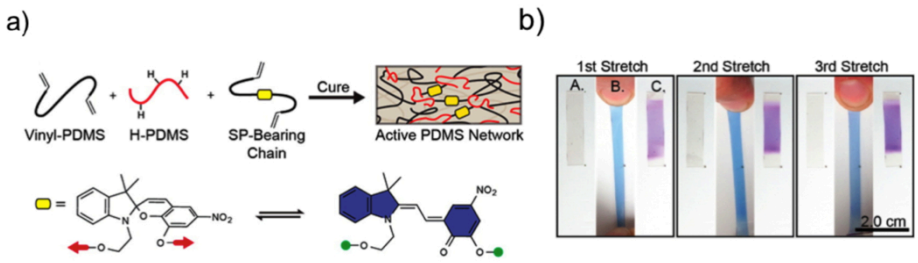


**Figure 2.6** *a) Covalent embedding of a general bis-alkene functionalized molecule via platinum-catalysed hydrosilylation among vinyl-terminated and H-terminated PDMS pre-polymer (top) and electrocyclic ring-opening of SP into the coloured MC form (bottom); b) Direct visualization of the covalent bond activation with full shape recovery, both repeatable over multiple cycles.*[18]

Clearly, for all reported systems, testing of the corresponding control samples was crucial to irrefutably correlate the applied mechanical stimulus to the desired response, excluding any other possible activation mechanism (e. g. thermal activation). These examples underline how, for the same stress-sensitive unit, the nature of the matrix plays a key role for the efficiency of the process; polymers with different mechanical features can not only confer different properties upon the system, but can also range from effective activation to complete failure in the desired responsiveness. Howsoever, 'effective activation' in this field refers to a situation in which large and typically irreversible strains[19] are efficiently channelled for acting on a relatively low percentage of mechanophores; thus the low yield of the desired mechanochemical reaction constitutes one of the major limitations of this strategy. Solutions proposed so far to overcome this issue can be essentially divided into molecular-level or material-level approaches. The former foresees a rational design of the 'stress-responsive unit' in terms of reactivity and structural connections to emphasize the desired response. The latter strategy involves the identification of those material architectures able to efficiently transduce macroscopic forces, through polymer actuators, to mechanophores. This result has been recently attained, without an irreversible deformation of the material, for elastomeric matrices.[10,20] As it often happens, in the design of stimuli-responsive materials, researchers took inspiration from nature;[21] indeed mechanochemistry processes play an important role in many biological systems. An example might be the case of transmembrane ion channels, whose opening is elicited by a mechanical stress acting on specific protein arrangements, or for touch sensitivity,[22] blood clotting,[23] or more generally in

the interactions of cells with their environment. Despite the activation of these processes requires much lower forces than those necessary to affect chemical bonds, even if strategically strained, weak forces in biological systems are efficiently transduced into chemical signals. Such a perfect mechanism is usually based on the induction of conformational changes either in complex supramolecular architectures (e. g. opening of ion channels in cell membranes[24]) or in single proteins (e. g. interactions between cells and their environment[25]). Interestingly, unlike artificial mechanochemical systems, these processes often present the advantage of being reversible, meaning that the initial state is recovered once mechanical stress is withdrawn. To differentiate from conventional mechanochemistry, this kind of approach, in which a complex system undergoes a specific conformational change suitable to elicit a chemical process, is called soft mechanochemistry (Figure 2.7).[26]

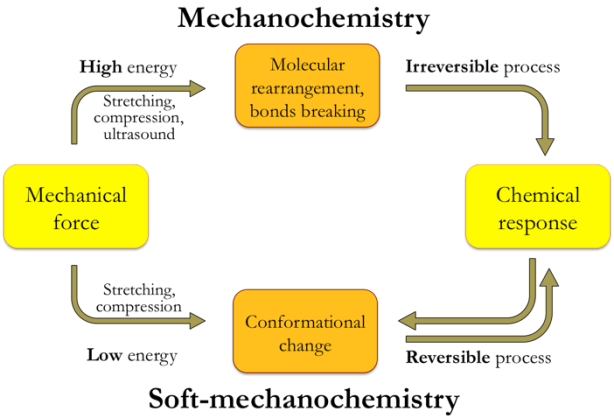


**Figure 2.7** *Diagram schematically resuming the comparison between conventional and soft mechanochemistry.*[26]

Despite this field appears still in its infancy, some examples of artificial systems exploiting the approach of soft-mechanochemistry have been recently reported by Jierry and co-workers.[27] In particular, mimicking the site exhibition strategy used by nature, they prepared a polyelectrolyte multilayer film on PDMS sheet that provides cryptic sites at rest and site exhibition under stress (Figure 2.8).

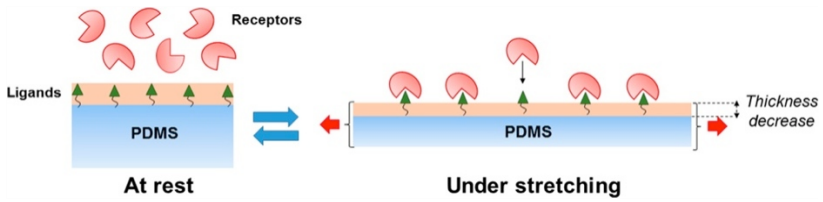


**Figure 2.8** *Schematic representation generally illustrating the cryptic site strategy: PDMS surface is covered with a properly designed polymeric coating whose hidden sites at rest are exhibited upon stretching.*[27]

Responsiveness of the system relies on the strong biotin/streptavidin interaction; indeed a poly(acrylic acid) film bearing biotin moieties (PAA-biotin) was deposited onto the silicone substrate and embedded under two (PAH/PAA-PC) bilayers, where PAA-PC represents poly(acrylic acid) functionalized at 5% with phosphorylcholine (PC) moieties. Thus, in the relaxed state, no adsorption of streptavidin is observed because of the shielding effect of PC protecting groups; by contrast, mechanical solicitation applied to the modified PDMS film led to the supramolecular recognition between the surface-grafted ligand and the receptor (Figure 2.9).

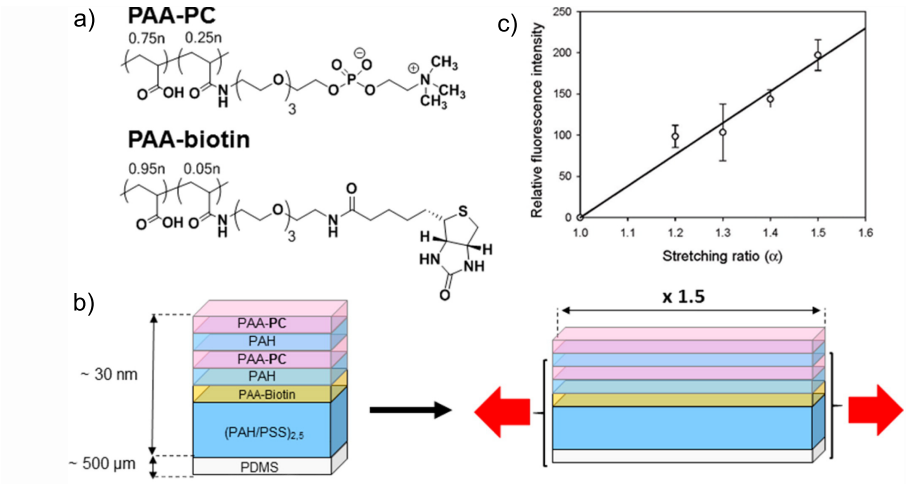


**Figure 2.9** *a) Chemical structures of PAA-biotin and PAA-PC used in the preparation of the mechanoresponsive film; b) Schematic representation of the multilayer film architecture adsorbed at rest (left) and in the stretched state (right); c) Linear dependence between the fluorescence*

*intensity of streptavidin (labelled with fluorescein thioisocyanate) adsorbed on the multilayer film and stretching ratio α.*[27]

Considering the outstanding potential of this almost unexplored field, in our group we applied soft-mechanochemistry tools for investigating the *vase* ⇆ *kite* switching of tetraquinoxaline cavitands in polymers. This study relies on the assumption that, besides conventional stimuli, the application of a tensile strain could lead to the opening of quinoxaline walls in the cavitand scaffold. To our knowledge this is not only the first example of polymer-embedded quinoxaline cavitands, but also the first case in which *vase* → *kite* switch is elicited *via* a mechanical solicitation.

### 2.1.2 Tetraquinoxaline cavitands

Since their first introduction in 1982 by Cram and co-workers,[28] resorcin[4]arene cavitands attracted a lot of interest because of their molecular receptor properties. These compounds, usually referred to as tetraquinoxaline cavitands (QxCav), are conveniently prepared by the fourfold bridging of corresponding resorcinarene scaffolds with 2,3-dichloroquinoxalines (Figure 2.10).

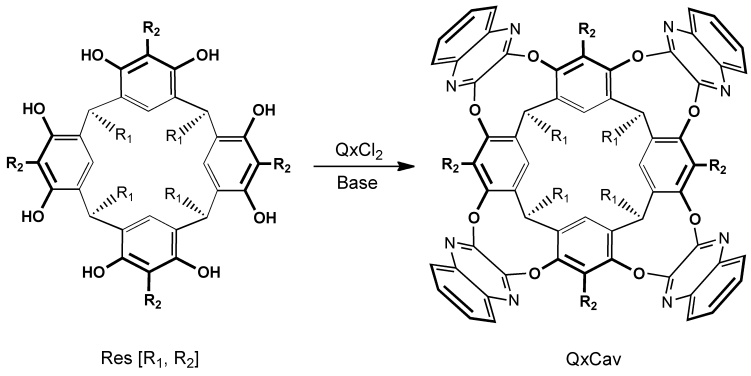


**Figure 2.10** *General synthesis of tetraquinoxaline cavitands.*

The introduction of quinoxaline walls creates a hydrophobic and electron rich cavity in the resulting cavitands, suitable for aromatics complexation. The

selective recognition properties of tetraquinoxaline cavitands towards aromatic hydrocarbons have been applied to fabricate low-cost systems with sub-ppb detection limits of toxic Volatile Organic Compounds (VOCs) in air.[29] Complex formation is driven by multiple π-π and CH-π interactions between the aromatic guest and the deep, hydrophobic cavity.[30] Beyond complexation properties, tetraquinoxaline cavitands show the ability to reversibly switch between two spatially well-defined conformations, an expanded *kite* ($C_{2v}$ symmetry) and a contracted *vase* conformation ($C_{4v}$ symmetry) (Figure 2.11). The 1,4-diazanaphtalene 'flaps', indeed, can occupy either axial or equatorial positions, leading respectively to the *vase* or *kite* conformer. Extensive studies performed by Cram's group pointed out the temperature-dependence of the interconversion; while *vase* conformation is prevalent in solution at room temperature and above, at temperatures approaching –60 °C the cavitand is present only in the expanded form. The origin of this behaviour should be traced back to solvation effects: at low temperature the *kite* conformer, exposing to the solvent a larger surface, results more stable, while the solvation entropic term becomes unfavourable at higher temperatures, promoting the *vase* form. Besides, the conformation of the four dioxanonane rings is significantly more strained in the expanded form than in the contracted one.

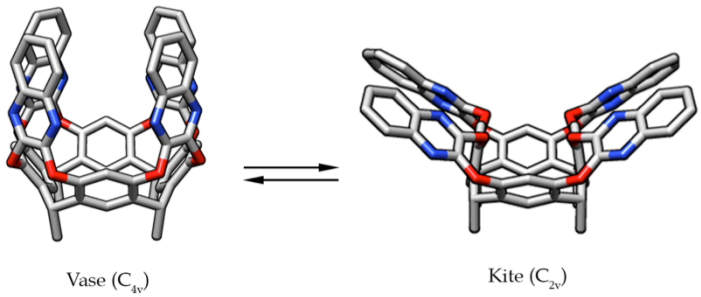


**Figure 2.11** *Cavitand switching between vase and kite conformations.*[31]

The definition of tetraquinoxaline cavitands as molecular switches[32] relies on their sensitivity towards different external stimuli; pH decrease upon addition of trifluoroacetic acid (TFA) to a solution of QxCav elicited *vase* → *kite* switching as consequence of Coulomb repulsion between protonated quinoxaline nitrogen atoms.[33] Furthermore, the increase of $Zn^{2+}$ ion concentration was

found to stabilize the *kite* conformation through the formation of coordination complexes between $Zn^{2+}$ and quinoxaline bases.[34] More recently electrochemical switching was reported by Diederich on a tetrathiafulvalene-functionalized Qx-Cav,[35] and subsequently on quinone-based cavitands able to form intramolecular hydrogen bonds.[36]

Remarkably, *vase* → *kite* interconversion is attended by a significant expansion of the molecule; moving from a closed *vase* conformation of about 1.18 nm wide to an open *kite* conformation with an extended surface approximately 1.59 x 2.04 nm in size (Figure 2.12)[37] leads to an increase of the cavitand size of about 1.4 nm along the molecular diagonal. The energy barrier for the interconversion has been estimated in 7.6 kcal $mol^{-1}$ by DFT calculations.[38] Interestingly, since all intermediate conformers resulted in being energetically disfavoured, only these two discrete forms exist.

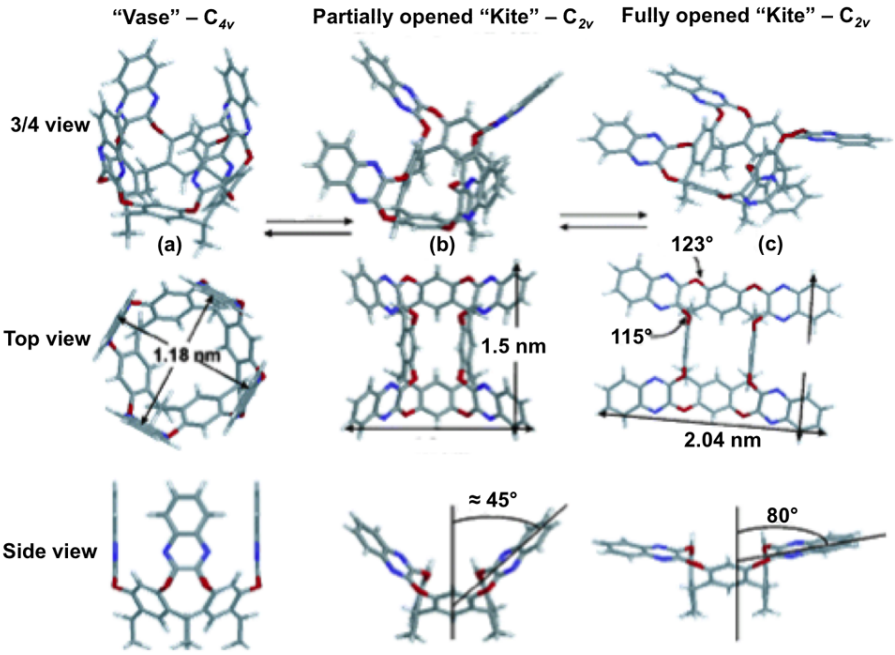


**Figure 2.12** *Molecular structures of QxCav: a) Vase; b) partially open and c) fully open "kite" structures. Molecular dimensions and angles are estimated after structure optimization (Macromodel) taking into account the van der Waals radii. The alkyl chains ($C_{11}H_{23}$) are omitted for clarity.*[37]

Considering these peculiar features, QxCav appear potentially interesting not only for their capability to act as molecular switches, but also for providing a dimensionally-variable unit which can be easily expanded/contracted through the application/removal of proper external stimuli. *Vase* ⇆ *kite* conformational equilibrium of variously substituted cavitands has been extensively studied both in solution, by variable-temperature NMR spectroscopy (VT-NMR)[39] and UV-Vis spectroscopy,[32] and at the interface, using sum-frequency vibrational spectroscopy (SFVS).[40] On the contrary, cavitands behaviour in solid matrices is still unexplored, though their significant expansion upon interconversion could confer interesting responsiveness to the resulting polymeric network. For this reason we considered exploiting cavitands peculiar properties in terms of conformationally expandable components for the development of materials featuring an auxetic behaviour at the molecular level.

### 2.1.3 Auxetic materials

The term *auxetic*, derived from the ancient Greek αὐξητικός (auxetikòs, 'that tend to increase'), is used with reference to a particular class of materials, possessing a counterintuitive behaviour in respect to conventional ones. The origin of their peculiar properties traces back to a negative value of the Poisson's ratio (ν), defined as the ratio of the lateral contractile strain to the longitudinal tensile strain for an object experiencing a uniaxial tension in the longitudinal direction.[41] In fact, while most common materials with a positive Poisson's ratio (typically between 0.2 – 0.4) shrink in the direction orthogonal to the applied stress, auxetic materials expand in the same direction. For their unconventional nature they are also identified as *anti-rubber* materials. Furthermore, a negative value of ν is also responsible for enhanced mechanical properties, such as a higher indentation resistance. This is easily explained considering that the hardness of an isotropic material with a Young's modulus E is proportional to $[(1-\nu^2)/E]^{-1}$. Since ν value should theoretically fall within the range $-1 \leq \nu \leq +½$, an improvement in the indentation resistance is obtained for values lower than – ½. Besides the mathematical evidence, this effect can be explained in a more intuitive way considering that, when auxetics are compressed by an object, they

contract laterally, thus leading to a densification of the material below the impact point (Figure 2.13).[42] Other important mechanical properties, such as shear resistance[43] and fracture toughness,[44] benefit from a negative Poisson's ratio.

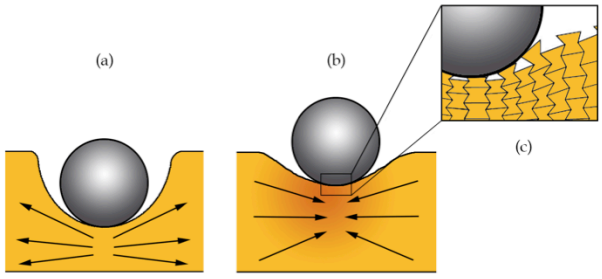


**Figure 2.13** *Representation of indentation response for a) non-auxetic and b) auxetic materials; c) a deformation of the re-entrant honeycomb structure is assumed.*[45]

Being the theory of elasticity scale-independent, examples of auxetic materials can be found, either natural or man-made, ranging from the macroscopic down to the molecular level. Examples of large-scale auxetics are Magnox nuclear reactors,[46] designed to withstand the horizontal components of the forces generated during an earthquake, or porous constructs based on re-entrant honeycomb structures.[47] The merit for the current interest in this field has to be acknowledged to Roderic Lakes who reported, in 1987, an isotropic open-cell auxetic foam based on a polyurethane scaffold.[48] Here the negative Poisson's ratio relies on a peculiar microscopic structure for the material, obtained through the conversion of the convex polyhedral cells, characteristic of conventional foams, to re-entrant structures *via* thermal/mechanical treatment (Figure 2.14).

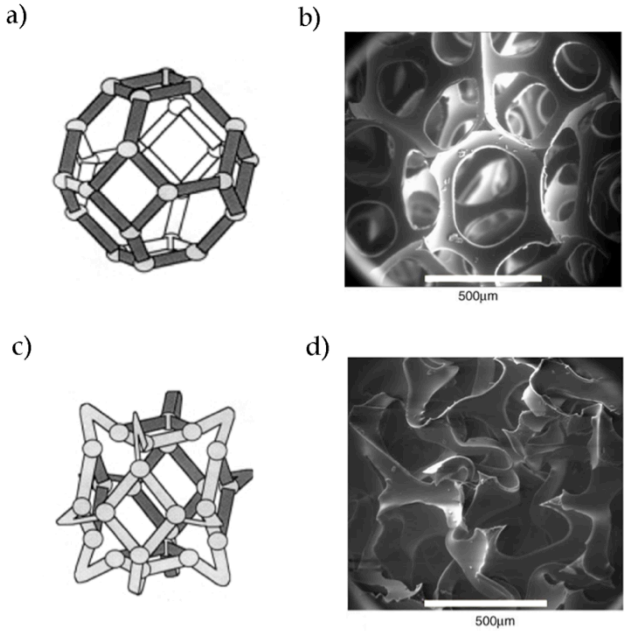


**Figure 2.14** *a), b)Tetrakaidecahedron cell models and SEM images of a conventional and c), d) an auxetic polyurethane foam.*[49]

Driven by the research of stiffer materials for wider engineering applications, at the University of Liverpool, Evans and co-workers developed in 1989 an expanded form of porous polytetrafluoroethylene (PTFE) with a highly strain-dependent and anisotropic auxetic behaviour, which exhibited a negative Poisson's ratio in one direction.[50] Morphological studies revealed that the effect is due to the microstructure of the polymer, consisting of a 3D array of nodules interconnected by fibrils.[51] Even if most studied and technologically relevant auxetics are man-made, a growing number of natural materials with negative Poisson's ratio have been discovered, such as cat skin[52] or human tendons,[53] whose auxeticity relies on a fibrillar architecture of the biomaterial at the microstructural level. All reported examples clearly show that at the meso- or macro-scale a negative Poisson's ratio is usually related to the use of the so-called meta-materials, constituted by elements arranged in repeating patterns, whose properties mainly depend on their peculiar structure rather than on the properties of the base material. Thus, the design and synthesis of auxetic materials at the molecular level still remains the most exciting and unattended

prospect in this field. Theoretical predictions, indeed, suggest that transferring the auxetic character at the molecular scale is not only likely to provide enhanced or even extreme properties to the resulting material, but could also offer additional features, such as the ability to act as tunable molecular sieves.[54]

### 2.1.4 Molecular auxetics

Among naturally occurring auxetic materials, α-cristobalite, a polymorph of crystalline silica, constitutes a known example of molecular auxetic,[55] where the cooperative rotation of tetrahedral units in the framework of corner-sharing $SiO_4$ building blocks is responsible for its negative Poisson's ratio.[56] Beyond nature, the very first attempts in designing man-made molecular level auxetics trace back to 1987, when Monte Carlo simulation was used for predicting the elastic properties and phase transformations of a 2D system of hard cyclic hexamers.[57] In the following years, in an attempt to reproduce the macroscopic re-entrant honeycomb structures, auxetic behaviour was theorized for a great variety of molecular networks based on cross-linked rigid aromatic alkynes (Figure 2.15a).[58] In 1993, Baughman and Galvão proposed a different design where auxeticity arises from the change in twist of polyacetylenes-based helical chains;[59] the predicted structure resulted from the covalent interconnection of bonds from two sets of non-parallel 'basis' chains, occupying alternating layers along the chain axis. Parallel bonds in the helical structure, such as $sp^2$-$sp^2$ single bonds in polyacetylene chains, provide 'hinges' which enable a soft shear deformation mode (Figure 2.15b). Unfortunately, none of these structures has been concretely realized due to the extreme synthetic challenges.
Evans and co-workers proposed an interesting approach, predicting an auxetic behaviour for a calix[4]arene-based 3D polymeric network, with an "egg rack" structure constituted by a square grid made of alternate facing "four-legged claws" (Figure 2.15c).[60]

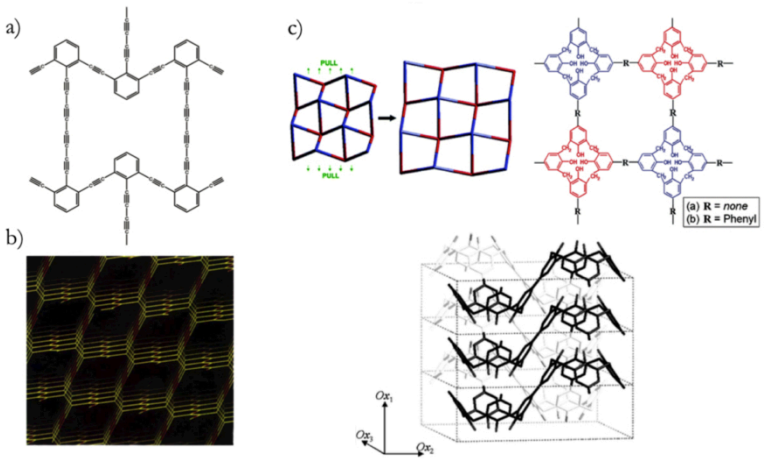


**Figure 2.15** *a) Unit cell of a theoretical auxetic molecular network;[57] b) Proposed crystal structure for the trans hinged polyacetylene carbon seen from the normal direction to the hinged bonds (for clarity, the C≡C bonds are indicated in red);[58] c) "Egg rack" structure (top left), scheme (top right) and minimum energy configuration (bottom) for the calix[4]arene network theorized by Evans' group.[59]*

In this system calix[4]arene units are supposed to behave as junctions able to propagate the elongation in the transversal direction; thus, when loaded in tension, a lateral expansion of the material is expected due to the force-induced opening of the calix[4]arene scaffold with respect to the equilibrium conformation. The connectivity between the junctions is chosen to be *via* a *para-para* biphenyl-like linkage, being the simplest way reported in literature[61] for connecting calix[4]arene units. Unfortunately, not only the synthesis of such highly cross-linked structures resulted in being infeasible, but also the rigidity of the proposed network would have likely led to materials with limited applicability because of the high melting temperature and poor tractability.

To avoid these issues, Griffin and co-workers proposed a molecular-level approach to auxetic materials based on site-connectivity driven rod re-orientation in main chain liquid crystalline polymers.[62] The basic idea is to invert the response of conventional polymers with positive Poisson's ratio, which exhibit a more ordered and compact structure when loaded in tension, and move towards a polymer whose interchain packing distance increases, upon stretching, in a direction perpendicular to the applied force. To achieve this peculiar responsiveness, Griffin *et al.* proposed the incorporation of

laterally attached rods into the polymer backbone; at rest, these rigid units lie parallel to the polymer chain direction while, under stress, the extension of flexible spacers forces them to a position normal to the tensile axis. As depicted in Fig. 2.16, under the assumption that lateral forces do not prevent the mechanical re-orientation of terphenyl units, this mechanism is expected to lead to an increased interchain distance and, consequently, to a lateral expansion of the material. Furthermore, the use of main chain liquid crystalline elastomers (MC-LCE),[63] thanks to the alignment in highly ordered domains, enables to obtain a unidirectional molecular response capable to induce a macroscopic expansion transversal to the tensile axis.

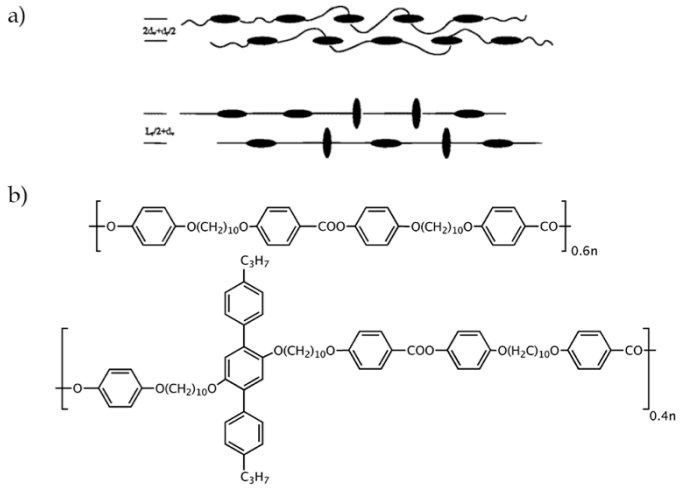


**Figure 2.16** *a) Sketch of the re-orientation mechanism of laterally attached units (depicted as black rods like mesogens) and resulting increase in the interchain distance; b) Chemical structure of the tested polymer.*[61a]

Although X-ray scattering showed a small increase in the interchain distance upon stretching, the reported system failed to evidence an auxetic behaviour.
More recently, 2D auxetic protein crystals have been proposed,[64] exhibiting seven interconnected conformational states ranging from a fully open to a fully closed state *via* a continuous motion of the self-assembled lattice (Figure 2.17). This large expansion, afforded by a remarkable extent of hinging about flexible disulfide linkages, could lead to a theoretical Poisson's ratio of -1; this value

was experimentally validated through a strain analysis of the seven conformational states by digital image correlation (DIC) on reconstructed TEM images.

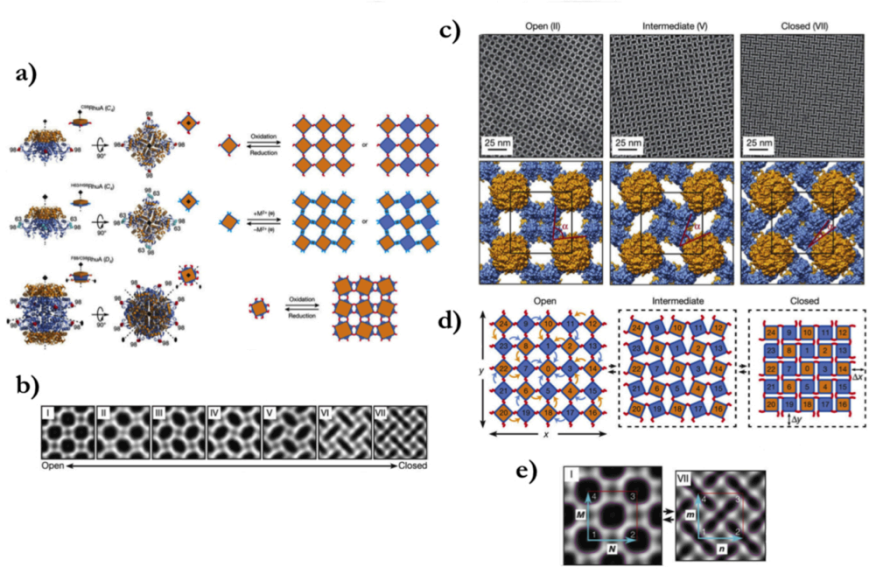


**Figure 2.17** *a) Schematic representations of the protein RhuA structures and expected 2D molecular arrangements of the lattice (top and bottom halves of RhuA are coloured orange and blue, respectively; Cys (red) and His (cyan) residues are shown; $M^{2+}$ refers to $Zn^{2+}$ or $Cu^{2+}$ ions); b) Reconstructed 2D images of seven distinct conformational states for RhuA crystals; c) High-magnification views and derived structural models of conformations II, V and VII; d) Schematic representation of the rotating, rigid-square model that describes the 2D RhuA lattice dynamics; e) DIC analysis of reconstructed TEM images of RhuA considering representative volume elements in the lattices of the two extreme states (I and VII).*[63]

Despite being theoretically the first example of isotropic material with negative Poisson's ratio designed and constructed at the molecular level, direct mechanical tests on the 2D protein crystals are practically unfeasible; thus the incorporation of this architecture into polymeric materials is required.

All the examples reported so far clearly highlight how, while the theoretical design and modelling of molecular auxetics has been widely pursued, its practical realization is still lacking. Therefore we propose a novel approach based on the incorporation into a polymeric matrix of tetraquinoxaline

cavitands as conformationally expandable monomeric units. The basic idea is the design of a material in which the introduction of molecules able to reversibly increase their size by switching from an initial contracted conformation to an expanded one upon tensile force could impart the expected auxetic responsiveness. Tetraquinoxaline cavitands, thanks to their interconversion between two discrete conformational states, provide the desired kinematic response; interestingly the so-called re-entrant cells, usually proposed as auxetic macro- or meso-scale structure modules in macroscopic architectures,[65] can be properly applied for representing and quantifying the nano-scale kinematic behaviour of cavitand molecules (Figure 2.18). The adoption of this re-entrant conformed element with proper geometrical features, called *auxeton*, allows a quantitative estimation of the effect of cavitand behaviour on the resulting stress-responsive polymer.

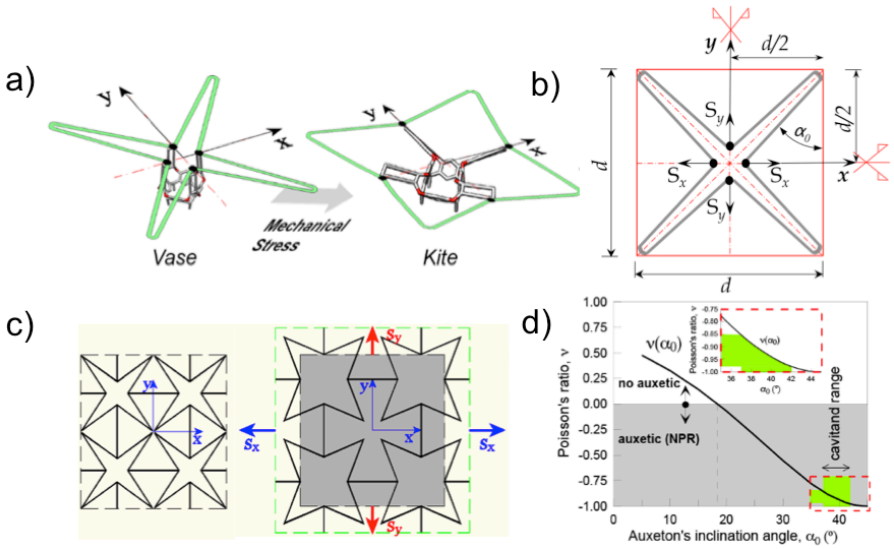


**Figure 2.18** *a) Representative auxeton for cavitand unit in the undeformed (Vase) and deformed (Kite) conformation; b) Geometrical parameters of the considered auxeton; c) Undeformed and deformed pattern of a patch of auxetic cells under an horizontal displacement; d) Dependence of the Poisson's ratio ν on the auxeton angle α; magnification of the ν vs. α region corresponding to the cavitand behaviour.*

Fig. 2.18b resumes the main geometrical parameters characterizing the *auxeton*, while in Fig. 2.18c the Poisson's coefficient for the re-entrant element (stretched along the x-direction by the displacements $S_x$) as a function of its opening angle $\alpha$ is shown. Being the Poisson's ratio defined as $\nu = -\varepsilon_y/\varepsilon_x$, where $\varepsilon_x = S_x/2d$ and $\varepsilon_y = S_y/2d$, the function $\nu$ *vs.* $\alpha$ shows that, for $\alpha \geq 18.5°$, $\nu$ becomes negative. Geometrical parameters obtained by the crystal structures of the two conformers[66] allowed an estimation of $\alpha$ as falling in the range of 37° to 42° for the representative *auxeton*, thus corresponding roughly to a Poisson's coefficient of -0.80 ÷ -0.95.
The schematic representation of the designed materials is depicted in Fig. 2.19; basically, in order to exploit the conformational expansion for achieving a macroscopic response, we decided to covalently link the cavitand units in a polymeric network by a proper functionalization of the quinoxaline wings.

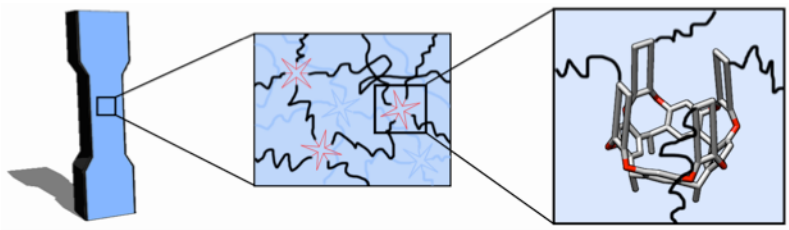

**Figure 2.19** *Schematic representation of the designed material: cavitands are connected to each other via polymeric chains covalently linked to the quinoxaline wings; auxeton elements are depicted as red stars.*

Being uniformly distributed in the matrix with a random orientation, the 2D auxetic behaviour of the single cavitand unit leads to an average 3D isotropic auxetic material.

## 2.2 Results and discussion

Considering the essential role played by the nature of the polymer in terms of efficiency of the mechanochemical transduction, we decided to investigate two different matrices, an elastomeric PDMS and a more rigid polyurethane; indeed, besides being both employed in literature for the force-induced activation of spiropyran mechanophores, they present a wide scale of material features, because of their extremely different mechanical properties.
Since DFT calculations on cavitands suggested that all intermediate states between the two discrete conformers are energetically disfavoured, we assumed that the application of a tensile force to two quinoxaline wings in distal position would elicit the opening of the other two, thus promoting the *vase* → *kite* interconversion. Starting from this assumption, we initially performed the synthesis of AC-difunctionalized tetraquinoxaline cavitands bearing proper moieties, suitable for the covalent incorporation into the polymeric network. In particular, terminal vinyl groups were introduced to ensure the embedding into the PDMS matrix, while hydroxy groups were exploited for the polyurethane one. In parallel, specimens with the corresponding tetrafunctionalized cavitand have been prepared and mechanically tested, in the hypothesis that the use of a cavitand molecule acting as cross-linking agent into the polymer could result in a more efficient channelling of the applied force to the mechanophore unit. Cavitands decoration at the upper rim was performed *via* a convergent approach through a bridging reaction with pre-functionalized 2,3-dichloroquinoxalines. The anchoring site for polymer grafting was connected to the cavitand core *via* easily accessible ester linkages and through long aliphatic spacers, in order to prevent a possible decrease in reactivity for steric effects. Since it is known that modification of the upper rim might affect *vase* ⇆ *kite* conformational equilibrium, even hampering a purely *vase* structure, we exclusively functionalized quinoxaline walls in 6 or 7 position, thus minimizing steric hindrance. Synthetic strategies to afford AC-difunctionalized and tetrafunctionalized cavitands with the required grafting moieties are conceptually analogous; obtained molecules have been subsequently employed as co-monomers in the preparation of polymeric specimens which were characterized and mechanically tested. Furthermore, for both matrices, specimens with physically dispersed non-functionalized cavitands or non-

properly anchored cavitands have been prepared and mechanically tested as control samples. Considered the need to study the effect of force application on insoluble polymeric matrices, *vase* ⇆ *kite* conformational equilibrium has been monitored *via* spectroscopic methods, in particular UV-Vis and fluorescence spectroscopy, which are reported in literature to be a powerful tool for visualizing the conformational switching.[32]

### 2.2.1 Alkene functionalized cavitands

As demonstrated by Craig and co-workers, polysiloxanes are suitable matrices for mechanochemical applications since, besides their well-known high stretchability and mechanical strength, they present an efficient transduction of applied forces to embedded mechanophore units. Conventional protocol for the covalent incorporation of stress-responsive elements into PDMS is *via* hydrosilylation reaction and requires their functionalization with terminal double bonds.[18] Accordingly, we synthesized ditopic cavitands **1a-1c** (Figure 2.20), where the length of the aliphatic spacers was varied to investigate its influence on the transduction of the macroscopic elongation. Furthermore, following the protocol developed by Moore and co-workers, samples containing monofunctionalized cavitand **2** (Figure 2.20) were tested to isolate the effects of the bidirectional strain. Maxima in UV-Vis spectra were compared to two unsubstituted reference compounds **5** and **6**, physically dispersed into the PDMS network; QxCav **6**, bearing four methyl groups in apical position, is forced in *kite* conformation by steric effects.[67] Finally, tetrafunctionalized QxCav **3** and **4** (Figure 2.20) were synthesized and used as cross-linkers, respectively in active and control samples, in order to maximize the applied tension. Unlike QxCav **3**, cavitand **4**, bearing the anchoring sites at the lower rim, is not expected to be affected by any conformational change upon stretching.

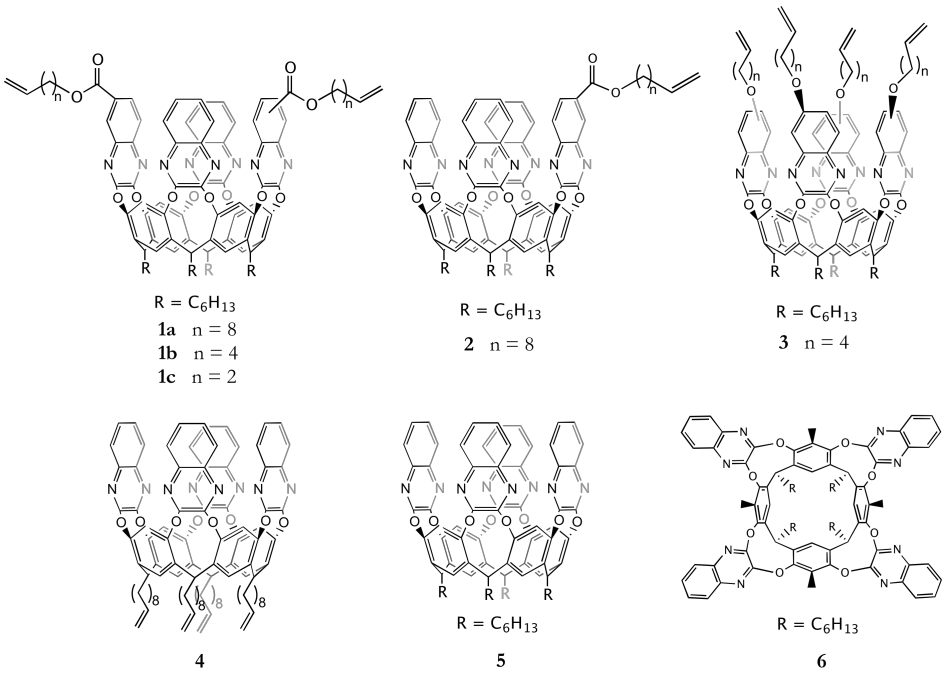


**Figure 2.20** *Overview of alkene functionalized and unsubstituted cavitands employed in the PDMS polymers preparation.*

Tetraquinoxaline cavitands were obtained *via* a convergent approach where either functionalized or non-functionalized quinoxalines were introduced on resorcinarenes or partially bridged cavitands. Quinoxalines were prepared from the easily accessible 2,3-dichloroquinoxaline-6-carbonyl chloride **8'**,[68] thanks to the convenient reaction of acyl chloride with nucleophiles under mild conditions (Scheme 2.1). In particular, 2,3-dihydroxy-quinoxaline-6-carboxylic acid **7**, obtained in quantitative yield from the condensation of commercially available 3,4-diaminobenzoic acid with oxalic acid, was reacted with Vilsmeier reagent[69] and directly employed for the nucleophilic acyl substitution with ω-alkene alcohols with different aliphatic spacers.

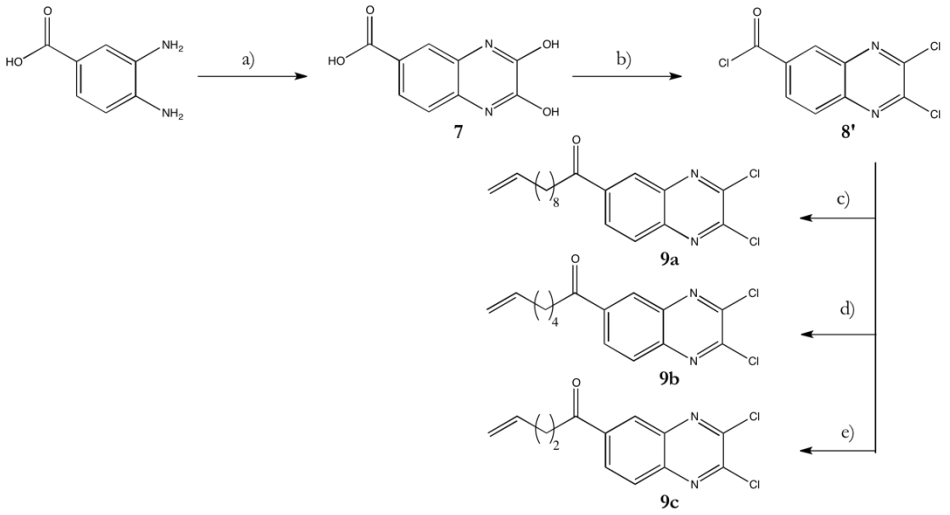


**Scheme 2.1** *Synthesis of ω-alkene functionalized 2,3-dichloroquinoxalines: a) oxalic acid, HCl 4 N, 12 h, reflux, quant.; b) thionyl chloride, DMF cat., 1,2-dichloroethane, reflux, 3 h; c) 9-decen-1-ol, $Et_3N$, $CH_2Cl_2$, r.t., 12 h, 76%; d) 5-hexen-1-ol, $Et_3N$, $CH_2Cl_2$, r.t., 12 h, 57%; e) 3-buten-1-ol, $Et_3N$, $CH_2Cl_2$, r.t., 12 h, 49%.*

Tetraquinoxaline cavitands with different functionalization at the upper rim were obtained by bridging reaction of ω-alkene dichloroquinoxalines **9a**, **9b** and **9c** on variously substituted scaffolds. As reported in literature, partially bridged cavitands were prepared in two steps from the corresponding resorcinarene; after the formation of tetraquinoxaline cavitand **5**, one or two quinoxaline walls were selectively removed by excision reaction with a proper amount of catechol under basic conditions (Scheme 2.2).

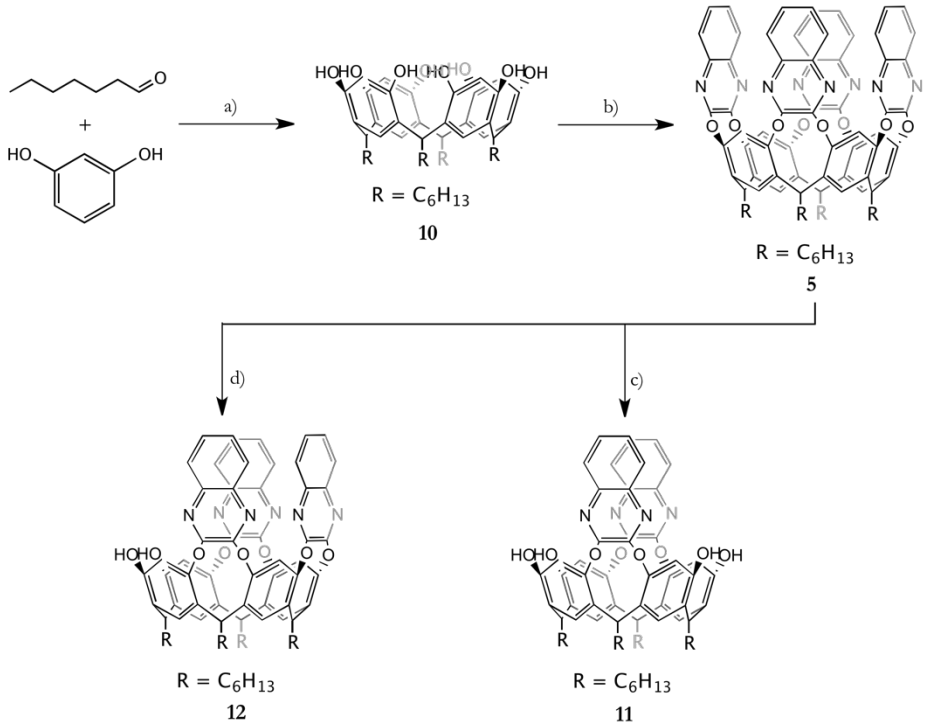


**Scheme 2.2** *Synthesis of resorcinarene **10** and partially bridged cavitands **11** and **12**: a) HCl 37%, MeOH, 50 °C, 5 d, 55%; b) 2,3-dichloroquinoxaline, $K_2CO_3$, DMF, 80 °C, 12 h, 59%; c) catechol, CsF, 80 °C, 1 h, 54%; d) catechol, CsF, 80 °C, 45 min, 57%.*

Stress-responsive units **1a-1c** were synthesized by reaction of the corresponding ω-alkene dichloroquinoxalines **9a-9c** with AC-diquinoxaline cavitand **11** (Scheme 2.3) in DMSO in presence of potassium carbonate. The use of microwave irradiation for all the nucleophilic substitutions on cavitands conveniently increased yields and, at the same time, allowed sensibly lower reaction times. Because of the prochirality of monosubstituted dichloroquinoxalines, column chromatography afforded **1a-1c** cavitands as a mixture of inseparable diastereoisomers.

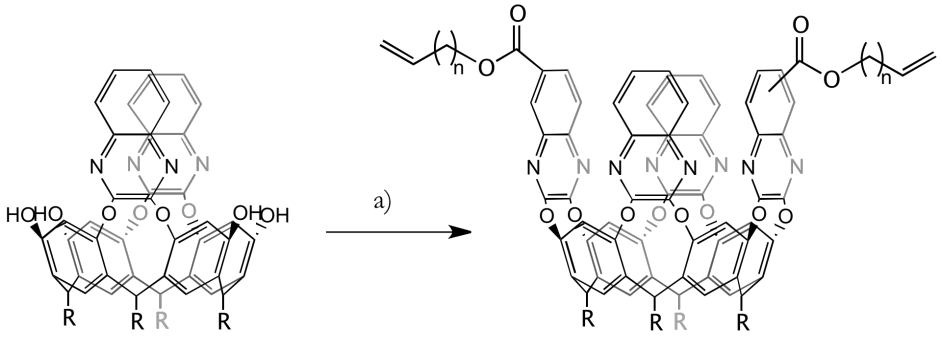


**Scheme 2.3** *Synthesis of bis-ω-alkene functionalized QxCav* ***1a-1c****: a)* ***9a-9c****,* $K_2CO_3$*, DMSO, 70 °C (MW), 1 h, n = 8, 42%; n = 4, 40%; n = 2, 39%.*

Compound **2**, used for the preparation of control specimens, was analogously obtained through bridging reaction on the corresponding triquinoxaline cavitand **12** (Scheme 2.4).

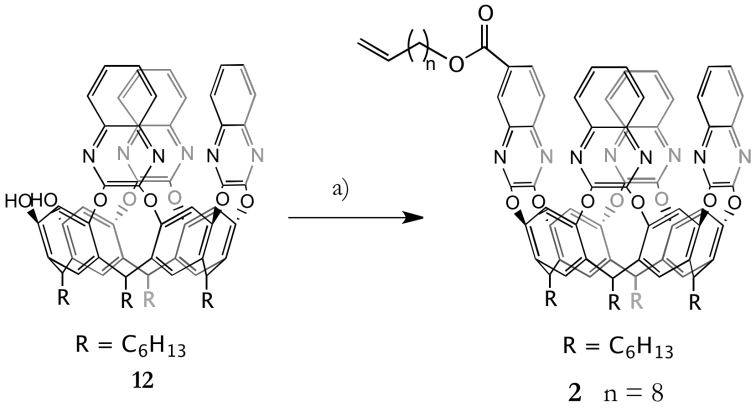


**Scheme 2.4** *Synthesis of mono-ω-alkene functionalized QxCav* **2***: a)* ***9a****,* $K_2CO_3$*, DMSO, 70 °C (MW), 30 min, 46%.*

To obtain precursors **11** and **12**, the excision approach experimentally resulted in being more efficient in terms of selectivity in respect to the direct reaction of resorcinarene with a stoichiometric amount of functionalized 2,3-dichloroquinoxaline. Finally, tetra-alkene cavitand **3** was obtained *via* the four-fold nucleophilic substitution of **9b** directly on resorcinarene scaffold (Scheme 2.5) in analogous reaction conditions.

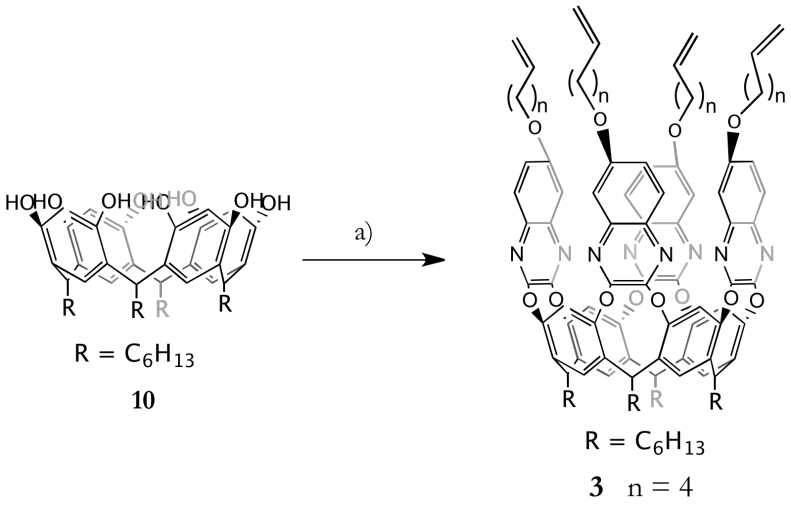


**Scheme 2.5** *Synthesis of tetra-ω-alkene functionalized QxCav* ***3****: a)* ***9b****,* $K_2CO_3$*, DMSO, 70 °C (MW), 2 h, 17%.*

Surprisingly, purification *via* column chromatography afforded, in this case, only one isomer with $C_{4v}$ symmetry. This selectivity can be explained with steric effects; in fact, after the first statistical bridging event, hindrance of the introduced aliphatic chain influenced the following insertions, thus leading to the only isomer with functionalization in alternate positions at expense of the overall yield. The high symmetry, revealed in very sharp signals in the $^1$H NMR spectrum, was unambiguously confirmed by X-rays (Figure 2.21).

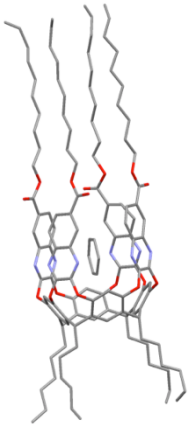

**Figure 2.21** *X-ray structure of tetra-ω-alkene functionalized QxCav* **3***; crystals grown from* $CHCl_3$*/CyHex.*

To provide an analogous cross-linking in control films, the ω-alkene tetrafunctionalized cavitand **4**, bearing double bonds at the lower rim, has been synthetized and used as cross-linker in the polymer network. Following the same procedure used for unfunctionalized *vase* cavitand **5**, QxCav **4** has been obtained *via* bridging of 2,3-dichloroquinoxaline on the corresponding resorcinarene with alkene functionality at the lower rim (Scheme 2.6).

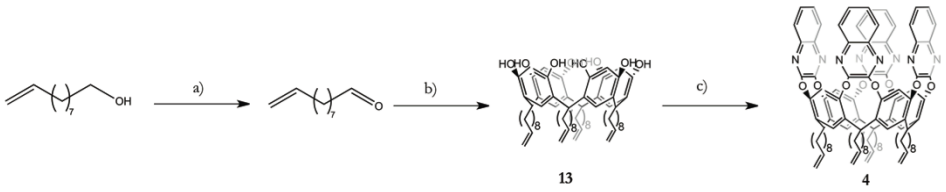


**Scheme 2.6** *Synthesis of tetrafunctionalized cavitand* **4** *for control specimens: a) PCC, AcONa,* $CH_2Cl_2$*, r.t., 4 h, 82%; b) Resorcinol, HCl 37%, EtOH, 100 °C (MW), 5 min, 36%; c) 2,3-dichloroquinoxaline,* $K_2CO_3$*, DMSO, 70 °C (MW), 30 min, 44%.*

Compounds **1a-1c**, **2**, **3** and **4** were characterized by $^1$H NMR and MALDI-TOF spectrometry. In particular, NMR spectroscopy is diagnostic not only for obtaining structural information to confirm the success of the adopted synthetic strategy, but also to determine the cavitand conformation; indeed, it is widely reported in literature[28a] that the resonance of methine protons in solution is

highly conformation-dependent, with a difference in chemical shift of more than 2 ppm between *vase* (≈5.6 ppm) and *kite* (≈3.9 ppm). Thus, the presence of a signal at around 5.6 ppm in all cases confirmed the retention of the *vase* conformation, even after the functionalization at the upper rim.
Finally, cavitand **6**, also called velcrand for its capability to form strong π-π dimers, was synthesized according to previously reported procedures[67] and used as a reference of the expanded QxCav form in control specimens.

### 2.2.2 PDMS functionalization

Alkene decorated QxCav presented in the previous paragraph and unfunctionalized cavitands **5** and **6** were employed in the preparation of PDMS specimens. The selected matrix, RTV 615, is a two-part (Base and Curing Agent, typically mixed in a 10:1 ratio) silicone elastomer comprising vinyl terminated poly(dimethylsiloxane), poly(methylhydrosiloxane-codimethylsiloxane) copolymer and a platinum catalyst.
In particular QxCav **1a-1c**, **2**, **3** and **4** have been covalently incorporated into PDMS matrix (0.05-0.7% w/w) *via* hydrosilylation protocol and their effective covalent embedding has been confirmed by Soxhlet extraction. (Details about samples preparation and extraction tests are reported in the Experimental Section). Unfunctionalized cavitands **5** and **6**, instead, have been physically dispersed into the matrix in order to provide a reference of the two conformers in PDMS. Characterization of the resulting specimens has been performed *via* UV-Vis spectroscopy, being a convenient technique both for monitoring the cavitands conformational state and for working on cross-linked insoluble matrices.
The initial comparison between UV-Vis spectra of **5** and **6** in solution and in PDMS revealed that optical properties are essentially retained in the substrate (Figure 2.22), with two maxima of absorption at 318 and 330 nm for *vase* QxCav and at 335 and 348 nm for the *kite* form.

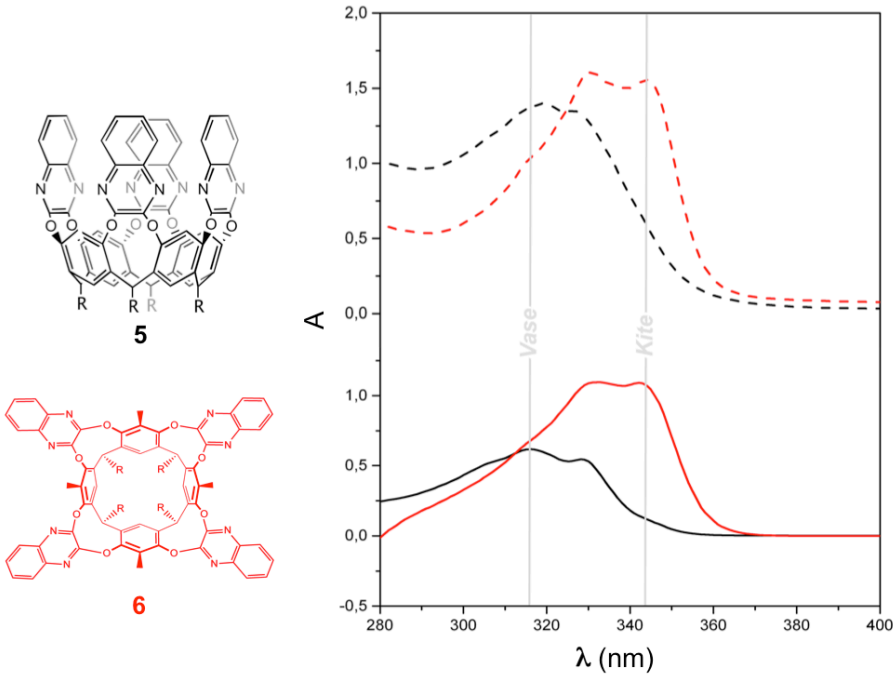


**Figure 2.22** *UV-Vis spectra of QxCav* ***5*** *(black) and* ***6*** *(red) in* $CHCl_3$ *(solid line) and in PDMS (dashed line; 0.1% w/w, Table S2.1, entry II and IV respectively).*

Once verified that UV-Vis spectroscopy can be a suitable technique for monitoring cavitand conformation, we firstly decided to test the protonation-driven interconversion in order to make sure that cavitand responsiveness to a conventional stimulus, such as pH, is still possible even when covalently embedded into a cross-linked network. Thus cavitands **1a-1c** were incorporated in PDMS (0.1-0.5%, Table S2.2) and the resulting specimens **PDMS-1a**, **PDMS-1b** and **PDMS-1c** were exposed to TFA vapours. Maxima analysis *via* UV-Vis spectroscopy (Fig. 2.23) clearly showed a quantitative *vase* → *kite* switching upon protonation of quinoxaline nitrogens in the polymers. Furthermore, TFA-treated samples, subsequently exposed to ammonia vapours, exhibited a UV-Vis spectrum consistent with the pristine one, proving the reversibility of the interconversion. As reported by Diederich *et al.*, although addition of TFA to the simple 2,3-dimethoxyquinoxaline moiety is known to lead to a sizable redshift, the overall maximum extinction coefficient does not increase

however.[32] Thus, the absorption changes that we observed result from the combination of the changes expected upon protonation of the quinoxaline wings and the conformational switch to the *kite* form.

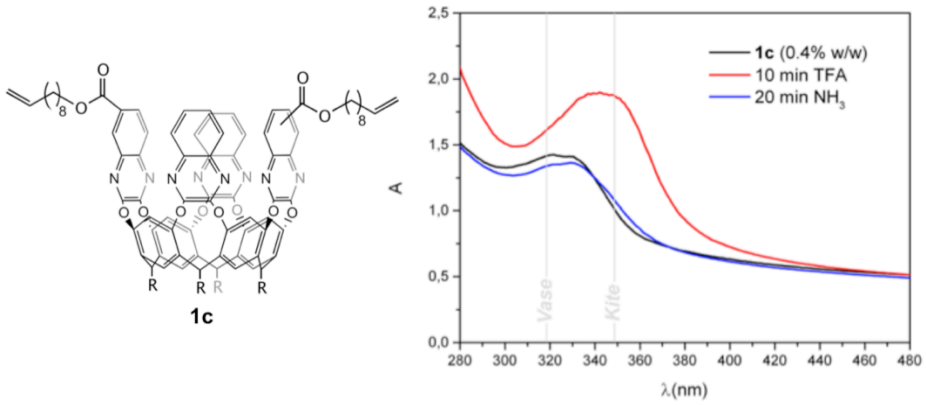


**Figure 2.23** *UV-Vis spectra of **PDMS-1c** (0.4% w/w, Table S2.2, entry XIII) (black), after 10 minutes of exposure to TFA vapours (red) and subsequent 20 minutes of exposure to $NH_3$ (blue).*

Same tests performed on **PDMS-1a** and **PDMS-1b** displayed an analogous behaviour. This result, far from being trivial, suggests that, even in a polymeric matrix, cavitands possess enough free volume to open up into the *kite* conformation. Finally, cavitands interconversion upon tensile stress was tested. Specimens containing mono and di-functionalized QxCav at different concentrations were uniaxially stretched and UV-Vis spectra were recorded at progressively increasing applied force. In all cases, no maxima variation was observed. Fig. 2.24, showing the experiment for **PDMS-1c**, is representative of the general behaviour observed for all tested specimens. Since the only visible effect is the λ-independent decrease in absorbance due to the thinning of polymer films upon elongation, we can conclude that the visual monitoring of *vase* → *kite* force-induced switching *via* UV-Vis spectroscopy was not possible.

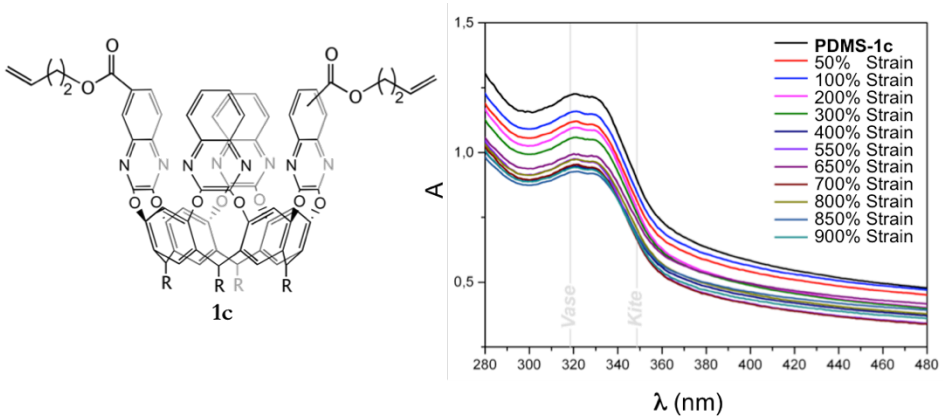


**Figure 2.24** *UV-Vis spectra of PDMS specimen with* ***PDMS-1c*** *(0.4% w/w, Table S2.2, entry XIII) upon progressive elongation.*

In the hypothesis that all four quinoxaline wings need to be stretched in order to induce the *vase* → *kite* interconversion, polymer specimens with tetrafunctionalized QxCav **3** were prepared and mechanically tested. In this case, UV-Vis spectrum in solution shows a slightly shifted maximum (323 nm instead of 318 nm for QxCav **5**), while the diagnostic shoulder attributed to the protonated *kite* form remained unaltered after functionalization (Figure 2.25). Interestingly, acid exposure of the resulting specimens **PDMS-3** with different cavitand concentration failed to evidence any maxima variation in the UV-Vis spectra. This result could be possibly explained by a lack of free volume for the cavitand, cross-linked into the PDMS network, which prevents the opening to the *kite* form.

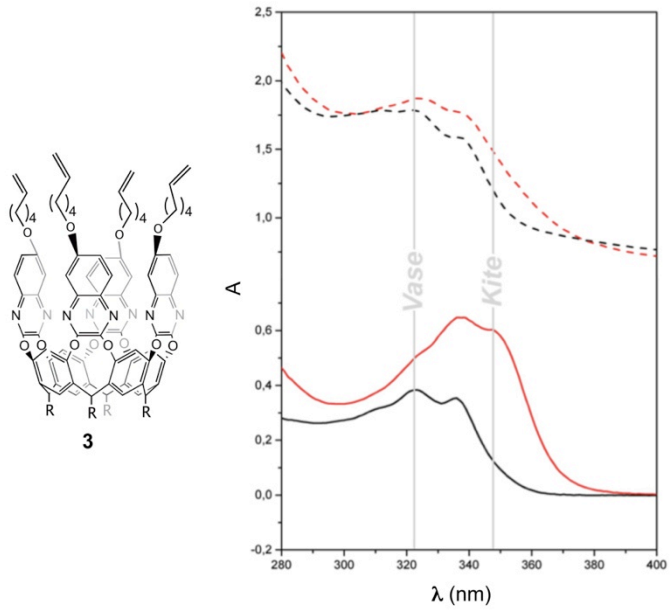


**Figure 2.25** *UV-Vis spectra of cavitand* **3** *before (black) and after (red) exposure to TFA in $CHCl_3$ solution (solid line) and in PDMS (dashed line, 0.3% w/w, Table S2.3, entry II).*

The lack of free volume in the resulting highly cross-linked system probably explains the missed response observed for these specimens in terms of maxima variation upon elongation (Figure 2.26). Considering the high number of cross-linking sites in pristine elastomeric PDMS, we hypothesized that the missed responsiveness of our system upon tensile force can be justified by a complete or partial prevention in the transmission of mechanical energy to the mechanophore.

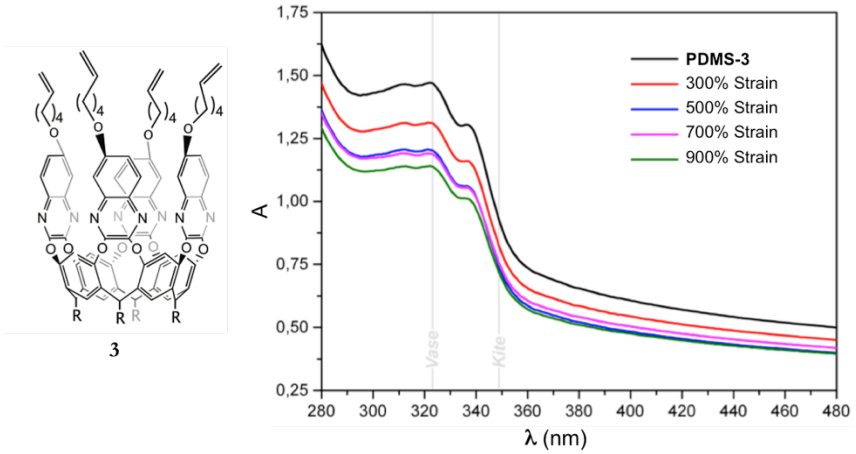


**Figure 2.26** *UV-Vis spectra of **PDMS-3** (0.3% w/w, Table S2.3 entry II) upon progressive elongation.*

Thus, in order to maximize the channelling of tensile force to the cavitand, we decided to modify the polymer backbone by replacing the conventional RTV 615 Curing Agent, consisting of a poly(methylhydrosiloxane-codimethylsiloxane) copolymer acting as cross-linker, with a ditopic H-terminated poly(dimethylsiloxane). Thus, in the resulting linear polymer **ℓPDMS** the unique cross-linking agent is represented by tetrafunctionalized cavitand **3** (Details about samples preparation are reported in the Experimental Section). Different polymeric samples have been prepared, both varying the ratio between vinyl-terminated and H-terminated pre-polymers and the amount of cross-linker, to find the optimal conditions in terms of mechanical properties of the resulting specimens (Table S2.4). To provide an analogous reticulation in the control films, tetra-ω-alkene functionalized cavitand **4**, bearing double bonds at the lower rim, has been used as a cross-linker in the polymer network. Mechanical testing on the samples failed to evidence a clear maxima variation in the UV-Vis spectra, although an increase in the absorbance at 335 nm was observed against the trend of thinning of the specimen upon elongation (Figure 2.27).

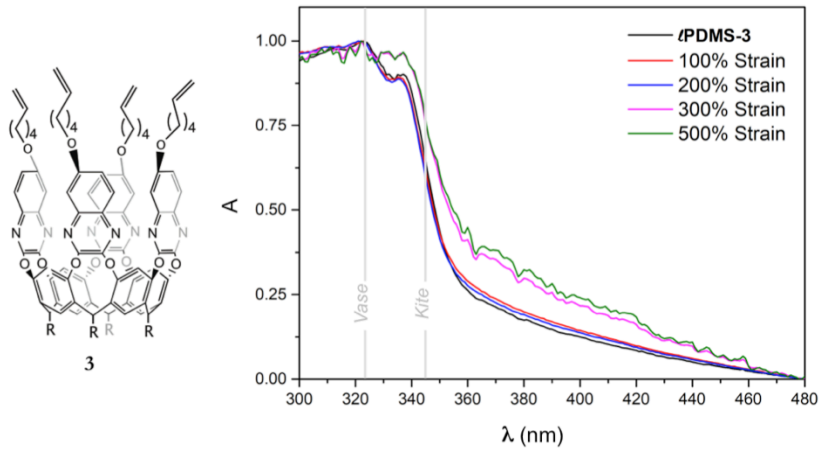


**Figure 2.27** *UV-Vis spectra of* ***ℓPDMS-3*** *(1% w/w, Table S2.4 entry VI) upon progressive elongation.*

Interestingly, the apparent increase in the extinction coefficient, occurring at the wavelength of the first maxima for the *kite* conformer, was not observed in the control specimens **ℓPDMS-4** (Figure 2.28).

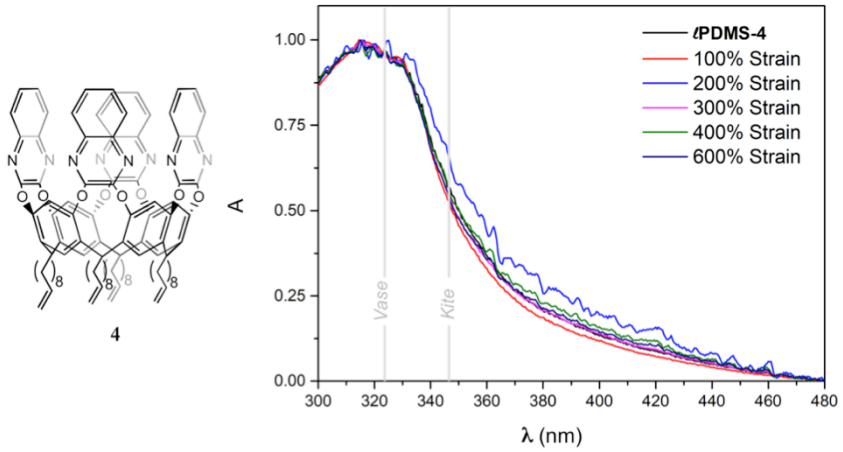


**Figure 2.28** *UV-Vis spectra of* ***ℓPDMS-4*** *(1% w/w, Table S2.4 entry IX) upon progressive elongation.*

Considering the quantitative interconversion detected upon TFA treatment, further studies were carried out in order to verify whether the dimensional increase associated with the *vase* → *kite* switching can be reflected at the macroscopic level in terms of expansion of the polymeric specimens. Thus, 2D-DIC (Digital Image Correlation) measurements were performed; this robust non-contact technique, widely used for measuring the Poisson's ratio, relies on image registration algorithms to track the relative displacements of materials points between a reference (typically, the undeformed) image and a current (typically, the deformed) image.[70] **PDMS-1a** samples with 0.5% w/w of QxCav were exposed to TFA vapours, recording pictures with a high-resolution digital camera (Further details about experimental setup and methods are reported in the Experimental Section). Clearly, in order to unbundle the contribution of pure swelling due to acid absorption, the expansion of pristine PDMS was measured and compared to the one of 'active' specimens. Therefore, in the measured expansion it was possible to isolate the component related to the opening of cavitands' quinoxaline wings. Furthermore, **PDMS-4** and **PDMS-5** specimens, in which the cavitand is respectively embedded or dispersed into the polymer matrix, were tested, in order to verify if the nature of the incorporation and the position of anchoring sites to the PDMS backbone have an influence on the detected expansion. The mean surface expansion, defined as $\varepsilon_S = \varepsilon_x + \varepsilon_y$, was considered over a TFA-exposure of 60 minutes and a meaningfully wider expansion was observed for **PDMS-1a** in respect to control specimens (Figure 2.29).

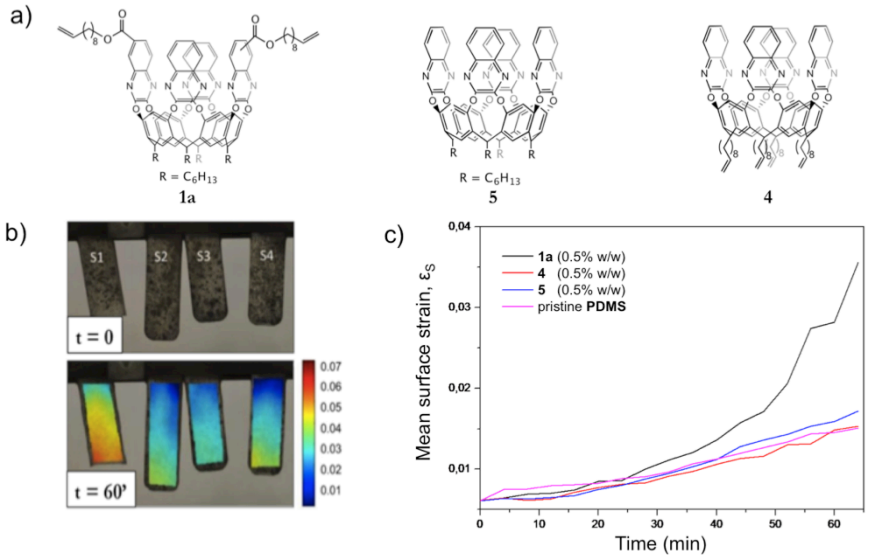


**Figure 2.29** *a) Scheme of QxCav **1a**, **5** and **4**; b) Top: Picture of PDMS specimens (S1: **PDMS-1a**, S2: **PDMS-4**, S3: **PDMS-5**, S4: pristine **PDMS**) to which a speckle pattern is applied with carbon at t = 0; Bottom: Surface strain maps at t = 60 min; c) Plot of the mean surface strain $\varepsilon_S$ vs. time.*

2D-DIC measurements, therefore, suggest that the presence of a covalent connection between polymer chains and expanding cavitand wings support the effect of QxCav opening on the material expansion. This macroscopic result, attained for a relatively low concentration (0.5% w/w) of QxCav, is in line with our recent micromechanics-based model accounting for the deformation processes in polymeric materials containing switchable molecules.[71]

In conclusion, although a similar matrix has been successfully used by Craig and co-workers for the mechanochemical activation of spiropyran, *vase* → *kite* interconversion for PDMS-embedded QxCav has not been clearly detected. A possible reason could be the low degree of force-elicited conversion, reported for being down to 5% in SP-based materials, which makes the detection of cavitands conformational switching *via* UV-Vis spectroscopy very difficult in respect to a visible colour change. Thus, a more efficient system ensuring a higher degree of conversion for the mechanophore unit is needed. Since the more promising results were obtained with a tetrafunctionalized quinoxaline

cavitand acting as cross-liker into the polymer network, we decided to exploit the same approach by replacing the elastomeric PDMS with a more rigid matrix, such as polyurethane.

### 2.2.3 Hydroxy functionalized cavitands

As PDMS, PU is known in literature for being an efficient matrix in the stress-induced activation of SP to MC. Moore and co-workers[17] reported the incorporation of hydroxy functionalized SP into linear PU *via* step growth polymerization, highlighting how the use of a more rigid matrix leads to a higher degree of conversion. Thus, the mechanophore units employed for this study are represented in Fig. 2.30. In particular, a bis-ω-hydroxy functionalized cavitand **14** and a mono-ω-hydroxy functionalized cavitand **15** were covalently incorporated into the PU matrix as co-monomers in the step growth polymerization. Furthermore, a tetra-ω-hydroxy functionalized QxCav **16** and the corresponding propanol-footed QxCav **17** were prepared to act as cross-linkers in active and control specimens, respectively. Finally, a tetra-ω-hydroxy functionalized velcrand **18** was used as a reference for the covalently embedded *kite* form into PU.

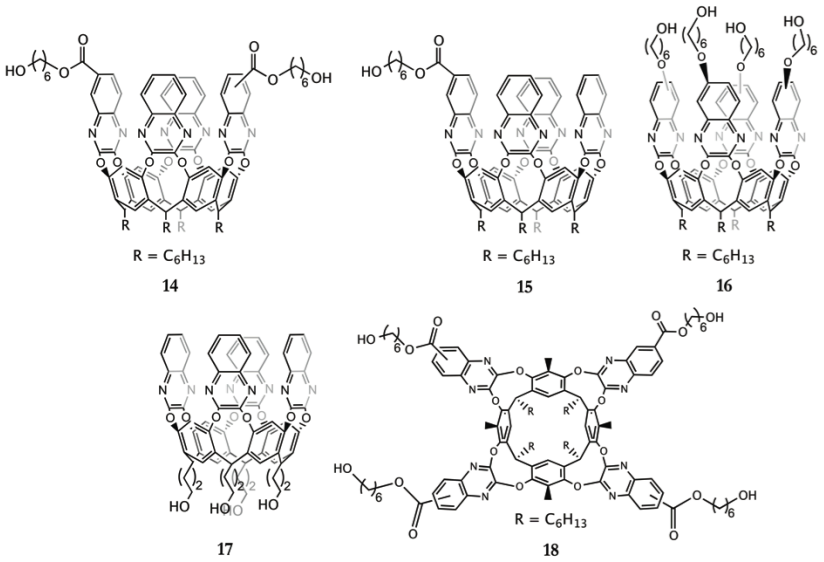


**Figure 2.30** *Overview of hydroxy functionalized cavitands employed in specimens' preparation.*

QxCav **14**, **15** and **16** were obtained, analogously to the corresponding alkene functionalized ones, *via* a convergent approach by bridging the corresponding dichloroquinoxaline onto variously substituted cavitand scaffolds. In detail, 2,3-dichloroquinoxaline **19**, bearing a hydroxy group protected as *tert*-butyl dimethylsilyl ether (TBDMS), was prepared from the easily accessible 2,3-dichloroquinoxaline-6-carbonyl chloride **8'**[68] through the convenient acyl substitution with mono-protected hexanediol **18** under mild conditions (Scheme 2.7).

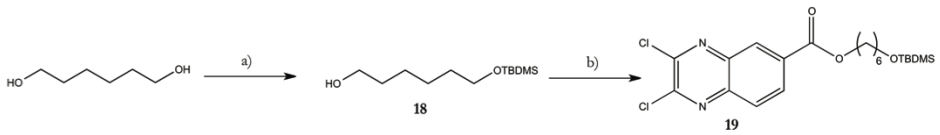


**Scheme 2.7** *Synthesis of TBDMSO-hexyl dichloroquinoxaline **19**: a) TBDMSCl, Imidazole, DMF, r.t., 3 h, 52%; b) **7'**, $Et_3N$, $CH_2Cl_2$, r.t., 12 h, 76%.*

Nucleophilic substitution of quinoxaline **19** onto AC-diquinoxaline and triquinoxaline QxCav **11** and **12**, followed by deprotection of TBDMS group, afforded respectively cavitands **14** and **15**, suitable for the covalent incorporation into PU matrix (Scheme 2.8). The choice of TBDMS, instead of more conventional protecting groups, is due to the possibility of achieving the deprotection under very mild conditions, where the stability of the cavitand scaffold is preserved.

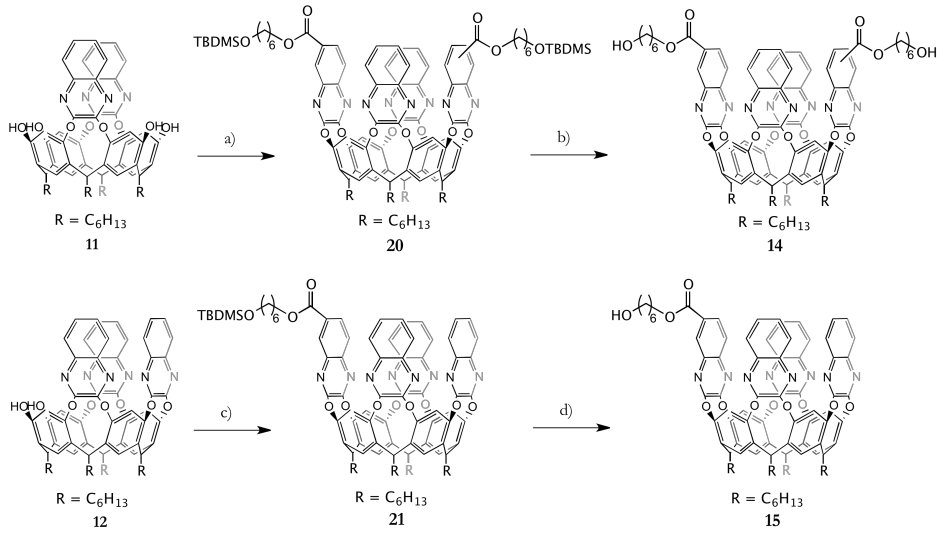


**Scheme 2.8** *Synthesis of bis- and mono-ω-hydroxy functionalized QxCav* ***14*** *and* ***15****: a)* ***19****, $K_2CO_3$, DMSO, 70 °C (MW), 1 h, 41%; b) NBS, DMSO/THF, $H_2O$, r.t., 12 h, 73%; c)* ***19****, $K_2CO_3$, DMSO, 70 °C (MW), 30 min, 49%; d) NBS, DMSO/THF, $H_2O$, r.t., 12 h, 79%.*

Once more, because of the prochirality of monosubstituted dichloroquinoxalines, purification by column chromatography afforded QxCav **20** and **14** as a mixture of inseparable diastereoisomers. Tetrafunctionalized cavitand **16**, designed for acting as cross-linker in the linear PU matrix, was obtained by the fourfold bridging of quinoxaline **19**, under microwave irradiation, onto resorcinarene **10** and the subsequent deprotection with NBS (Scheme 2.9).

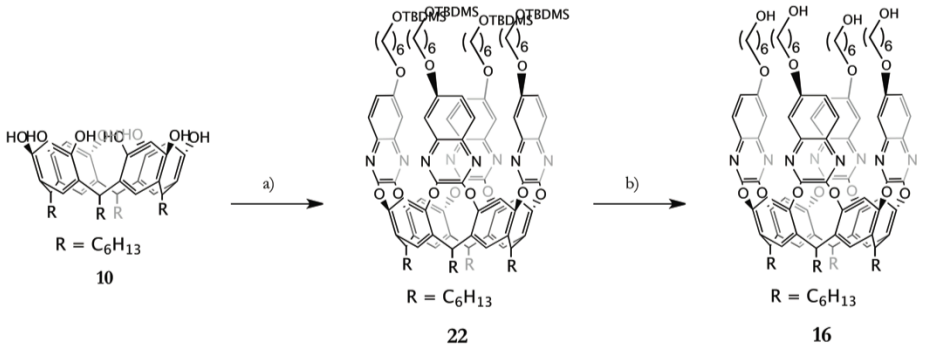


**Scheme 2.9** *Synthesis of tetra-ω-hydroxy functionalized QxCav* ***16****: a)* ***19****,* $K_2CO_3$*, DMSO, 70 °C (MW), 2 h, 12%; b) NBS, DMSO/THF,* $H_2O$*, r.t., 12 h, 55%.*

The high resolution of $^1$H NMR signals for cavitand **16** confirmed that, also in this case, the only isomer bearing alkyl functionalities in alternate positions was obtained. This selectivity, due to steric effects, probably justifies the low yield of the bridging reaction. Cavitand **17** decorated with hydroxy groups at the lower rim was prepared from the known propanol-footed resorcinarene scaffold,[72] by the four-fold bridging of unsubstituted 2,3-dichloroquinoxaline (Scheme 2.10). QxCav **17**, acting as cross-linker for further control specimen, clearly differs from QxCav **16** for being anchored to the PU backbone in the "wrong" position, so that mechanical solicitations do not affect the opening of quinoxaline wings.

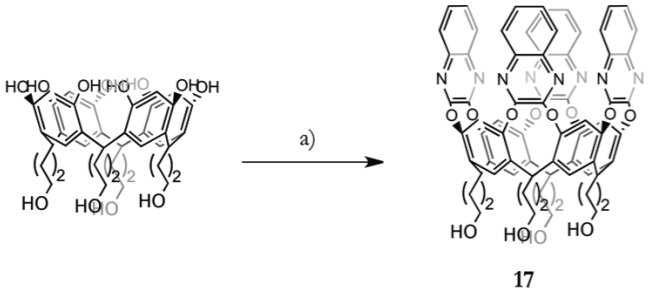


**Scheme 2.10** *Synthesis of propanol-footed QxCav* ***17****: a) 2,3-dichloroquinoxaline,* $K_2CO_3$*, DMSO, 70 °C (MW), 1 h, 42%.*

Finally QxCav **18**, forced in the *kite* conformation, was obtained from the corresponding resorcinarene scaffold **24** *via* the four-fold bridging of functionalized quinoxaline **19** and the subsequent deprotection (Scheme 2.11).

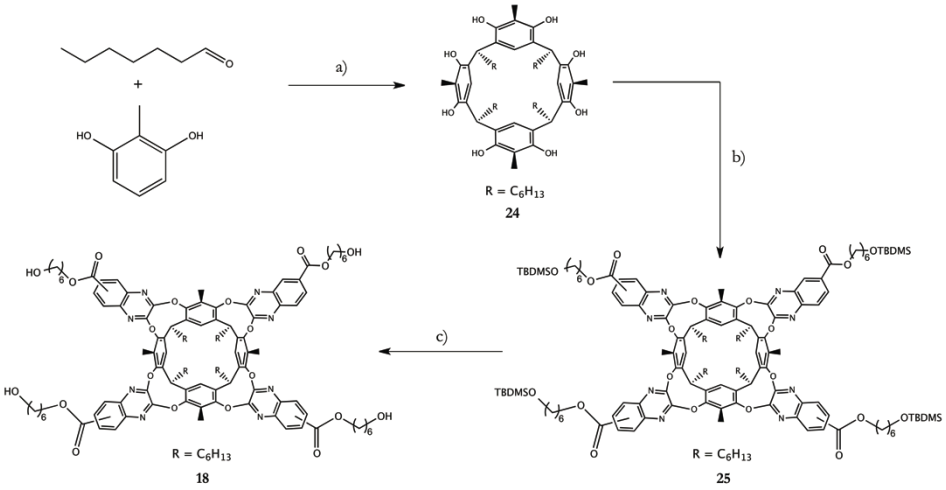


**Scheme 2.11** *Synthesis of QxCav* ***18****: a) HCl 37%, MeOH, 80 °C, 4 d, 81%; b)* ***19****, $K_2CO_3$, DMSO, 70 °C (MW), 2 h, 51%; c) NBS, DMSO/THF, $H_2O$, r.t., 12 h, 49%.*

In this case the broad signals in the $^1$H NMR spectra suggest that both cavitands **25** and **18** are obtained as an inseparable mixture of constitutional isomers. The expected lack of selectivity for the bridging reaction is probably due to the expanded conformation of the resulting QxCav, where the absence of steric effects does not impose any geometrical constraints for the insertion of functionalized dichloroquinoxaline **19**.

### 2.2.4 PU functionalization

Hydroxy functionalized cavitands presented in the previous paragraph, together with unfunctionalized QxCav **5** and **6**, were employed in PU specimens' preparation. The selected matrix is a relatively rigid polymer obtained by step growth polymerization between poly(tetramethylene glycol) (PTMG, $M_n$ = 1000) and isophorone diisocyanate, followed by the addition of

hexamethylene diisocyanate as chain extender. The use of isophorone instead of the more common methylene diisocyanate is related to the need for maximizing the optical transparency of the resulting films and thus facilitating the visualization of *vase* → *kite* switching *via* UV-Vis spectroscopy (Details about samples preparation are reported in the Experimental Section). As for PDMS matrix, polymer specimens with physically dispersed cavitands **5** and **6** were firstly prepared, in order to provide a reference of the two conformers in PU matrix. Characterization *via* UV-Vis spectroscopy confirmed that the optical properties of the conformers are essentially retained in the substrate (Figure 2.31), even if a small redshift (from 342 nm to 345 nm) for the second maximum in the *kite* form is observed when moving from solution to the solid matrix.

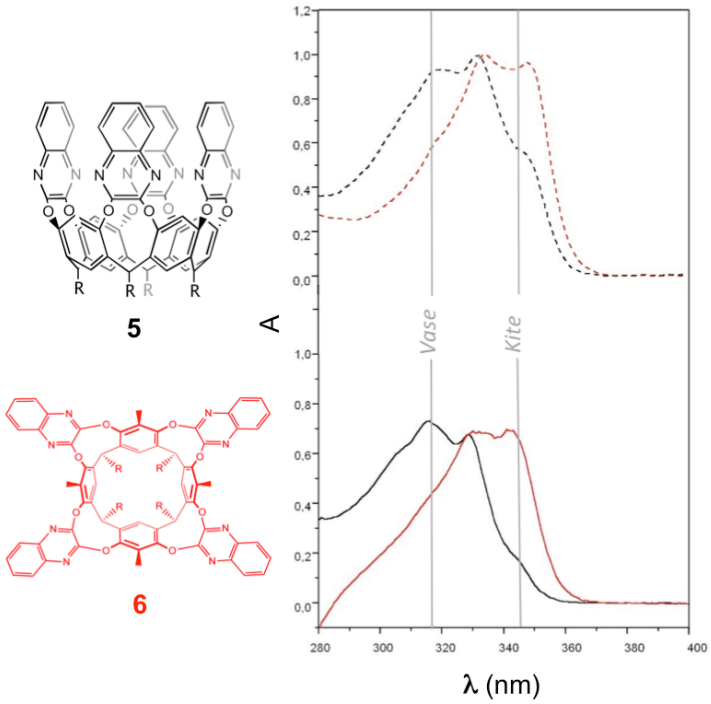


**Figure 2.31** *UV-Vis spectra of cavitands* **5** *(black) and* **6** *(red) in* $CH_2Cl_2$ *(solid line) and in PU (dashed line).*

Compounds **14**, **15**, **16** and **17**, bearing a hydroxy group, were employed as co-monomers in the step growth polymerization. Unfortunately, because of the poor solubility of the cavitand, realization of control specimens with PU-embedded QxCav **17** was not possible. Thus, tetra-ω-hydroxy functionalized QxCav **16** was employed in the preparation of force-responsive films **PU-16**, while functionalized QxCav **14** and **15**, together with QxCav **5**, were used for control films **PU-14**, **PU-15** and **PU-5**. Finally, since the investigation of protonation-driven interconversion was not feasible because of the fast degradation of the PU substrate when exposed to TFA vapours, cavitands interconversion upon tensile stress was directly tested, recording UV-Vis spectra at progressively increasing applied force. **PU-16** specimens revealed, when stretched, the rise of a shoulder at 345 nm, corresponding to the second maximum of the *kite* conformer. Fig. 2.32, illustrating the experiment for **PU-16** (0.3% w/w, Table S2.6 entry II), is representative of the general behaviour observed for all tested specimens, where changes in the UV-Vis spectra start to be sizable for a degree of stretching of about 200%.

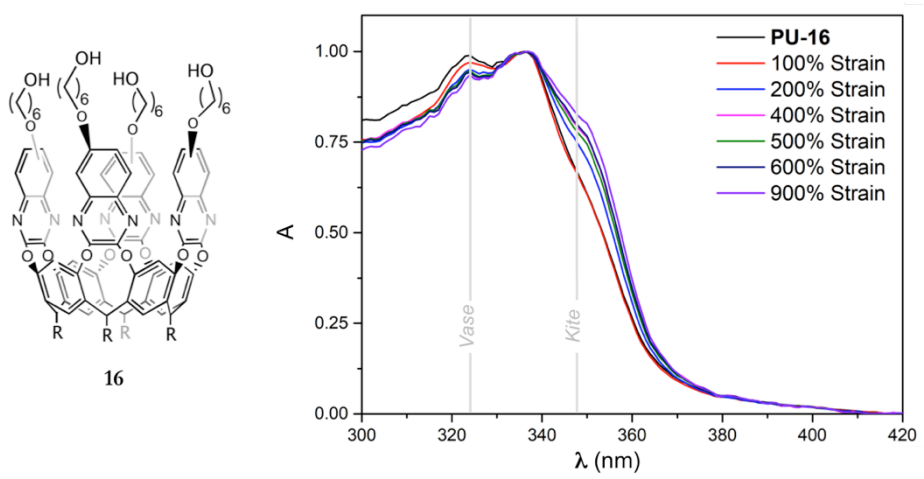


**Figure 2.32** *UV-Vis spectra of **PU-16** (0.3% w/w, Table S2.6 entry II) upon progressive elongation.*

Same mechanical tests performed on control specimens failed to evidence any change in the UV-Vis spectra; Fig. 2.33, showing the spectra recorded for **PU-5** upon elongation, resumes the general behaviour observed for all control

samples. The observed spectroscopic variations seem to confirm that force-elicited conformational change of tetraquinoxaline cavitands in polymeric matrices is possible. The low magnitude of the measured shift can be partially justified with the expected limited degree of conversion from *vase* to *kite*, which implies the coexistence of both species in the stretched specimen.

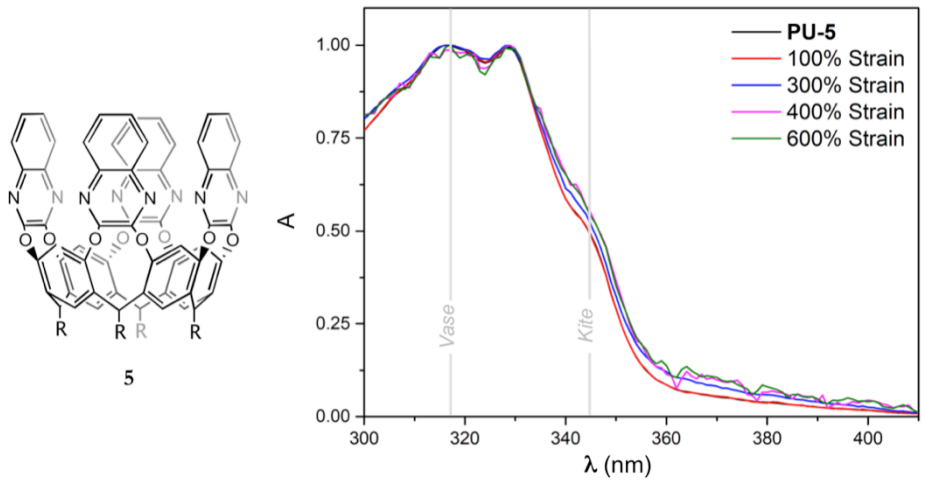


**Figure 2.33** *UV-Vis spectra of **PU-5** (0.3% w/w, Table S2.5 entry II) upon progressive elongation.*

Thus, in order to prove unambiguously the occurrence of the conformational switching, fluorescence spectra under tensile stress for 'active' and control films were recorded. Fluorescence spectroscopy provides a more sensitive technique for monitoring *vase* → *kite* interconversion, being suitable for working on cross-linked insoluble matrices. Initial fluorescence studies in solution for cavitands **5** and **6** suggested a solvatochromic nature of the emission band; in particular, a redshift was observed when increasing the solvent polarity (Figure 2.34). Despite being composed by the same fluorophoric units, the dependence of the emission wavelength from the solvent polarity is not the same for the two conformers. In medium-high polarity solvents, such as $CHCl_3$ and DMF, the emission band of the *vase* is located roughly at the same position as the emission band of the *kite*; in low polarity media, such as $CCl_4$ and toluene, the fluorescence band of the *vase* falls at shorter wavelengths with respect to the

*kite*. This observation suggests that fluorophoric units in the contracted conformation are less solvated than in the expanded one, especially in low polarity solvents. A likely explanation for this behaviour relies on the different molecular structure, where cavitand **5**, having the fluorophoric units closer to one another, forms an intermolecular 'quadrimer' hardly solvated by low polarity solvents.

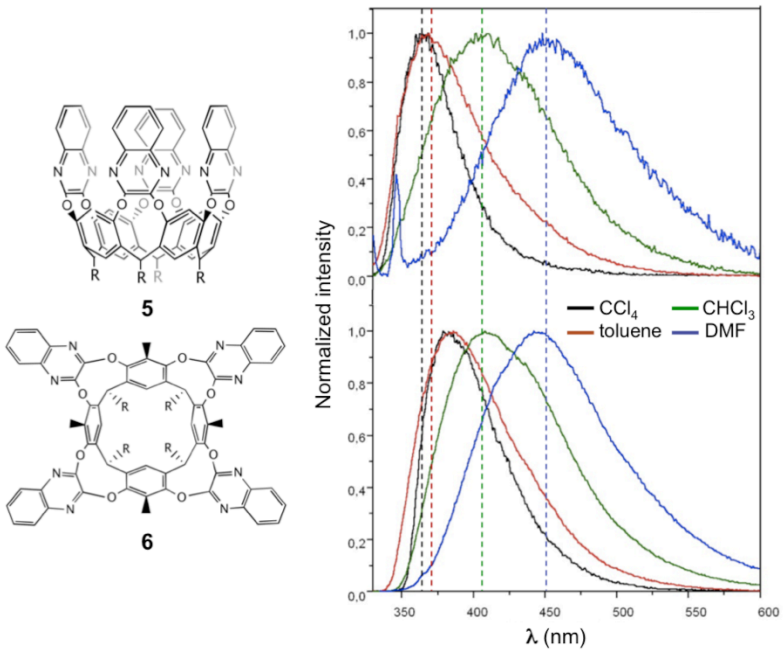


**Figure 2.34** *Normalized fluorescence emission spectra of QxCav* **5** *and* **6** *in different polarity solvents; vertical dashed lines are a guide to the eye in order to appreciate the shift.*

Analogous behaviour was observed for the emission spectra of the same compounds dispersed in PU films; fluorescence band of the *vase* conformer, indeed, appears blueshifted of about 15 nm with respect to the *kite* one. Being the emission spectra more similar to the ones recorded in toluene, the polymeric matrix seems to behave like a low-polarity environment. An even stronger shift between the two bands (of about 30 nm) was observed in films where cavitands are part of the polymeric network, as for the case of **PU-16** and **PU-18**, further confirming that the *vase* conformer is less solvated than the *kite*

one also in solid matrix. Remarkably, while the contracted form shows a redshift of 10 nm when passing from being physically dispersed to being covalently linked to the polymeric network, the expanded one moves of 30 nm (Figure 2.35). This observation strongly suggests that *kite* compound, when dispersed, tends to form intermolecular aggregates, resulting in an emission behaviour closer to the intramolecular quadrimer situation showed by *vase* compound in low-polarity media. On the other hand, covalent embedding into the polymeric structure prevents the formation of *J*-aggregates, leading to an emission behaviour more similar to the one observed in medium-high polarity solvents. By contrast, aggregation effect for *vase* compound, having mainly an intramolecular origin, is essentially non-influenced by the nature of cavitand incorporation into PU.

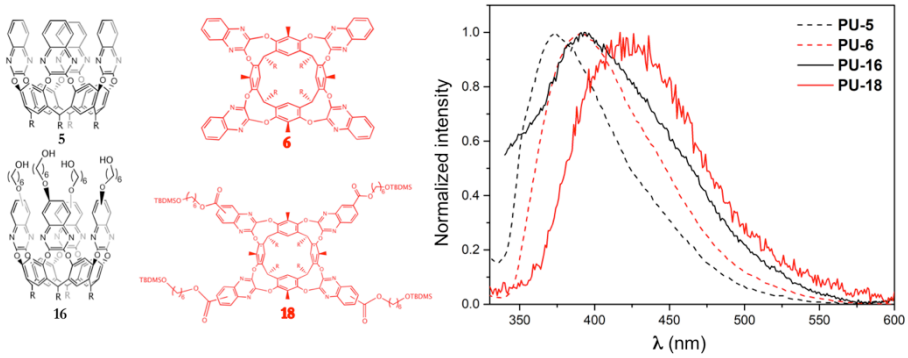


**Figure 2.35** *Normalized fluorescence emission spectra of vase (black) and kite cavitand (red) physically dispersed (**PU-5** and **PU-6**, dashed line) and covalently linked (**PU-16** and **PU-18**, solid line) to the polymer backbone.*

To confirm the tendency of *kite* compound to form intermolecular aggregates, concentration dependence of the emission in a medium polarity solvent such as $CHCl_3$ was studied. In particular, comparison between the emission spectra recorded for $10^{-4}$ M and $10^{-6}$ M solutions showed that, while fluorescence band for *vase* QxCav **5** remains unchanged irrespectively of the concentration, the band of *kite* QxCav **6** is blueshifted in the most concentrated solution, pointing to a less polar environment experienced by the fluorophores, consistently with the formation of intermolecular aggregates (Figure 2.36). Self-absorption effects were checked and demonstrated to be negligible

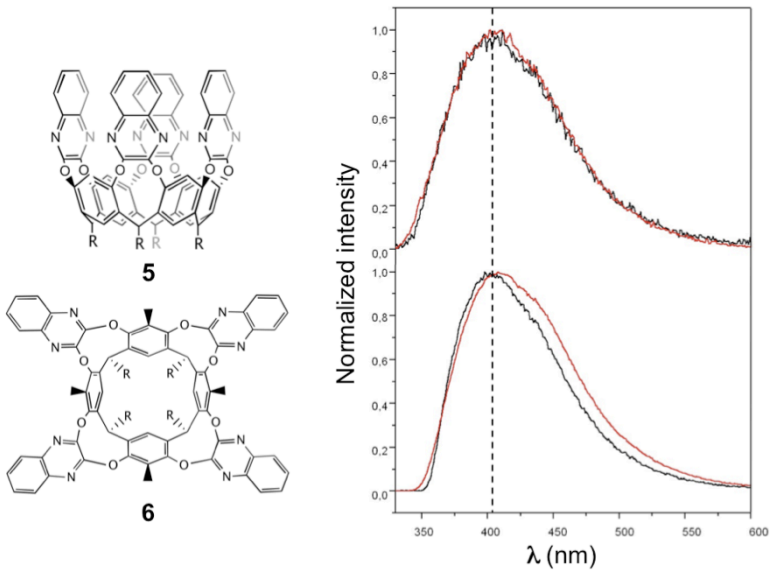


**Figure 2.36** *Normalized fluorescence emission spectra of vase QxCav* ***5*** *(top) and kite QxCav* ***6*** *(bottom) in $10^{-4}$ M (black) and $10^{-6}$ M (red) $CHCl_3$ solutions.*

Once verified that the four-fold opening of quinoxaline wings leads to a bathocromically-shifted emission into the PU matrix, mechanical tests on **PU-16** films were performed. Because of the thinning of loaded specimens, a quantitative evaluation of the eventual increase in the absolute emission intensity upon interconversion has been considered not reliable. Thus, the only shift of the emission maxima has been monitored during the performed tests. As expected, films with physically dispersed QxCav **5** didn't reveal any shift upon elongation; by contrast, coherently with what observed *via* UV-Vis spectroscopy, a change in the emission profile of PU films cross-linked with cavitand **16** was observed. Interestingly, mechanical tests performed on several specimens pointed out an apparently different responsiveness; Fig. 2.37a resumes the most common behaviour observed in active films: upon stretching, the emission band broadens in the long-wavelength side, with a maximum shift of about 10 nm to the red. One specific sample showed a most prominent behaviour (Figure 2.37b): emission of the relaxed film, besides the main band at 390 nm, already shows a strong shoulder at about 450 nm, whose intensity became the major under tensile stress.

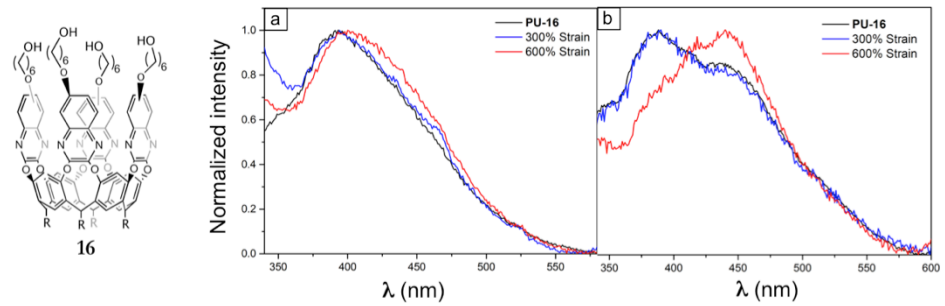


**Figure 2.37** *Emission spectra showing the two different behaviours observed for* ***PU-16*** *specimens (0.01% w/w, Table S2.6 entry V) upon tensile elongation.*

Considering the position of the emission band measured for the **PU-18** (cyan line in Figure 2.38), these results strongly confirm the opening of the *vase* form upon elongation.

Deconvolution of the emission spectra on the frequency scale with Gaussian lines was performed (results in Figure 2.38). Starting from the experimental spectrum in Fig. 2.37b, where the two components are better resolved, we observed that the emission band of the pristine film can be nicely fitted as a sum of two Gaussian functions. The two deconvolved components have a clear resemblance with the emission spectra of **PU-5** (magenta line) and **PU-18** (cyan line). In order to fit the emission spectrum of the stretched film, the position and width of the two Gaussians were kept fixed and only their relative intensity was varied (red lines in Figure 2.38). In this way, we estimate a relative increase of the long-wavelength band of about a 1.5 factor. Same analysis was performed on experimental spectra in Fig. 2.37a; since in this case the two components of the emission band are more difficult to recognize, we chose to fix the position of two Gaussian lines as extracted from the previous fitting, while allowing the optimization of their width. The best fit obtained (black thin line) corresponds to the sum of the two Gaussians (dotted and dashed lines). In order to fit the emission spectrum of the stretched film, the position and width of the two Gaussians was kept fixed, while varying only their relative intensity (red lines). In this case, analogously to the previous one, a relative increase of the long-wavelength band of about a 1.4 factor was estimated.

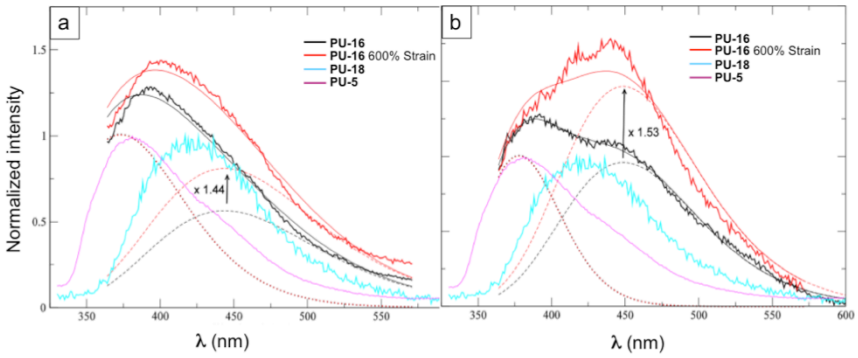


**Figure 2.38** *Deconvolution of the emission spectra of two different pristine (black) and stretched (red)* ***PU-16*** *specimens (0.01% w/w); dotted and dashed lines correspond to the Gaussian bands used for the fitting. Emission spectra of* ***PU-5*** *(0.01% w/w, magenta lines) and* ***PU-18*** *(0.01% w/w, cyan lines) are reported as references.*

In conclusion, reported results strongly support the idea that, upon stretching, the *vase* conformer cross-linked into the polymer tends to open into the *kite* one. In particular, two components in the fluorescence profile can be recognized, one well corresponding to the emission of the contracted form dispersed in PU and the other, strongly redshifted, similar to the emission of the expanded form cross-linked in the polymeric network. The relative contribution of this latter band clearly increases under tensile stress, proving the occurrence of the mechanochemical interconversion. Deconvolution analysis suggests that a certain amount of *kite* structure is already present in the pristine films. In particular, for most of the analysed samples, an about 30% contribution of the open conformation is observed in the relaxed state, while in one particular sample this contribution amounts to about 50%. A likely explanation can rely on the nature of the chosen matrix, whose rigidity exerts, during the polymerization process, enough tension on cavitand molecules to induce a partial *vase* → *kite* interconversion. In all cases, however, upon mechanical solicitation, the open component increases of a relative factor of about 1.5.

## 2.3 Conclusions

In conclusion two different polymeric matrices have been investigated for promoting the *vase* → *kite* interconversion of tetraquinoxaline cavitands *via*

mechanochemical stimulus. Elastomeric PDMS, despite being known for the successful activation of spiropyran mechanophores, failed to evidence any maxima variation *via* UV-Vis spectroscopy; we hypothesized that the elastomeric nature of the matrix results in a dissipation of the applied tension, thus leading to a lack of efficient mechanical solicitation on QxCav units. Nonetheless, thanks to the chemical stability of the matrix, exposure of PDMS specimens to harsh acid conditions resulted in a quantitative interconversion of QxCav units from *vase* to *kite*. Remarkably, besides a clear shift of the maxima in the UV-Vis spectra, 2D DIC measurements displayed that the dimensional increase associated with the *vase* → *kite* interconversion is reflected at the macroscopic level in a meaningfully wider expansion of the material with respect to control specimens. By contrast, the use of a more rigid matrix together with the incorporation of tetrafunctionalized QxCav units as unique cross-linkers into the polymeric network, resulted in the expected responsiveness upon tensile elongation, detected both *via* UV-Vis and fluorescence spectroscopy. Considering the lack of any spectroscopic variation for control specimens, it sounds reasonable to conclude that the observed response can be traced back to a mechanically induced conformational change of QxCav units embedded into the PU matrix. In particular, experimental data suggest that, contrary to the initial suppositions, all four quinoxaline wings need to be covalently anchored to the polymer backbone in order to experience an efficient transduction of tensile stress. Furthermore, fluorescence spectra allowed a preliminary quantification of the degree of activation in terms of relative increase in the intensity of the long-wavelength band. Future studies will aim to verify whether the incorporation of QxCav in the matrix can lead to the desired auxetic properties or, at least, to a decrease of the Poisson's ratio in respect to plain PU. Thus, 2D DIC measurements will be performed on PU specimens with variable concentration of cavitand units in order to identify the optimum balance between rigidity and Poisson's ratio of the resulting material. Furthermore, considering the high value of ν for pristine polymers (about 0.4-0.5), attempts for moving from polymeric matrices to organogels and aerogels networks will be made. Indeed, the use of a material with an intrinsically lower value of ν sounds a more appealing starting point for achieving the desired auxetic properties.

## 2.4 Acknowledgments

Special thanks to Francesca Guagnini, Dr. Alessandro Pedrini and Dr. Ilaria Domenichelli from the University of Parma. Thanks to Dr. Gianluca Paredi of SITEIA, University of Parma, for high-resolution MALDI-TOF MS analyses and Centro Intefacoltà di Misure "G. Casnati" of the University of Parma for the use of NMR facilities. Particular acknowledgments to Prof. Francesca Terenziani from the Department of Chemistry for fluorescence measurements and to Federico Artoni from the Department of Engineering and Architecture for DIC analyses. Thanks to Elantas Europe for providing samples of RTV 615.

## 2.5 Experimental section

**2,3-dihydroxyquinoxaline-6-carboxylic acid (7)**
A solution of 3,4-diaminobenzoic acid (2 g, 13.2 mmol) in 15 mL of HCl 4 N was slowly added to a suspension of oxalic acid (1.3 g, 14.6 mmol) in 15 mL of HCl 4 N. The resulting mixture was heated at reflux for 12 h under stirring. The red-brownish precipitate was filtered, washed with water and dried to give product **7** in quantitative yield (2.7 g, 13.2 mmol).
**$^1$H NMR** (DMSO-$d_6$, 300 MHz): δ (ppm) = 12.90 (s, 1H, COO**H**), 12.16 (s, 1H, ArO**H**), 12.04 (s, 1H, ArO**H**), 7.73 (s, 1H, Ar**H**), 7.67 (d, 1H, $J_o$=9.0 Hz, Ar**H**), 7.18 (d, 1H, $J_o$=9.0 Hz, Ar**H**).

**General procedure for alkenyl 2,3-dichloroquinoxaline-6-carboxylates (9a-c)**
2,3-dihydroxyquinoxaline-6-carboxylic acid **7** (0.2 g, 1 mmol) was suspended in 8 mL of dry 1,2-dichloroethane; thionyl chloride (0.66 mL, 10 mmol) and a catalytic amount of DMF were added and the reaction mixture was refluxed for 3 h under stirring. Volatiles were removed under reduced pressure and the orange-brownish precipitate was re-dissolved in 8 mL of dry $CH_2Cl_2$. After the addition of $Et_3N$ (0.15 mL, 1.1 mmol) and alken-1-ol (1.1 mmol, 1.1 eq), the mixture was stirred at room temperature for 12 h. The crude was diluted with $CH_2Cl_2$ and washed with a saturated solution of $NaHCO_3$, HCl 1 N and brine. The solvent was removed under reduced pressure and the crude was purified by flash column chromatography.

**Dec-9-en-1-yl 2,3-dichloroquinoxaline-6-dicarboxylate (9a)**
Eluent: hexane/AcOEt 95:5; colourless oil that solidified upon standing (yield 76%)
**$^1$H NMR** ($CDCl_3$, 400 MHz): δ (ppm) = 8.75 (s, 1H, Ar**H**), 8.43 (d, 1H, $J_o$=8.8 Hz, Ar**H**), 8.11 (d, 1H, $J_o$=8.8 Hz, Ar**H**), 5.82 (m, 1H, C**H**=$CH_2$), 4.99 (m, 2H, CH=C**H$_2$**), 4.43 (t, 2H, J=6.5 Hz, OC**H$_2$**), 2.07 (m, 2H, C**H$_2$**CH=$CH_2$), 1.84 (m, 2H, $OCH_2$C**H$_2$**), 1.55-1.29 (m, 10H, -C**H$_2$**-).
**$^{13}$C NMR** ($CDCl_3$, 100 MHz): δ (ppm) = 165.2, 147.7, 146.6, 142.5, 139.9, 139.1, 133.0, 131.0, 130.4, 128.4, 114.2, 66.1, 33.8, 29.4, 29.2, 29.0, 28.9, 28.7, 26.1.

**Hex-5-en-1-yl 2,3-dichloroquinoxaline-6-dicarboxylate (9b)**
Eluent: $CH_2Cl_2$/hexane 9:1; colourless oil (yield 57%)
**$^1$H NMR** ($CDCl_3$, 300 MHz): δ (ppm) = 8.75 (s, 1H, Ar**H**), 8.45 (d, 1H, $J_o$=8.7 Hz, Ar**H**), 8.10 (d, 1H, $J_o$=8.7 Hz, Ar**H**), 5.84 (m, 1H, C**H**=$CH_2$), 5.03 (m, 2H, CH=C**H$_2$**), 4.43 (t, 2H, J=7.1 Hz, OC**H$_2$**), 2.14 (m, 2H, C**H$_2$**CH=$CH_2$), 1.86 (m, 2H, $OCH_2$C**H$_2$**), 1.63 (m, 2H, -C**H$_2$**-).

**But-3-en-1-yl 2,3-dichloroquinoxaline-6-dicarboxylate (9c)**
Eluent: $CH_2Cl_2$; colourless oil (yield 49%)
**$^1$H NMR** ($CDCl_3$, 300 MHz): δ (ppm) = 8.75 (s, 1H, Ar**H**), 8.43 (d, 1H, $J_o$=8.7 Hz, Ar**H**), 8.10 (d, 1H, $J_o$=8.7 Hz, Ar**H**), 5.92 (m, 1H, C**H**=$CH_2$), 5.19 (m, 2H, CH=C**H$_2$**), 4.49 (t, 2H, J=7.1 Hz, OC**H$_2$**), 2.60 (m, 2H, C**H$_2$**CH=$CH_2$).
**$^{13}$C NMR** ($CDCl_3$, 75 MHz): δ (ppm) = 164.9, 142.4, 139.7, 133.7, 132.7, 130.9, 130.4, 128.4, 117.7, 64.9, 33.1.

**Tetraquinoxaline Cavitand (5)**
$K_2CO_3$ (2 g, 14.5 mmol) was added to a solution of resorcinarene **10**[72] (2 g, 2.42 mmol) in 40 mL of dry DMF, followed by 2,3-dichloroquinoxaline (2.12 g, 10.7 mmol). The pink suspension was stirred at 80 °C for 12 h. The reaction was quenched with HCl 1 N and the precipitate was filtered, washed with water and dried. Recrystallization from AcOEt afforded cavitand **5** as a white solid (2.33 g, 1.75 mmol, 59%).
**$^1$H NMR** ($CDCl_3$, 400 MHz): δ (ppm) = 8.17 (s, 4H, Ar**H$_{up}$**), 7.82 (m, 8H, Ar**H**), 7.82 (m, 8H, Ar**H**), 7.49 (m, 8H, Ar**H**), 7.23 (s, 4H, Ar**H$_{down}$**), 5.58 (t, 4H, J=7.8 Hz, C**H**$CH_2$), 2.28 (q, 8H, J=7.8 Hz, CHC**H$_2$**), 1.55-1.31 (m, 32H, -C**H$_2$**-), 0.95 (t, 12H, J=6.8 Hz, $CH_2$C**H$_3$**).

**MALDI-TOF:** calculated for $C_{84}H_{80}N_8O_8$ $[M+H]^+$ *m/z* = 1329.618, found *m/z* = 1329.567.

**AC-bisquinoxaline cavitand (11)**

A suspension of cavitand **5** (0.500 g, 0.38 mmol) and CsF (1.154 g, 7.60 mmol) in DMF was heated to 80 °C and catechol (0.133 g, 1.20 mmol) was added. The mixture was stirred for 1 h at 80 °C, then the reaction was poured into 500 mL of ice-cold brine. The precipitate was filtered, washed with water, and dried. The crude product was purified by flash column chromatography (gradient from $CH_2Cl_2$/AcOEt 95:5 to $CH_2Cl_2$/AcOEt 85:15) affording compound **11** as an off-white solid (0.219 g, 0.20 mmol, 54%).

**$^1$H NMR** (Acetone-$d_6$, 300 MHz): δ (ppm) = 9.03 (bs, 4H, ArO**H**), 7.77 (s, 4H, Ar$\mathbf{H_{down}}$), 7.54 (m, 4H, Ar**H**), 7.24 (m, 4H, Ar**H**), 7.16 (s, 4H, Ar$\mathbf{H_{up}}$), 5.52 (t, J=8.0 Hz, 2H, C**H**$CH_2$ below Qx's), 4.47 (t, J=7.6 Hz, 2H, C**H**$CH_2$ below OH's), 2.41 (m, 8H, CHC$\mathbf{H_2}$), 1.47-1.26 (m, 32H, -C$\mathbf{H_2}$-), 0.92 (m, 12H, $CH_2$C$\mathbf{H_3}$).

**ESI-MS:** *m/z* = 1077.6 $[M+H]^+$, 1099.6 $[M+Na]^+$, 1115.5 $[M+K]^+$.

**Triquinoxaline Cavitand (12)**

A suspension of cavitand **5** (0.500 g, 0.38 mmol) and CsF (1.154 g, 7.60 mmol) in 100 mL of DMF was heated at 80 °C. Catechol was added (0.045 g, 0.41 mmol) and the mixture was stirred for 45 min. After cooling to room temperature the reaction mixture was poured in 500 mL of ice-cold brine and the precipitate was filtered, washed with water and dried. The crude was purified by flash column chromatography (gradient from 100% $CH_2Cl_2$ to $CH_2Cl_2$/AcOEt 95:5) affording compound **12** as pale yellow solid (0.263 g, 0.21 mmol, 57%).

**$^1$H NMR** ($CDCl_3$, 300 MHz): δ (ppm) = 8.25 (bs, 4H, ArO**H** + $\mathbf{H_i}$), 7.96 (d, 2H, J=8.3 Hz, $\mathbf{H_d}$), 7.85 (m, 2H, $\mathbf{H_e}$), 7.68 (d, 2H, J=8.3 Hz, $\mathbf{H_a}$), 7.62-7.44 (m, 6H, $\mathbf{H_c}$ + $\mathbf{H_b}$ + $\mathbf{H_f}$), 7.30 (s, 2H, $\mathbf{H_g}$), 7.15 (s, 2H, $\mathbf{H_l}$), 7.12 (s, 2H, $\mathbf{H_k}$), 5.65-5.43 (m, 3H, $\mathbf{H_m}$ + $\mathbf{H_n}$), 4.32 (t, 1H, J=7.7 Hz, $\mathbf{H_o}$), 2.28 (m, 8H, CHC$\mathbf{H_2}$), 1.57-1.21 (m, 32H, -C$\mathbf{H_2}$-), 0.93 (m, 12H, $CH_2$C$\mathbf{H_3}$).

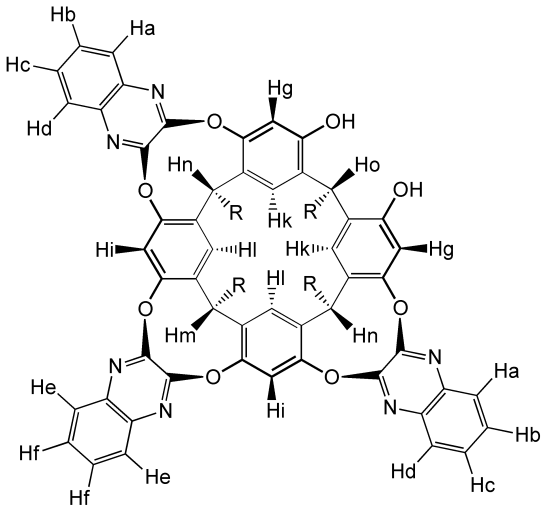


**ESI-MS:** *m/z* = 1203.6 $[M+H]^+$, 1225.6 $[M+Na]^+$, 1241.5 $[M+K]^+$.

**General procedure for bis-ω-alkene functionalized tetraquinoxaline cavitands:**

ω-alkene-dichloroquinoxaline (0.20 mmol, 2.2 eq) was added to a suspension of AC-bisquinoxaline cavitand (0.100 g, 0.09 mmol) and $K_2CO_3$ (0.038 g, 0.28 mmol) in 4 mL of dry DMSO. The mixture was heated at 70 °C under microwave irradiation for 1 h. The reaction was quenched with water and the resulting precipitate was filtered, washed with water and dried. The crude was purified by flash column chromatography affording pure bis-ω-alkene cavitands.

**Bis-decene functionalized tetraquinoxaline cavitand (1a)**

Eluent: hexane/AcOEt 95:5; white solid (yield 42%).

**$^1$H NMR** ($CDCl_3$, 400 MHz): δ (ppm) = 8.67 (s, 2H, $\mathbf{H_a}$), 8.20 (m, 4H, $\mathbf{H_f}$), 8.12 (d, 2H, J=8.7 Hz, $\mathbf{H_b}$), 7.88-7.74 (m, 6H, $\mathbf{H_c}$ + $\mathbf{H_d}$), 7.56 (m, 1H, $\mathbf{H_e}$), 7.45 (t, 1H, J=7.8 Hz, $\mathbf{H_e}$), 7.37 (t, 1H, J=7.8 Hz, $\mathbf{H_e}$), 7.30-7.20 (m, 5H, $\mathbf{H_g}$ + $\mathbf{H_e}$), 5.82 (m, 2H, C**H**=$CH_2$), 5.61 (m, 4H, C**H**$CH_2$), 4.98 (m, 4H, CH=C$\mathbf{H_2}$), 4.49 (m, 4H, OC$\mathbf{H_2}CH_2$), 2.29 (m, 8H, CHC$\mathbf{H_2}$), 2.06 (m, 4H, C$\mathbf{H_2}$CH=$CH_2$), 1.92 (m, 4H, $OCH_2$C$\mathbf{H_2}$), 1.68-1.26 (m, 52H, -C$\mathbf{H_2}$-), 0.96 (t, 12H, J=6.4 Hz, $CH_2$C$\mathbf{H_3}$).

**MALDI-TOF:** calculated for $C_{106}H_{117}N_8O_{12}$ $[M+H]^+$ *m/z* = 1694.883, found *m/z* = 1694.834; calculated for $C_{106}H_{116}N_8NaO_{12}$ $[M+Na]^+$ *m/z* = 1716.864, found *m/z* = 1716.824.

**Bis-hexene functionalized tetraquinoxaline cavitand (1b)**
Eluent: gradient from $CH_2Cl_2$ to $CH_2Cl_2$/AcOEt 98:2; white solid (yield 40%).
**$^1$H NMR** ($CDCl_3$, 400 MHz): δ (ppm) = 8.66 (s, 2H, $\mathbf{H_a}$), 8.18 (m, 4H, $\mathbf{H_f}$), 8.11 (d, 2H, J=8.7 Hz, $\mathbf{H_b}$), 7.83 (m, 6H, $\mathbf{H_c}$ + $\mathbf{H_d}$), 7.79 (m, 1H, $\mathbf{H_e}$), 7.77 (m, 2H, $\mathbf{H_e}$), 7.30-7.20 (m, 5H, $\mathbf{H_g}$ + $\mathbf{H_e}$), 5.84 (m, 2H, C**H**=$CH_2$), 5.59 (m, 4H, C**H**$CH_2$), 5.09 (m, 4H, CH=C$\mathbf{H_2}$), 4.51 (m, 4H, OC$\mathbf{H_2}CH_2$), 2.30 (m, 8H, CHC$\mathbf{H_2}$), 1.96 (m, 4H, C$\mathbf{H_2}$CH=$CH_2$), 1.90 (m, 4H, $OCH_2C\mathbf{H_2}$), 1.70-1.28 (m, 36H, -C$\mathbf{H_2}$-), 0.96 (m, 12H, $CH_2C\mathbf{H_3}$).
**MALDI-TOF:** calculated for $C_{98}H_{101}N_8O_{12}$ $[M+H]^+$ *m/z* = 1582.757, found *m/z* = 1582.867.

**Bis-butene functionalized tetraquinoxaline cavitand (1c)**
Eluent: gradient from $CH_2Cl_2$ to $CH_2Cl_2$/AcOEt 98:2; white solid (yield 39%).
**$^1$H NMR** ($CDCl_3$, 300 MHz): δ (ppm) = 8.65 (s, 2H, $\mathbf{H_a}$), 8.19 (m, 4H, $\mathbf{H_f}$), 8.12 (d, 2H, J=8.7 Hz, $\mathbf{H_b}$), 7.83 (m, 6H, $\mathbf{H_c}$ + $\mathbf{H_d}$), 7.78 (m, 1H, $\mathbf{H_e}$), 7.77 (m, 2H, $\mathbf{H_e}$), 7.29-7.19 (m, 5H, $\mathbf{H_g}$ + $\mathbf{H_e}$), 5.96 (m, 2H, C**H**=$CH_2$), 5.58 (m, 4H, C**H**$CH_2$), 5.25 (m, 4H, CH=C$\mathbf{H_2}$), 4.55 (m, 4H, OC$\mathbf{H_2}CH_2$), 2.66 (m, 4H, C$\mathbf{H_2}$CH=$CH_2$), 2.30 (m, 8H, CHC$\mathbf{H_2}$), 1.44-1.27 (m, 32H, -C$\mathbf{H_2}$-), 0.96 (m, 12H, $CH_2C\mathbf{H_3}$).
**MALDI-TOF:** calculated for $C_{94}H_{93}N_8O_{12}$ $[M+H]^+$ *m/z* = 1526.696, found *m/z* = 1526.488; calculated for $C_{94}H_{93}N_8O_{12}Na$ $[M+Na]^+$ *m/z* = 1548.679, found *m/z* = 1548.414.

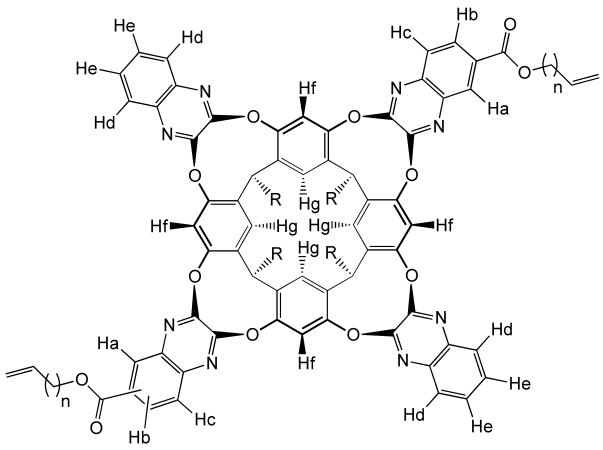


**Mono-ω-alkene functionalized tetraquinoxaline cavitand (2)**

Triquinoxaline cavitand **12** (0.260 g, 0.22 mmol) and $K_2CO_3$ (0.039 g, 0.28 mmol) were suspended in 5 mL of DMSO. After the addition of dichloroquinoxaline **9a** (0.091 g, 0.24 mmol) the mixture was heated at 70 °C under microwave irradiation for 30 min. The reaction was quenched with water (100 mL) and the precipitate was filtered, washed with water and dried. Flash column chromatography (hexane/AcOEt 9:1) afforded pure cavitand **2** as a white solid (0.215 g, 0.14 mmol, 46%).

**$^1$H NMR** ($CDCl_3$, 400 MHz): δ (ppm) = 8.65 (s, 1H, $\mathbf{H_a}$), 8.19 (m, 4H, $\mathbf{H_g}$), 8.09 (d, 1H, J=8.7 Hz, $\mathbf{H_b}$), 7.87-7.73 (m, 7H, $\mathbf{H_c}$ + $\mathbf{H_d}$), 7.52 (m, 4H, $\mathbf{H_e}$), 7.42 (t, 1H, J=7.5 Hz, $\mathbf{H_f}$), 7.33 (t, 1H, J=7.5 Hz, $\mathbf{H_f}$), 7.24 (m, 4H, $\mathbf{H_i}$), 5.82 (m, 1H, C**H**=$CH_2$), 5.60 (m, 4H, C**H**$CH_2$), 4.98 (m, 2H, CH=C$\mathbf{H_2}$), 4.48 (m, 2H, OC$\mathbf{H_2}CH_2$), 2.29 (m, 8H, CHC$\mathbf{H_2}$), 2.06 (m, 2H, C$\mathbf{H_2}$CH=$CH_2$), 1.92 (quint, 2H, J=6.9 Hz, $OCH_2C\mathbf{H_2}$), 1.60-1.26 (m, 42H, -C$\mathbf{H_2}$-), 0.95 (t, 12H, J=6.4 Hz, $CH_2C\mathbf{H_3}$).

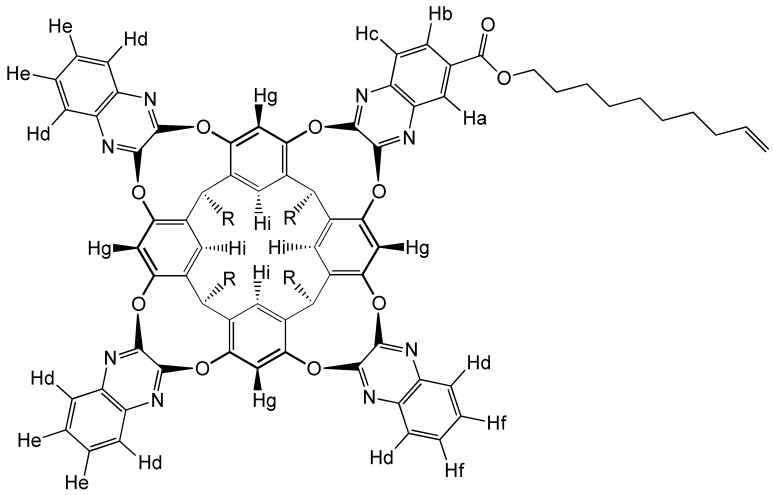


**MALDI-TOF:** calculated for $C_{95}H_{99}N_8O_{10}$ $[M+H]^+$ *m/z* = 1511.748, found *m/z* = 1511.745.

**Tetra-ω-hexene functionalized tetraquinoxaline cavitand (3)**

$K_2CO_3$ (0.044 g, 0.26 mmol) was added to a solution of Res[$C_6H_{13}$, H] (0.051 g, 0.06 mmol) in 2 mL of DMSO, followed by dichloroquinoxaline **9b** (0.085 g, 0.26 mmol). The reaction mixture was heated at 70 °C under microwave irradiation for 2 h. Water (100 mL) was added and the precipitate was filtered, washed with water and dried. The crude was purified by flash column chromatography ($CH_2Cl_2$/AcOEt 98:2) affording cavitand **3** as a white solid (0.019 g, 0.01 mmol, 17%).

**$^1$H NMR** ($CDCl_3$, 300 MHz): δ (ppm) = 8.60 (s, 4H, Ar**H**), 8.02 (d, 4H, Ar$\mathbf{H_{up}}$), 8.12 (d, 4H, J=8.7 Hz, Ar**H**), 7.86 (d, 4H, J=8.7 Hz, Ar**H**), 7.26 (s, 4H, Ar$\mathbf{H_{down}}$), 5.85 (m, 4H, C**H**=$CH_2$), 5.57 (t, 4H, J=8.0 Hz, C**H**$CH_2$), 5.00 (m, 8H, CH=C$\mathbf{H_2}$), 4.48 (t, 8H, J=6.6 Hz, OC$\mathbf{H_2}CH_2$), 2.37-2.13 (m, 16H, CHC$\mathbf{H_2}$ + $OCH_2C\mathbf{H_2}$), 1.92 (m, 8H, C$\mathbf{H_2}$CH=$CH_2$), 1.74-1.19 (m, 40H, -C$\mathbf{H_2}$-), 0.93 (m, 12H, $CH_2C\mathbf{H_3}$).

**MALDI-TOF:** calculated for $C_{112}H_{121}N_8O_{12}$ $[M+H]^+$ *m/z*: 1835.888, found *m/z*: 1535.888; calculated for $C_{112}H_{120}N_8O_{12}Na$ $[M+Na]^+$ *m/z*: 1856.907, found *m/z*: 1856.908.

**9-decenal**

A solution of 9-decen-1-ol (1.7 mL, 9.53 mmol) in 20 mL of dry $CH_2Cl_2$ was slowly added to an ice-cold suspension of pyridinium chlorochromate (3.08 g, 14.29 mmol) and sodium acetate anhydrous (1.17 g, 14.29 mmol) in 50 mL of dry $CH_2Cl_2$. The reaction mixture was stirred at room temperature for 4 h and then filtered on silica. After washing with $Et_2O$, the filtrate was concentrated under reduced pressure affording a colourless liquid (1.2 g, 7.8 mmol, 82%).

**$^1$H NMR** ($CDCl_3$, 300 MHz): δ (ppm) = 9.79 (s, 1H, C**H**O), 5.81 (m, 1H, C**H**=$CH_2$), 4.98 (m, 2H, CH=C**$H_2$**), 2.43 (m, 2H, C**$H_2$**CHO), 2.05 (m, 2H, C**$H_2$**CH=$CH_2$), 1.65 (m, 2H, **$CH_2$**$CH_2$CHO), 1.24 (m, 6H, -C**$H_2$**-).

**Resorcinarene [$C_8H_{15}$, H] (13)**

A 37% solution of HCl (2 mL, 6.6 mmol) was slowly added to an ice-cold solution of resorcinol (0.428 g, 3.89 mmol) in 2 mL of MeOH. At the same temperature 9-decenal (0.6 g, 3.89 mmol) in 4 mL of EtOH was added drop-wise over 20 min. The mixture was stirred at 100 °C for 5 min under microwave irradiation. Water (250 mL) was added and the precipitate was filtered, washed with water and dried. The crude was purified by recrystallization from $CH_3CN$ affording Res[$C_8H_{15}$, H] **13** as a white solid (1.38 g, 1.4 mmol, 36%).

**$^1$H NMR** (Acetone-$d_6$, 300 MHz): δ (ppm) = 8.46 (s, 8H, O**H**), 7.56 (s, 4H, Ar**$H_{up}$**), 6.25 (s, 4H, Ar**$H_{down}$**), 5.81 (m, 4H, C**H**=$CH_2$), 4.98 (m, 8H, CH=C**$H_2$**), 4.31 (t, 4H, J=8.1 Hz, C**H**$CH_2$), 2.30 (q, 8H, J=8.1 Hz, CHC**$H_2$**) 1.39-1.25 (m, 48H, -C**$H_2$**-).

**ESI-MS:** *m/z* = 986 $[M+H]^+$, 1008 $[M+Na]^+$.

**Dec-9-en-1-yl-footed tetraquinoxaline cavitand (4)**

$K_2CO_3$ (0.152 g, 1.10 mmol) was added to a solution of Res[$C_8H_{13}$, H] (0.25 g, 0.245 mmol) in 10 mL of dry DMSO, followed by 2,3-dichloroquinoxaline (0.219 g, 1.10 mmol). The reaction mixture was heated at 70 °C under microwave irradiation for 30 min. Water (200 mL) was added and the precipitate was filtered, washed with water and dried. The crude was purified by recrystallization from acetone affording cavitand **4** as a white solid (0.167 g, 0.11 mmol, 44%).

**$^1$H NMR** ($CDCl_3$, 300 MHz): 8.18 (s, 4H, Ar**$H_{up}$**), 7.82 (m, 8H, Ar**H**), 7.49 (m, 8H, Ar**H**), 7.23 (s, 4H, Ar**$H_{down}$**), 5.84 (m, 4H, C**H**=$CH_2$), 5.56 (t, 4H, J=7.9 Hz,

C**H**$CH_2$), 4.98 (m, 8H, CH=C**H$_2$**), 2.29 (q, 8H, J=7.9 Hz, CHC**H$_2$**), 1.39-1.25 (m, 48H, -C**H$_2$**-).

**PDMS samples preparation**

a. General Information

RTV 615, used as polysiloxane substrate, is a two-part (Base and Curing Agent, typically mixed in a 10:1 ratio) silicone elastomer comprising vinyl terminated poly(dimethylsiloxane), poly(methylhydrosiloxane-codimethylsiloxane) copolymer and a platinum catalyst. The covalent incorporation of a molecule of interest into the resulting polymer network can be achieved through the introduction of an alkene functionalization suitable for hydrosilylation protocol.

b. Typical Procedure for Film Preparation

RTV 615 Base (3.0 g) and a THF cavitand solution were homogenized with a vortex in a 15 mL Falcon tube. RTV 615 Curing Agent (0.3 g) was added and the tube was extensively shacked with a vortex. The homogenous mixture was degassed under vacuum and poured onto a PTFE plate. After a second degassing, the sample was cured in an oven at 60 °C for 16 h. Once cured the film was peeled away and cut into stripes for testing.

| | **Cavitand** | **Conc. (% w/w)** |
|---|---|---|
| **I** | **5** | 0.05 |
| **II** | **5** | 0.1 |
| **III** | **5** | 0.5 |
| **IV** | **6** | 0.05 |
| **V** | **6** | 0.1 |
| **VI** | **2a** | 0.1 |

**Table S2.1** *Control specimens containing mono functionalized or unfunctionalized cavitands.*

| | Cavitand | Conc. (% w/w) |
|---|---|---|
| **I** | **1a** | 0.05 |
| **II** | **1a** | 0.1 |
| **III** | **1a** | 0.2 |
| **IV** | **1a** | 0.3 |
| **V** | **1a** | 0.5 |
| **VI** | **1a** | 0.6 |
| **VII** | **1a** | 0.7 |
| **VIII** | **1b** | 0.1 |
| **IX** | **1b** | 0.3 |
| **X** | **1b** | 0.5 |
| **XI** | **1b** | 0.7 |
| **XII** | **1c** | 0.1 |
| **XIII** | **1c** | 0.4 |
| **XIV** | **1c** | 0.5 |
| **XV** | **1c** | 0.7 |

**Table S2.2** *Specimens containing bis-alkene functionalized cavitands.*

| | Cavitand | Conc. (% w/w) |
|---|---|---|
| **I** | **3** | 0.1 |
| **II** | **3** | 0.3 |
| **III** | **3** | 0.5 |
| **IV** | **4** | 0.5 |
| **V** | **4** | 0.3 |

**Table S2.3** *Specimens containing tetrafunctionalized cavitands.*

| | Cavitand | Conc. (% w/w) | RTV 615 base/ H-term. (w/w) | |
|---|---|---|---|---|
| **I** | **3** | 1 | 1/1 | ✗ |
| **II** | **3** | 1 | 1/2 | ✗ |
| **III** | **3** | 1 | 2/1 | ✗ |
| **IV** | **3** | 3 | 1/2 | ✓ |
| **V** | **3** | 1 | 1/5 | ✓ |
| **VI** | **3** | 1 | 1/10 | ✓ |
| **VII** | **3** | 0.5 | 1/10 | ✓ |
| **VIII** | **3** | 0.3 | 1/10 | ✗ |
| **IX** | **4** | 1 | 1/10 | ✓ |
| **X** | **4** | 0.5 | 1/10 | ✓ |
| **XI** | **4** | 0.3 | 1/10 | ✗ |

**Table S2.4** *Optimization of the curing conditions for PDMS specimens with different concentrations of tetrafunctionalized cavitands* ***3*** *and* ***4*** *as cross-linkers and different ratio between vinyl-terminated and H-terminated pre-polymers. Curing is indicated with (✓) while non-curing is indicated with (✗).*

**Soxhlet extraction tests**

In order to prove the effective participation of cavitand double bonds in the hydrosilylation reaction and thus validate the proposed method, Soxhlet extraction with $CHCl_3$ on two PDMS samples, one cured in the presence of bis-alkene functionalized cavitand **1a** (Table S2.1, Entry II) and the other with unfunctionalized QxCav **5** (Table S2.2, Entry III) were performed. The extracted polymer and the organic phase were analysed by UV-Vis spectroscopy. As shown in Fig. S2.1, for **PDMS-1a** the absorption pattern of the cavitand is retained in the polymer, while it is not present in the organic phase. Opposite result has been obtained for **PDMS-5**. This experiment, although being crucial for proving the covalent incorporation of cavitands in the polysiloxane network, does not demonstrate the effective reaction of all their functionalities.

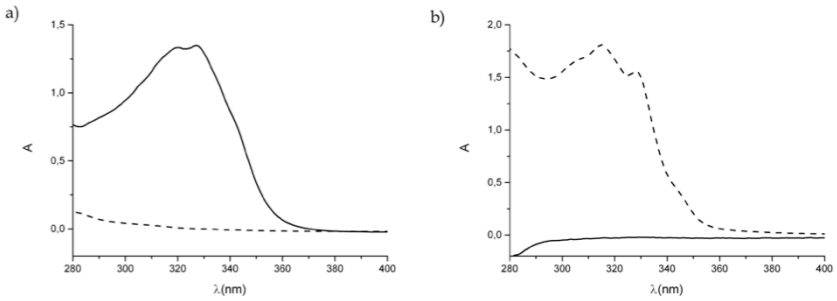


**Figure S2.1** *UV-Vis spectra of Soxhlet treated samples (solid line) and extracts (dashed line) from* ***PDMS-1a*** *(a) and* ***PDMS-5*** *(b).*

**DIC measurements**

In order to detect the macroscopic expansion of PDMS films upon acid exposure and investigate the role of cavitand interconversion, Digital Image Correlation measurements were performed. Thus 3 different polymeric samples containing QxCav **1a**, **4**, **5** (respectively, Table S2.1 entry III, Table S2.3 entry IV, Table S2.2 entry V), together with plain PDMS, were tested; for each type of sample 3 specimens, cut in stripes of 15x50 mm, were suspended in a closed environment and exposed to TFA vapours over 1 h, recording pictures with a high resolution camera. DIC analysis, thanks to the application of a speckle pattern on polymer samples, allowed the measurement of their areal deformation, defined as $\varepsilon_S = \varepsilon_x + \varepsilon_y$. Collected strain data about films' expansion were processed by removing any negative value and retaining only values between the tenth and ninetieth percentile. (For further details about data analysis and processing see Appendix A). Calculation of the mean surface strain with the remaining data revealed a meaningfully wider expansion for **PDMS-1a** in respect to the others specimens.

**6-[(*tert*-butyldimethylsilyl) oxy] hexan-1-ol (18)**

Imidazole (0.160 g, 2.35 mmol) was added to a solution of 1,6-hexandiol (2.5 g, 21.2 mmol) in 5 mL of dry DMF. A solution of TBDMSCl (1 M in THF; 2.35 mL, 2.35 mmol) in 3 mL of dry $CH_2Cl_2$ was slowly added and the resulting mixture was stirred at room temperature for 3 h. Solvent was evaporated under reduced

pressure; the crude was diluted with $CH_2Cl_2$ and washed with water. Flash column chromatography (hexane/AcOEt 9:1) afforded compound **18** (0.283 g, 1.22 mmol, 52%) as a colourless oil.
**$^1$H NMR** ($CDCl_3$, 300 MHz): δ (ppm) = 7.28 (s, 1H, O**H**); 3.64 (m, 4H, OC**H**$_2$); 1.5 (m, 8H, -C**H**$_2$-); 0.91 (s, 9H, Si$^t$**Bu**); 0.07 (s, 6H, SiC**H**$_3$).

**6-[(*tert*-butyldimethylsilyl)oxy]hexyl 2,3-dichloroquinoxaline-6-carboxylate (19)**
2,3-dihydroxyquinoxaline-6-carboxylic acid **7** (0.22 g, 1.11 mmol) was suspended in 10 mL of dry 1,2-dichloroethane; thionyl chloride (0.8 mL, 11.1 mmol) and a catalytic amount of DMF were added and the reaction mixture was refluxed for 3 h under stirring. Volatiles were removed under reduced pressure and the orange-brownish precipitate was re-dissolved in 10 mL of dry $CH_2Cl_2$. After the addition of $Et_3N$ (0.154 mL, 1.11 mmol) and **18** (0.258 g, 1.11 mmol), the mixture was stirred at room temperature for 12 h. The crude was diluted with $CH_2Cl_2$ and washed with a saturated solution of $NaHCO_3$, HCl 1 N and brine. The solvent was removed under reduced pressure and the crude was purified by flash column chromatography (hexane/AcOEt 95:5) affording compound **19** (0.386 g, 0.84 mmol, 76%) as a colourless oil.
**$^1$H NMR** ($CDCl_3$, 300 MHz): δ (ppm) = 8.57 (s, 1H, Ar**H**); 8.36 (dd, 1H, $J_o$=8.8 Hz, $J_m$=1.9 Hz, Ar**H**); 8.21 (d, 1H, $J_o$=8.7 Hz, Ar**H**); 4.37 (t, 2H, J=6.6 Hz, (CO)OC**H$_2$**); 3.59 (t, 2H, J=6.4 Hz, C**H$_2$**OSi); 1.5 (m, 8H, -C**H$_2$**-); 0.91 (s, 9H, Si$^t$**Bu**); 0.07 (s, 6H, Si**CH$_3$**).

**Bis-TBDMSO-hexyl functionalized tetraquinoxaline cavitand (20)**
Dichloroquinoxaline **19** (0.094 g, 0.205 mmol) was added to a suspension of AC-bisquinoxaline cavitand **11** (0.100 g, 0.093 mmol) and $K_2CO_3$ (0.038 g, 0.28 mmol) in 4 mL of dry DMSO. The mixture was heated at 70 °C under microwave irradiation for 1 h. The reaction was quenched with water and the resulting precipitate was filtered, washed with water and dried. The crude was purified by flash column chromatography (hexane/AcOEt 95:5) affording cavitand **20** (0.070 g, 0.038 mmol, 41%) as a white solid.
**$^1$H NMR** ($CDCl_3$, 400 MHz): δ (ppm) = 8.68 (s, 2H, **H$_a$**), 8.20 (m, 4H, **H$_f$**), 8.13 (dd, 2H, $J_o$=8.7 Hz, $J_m$=6.9 Hz, **H$_b$**), 7.85-7.75 (m, 6H, **H$_c$** + **H$_d$**), 7.56 (m, 1H, **H$_e$**), 7.45 (m, 1H, **H$_e$**), 7.37 (m, 1H, **H$_e$**), 7.29-7.22 (m, 5H, **H$_g$** + **H$_e$**), 5.60 (m, 4H, C**H**CH$_2$), 4.49 (m, 4H, (CO)OC**H$_2$**), 3.66 (m, 4H, C**H$_2$**OSi), 2.29 (m, 8H, CHC**H$_2$**),

1.93 (m, 4H, (CO)OCH$_2$C**H$_2$**), 1.61-1.37 (m, 36H, -C**H$_2$**-), 0.96 (t, 12H, J=7 Hz, CH$_2$C**H$_3$**), 0.92 (d, 18H, Si**$^t$Bu**), 0.07 (d, 12H, Si**CH$_3$**).

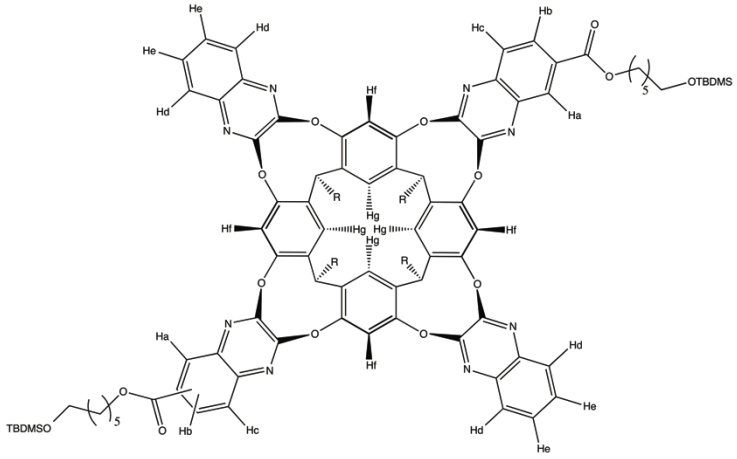


**MALDI-TOF:** calculated for $C_{110}H_{133}N_8O_{14}Si_2$ [M+H]$^+$ *m/z*: 1847.441, found *m/z*: 1847.458; calculated for $C_{110}H_{133}N_8O_{14}$ $Si_2Na$ [M+Na]$^+$ *m/z*: 1869.431, found *m/z*: 1869.488.

**Bis-ω-hydroxy functionalized tetraquinoxaline cavitand (14)**

DMSO (2 mL) was added to a solution of cavitand **20** (0.040 g, 0.022 mmol) in 1 mL of THF purified *via* alumina percolation, followed by $H_2O$ (160 μL) and N-bromosuccinimide (0.008 g, 0.048 mmol). The reaction mixture was stirred at room temperature for 12 h in the dark. Volatiles were evaporated under reduced pressure and the crude was dissolved in $CHCl_3$ and washed with water. Purification *via* flash column chromatography ($CH_2Cl_2$/MeOH 97:3) afforded cavitand **14** (0.026 g, 0.016 mmol, 73%) as a white solid.

**$^1$H NMR** ($CDCl_3$, 400 MHz): δ (ppm) = 8.69 (s, 2H, **H$_a$**), 8.19 (m, 4H, **H$_f$**), 8.11 (dd, 2H, $J_o$=8.7 Hz, $J_m$=1.6 Hz, **H$_b$**), 7.85-7.75 (m, 6H, **H$_c$** + **H$_d$**), 7.55 (m, 1H, **H$_e$**), 7.45 (m, 1H, **H$_e$**), 7.36 (m, 1H, **H$_e$**), 7.24 (m, 5H, **H$_g$** + **H$_e$**), 5.60 (m, 4H, C**H**CH$_2$), 4.50 (m, 4H, (CO)OC**H$_2$**), 3.69 (t, 4H, J=6.3 Hz, C**H$_2$**OH), 2.29 (m, 8H, CHC**H$_2$**), 1.93 (m, 4H, (CO)OCH$_2$C**H$_2$**), 1.61-1.37 (m, 36H, -C**H$_2$**-), 0.96 (t, 12H, J=7 Hz, CH$_2$C**H$_3$**).

**MALDI-TOF:** calculated for $C_{98}H_{105}N_8O_{14}$ $[M+H]^+$ *m/z*: 1618.919, found *m/z*: 1618.892.

**Mono-TBDMSO-hexyl functionalized tetraquinoxaline cavitand (21)**

Triquinoxaline cavitand **12** (0.100 g, 0.083 mmol) and $K_2CO_3$ (0.015 g, 0.11 mmol) were suspended in 3 mL of dry DMSO. After the addition of dichloroquinoxaline **19** (0.042 g, 0.081 mmol) the mixture was heated at 70 °C under microwave irradiation for 30 min. The reaction was quenched with water (100 mL) and the precipitate was filtered, washed with water and dried. Flash column chromatography (hexane/AcOEt 95:5) afforded pure cavitand **21** (0.065 g, 0.041 mmol, 49%) as a white solid.

**$^1$H NMR** ($CDCl_3$, 300 MHz): δ (ppm) = 8.66 (s, 1H, $\mathbf{H_a}$), 8.19 (m, 4H, $\mathbf{H_g}$), 8.09 (dd, 1H, $J_o$=8.7 Hz, $J_m$=1.4 Hz, $\mathbf{H_b}$), 7.84-7.76 (m, 7H, $\mathbf{H_c}$ + $\mathbf{H_d}$), 7.52 (m, 4H, $\mathbf{H_e}$), 7.42 (t, 1H, J=7.4 Hz, $\mathbf{H_f}$), 7.34 (t, 1H, J=7.4 Hz, $\mathbf{H_f}$), 7.24 (m, 4H, $\mathbf{H_i}$), 5.61 (m, 4H, C**H**$CH_2$), 4.48 (m, 2H, (CO)OC$\mathbf{H_2}$), 3.67 (m, 2H, C$\mathbf{H_2}$OSi), 2.29 (m, 8H, CHC$\mathbf{H_2}$), 1.93 (m, 2H, (CO)OC$H_2$C$\mathbf{H_2}$), 1.60-1.26 (m, 30H, -C$\mathbf{H_2}$-), 0.95 (t, 12H, J=6.4 Hz, $CH_2$C$\mathbf{H_3}$), 0.92 (s, 9H, Si$^t$**Bu**), 0.07 (s, 6H, Si**C**$\mathbf{H_3}$).

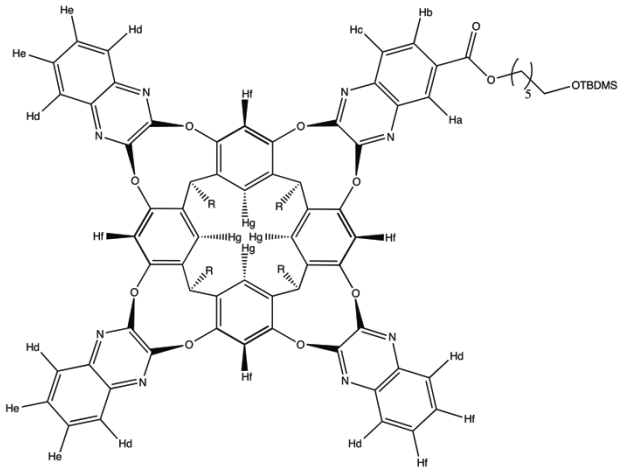


**MALDI-TOF:** calculated for $C_{97}H_{107}N_8O_{11}Si$ $[M+H]^+$ *m/z*: 1587.775, found *m/z*: 1587.549; calculated for $C_{97}H_{107}N_8O_{11}SiNa$ $[M+Na]^+$ *m/z*: 1611.002, found *m/z*: 1611.455.

**Mono-ω-hydroxy functionalized tetraquinoxaline cavitand (15)**

DMSO (2.7 mL) was added to a solution of cavitand **21** (0.062 g, 0.04 mmol) in 1.5 mL of purified THF, followed by $H_2O$ (260 μL) and N-bromosuccinimide (0.016 g, 0.009 mmol). The reaction mixture was stirred at room temperature for 12 h in the dark. Volatiles were evaporated under reduced pressure and the crude was dissolved in $CHCl_3$ and washed with water. Purification *via* flash column chromatography ($CH_2Cl_2$/MeOH 99:1) afforded cavitand **15** (0.047 g, 0.031 mmol, 79%) as a white solid.

**$^1$H NMR** ($CDCl_3$, 300 MHz): δ (ppm) = 8.66 (d, 1H, $J_m$=1.7 Hz, $\mathbf{H_a}$), 8.19 (m, 4H, $\mathbf{H_g}$), 8.09 (dd, 1H, $J_o$=8.7 Hz, $J_m$=1.7 Hz, $\mathbf{H_b}$), 7.84-7.76 (m, 7H, $\mathbf{H_c}$ + $\mathbf{H_d}$), 7.54-7.50 (m, 4H, $\mathbf{H_e}$), 7.42 (t, 1H, J=7.4 Hz, $\mathbf{H_f}$), 7.34 (t, 1H, J=7.4 Hz, $\mathbf{H_f}$), 7.24 (m, 4H, $\mathbf{H_i}$), 5.58 (m, 4H, C**H**$CH_2$), 4.49 (m, 2H, (CO)OC$\mathbf{H_2}$), 3.71 (t, 2H, J=6.2 Hz, C$\mathbf{H_2}$OH), 2.29 (m, 8H, CHC$\mathbf{H_2}$), 1.93 (m, 2H, (CO)O$CH_2$C$\mathbf{H_2}$), 1.60-1.26 (m, 30H, -C$\mathbf{H_2}$-), 0.95 (t, 12H, J=6.4 Hz, $CH_2$C$\mathbf{H_3}$).

**MALDI-TOF:** calculated for $C_{91}H_{93}N_8O_{11}$ $[M+H]^+$ *m/z*: 1474.751, found *m/z*: 1474.449.

**Tetra-TBDMSO-hexyl functionalized tetraquinoxaline cavitand (22)**

$K_2CO_3$ (0.159 g, 1.15 mmol) was added to a solution of Res[$C_6H_{13}$, H] (0.158 g, 0.19 mmol) in 5 mL of dry DMSO, followed by dichloroquinoxaline **19** (0.386 g, 0.84 mmol). The reaction mixture was heated at 70 °C under microwave irradiation for 2 h. Water (100 mL) was added and the precipitate was filtered, washed with water and dried. The crude was purified by flash column chromatography ($CH_2Cl_2$/AcOEt 98:2) affording cavitand **22** (0.054 g, 0.023 mmol, 12%) as a white solid.

**$^1$H NMR** ($CDCl_3$, 300 MHz): δ (ppm) = 8.61 (d, 4H, J=1.6 Hz, Ar$\mathbf{H_a}$), 8.18 (s, 4H, Ar$\mathbf{H_{up}}$), 8.03 (dd, 4H, $J_o$=8.7 Hz, $J_m$=1.8 Hz, Ar$\mathbf{H_b}$), 7.85 (d, 4H, J=8.7 Hz, Ar$\mathbf{H_c}$), 7.23 (s, 4H, Ar$\mathbf{H_{down}}$), 5.55 (t, 4H, J=7.8 Hz, C**H**$CH_2$), 4.48 (t, 8H, J=6.7 Hz, (CO)OC$\mathbf{H_2}$), 3.64 (t, 8H, J=6.4 Hz, C$\mathbf{H_2}$OSi), 2.29 (m, 8H, CHC$\mathbf{H_2}$), 1.92 (m, 8H, (CO)O$CH_2$C$\mathbf{H_2}$), 1.58-1.28 (m, 56H, -C$\mathbf{H_2}$-), 0.94 (m, 12H, $CH_2$C$\mathbf{H_3}$), 0.90 (s, 36H, Si$^t$**Bu**), 0.09 (s, 24H, SiC$\mathbf{H_3}$).

**MALDI-TOF:** calculated for $C_{136}H_{185}N_8O_{20}Si_4$ $[M+H]^+$ *m/z*: 2364.299, found *m/z*: 2364.428.

**Tetra-ω-hydroxy functionalized tetraquinoxaline cavitand (16)**

DMSO (1 mL) was added to a solution of cavitand **22** (0.054 g, 0.023 mmol) in 0.5 mL of purified THF, followed by $H_2O$ (100 μL) and N-bromosuccinimide (0.027 g, 0.23 mmol). The reaction mixture was stirred at room temperature for 12 h in the dark. Volatiles were evaporated under reduced pressure and the crude was dissolved in $CHCl_3$ and washed with water. Purification *via* flash column chromatography ($CH_2Cl_2$/MeOH 95:5) afforded cavitand **16** (0.024 g, 0.013 mmol, 55%) as a white solid.

**$^1$H NMR** ($CDCl_3$, 300 MHz): δ (ppm) = 8.61 (d, 4H, J=1.6 Hz, Ar**H$_a$**), 8.21 (s, 4H, Ar**H$_{up}$**), 8.01 (dd, 4H, $J_o$=8.7 Hz, $J_m$=1.7 Hz, Ar**H$_b$**), 7.85 (d, 4H, J=8.7 Hz, Ar**H$_c$**), 7.25 (s, 4H, Ar**H$_{down}$**), 5.61 (t, 4H, J=7.7 Hz, C**H**$CH_2$), 4.48 (t, 8H, J=6.7 Hz, (CO)OC**H$_2$**), 3.71 (t, 8H, J=6.1 Hz, C**H$_2$**OH), 2.29 (m, 8H, CHC**H$_2$**), 1.92 (m, 8H, (CO)OC$H_2$C**H$_2$**), 1.59-1.36 (m, 56H, -C**H$_2$**-), 0.92 (m, 12H, $CH_2$C**H$_3$**).

**MALDI-TOF:** calculated for $C_{112}H_{129}N_8O_{20}$ $[M+H]^+$ *m/z*: 1906.256, found *m/z*: 1906.724; calculated for $C_{112}H_{129}N_8O_{20}Na$ $[M+Na]^+$ *m/z*: 1929.246, found *m/z*: 1929.367; calculated for $C_{112}H_{129}N_8O_{20}K$ $[M+K]^+$ *m/z*: 1945.355, found *m/z*: 1945.886.

**Propanol-footed tetraquinoxaline cavitand (17)**

$K_2CO_3$ (0.100 g, 0.721 mmol) was added to a solution of Res[$C_3H_6OH$, H][73] (0.100 g, 0.138 mmol) in 3 mL of dry DMSO, followed by 2,3-dichloroquinoxaline (0.122 g, 0.61 mmol). The reaction mixture was heated at 70 °C under microwave irradiation for 1 h. Water (100 mL) was added and the precipitate was filtered, washed with water and dried. The crude was purified by flash column chromatography (gradient from $CH_2Cl_2$/MeOH 99:1 to $CH_2Cl_2$/MeOH 93:7) affording cavitand **17** (0.071 g, 0.058 mmol, 42%) as a white solid.

**$^1$H NMR** (DMSO-$d_6$, 300 MHz): 8.04 (s, 4H, Ar**H$_{up}$**), 7.89 (m, 8H, Ar**H**), 7.84 (s, 4H, Ar**H$_{down}$**), 7.61 (m, 8H, Ar**H**), 5.52 (t, 4H, J=7.5 Hz, C**H**$CH_2$), 4.55 (m, 8H, C**H$_2$**OH), 3.56 (m, 8H, CHC**H$_2$**), 1.50 (m, 8H, C**H$_2$**$CH_2$OH).

**MALDI-TOF:** calculated for $C_{72}H_{57}N_8O_{12}$ $[M+H]^+$ *m/z*: 1226.261, found *m/z*: 1226.298; calculated for $C_{72}H_{56}N_8O_{20}Na$ $[M+Na]^+$ *m/z*: 1248.251, found *m/z*: 1248.368.

**Tetra-TBDMSO-hexyl functionalized tetraquinoxaline *kite* cavitand (25)**

$K_2CO_3$ (0.093 g, 0.67 mmol) was added to a solution of Res[$C_6H_{13}$, $CH_3$][67] (0.098 g, 0.11 mmol) in 4 mL of dry DMSO, followed by dichloroquinoxaline **19** (0.225

g, 0.49 mmol). The reaction mixture was heated at 70 °C under microwave irradiation for 1 h. Water (100 mL) was added and the precipitate was filtered, washed with water and dried. The crude was purified by flash column chromatography ($CH_2Cl_2$/AcOEt 96:4) affording cavitand **25** (0.135 g, 0.056 mmol, 51%) as a white solid.

**$^1$H NMR** ($CDCl_3$, 400 MHz): 8.69 (m, 4H, Ar**H$_a$**), 8.28 (m, 4H, Ar**H$_b$**), 7.80 (m, 4H, Ar**H$_c$**), 6.91 (s, 2H, Ar**H$_{down}$**), 6.18 (s, 2H, Ar**H$_{down}$**), 4.50 (m, 4H, C**H**$CH_2$), 4.39 (m, 8H, (CO)OC**H$_2$**), 3.64 (m, 12H, CHC**H$_2$** + C**H$_2$**OSi), 3.15 (s, 6H, ArC**H$_3$**), 2.23 (s, 6H, ArC**H$_3$**), 1.84 (m, 8H, CHC**H$_2$**), 1.60-1.22 (m, 56H, -C**H$_2$**-), 0.93 (s, 12H, $CH_2$C**H$_3$**), 0.89 (s, 36H, Si**$^t$Bu**), 0.03 (s, 24H, SiC**H$_3$**).

**MALDI-TOF:** calculated for $C_{140}H_{193}N_8O_{20}Si_4$ $[M+H]^+$ *m/z*: 2419.406, found *m/z*: 2419.529; calculated for $C_{140}H_{192}N_8O_{20}Si_4Na$ $[M+Na]^+$ *m/z*: 2442.396, found *m/z*: 2442.246.

**Tetra-ω-hydroxy functionalized tetraquinoxaline *kite* cavitand (18)**

DMSO (2 mL) was added to a solution of cavitand **25** (0.100 g, 0.041 mmol) in 1 mL of destabilized THF, followed by $H_2O$ (200 μL) and N-bromosuccinimide (0.054 g, 0.46 mmol). The reaction mixture was stirred at room temperature for 12 h in the dark. Volatiles were evaporated under reduced pressure and the crude was dissolved in $CHCl_3$ and washed with water. Purification *via* flash column chromatography ($CH_2Cl_2$/MeOH 94:6) afforded cavitand **18** (0.040 g, 0.02 mmol, 49%) as a white solid.

**$^1$H NMR** ($CDCl_3$, 400 MHz): 8.52 (m, 2H, Ar**H**), 8.29 (m, 4H, Ar**H**), 8.13 (m, 2H, Ar**H**), 7.83 (m, 4H, Ar**H**), 6.93 (s, 2H, Ar**H$_{down}$**), 6.21 (s, 2H, Ar**H$_{down}$**), 4.54 (m, 4H, C**H**$CH_2$), 4.37 (m, 8H, (CO)OC**H$_2$**), 3.78 (m, 12H, CHC**H$_2$** + C**H$_2$**OH), 3.19 (s, 6H, ArC**H$_3$**), 2.25 (s, 6H, ArC**H$_3$**), 1.83 (m, 8H, CHC**H$_2$**), 1.69-1.16 (m, 56H, -C**H$_2$**), 0.92 (s, 12H, $CH_2$C**H$_3$**).

**MALDI-TOF:** calculated for $C_{116}H_{137}N_8O_{20}$ $[M+H]^+$ *m/z*: 1962.363, found *m/z*: 1962.914; calculated for $C_{140}H_{192}N_8O_{20}Si_4Na$ $[M+Na]^+$ *m/z*: 1985.353, found *m/z*: 1985.591.

**PU samples preparation**

A solution of isophorone diisocyanate (59 equiv) in dry THF was slowly added to a solution of cavitand and DABCO (8.42 equiv) in dry THF. The mixture was stirred at 60 °C for 2 h. The solution was cooled at room temperature and added to a solution of poly(tetramethylene glycol) ($M_w$ 1000; 1216 equiv) and DABCO

(1.05 equiv) in dry THF. The mixture was stirred under vacuum and heated at 50 °C to remove volatiles. After the addition of hexamethylene diisocyanate (1180 equiv), the viscous pre-polymer was degassed under vacuum and poured onto a PTFE plate. After a second degassing, the sample was cured in an oven for 48 h at 60 °C and for 48 h at room temperature before testing. Once cured, the film was peeled away and cut into stripes.

| | Cavitand | Conc. (% w/w) |
|---|---|---|
| **I** | **5** | 0.5 |
| **II** | **5** | 0.3 |
| **III** | **5** | 0.01 |
| **IV** | **6** | 0.5 |
| **V** | **6** | 0.3 |
| **VI** | **6** | 0.01 |
| **VII** | **15** | 0.1 |
| **VIII** | **15** | 0.3 |
| **IX** | **14** | 0.5 |
| **X** | **14** | 0.3 |
| **XI** | **14** | 0.1 |

**Table S2.5** *Control specimens containing mono functionalized, difunctionalized and unfunctionalized cavitands.*

| | Cavitand | Conc. (% w/w) |
|---|---|---|
| **I** | **16** | 0.5 |
| **II** | **16** | 0.3 |
| **III** | **16** | 0.2 |
| **IV** | **16** | 0.1 |
| **V** | **16** | 0.01 |

| | | |
|---|---|---|
| **VI** | **16** | 0.02 |
| **VII** | **18** | 0.01 |

**Table S2.6** *Specimens containing tetrafunctionalized cavitands.*

## 2.6 References

[1] M. M. Caruso, D. A. Davis, Q. Shen, S. A. Odom, N. R. Sottos, S. R. White, J. S. Moore, *Chem. Rev*. **2009**, *109*, 5755-5798.

[2] a) A. L. Black, J. M. Lenhardt, S. L. Craig, *J. Mater. Chem*. **2011**, *21*, 1655-1663; b) G. Kaupp, *Cryst. Eng. Commun*. **2009**, *11*, 388-403; c) M. K. Beyer, H. Clausen-Schaumann, *Chem. Rev*. **2005**, *105*, 2921-2948.

[3] J. N. Brantley, K. M. Wiggings, C. W. Bielawski, *Polym. Int*. **2013**, *62*, 2-12.

[4] a) H. Staudinger, H. F. Bondy, *Ber. Dtsch. Chem. Ges*. **1930**, *63*, 734-736; b) H. Staudinger, W. Heuer, *Ber. Dtsch. Chem. Ges.* **1934**, *67*, 1159-1164; c) H. Staudinger, E. O. Leupold, *Ber. Dtsch. Chem. Ges*. **1930**, *63*, 730-733.

[5] W. Kauzmann, H. Eyring, *J. Am. Chem. Soc*. **1940**, *62*, 3113-3125.

[6] M. V. Encina, E. Lissi, M. Sarasúa, L. Gargallo, D. J. Radic, *Polym. Sci. Polym. Lett. Ed*. **1980**, *18*, 757-760.

[7] J. Li, C. Nagamani, J. S. Moore, *Acc. Chem. Res*. **2015**, *48*, 2181-2190.

[8] a) D. A. Davis, A. Hamilton, J. Yang, L. D. Cremar, D. V. Gough, S. L. Potisek, M. T. Ong, P. V. Braun, T. J. Martın ez, S. R. White, J. S. Moore, N. R. Sottos, *Nature* **2009**, *459*, 68−72; b) Y. L. Chen, A. J. H. Spiering, S. Karthikeyan, G. W. M. Peters, E. W. Meijer, R. P. Sijbesma, *Nat. Chem*. **2012**, *4*, 559−562.

[9] C. R. Hickenboth, J. S. Moore, S. R. White, N. R. Sottos, J. Baudry, S. R. Wilson, *Nature* **2007**, *446*, 423−427.

[10] J. M. Lenhardt, M. T. Ong, R. Choe, C. R. Evenhuis, T. J. Martıń ez, S. L. Craig *Science* **2010**, *329*, 1057−1060.

[11] M. B. Larsen, A. Boydston, *J. Am. Chem. Soc*. **2013**, *135*, 8189−8192.

[12] a) A. Piermattei, S. Karthikeyan, R. P. Sijbesma, *Nat. Chem*. **2009**, *1*, 133−137; b) A. G. Tennyson, K. M. Wiggins, C. W. Bielawski, *J. Am. Chem. Soc*. **2010**, *132*, 16631−16636.

[13] K. L. Berkowski, S. L. Potisek, C. R. Hickenboth, J. S. Moore, *Macromolecules* **2005**, *38*, 8975−8978.

[14] T. Bercovici, E. Fischer, *J. Am. Chem. Soc*. **1964**, *86*, 5687-5688.

[15] S. L. Potisek, D. A. Davis, N. R. Sottos, S. R. White, J. S. Moore, *J. Am*. *Chem. Soc*. **2007**, *129*, 13808−13809.

[16] B. A. Beiermann, S. L. B. Kramer, J. S. Moore, S. R. White, N. R. Sottos, *ACS Macro Lett*. **2012**, *1*, 163-166.

[17] C. K. Lee, D. A. Davis, S. R. White, J. S. Moore, N. R. Sottos, P. V. Braun, *J. Am. Chem. Soc*. **2010**, *132*, 16107-16111.

[18] G. R. Gossweiler, G. B. Hewage, G. Soriano, Q. Wang, G. W. Welshofer, X. Zhao, S. L. Craig, *ACS Macro Lett*. **2014**, *3*, 216-219.

[19] a) B. A. Beiermann, D. A. Davis, S. L. B. Kramer, J. S. Moore, N. R. Sottos, S. R. White, *J. Mater. Chem*. **2011**, *21*, 8443-8447; b) A. L. Black, J. A. Orlicki, S. L. Craig, *J. Mater. Chem*. **2011**, *21*, 8460-8465; c) C. M. Kingsbury, P. A. May, D. A. Davis, S. R. White, J. S. Moore, N. R. Sottos, *J. Mater. Chem*. **2011**, *21*, 8381-8388; d) J. M. Lenhardt, A. L. Black, B. A. Beiermann, B. D. Steinberg, F. Rahman, T. Samborski, J. Elsakr, J. S. Moore, N. R. Sottos, S. L. Craig, *J. Mater. Chem*. **2011**, *21*, 8454-8459.

[20] M. B. Larsen, A. J. Boydston, *J. Am. Chem. Soc*. **2014**, *136*, 1276-1279.

[21] L. M. de Espinosa, W. Meesorn, D. Moatsou, C. Weder, *Chem. Rev*. **2017**, doi: 10.1021/acs.chemrev.7b00168.

[22] P. G. Gillespie, R. G. Walker, *Nature* **2001**, *413*, 194−202.

[23] J. T. B. Crawley, R. de Groot, Y. Z. Xiang, B. M. Luken, D. A. Lane, *Blood* **2011**, *118*, 3212−3221.

[24] M. Chalfie, *Nat. Rev. Mol. Cell Biol*. **2009**, *10*, 44−52.

[25] V. Vogel, *In Annual Review of Biophysics and Biomolecular Structure; Annual*

*Reviews: Palo Alto, CA* **2006**, *35*, 459−488.

[26] P. Lavalle, F. Boulmedais, P. Schaaf, L. Jierry, *Langmuir* **2016**, *32*, 7265-7276.

[27] a) J. Davila, A. Chassepot, J. Longo, F. Boulmedais, A. Reisch, B. Frisch, F. Meyer, J. C. Voegel, P. J. Mesini, B. Senger, M. H. Metz-Boutigue, J. Hemmerle, P. Lavalle, P. Schaaf, L. Jierry, *J. Am. Chem. Soc*. **2012**, *134*, 83−86; b) J. Longo, C. Y. Yao, C. Rios, N. T. T. Chau, F. Boulmedais, J. Hemmerle, P. Lavalle, S. M. Schiller, P. Schaaf, L. Jierry, *Chem. Commun*. **2015**, *51*, 232−235; c) C. Rios, J. Longo, S. Zahouani, T. Garnier, C. Vogt, A. Reisch, B. Senger, F. Boulmedais, J. Hemmerle, K. Benmlih, B. Frisch, P. Schaaf, L. Jierry, P. Lavalle, *Chem*. *Commun*. **2015**, *51*, 5622−5625.

[28] a) J. R. Moran, S. Karbach, D. J. Cram, *J. Am. Chem. Soc.* **1982**, *104*, 5826-5828; b) J. R. Moran, J. L. Ericson, E. Dalcanale, J. A. Bryant, C. B. Knobler, D. J. Cram, *J. Am. Chem. Soc.* **1991**, *113*, 5707-5714.

[29] a) S. Zampolli, P. Betti, I. Elmi, E. Dalcanale, *Chem. Commun.* **2007**, 2790-2792; b) L. Pirondini, E. Dalcanale, *Chem. Soc. Rev.* **2007**, *36*, 695-706; c) G. G. Condorelli, A. Motta, M. Favazza, E. Gurrieri, P. Betti, E. Dalcanale, *Chem. Commun.* **2010**, *46*, 288-290; d) S. Zampolli, I. Elmi, F. Mancarella, P. Betti, E. Dalcanale, G. C. Cardinali, M. Severi, *Sens. Actuators B* **2009**, *141*, 322-328; e) F. Bianchi, M. Matarozzi, P. Betti, F. Bisceglie, M. Careri, A. Mangia, L. Sidisky, S. Ongarato, E. Dalcanale, *Anal. Chem.* **2008**, *80*, 6423-6430; f) F. Bertani, N. Riboni, F. Bianchi, G. Brancatelli, E. S. Sterner, R. Pinalli, S. Geremia, T. M. Swager, E. Dalcanale, *Chem. Eur. J.* **2016**, 22, 3312-3319.

[30] a) P. Soncini, S. Bonsignore, E. Dalcanale, F. Ugozzoli, *J. Org. Chem.* **1992**, *57*, 4608-4612; b) M. Vincenti, E. Dalcanale, *J. Chem. Soc. Perkin Trans. 2* **1995**, 1069-1076; c) F. Bianchi, R. Pinalli, F. Ugozzoli, S. Spera, M. Careri, E. Dalcanale, *New J. Chem*. **2003**, *27*, 502-509.

[31] L. Roncucci, L. Pirondini, G. Paderni, C. Massera, E. Dalcanale, V. A. Azov, F. Diederich, *Chem. Eur. J.* **2006**, *12*, 4775–4784.

[32] V. A. Azov, A. Beeby, M. Cacciari, A. G. Cheetham, F. Diederich, M. Frei, J. K. Gimzewski, V. Gramlich, B. Hecht, B. Jaun, T. Latychevskaia, A. Lieb, Y. Lill, F. Marotti, A. Schlegel, R. R. Schlittler, P. J. Skinner, P. Seiler, Y. Yamakoshi, *Adv. Funct. Mater.* **2006**, *16*, 147-156.

[33] P. J. Skinner, A. G. Cheetham, A. Beeby, V. Gramlich, F. Diederich, *Helv. Chim. Acta* **2001**, *84*, 2146-2153.

[34] a) P. Amrhein, A. Shivanyuk, D. W. Johnson, J. Rebek Jr., *J. Am. Chem. Soc.* **2002**, *124*, 10349-10358; b) M. Frei, F. Marotti, F. Diederich, *Chem. Commun.* **2004**, 1362-1363.

[35] M. Frei, F. Diederich, R. Tremont, T. Rodriguez, L. Echegoyen, *Helv. Chim. Acta* **2006**, *89*, 2040-2057.

[36] a) I. Pochorovski, C. Boudon, J. -P. Gisselbrecht, M. -O. Ebert, W. B. Schweizer, F. Diederich, *Angew. Chem. Int. Ed.* **2012**, *51*, 262-266; b) I. Pochorovski, M. O. Ebert, J. P. Gisselbrecht, C. Boudon, W. B. Schweizer, F. Diederich, *J. Am. Chem. Soc.* **2012**, *134*, 14702-14705; c) I. Pochorovski, J. Milić, D. Kolarski, C. Gropp, W. B. Schweizer, F. Diederich, *J. Am. Chem. Soc.* **2014**, *136*, 3852-3858.

[37] F. Lagugné-Labarthet, Y. Q. An, T. Yu, Y. R. Shen, E. Dalcanale, D. K. Shenoy, *Langmuir* **2005**, *21*, 7066-7070.

[38] I. Pochorovski, *Redox-Switchable Cavitands: Conformational Analysis and Binding Studies*, Ph.D. thesis, ETH- Dissertation Nr. 21351, ETH Zürich, 2013.

[39] V. A. Azov, B. Jaun, F. Diederich, *Helv. Chim. Acta.* **2004**, *87*, 449-462.

[40] P. Pagliusi, F. Lagugné-Labarthet, D. K. Shenoy, E. Dalcanale, Y. R. Shen, *J. Am. Chem. Soc.* **2006**, *128*, 12610-12611.

[41] A. Alderson, *Chem. Ind. (Londo*n) **1999**, *10*, 384-391.

[42] K. E. Evans, A. Alderson, *Adv. Mater*. **2000**, *12*, 617-628.

[43] J. B. Choi, R. S. Lakes, *J. Mater. Sci.* **1992**, *27*, 4678-4684.

[44] J. B. Choi, R. S. Lakes, *International Journal of Fracture* **1996**, *80*, 73-83.

[45] J. N. Grima, D. Attard, R. Gatt, R. N. Cassar, *Adv. Eng. Mater.* **2009**, *11*, 533–535.

[46] K. Muto, R. W. Bailey, K. J. Mitchell, *Proc. Inst. Mech. Eng*. **1963**, *177*, 155-203.

[47] D. J. Fozdar, P. Soman, J. W. Lee, L. H. Han, S. Chen, *Adv. Funct. Mater.* **2011**, *21*, 2712–2720.

[48] R. Lakes, *Science* **1987**, *235*, 1038-1040.

[49] J. N. Grima, R. Gatt, N. Ravirala, A. Alderson, K. E. Evans, *Materials Science and Engineering A* **2006**, *423*, 214–218.

[50] B. D. Caddock, K. E. Evans, *J. Phys. D: Appl. Phys.* **1989**, *22*, 1877-1882.

[51] K. E. Evans, B. D. Caddock, *J. Phys. D: Appl. Phys.* **1989**, *22*, 1883-1887.

[52] D. R. Veronda, R. A. Westmann, *J. Biomechanics* **1970**, *3*, 111-124.

[53] R. Gatt, M. V. Wood, A. Gatt, F. Zarb, C. Formosa, K. M. Azzopardi, A. Casha, T. P. Agius, P. Schembri-Wismayer, L. Attard, N. Chockalingam, J. N. Grima, *Acta Biomaterialia* **2015**, *24*, 201–208.

[54] a) J. N. Grima, R. Jackson, A. Alderson and K. E. Evans, *Adv. Mater*. **2000**, *12*, 1912-1918; b) A. Alderson, K. E. Evans and J. Rasburn, *International Patent*, WO 99/22838, **1999**.

[55] Y. Yeganeh-Haeri, D. J. Weidner, J. B. Parise, *Science* **1992**, *257*, 650-652.

[56] N. R. Keskar, J. R. Chelikowsky, *Nature* **1992**, *358*, 222-224.

[57] K. W. Wojciechowski, *Mol. Phys.* **1987**, *61*, 1247-1258.

[58] a) K. E. Evans, M. A. Nkansah, I. J. Hutchinson, S. C. Rogers, *Nature* **1991**, *353*, 124-125; b) G. Wei, S. F. Edwards, *Comput. Polym. Sci.* **1992**, *2*, 44-54; c) K. E. Evans, A. Alderson, F. R. Christian, *J. Chem Soc. Faraday Trans*. **1995**, *91*, 2671-2680.

[59] R. H. Baughman, D. S. Galvão, *Nature* **1993**, *365*, 735-737.

[60] J. N. Grima, J. J. Williams, K. E. Evans, *Chem. Commun.* **2005**, 4065–4067.

[61] P. Neri, A. Bottino, F. Cunsolo, M. Piatterelli, E. Gavuzzo, *Angew. Chem. Int. Ed.* **1998**, *37*, 166-169.

[62] a) C. He, P. Liu, A. C. Griffin, *Macromolecules* **1998**, *31*, 3145-3147; b) D. Kang, M. P. Mahajan, S. Zhang, R. G. Petschek, C. Rosenblatt, C. He, P. Liu, A. C. Griffin, *Phys. Rev. E* **1999**, *60*, 4980-4982; c) W. H. de Jeu, E. P. Obraztsov, B. I. Ostrovskii, W. Ren, P. J. McMullan, A. C. Griffin, A. Sánchez-Ferrer, H. Finkelmann, *Eur. Phys. J. E* **2007**, *24*, 399–409; d) W. Ren, P. J. McMullan, A. C. Griffin, *Phys. Status Solidi B* **2009**, *246*, 2124–2130.

[63] W. H. de Jeu, *Liquid Crystal Elastomers: Materials and Applications* **2012**, Springer, Berlin.

[64] Y. Suzuki, G. Cardone, D. Restrepo, P. D. Zavattieri, T. S. Baker, F. A. Tezcan *Nature* **2016**, *533*, 369-373.

[65] W. Yang, Z. M. Li, W. Shi, M. B. Yang, *J. Mater. Sci.* **2004**, *39*, 3269-3279.

[66] a) Vase form: E. Dalcanale, P. Soncini, G. Bacchilega, F. Ugozzoli, *J. Chem. Soc., Chem. Commun.* **1989**, 500-501; b) Kite form: L. Pirondini, A. G. Stendardo, S. Geremia, M. Campagnolo, P. Samorì, J. P. Rabe, R. Fokkens, E. Dalcanale *Angew. Chem. Int. Ed.* **2003**, *42*, 1384-1387.

[67] D. J. Cram, H. J. Choi, J. A. Bryant, C. B. Knobler, *J. Am. Chem. Soc*. **1992**, *114*, 7748-7765.

[68] K. G. Kleb, *Agew. Chem. Int. Ed*. **1964**, *3*, 408-416.

[69] D. R. Romer, *J. Heterocyclic Chem*. **2009**, *46*, 317-319.

[70] a) R. H. Pritchard, P. Lava, D. Debruyne, E. M. Terentjev, *Soft Matter* **2013**, *9*, 6037-6045; b) J. Blaber, B. Adair, A. Antoniou, *Exp. Mech*. **2015**, *55*(6), 1105-1122; c) M. Palanca, G. Tozzi, L. Cristofolini, *Int. Biomech*. **2016**, *3*(1), 1-21.

[71] R. Brighenti, F. Artoni, F. Vernerey, M. Torelli, A. Pedrini, I. Domenichelli, E. Dalcanale, *J. Mech. Phys. Solids* **2018**, 113, 65-81.

[72] L. M. Tunstad, J. A. Tucker, E. Dalcanale, J. Weiser, J. A. Bryant, J. C. Sherman, R. C. Helgeson, C. B. Knobler, D. J. Cram, *J. Org. Chem*. **1989**, *54*, 1305-1312.

[73] B. C. Gibb, R. G. Chapman, J. C. Sherman, *J. Org. Chem*. **1996**, *61*, 1505-1509.

# CHAPTER 3

# EXPLOITING AGGREGATION INDUCED ENHANCED EMISSION OF Pt(II) COMPLEXES FOR CELLULAR BIO-IMAGING AND MECHANOCHROMIC MATERIALS*

*The work described in this chapter has been carried out in the group of Prof. Luisa De Cola at the Institut de Science at d'Ingégnerie Supramoléculaire (ISIS), Strasbourg, France.

## 3.1 Introduction

### 3.1.1 Photophysical properties of platinum(II) complexes

The beautiful colours of transition metal complexes (TMCs) have always been subject of admiration and curiosity, but a deep understanding of the phenomena responsible for their surprising properties arrived relatively late. Indeed, molecular photochemistry is a fairly young field; starting in the middle of last century, photochemistry began to be extensively studied in parallel with the advances in spectroscopic techniques but was, in its first stage, exclusively limited to the organic sphere. Thus, despite the photosensitivity of metal complexes was known for a long time (the effect of light on AgCl for photography was exploited since 1830s), investigations on the photophysics and photochemical processes of transition metal complexes were, until the 70's, rather scarce.[1] In respect to purely organic chromophores, photoactive transition metal complexes (TMCs), thanks to the presence of heavy atoms, present a complicated but extremely peculiar and intriguing photophysical scenario. In the last decades, their unique properties were studied with a particular focus on second and third row transition metals such as Ir(III), Ru(II), Os(II), Re(I), Pd(II), Pt(II), Ag(I) and Au(I)[1] as well as to the first row ones, such as Cu(I) and Zn(II).[2] Features of the resulting complexes, in terms of photo- and electro-chemical stability, photoluminescence quantum yield, emission colour and lifetime of the emissive excited state, can be finely tuned by a judicious choice of the metal ion and ligands. Besides, thanks to the pronounced spin-orbit coupling (SOC) exerted by the heavy atom, intersystem crossing (ISC) phenomena allow the population of energetically low-lying triplet excited states, leading to unusual radiative decays. Nowadays, photoactive TMCs find real-market applications in a wide range of technological fields such as optoelectronics,[3] non-linear optical materials,[4] photo-catalysis for organic synthesis,[5] electro-chemiluminescence,[6] metallogelators,[7] bio-sensing[8] and bio-imaging.[9] Furthermore, they have been recently used as active species in photonic devices for providing attractive alternatives to conventional lightning; this is the case of energy-saving organic light emitting diodes (OLEDs) and light-emitting electrochemical cells (LEECs),[10] as well as solar light harvesting materials for photovoltaic technology, such as in dye-sensitized solar cells (DSSCs).[11] Among transition metals, Pt(II) coordination complexes are particularly interesting, largely on account of their optoelectronic properties,[12] which are directly related to the intermolecular interactions between adjacent

metal atoms. The peculiar tunability of their luminescence as a function of metal···metal distance and their aggregation tendency open new avenues for applications in which responsiveness to external stimuli and self-assembly are required.

Pt(II) usually prefers a square planar coordination, irrespectively of the strength of the ligands, as rationalized by the Ligand-Field Theory (LFT).[13] The typical splitting of degenerate *d*-orbitals experiencing a square planar ligand field is represented in Fig. 3.1; the high stacking tendency displayed by Pt(II) complexes, based on ground-state intermolecular non-covalent weak metal···metal[14] and/or ligand-ligand interactions,[15] traces back to their constant coordination geometry. Perturbations on molecular orbitals closer to the frontier region, elicited by two axially interacting Pt complexes, lead to their peculiar absorption and luminescence characteristics.

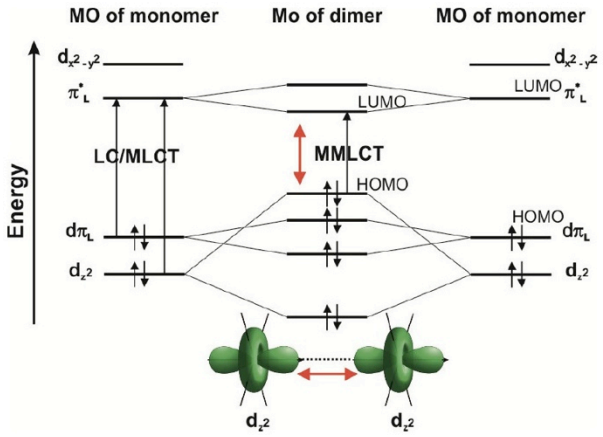


**Figure 3.1** *Simplified MO diagram for two interacting Pt(II) complexes, showing the intermolecular $d_{z^2}$ orbital overlap in the ground-state and its influence on the energy of the MO levels. Red arrows display the correlation between the Pt···Pt distance and the HOMO-LUMO gap.*[16]

The typical electronic configuration for luminescent Pt complexes bearing strong field cyclometalating ligands as well as good π-accepting moieties presents highest occupied HOMO and lowest unoccupied LUMO, with respectively *d*π and *d*π* character. Generally, for the monomeric form, the HOMO is mainly constituted by ligands' bonding orbitals $\pi_L$, while the LUMO displays main contributions from the ligands' anti-bonding orbitals $\pi_L$*. Thus,

the relative energy of MLCT (metal-to-ligand charge transfer) and LC (ligand-centred) transitions are directly related to the energy of $\pi_L$ and $d_z^2$ orbitals, involved in the electronic configuration of the excited state. According to LFT, for a metal centre in a square-planar arrangement of coordinating ligands, the occupied $d_z^2$ orbital, pointing in the orthogonal direction in respect to the molecular plane, is prone to interact with surrounding species, such as solvent molecules or neighbouring Pt complexes. In the latter case, destabilization of the occupied $d_z^2$ orbital, due to the formation of sizeable metallophilic interactions along the free axial position, leads to a switch of the character of the HOMO level from $d\pi$ to $\sigma^*$. Hence, the new excited-states, such as metal-metal-to-ligand charge transfer (MMLCT[5]) and ligand-to-metal-metal charge transfer (LMMCT) typically display bathochromically shifted absorption and luminescence spectra compared to the parent non-interacting Pt complexes (Figure 3.1). The strong anti-bonding character of the unoccupied $d_{x^2-y^2}$ orbital, due to ligand field stabilization, justifies the fact that population of this orbital is usually accompanied by the elongation of Pt-L bonds and a severe distortion of the complex geometry; thus, non-radiative decays from the MC (*d* - *d*) excited states to the ground state at the isoenergetic crossing point of the potential energy surfaces are promoted. Despite the presence of less-energetic excited states with a different character, such as MLCT (*d* - $\pi^*$) or LC ($\pi$ - $\pi^*$), the *d* – *d* state, if thermally accessible, can still exert a deleterious influence; as schematized in Fig. 3.2, this happens when $\Delta E$ is comparable with kT.[17]

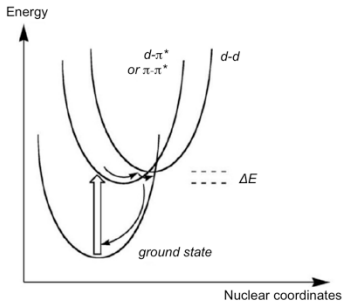


**Figure 3.2** *Displacement of the potential energy surfaces of d-d excited state in respect to the ground state, due to the strong anti-bonding character of the populated $d_{x^2-y^2}$ orbital. Thick arrow represents the absorption of light, while thin ones indicate vibrational relaxation and non-radiative decay.*[17a]

For promoting the emission of Pt(II) complexes at room temperature, two parameters need to be complied, namely (i) the lowest-lying excited state has to be not a metal-centred *d* – *d* state but rather a ligand-centred or charge-transfer state; and (ii) there has to be a large energy gap (E) between the lowest-lying excited state and the higher-lying *d* – *d* state, so that thermally activated depopulation *via* the latter is inhibited. Clearly, lowering the energy of the emitting state *d* - π* or π - π*, or raising that of the *d* – *d* state end up with the desired increase of E. Typical ways to achieve low-energy emitting states foresee the use of rigid ligands, like porphyrins, or the functionalization of non-emissive complexes with electron-rich pendants.[18] In order to make *d* – *d* states thermally inaccessible by raising their energy, strong-field ligands or co-ligands are required. Several examples reported in literature pursue this approach by substituting weak-field halide ligands with strong-field cyanides[19] or by using acetylide-based co-ligands.[20] Another frequently adopted strategy forecasts the use of cyclometalating ligands, namely polydentate species, closely related to bipyridine and terpyridine, that bind to the metal *via* a covalent metal-carbon bond, while the remaining coordination positions are typically occupied by heteroatoms such as nitrogen. The use of these organometallic compounds, involving a net deprotonation of the aromatic C-H, provides to the metal ion a very strong ligand field, thanks to the pronounced σ-donor character of the carbanion conjugated with the good π-acceptor nature of the pyridyl group. Because of their sizable luminescence at ambient conditions, many cyclometalated Pt complexes have been recently employed as triplet emitters in OLEDs.[21] Furthermore, bidentate ligands comprising the combination of a pyridine ring and a 5-membered azole ring (pyrazole, imidazole or triazole) have received steadily rising attention in coordination chemistry over recent years.[22] When binding to the metal implies a deprotonation, the resulting anionic ligand is essentially an analogue of a cyclometalating compound. As it is easy to imagine, these pseudo-cyclometalates complexes, either with Pt(II)[23] or with others transition metals like Ir(III),[24] have been widely investigated in literature. As stated above, the lively and fascinating photophysical scenario of Pt(II) complexes largely relies on their strong tendency to aggregate, which paves the way to the establishment of novel excited states. Considering that the electronic interaction between neighbouring Pt atoms occurs below 3.5 Å, the energy of the aforementioned transitions strongly depends on the metal···metal distance. Interestingly, even if repulsion would be normally expected between two closed shell cations, evidences of the presence of attractive interactions

generally referred to as metallophilic,[25] have been extensively studied. Besides the numerous theoretical studies, which describe these van der Waals-type interactions by taking into account relativistic and correlation effects,[26] solid state data obtained by X-ray diffraction provided precise structural information about metal···metal distance. Considering that the strength of such metallophilic interactions has been compared to the one of hydrogen bonding (around 29-46 kcal $mol^{-1}$),[27] they can be actively employed in the preparation of novel supramolecular structures.

### 3.1.2 Self-assembly of platinum(II) complexes

The possibility to achieve self-assembled nanostructures based on TMCs by means of supramolecular approaches provides an efficient *bottom up* approach for the preparation of supramolecular architectures up to the micrometre scale.[28] Growing interest in this direction is justified by the possibility to fabricate functional materials with emerging properties with respect to the bulk, exploiting the peculiar features of metal complexes. In this framework, square planar Pt(II) compounds containing π-conjugated ligands, thanks to the presence of protruding occupied $d_{z^2}$ orbitals, show a high tendency towards stacking *via* Pt···Pt and/or ligand-ligand interactions. To date, different homo-[29] and hetero-metallic[30] supramolecular architectures have been reported, either in organic or aqueous media, which present very appealing (electro)optical,[28d,31] sensing[32] and semiconducting properties.[33] The rich variety of reported supramolecular architectures ranges from pseudo-0D structures like micelles, to 1D arrays (i.e. nanowires,[34] nanotubes[35] and liquid crystals[36]), to 2D layers (i.e. nanosheets and nanowheels) and up to 3D networks (i.e. metallogels[37]). As consequence of the complex square-planar geometry, 1D-fibrils are certainly the most commonly observed form; their bundling into entangled 3D networks leads, in some cases, to the formation of supramolecular gels.[28c,38] Their anisotropic growth suggests that molecular propagation is faster along the Pt···Pt axis than in the lateral direction.[39] Moreover, recent evidences of a cooperative growth mechanism[40] for Pt(II) complexes explains the formation of highly organized aggregates with well-defined size, shape and properties. Changes in the microenvironment, such as temperature, solvent or counterions, can significantly affect the resulting self-assembled architectures, because of the weak and non-covalent nature of Pt···Pt interactions. In addition, complete control over the assembling/disassembling behaviour of building blocks

through external stimuli can be achieved by the incorporation of stimuli-responsive groups.[41] As stated above, dramatic changes in the spectroscopic properties upon the establishment of Pt···Pt interactions can be considered as a fingerprint and thus act as a probe for dynamic transformations of the supramolecular assemblies.[38b,42] Chan *et al.*[43] reported an interesting example of how colour changes can be used to monitor the self-assembling process, by employing synthetic helical polyacetylene to induce the aggregation of alkynylplatinum (II) terpyridyl complexes *via* electrostatic, metal···metal and ligand π-π stacking interactions. This latter case highlights how, besides the more conventional sensitivity to pH or solvents, positively charged Pt(II) complexes interact with (bio-)polymers carrying multiple negatively charged functional groups[44] or biologically relevant biomolecules, thus allowing to monitor enzymatic activities.[45] Significant enhancement in the circular dichroic signal revealed that even oligonucleotides interact with Pt(II) complexes, resulting in a stabilization of the helical conformation through Pt···Pt and π-π interactions.[28a] Among all reported alkynylplatinum(II) complexes, those bearing an amphiphilic anionic bzimpy (2,6-bis(N-alkylbenzimidazol-2'-yl)pyridine) as terdentate ligand, have shown particularly interesting properties displaying an aggregation-partial disaggregation-aggregation process driven by the variation of the solvent composition. The use of amphiphilic moieties typically leads to the formation of highly ordered structures featuring a peculiar morphology, due to the differential interaction of the hydrophilic and hydrophobic part with the solvent (Figure 3.3).[46] The observed conversion from vesicles to nanofibers, systematically controlled by solvent composition, can be readily probed *via* UV-Vis absorption, emission, NMR, TEM and even with naked eyes. At high water content, indeed, pseudo-0D micellar structures, displaying a broad featureless emission band around 675-683 nm related to the $^3$MMLCT band of ground-state Pt···Pt interactions, are observed. Upon addition of acetone to the water solution, a dramatic colour change was detected; moving from 100% of water to 1:1 and finally 9:1 acetone: water ratio, variations from red to yellow to blue occurred.

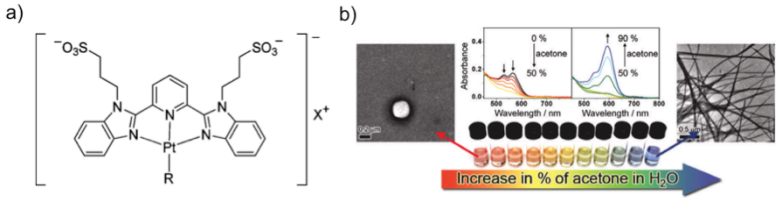


**Figure 3.3** *a) Structure of the complex and b) correlation between the morphology and the spectroscopic properties by varying solvent composition in the complex solution.*[46]

Spectroscopic changes were attributed to the variation of the low-lying $^1$MMLCT absorption bands; in particular, the drop of the bands at 532 and 564 nm, upon increasing the acetone content, were explained as a partial disaggregation with disruption of Pt···Pt and π-π interactions. SEM and TEM images correlated unambiguously the change of the spectroscopic properties with a neat variation in the morphological features of the aggregates in solution. In water, charged sulfonate groups are expected to point towards the solvent, while hydrophobic Pt(bzimpy) moieties are forced to pack together forming bilayer structures like vesicles. By increasing the content of acetone, which is expected to solvate the ligand conjugated core, the complexes are well dispersed, thus leading to a drop of the $^1$MMLCT absorption band. Finally, as the acetone content is further increased at a concentration above 50%, the sulfonate groups are no longer well solvated by the organic solvent; aggregation of the ionic heads, thus, pulls the complexes in close proximity, promoting the formation of nanofibers and nanorods. The appearance of this second aggregated form results in a new $^1$MMLCT band at lower energy. Furthermore, a systematic study[47] pointed out the significant influence that structural characteristics play on the self-assembling properties. In particular, the introduction of alkyl chains of different length on a series of amphiphilic sulfonate-pendant Pt(II) bzimpy complexes was found to exert a severe effect on the molecular packing and thus on the resulting spectroscopic properties. The definition of a packing parameter allowed the rationalization of the morphological variations in terms of an increase in the hydrophobicity of the complexes along with the length of the alkyl chain. Besides the functionalization with ionic heads, another widely adopted strategy to confer amphiphilicity is based on the incorporation of neutral triethylene glycol (TEG) chains into the Pt(II) bzimpy scaffold. Also in this case, Yam *et al*. observed a severe correlation between structural features and aggregation tendency.[48]

Despite the pronounced similarities between the two investigated amphiphilic complexes, which differ only by the relative position of the TEG and dodecyl alkyl chains, only compound **1** resulted in being water-soluble (Figure 3.4). More interestingly, an unusual thermo-responsive behaviour was observed; UV-Vis absorption studies, performed over multiple heating-cooling cycles, revealed a counterintuitive enhancement of the $^{1}$MMLCT absorption and $^{3}$MMLCT emission bands at higher temperature.

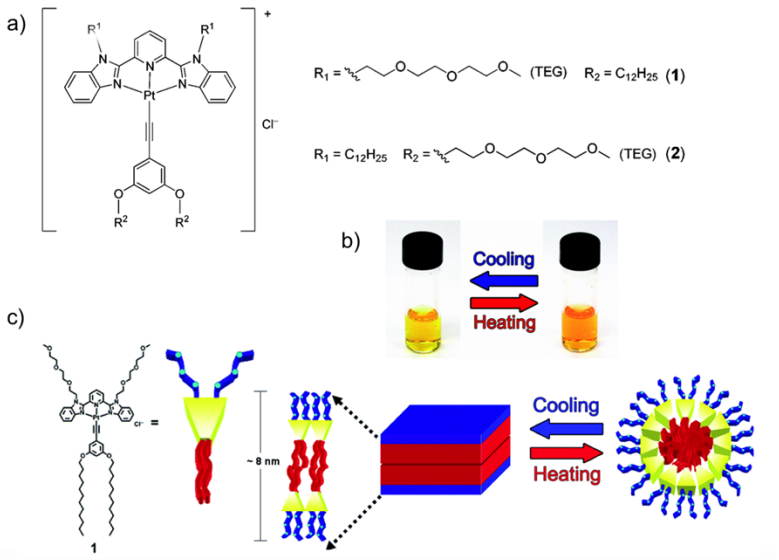


**Figure 3.4** *a) Structure of the investigated complexes; b) Photographs of the aqueous solution of* ***1*** *at room temperature after cooling and heating and c) Schematic diagram showing the formation of the bilayer sheet and micelle of* ***1****.*[48]

This observation, contradictory to the common findings by which heating should favour the disruption of Pt···Pt interactions, pointed towards an interconversion between two distinct states in different temperature regimes, namely micellar *vs.* bilayer structure. Soft nanomaterials based on phosphorescent organoplatinum(II) complexes have been also obtained by combining metallophilic interactions with ionic self-assembly. Chen *et al.*[49] reported a series of cationic Pt(II) complexes salts which become soluble in non-polar solvents upon switching the counter-ion to a highly lipophilic anion; novel spectroscopic features observed in non-polar solvents have been used to distinguish monomeric from oligomeric species. Interestingly, drop casting of a

dilute $CH_2Cl_2$ solution onto a $SiO_2$ wafer results in extended honeycomb mesostructures assembled through metallophilic and ionic self-assembly (Figure 3.5).

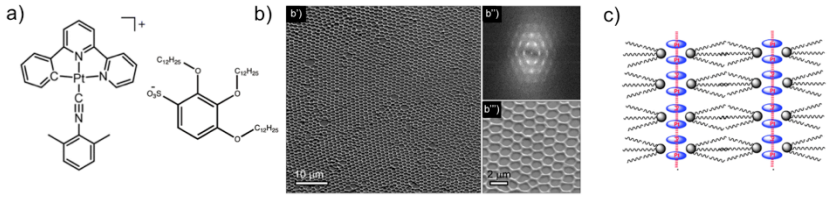


**Figure 3.5** *a) Molecular structure of the investigated complex; b) SEM micrograph (b') and its corresponding fast Fourier transform image (b'') of the honeycomb pattern onto the silicon wafer; amplified SEM micrograph (b''') and c) proposed molecular packing.*[49]

Chiral supramolecular architectures such as helicoidal fibers[50] and metallogels[51] can be obtained through the incorporation of chiral moieties on the building block structure. Yi and co-workers[52] reported several amphiphilic alkynylplatinum(II) complexes bearing cholesterol groups and ethylene glycol chains with different length. Besides a common tendency to self-assemble into gel networks in DMSO, the complex bearing the longer chain shows an interesting solvent-dependent chiral switching. In aqueous ethanol solution, at $H_2O$ content below 5% (v/v), perfect regular left-handed helical structures are formed; by increasing the $H_2O$ ratio, chirality moves from a left-handed to a right-handed helix, together with a variation of the packing mode from a monolayer to a hexagonal structure. A further increase of the $H_2O$ content above 50% (v/v) causes a final transformation into bilayer vesicles, with a subsequent loss of the CD signal. Observed results suggest that a polar solvent like $H_2O$ acts as a trigger to change the morphology of the system on the basis of a delicate balance between hydrophobic and hydrophilic interactions.

A deeper and systematic investigation about the structural dependence of the photophysical properties for Pt(II)-based complexes was performed by De Cola *et al.*[53] A series of cationic complexes was reported, where the variation of the substitution pattern on the tridentate triazole moieties and the nature of the ancillary ligand were exploited to tune the intermolecular interactions and, therefore, the degree of electronic overlap between the metal centres (Figure 3.6). While compounds bearing a $Cl^-$ ancillary ligand displayed no photoluminescence at room temperature, $CN^-$ based complexes, due to the π-accepting nature of the ligand, revealed a strong tendency to aggregate,

irrespectively of the bulk substitution pattern on the tridentate moiety. In particular, as displayed in Fig. 3.6, the choice of bulky adamantyl or planar phenyl substituents led, respectively, to non-luminescent rod-like structures or to luminescent square-shaped platelets.

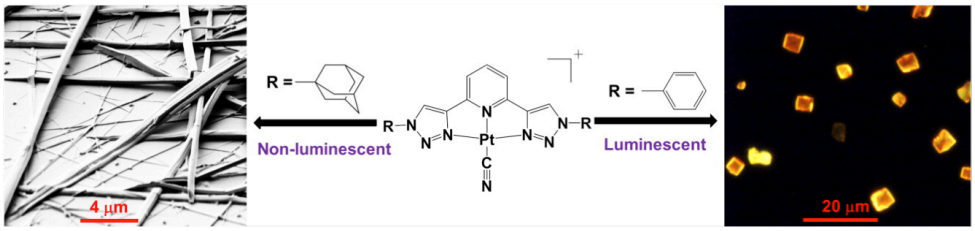


**Figure 3.6** *Effects of the functionalization of the triazole ligands on the morphological and luminescence properties of the resulting self-assembled structures.*[53]

The same group reported a straightforward one-pot synthetic strategy to afford triplet emitter Pt(II) complexes bearing a dianionic terpyridine-like ligand.[54] Replacement of 1,2,3-triazolyl moieties with 1,2,3,4-tetrazolyl rings, together with the use of an alkyl pyridine ancillary moiety, results in neutral and soluble coordination compounds displaying a PLQY up to 87% in thin films. Their high stacking tendency can be exploited to induce the formation of 1D fibrils, which often bundle into entangled 3D networks like highly emissive supramolecular gels (PLQY up to 90%). The nature of the alkyl functionality onto the pyridine ancillary ligand usually plays a non-innocent role in tuning the self-assembly properties of Pt complexes. Control on the aggregation degree in polar solvents was indeed obtained by the introduction of a tetraethylene glycol (TEG) chain;[55] the resulting complex displayed the reversible formation of highly luminescent gels either in $CH_2Cl_2$ or DMF with solvent-dependent photophysical and morphological properties. Metallogel formation was observed in $CH_2Cl_2$ solution when the critical gelating concentration was reached; the so-formed supramolecular architectures collapsed into sol simply by shacking or sonication. By contrast, thermal treatment can be used to induce the formation or collapse of the DMF gel (Figure 3.7).

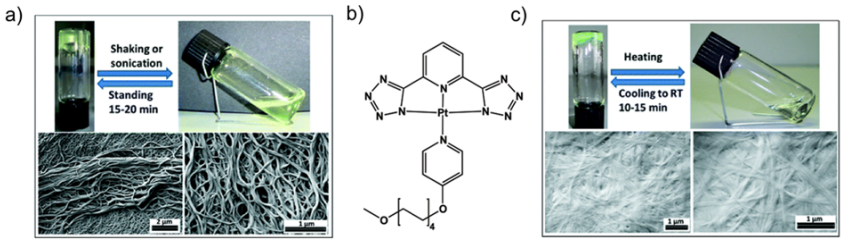


**Figure 3.7** *a) Reversible gelation process in $CH_2Cl_2$ and corresponding SEM images; b) molecular structure of the Pt(II) complex; c) reversible gelation process in DMF and corresponding SEM images.*[55]

Both gels are photoluminescent under UV excitation, whereas the corresponding sols are not emissive in the same conditions. Interestingly, the different PLQY values of 7.5 and 60% measured, respectively, for the $CH_2Cl_2$ and DMF gel, were attributed to the different efficiency in the solvation of the polar TEG tail and the apolar chromophoric part. In apolar $CH_2Cl_2$, indeed, stronger metallophilic interactions are expected, while the polar chains entangle to minimize the solvent exposure. On the other hand, in DMF, Pt···Pt interactions are weaker because of the effective solvation of TEG tails, which prevents a closer approach of the metal centres. As a consequence, TEG chains adopt an alternating configuration that favours a longer-range order, thus increasing the emission quantum yield. To amplify the amphiphilic character of the complex, a second TEG chain was added to the ancillary ligand;[56] increased water solubility of the resulting compound thus led to the formation of assemblies in concentrated water solutions, rather than the usual gelating network. Gelation can be induced *via* addition of cyclodextrins (CDs), thanks to the establishment of host-guest interactions between the TEG chains of the complex and the CD hydrophobic cavity.

From all the reported examples, it is easy to understand that the use of square planar Pt(II) complexes as building blocks for highly luminescent self-assembled architectures has been widely investigated in literature. Furthermore, a proper molecular design of the ligands, either in terms of bulkiness or electronic properties, allows a fine morphological tuning of the resulting structures, thus leading to a direct modulation of their photophysical features. This, in combination with their sensitivity to external stimuli, clearly justifies their use in a wide range of applications.

### 3.1.3 Mechanocromic properties of platinum(II) complexes

Research on stimuli-responsive materials is essentially driven by the development of artificial systems that can dynamically interact with the surrounding environment with steadily increasing efficiency and sensitivity. The specific *input* and *output* of the system, namely the external stimulus and the material property subject to change, play a crucial role in determining the field of application and the efficiency of the system. In this regard, square planar Pt(II) complexes, whose absorption and emission profile dramatically changes in response to a variety of stimuli, can represent an interesting alternative to purely organic dyes. Besides the more conventional sensitivity upon exposure to volatile organic compounds,[57] responsiveness to mechanical stimuli such as grinding, scraping or compression,[58] has been reported. Even if both absorption and emission colours are excellent signal candidates for sensing applications, luminescence overcomes absorption by several orders of magnitude in terms of sensitivity, becoming the signal of choice when miniaturization is required. As stated above, the interest on Pt(II) complexes as mechanochromic materials relies on the tunability of their emission spectrum as a function of the distance between metal centres. The establishment of metallophilic interactions for a Pt···Pt distance below 3.5 Å, indeed, triggers an energy levels splitting and the rise of a new $^3$MMLCT band. This change in the MO diagram is reflected in the emission spectrum with the appearance of a broader, unstructured band, while the structured band attributable to the $^3$MLCT transition disappears. This sharp transition clearly provides an efficient *ON-OFF* switch with a strong, ratiometric signal falling in the visible range. Furthermore, tuning the Pt···Pt distance within the value of 3.5 Å leads to a smoother transition in the emission profile; in particular, a continuous bathochromic shift of the $^3$MMLCT band is observed, which allows the discrimination of aggregates with different morphology. Among the large amount of reported examples describing the mechanochromic response of Pt(II) complexes in the bulk phase, we can cite the contribution of Ni and co-workers,[59] whose square planar diimine-Pt(II) complex, Pt(4-Brbpy)(C≡C$C_6H_5$)$_2$ (4-Brbpy = 4-bromo-2,2′-bipyridine), exhibited concurrent, naked eye perceivable and reversible colour and luminescence changes in response to heating and mechanical grinding. Spectroscopic characterization displayed, upon grinding, the typical transition from a structured band to an unstructured broad emission, reflected by a crystalline-to-amorphous state transition (Figure

3.8). Interestingly, the size of the observed redshift for the broad emission band is different upon mechanical or thermal treatment, being respectively of 165 and 100 nm. This result suggests how the distance between metal centres in the final amorphous state strongly depends on the way energy is delivered to the crystalline powder and confirms that mechanical grinding is able to force Pt centres in closer proximity. In both cases, exposure to solvent vapours restores the original state.

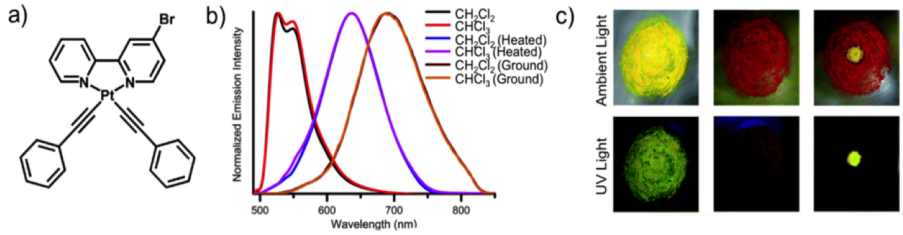


**Figure 3.8** *a) Molecular structure of the Pt(II) complex; b) Solid-state emission spectra of crystalline sample from $CH_2Cl_2$ (black) and $CHCl_3$ (red), together with the corresponding heated (blue for $CH_2Cl_2$ and magenta for $CHCl_3$) and ground species (wine for $CH_2Cl_2$ and orange for $CHCl_3$); c) Photographs of the complex under ambient and UV light irradiation (365 nm) showing the colour changes from yellow-green to red upon grinding and in the reverse process on addition of $CH_2Cl_2$.*[59]

Systematic investigations highlighted the strong dependence of mechanochromism from structural features such as the nature of the counter anion[60] or the bulkiness of ligand substituents.[61] Swager *et al*. reported a cationic Pt(II) complex that displays a thermotropic columnar liquid crystalline behaviour with hexagonal packing.[62] Observed liquid crystallinity was attributed to sizeable intermolecular Pt···Pt interactions and enhanced dispersive forces due to distortions from square planarity. Once more, interconversion between the two distinct polymorphs identified in the crystal form can be promoted *via* mechanical grinding, heating or solvent exposure. To further probe metallophilic interactions, the complex was doped into four different polymeric matrices (concentrations ranging from 6 to 8% w/w relative to the polymer). Films of polystyrene (PS), polyethylene oxide (PEO), poly(methyl methacrylate) (PMMA) and poly(4-vinylpyridine) (P4VP) were prepared by spin-coating. In PS and PEO, which act as inert hosts, the complex exhibits red emission, while in PMMA an incomplete aggregation was observed. P4VP films, by contrast, primarily display green emission and well-defined vibrational splitting patterns, indicating the presence of monomeric

species. The lack of aggregation in the latter case can be likely attributed to a non-innocent role played by the matrix, whose pyridyl groups coordinate to the metal centres, preventing intermolecular interactions (Figure 3.9).

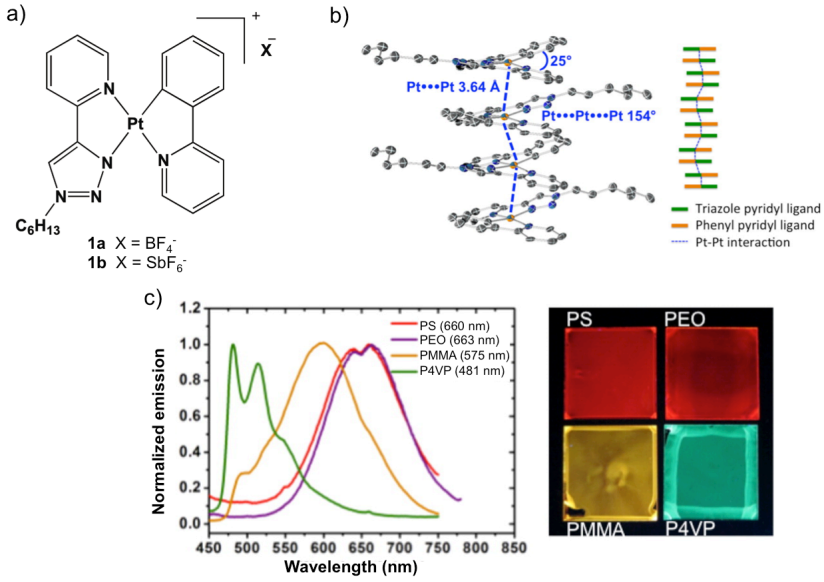


**Figure 3.9** *a) Molecular structure of the investigated Pt(II) complexes; b) Crystal structure packing and stacking orientation for **1a**; c) Solid-state emission spectra of polymer films doped with **1b** and film colour contrast observed under UV irradiation (365 nm).*[62]

This example, apart from being a further demonstration of the dependence of spectral features from the aggregation degree, represents a key step for practical application of Pt complexes as responsive materials. Embedding into a polymer matrix is compulsory for exploiting their peculiar properties in the realization of sensors or memory devices. Methacrylates resulted particularly convenient for the preparation of mechanically stable and responsive films. Furthermore, the possibility to tune the $T_g$ of the polymer according to the monomer composition allowed investigating the role of matrix properties on the responsiveness. Notably, both vapochromic and mechanical response resulted stable for high $T_g$ polymers [i.e. poly(methyl methacrylate $T_g \approx 90$ °C)] and only temporary for a $T_g$ close to room temperature [i.e. poly(butyl methacrylate $T_g \approx 30$ °C)]. Blends prepared with matrices with $T_g$s well above

room temperature showed only a slight reversal after 24 h; heating the matrix, however, gave an immediate recovery to the initial state. Analogously, attempts to stress the films above $T_g$ gave no observable response, due to the tendency of the polymer to flow, absorbing and dissipating the mechanical energy conveyed for structural rearrangements of the Pt(II) complexes.[63]

Chen *et al*.[64] described a device that can be considered as a multi-state logic gate displaying a vapo-, thermo- and mechano-triggered responsiveness. In this case, apart from the typical *ON-OFF* signal due to the transition from absence to presence of metallophilic interactions, Pt(II) complexes bearing 4-trifluoromethylphenylacetylide ligands (Figure 3.10), dispersed in PMMA films, showed additional transitions between structures with different Pt···Pt distances.

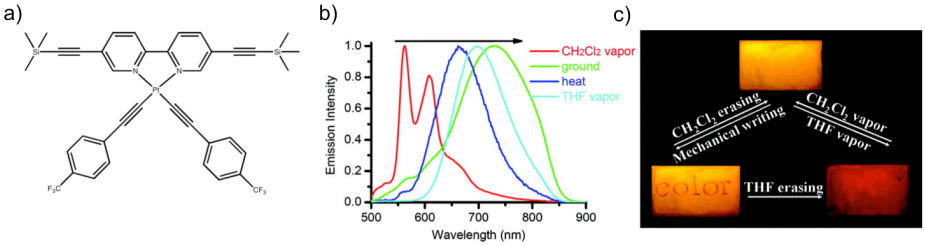


**Figure 3.10** *a) Molecular structure of the Pt(II) complex; b) Solid state emission spectra upon different stimuli; c) Photographic images of doped PMMA films in response to $CH_2Cl_2$ vapour or mechanical stimuli under UV irradiation (365 nm).*[64]

Control over these well-defined aggregation states was achieved through the inclusion of different VOCs in the crystal structure. In particular, solid-state sample was selectively sensitive to the vapours of oxygen-containing VOCs such as THF, dioxane or tetrahydropyrane (THP), exhibiting vapochromic phosphorescent response. The emission wavelength red shifted from 561 and 608 nm to 698 nm (THF), 689 nm (dioxane) and 715 nm (THP). Photographic images of the films showed remarkable luminescence colour switches under UV light irradiation.

Kanbara and co-workers[65] studied the photophysical properties of a series of pincer Pt(II) complexes bearing amide groups. In this case, an interesting two-step luminescence colour change from green to yellow to orange was observed in the solid state. Responsiveness is driven by the establishment of different hydrogen-bonding networks with solvent molecules such as DMF and MeOH; these interactions are clearly reflected in different molecular orientations and, consequently, in different Pt···Pt distances in the crystals.

Overall, the capability to dynamically tune metallophilic interactions in Pt(II) complexes at the solid state represent an efficient tool for achieving stimuli-responsive materials with optical read-outs.

### 3.1.4 Platinum(II) complexes for cellular bio-imaging

Beyond the aforementioned uses in the field of material science, Pt(II) complexes have been extensively studied for applications in biology. These applications, however, are almost exclusively represented by cancer therapies; thus, the use of TMCs for sensing of bio-related molecules and as luminescent labels for bio-imaging is relatively new, compared with their organic and bio-organic counterparts. Nevertheless, TMCs, apart from the wide emission colour tunability, conjugate a high photo- and chemical stability with large Stokes shifts and long-lived excited states. Some examples of luminescent Pt(II) complexes able to enter living cells and, in some cases, to selectively stain specific compartments[66] have been reported. Williams *et al*.[67] showed the use of highly emissive and photostable Pt(II) complexes for bio-imaging, exploiting a combination of confocal one-photon excitation or non-linear two photon excitation (TPE) with time-resolved emission imaging microscopy (TREM). The long lifetime of the Pt(II) complex (up to μs) allows to eliminate any short-lived background fluorescence, while lifetime mapping can be used to image live cells and tissue section. Furthermore, emission lifetime was found to vary by more than a factor of 20 depending on the location, ranging from 300 ns in the membrane to 2 μs in the cytoplasm up to 4 μs in the nucleus. Such differences were explained with an increasing shielding of complex luminescence from oxygen quenching.
Yam and co-workers[68] reported an interesting example about the use of Pt(II) complexes as dynamic labels for cell imaging based on the exploitation of their self-assembly properties. The reversible aggregation of a water soluble alkynylplatinum(II) terpyridine complex upon pH changes in physiological conditions allowed a "switch on" of the emission in the NIR region (Figure 3.11). At pH between 3.5 and 5.6, indeed, an intense $^3$MMLCT emission is observed; above 5.6 the deprotonation of the phenolic moiety increases the hydrophilicity of the complex, leading to its de-aggregation in aqueous

medium. Consequently, a significant drop in the emission intensity was detected.

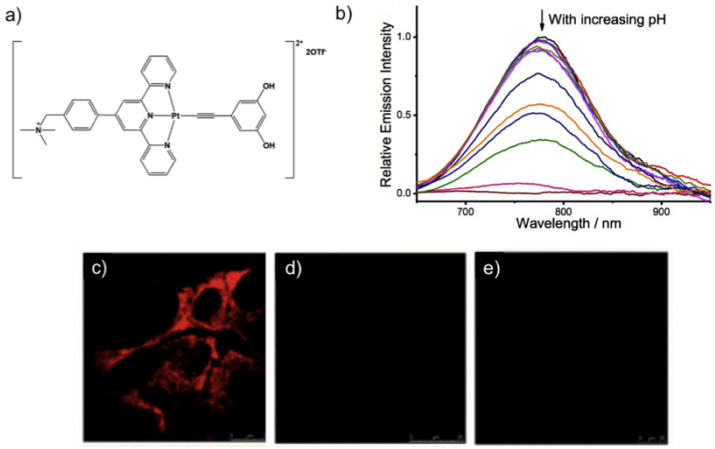


**Figure 3.11** *a) Molecular structure of the Pt(II) complex; b) Emission spectra of the complex in aqueous solution at variable pH ($\lambda_{exc}$ = 480 nm); Confocal microscopy images of fixed MDCK cells incubated with 20 μM of the complex followed by incubation with buffer solutions at different pH: 5.72 (c), 6.75 (d) and 7.80 (e). $\lambda_{exc}$ = 488 nm.*[68]

Besides the interactions with healthy cells, Pt(II) complexes have been employed also for targeting cancer cells, either in terms of bio-imaging[69] or in terms of therapeutic applications.[70] Traditionally, interactions with cells are investigated in the context of two-dimensional (2D) environments, despite many evidences suggest that cells cultured on conventional flat substrates often tend to adopt non-natural behaviours.[71] Thus, the use of three-dimensional (3D) cell culture platforms closer to biological systems could allow more realistic cell proliferation during *in vitro* analyses; in this regard, hydrogels have been successfully employed to support cell growth, since their cross-linked hydrophilic network nicely mimics the extracellular matrix. In this framework, research efforts aim not only to develop proper scaffolds for cell proliferation, but also to provide a direct, real-time visualization of living cells growth on 3D platforms. Since the use of dyes as stains can induce a significant alteration of the natural cell cycle, the possibility to achieve a visualization of living organisms in the absence of internalized dyes is extremely appealing.

### 3.1.5 Hybrid PAAs hydrogels

Hydrogels are 3D polymer networks made of cross-linked hydrophilic chains, displaying the ability to swell, without dissolution, by absorption of up to thousands of times their dry weight in water.[72] Since their introduction in 1960,[73] thanks to the pioneering work of Lim *et al*., hydrogels have attracted a steadily rising attention in the biomedical[74] and tissue engineering fields.[75] This interest essentially relies on their biocompatibility, high water content, tissue-like elastic properties and 3D porous structure, which make them more similar to natural living tissue than any other class of synthetic biomaterials. Over the last decades a wide range of scaffolds have been investigated, with the aim to tailor the properties of the resulting hydrogel for different applications. In this regard, polyamidoamines (PAAs), thanks to their low cytotoxicity and extreme versatility, seem to be promising candidates. Firstly introduced by Danusso and Ferruti in 1970,[76] PAAs have been initially studied in the form of linear polymers and dendrimers as soluble bioactive scaffolds. The synthetic network is obtained *via* stepwise aza-Michael polyaddition of primary or secondary aliphatic amines to bis-acrylamides, leading to a structure characterized by amido and tertiary amino groups regularly arranged along the polymer chain.

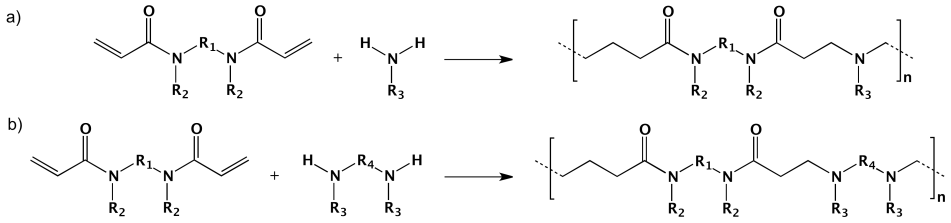


**Figure 3.12** *Traditional synthesis of linear PAAs with (a) primary and (b) secondary amines.*[77]

As anticipated, their versatility is translated into the possibility to introduce different functional groups as side substituents, while their excellent biocompatibility is confirmed by the fact that, for some structures, they display a consistently lower cytotoxicity than poly-L-lysine.[78] The use of a multifunctional monomer during the polymerization gives cross-linked networks, displaying the typical massive swelling of hydrogels upon water absorption. Despite the potential of these 3D scaffolds for biomedical applications emerged relatively late, several examples about their use as substrates for *in vitro* neuronal cell culturing[79] or drug delivery[80] suggest

extremely fascinating perspectives yet to come.

De Cola and co-workers reported the use of a PAAs-based hydrogel decorated with switchable chromophores as a 3D bio-imaging platform for real-time visualization of cell proliferation, without the need for additional staining.[81] In particular, they presented an hybrid PAA-based hydrogel obtained *via* aza-Michael reaction between γ-aminobutyric acid (GABA) and N,N'-methylene bisacrylamide (MBA) together with pentaethylenehexamine (PEHA) as cross-linker. The use of GABA as co-monomer, which is a common neurotransmitter in neuronal cells, was proven to be beneficial in terms of cyto-compatibility.[82] Indeed, the presence of carboxylic functionalities as side-chain groups leads to an increased hydrophilicity and water uptake ability of the scaffold through additional hydrogen bonding. The resulting amphoteric structure, containing amide, amine and carboxylate groups in regular sequence, can be somehow considered as a protein-like synthetic material. Covalent grafting of a luminescent Ir(III) complex, conveniently equipped with a terminal amine moiety, was achieved through a conventional 1,4-addition to MBA. The resulting optically transparent, porous Ir-PAA hydrogel showed a bright red emission in its dry state, while no luminescence was detected in the water-equilibrated sample, as effect of the turn on/turn off behaviour of the embedded Ir(III) complex in response to the different environment. Viability studies with cervical cancer cells, HeLa, were performed and confirmed the high cyto-compatibility of the hybrid scaffold. Furthermore, the red emission detected throughout cells plasma membrane allowed a real-time, 3D live cell imaging (Figure 3.13).

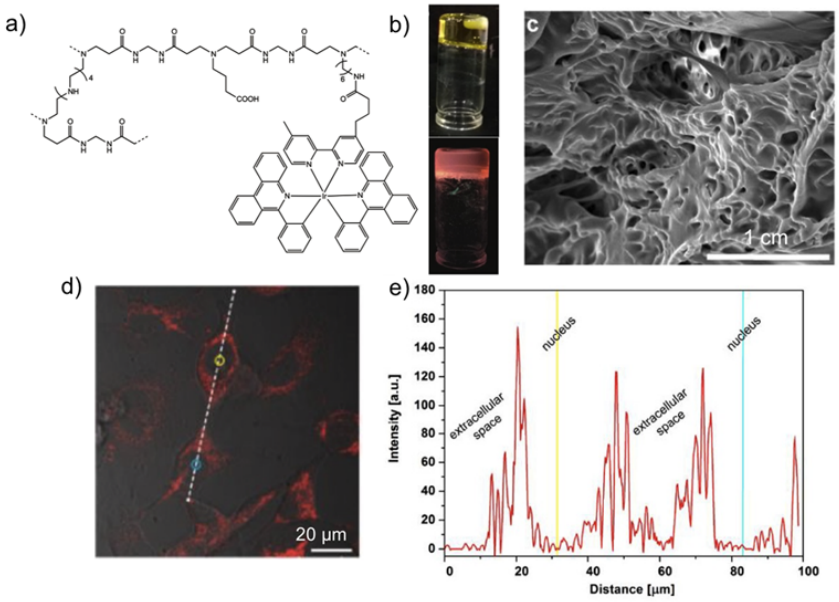


**Figure 3.13** *a) Chemical structure of the Ir-PAA; b) 'Inverted vial' test for dry hydrogel under visible light and UV irradiation; c) SEM image showing the porous morphology; d) Confocal image of living HeLa cells on Ir-PAA after 96 h; e) Luminescence intensity profile across the line shown in (d) corresponding to extracellular region, membrane and nuclear region (yellow and blue circles and lines) of two cells.*[81]

Considering the success of the reported approach, we investigated the possibility to move from an *OFF/ON* responsiveness of the system to a finer modulation of the emission; the use of Pt(II) complexes, whose luminescence is strongly affected by even slight variations of their environment, could represent a sound alternative. Furthermore, relying on the dramatic drop of the emission upon de-aggregation, we studied the possibility to covalently incorporate Pt(II) complexes into polymeric matrices for the realization of mechanochromic materials.

## 3.2 Results and discussion

An hybrid PAA-based hydrogel with pendant Pt(II) complexes was designed, in order to exploit the peculiar responsiveness of the luminescent probe for cellular bio-imaging. Analogously to the Ir(III)-PAA hydrogel described above, the presence of a terminal amino group is required to guarantee the covalent grafting of the Pt(II) complex to the PAA network. The designed target compound **1**, depicted in Fig. 3.14, consists of a square planar Pt(II) complex bearing a 2,6-bis(3-(trifluoromethyl)-1H-1,2,4-triazol-5-yl)pyridine (py-$CF_3$-trz) tridentate ligand and a pyridine ancillary ligand equipped with the required anchoring site.

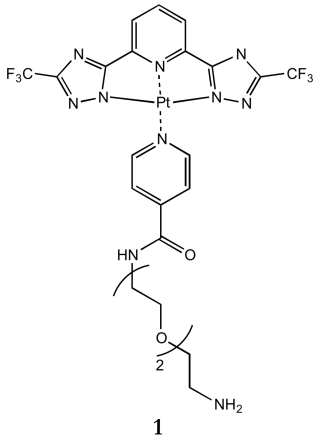


**1**

**Figure 3.14** *Chemical structure of the designed target molecule **1**.*

The use of a long triethylene glycol (TEG) spacer has a twofold advantage: on the one side, it ensures the solubility of the complex in MeOH, which is, together with $H_2O$, one of the solvents currently used for PAA gelation. Furthermore, it provides enough spacing between the metal core of the complex and the polymeric backbone of the resulting material, thus allowing the establishment of Pt···Pt interactions. The adopted synthetic strategy foresees a convergent approach; coordination of the pre-functionalized pyridine ligand to a highly reactive Pt(II) precursor by replacement of a labile DMSO ligand afforded compound **1** under very mild conditions. Deprotection under acid conditions provided the required amino group; the resulting Pt(II) complex can act as a co-monomer in the aza-Michael poly-addition together with MBA, GABA and PEHA as cross-linker.

### 3.2.1 Synthesis of amino-functionalized Pt(II) complex

De Cola and co-workers[83] reported a highly reactive Pt(II)-DMSO precursor as a convenient starting point to achieve a wide range of luminescent complexes; simple exchange of the labile DMSO ligand occurs under very mild conditions, in contrast with common synthetic protocols where a strong base and a pyridine derivative are reacted for 12-18 h at high temperature. The synthesis of the Pt(II)-DMSO precursor has been performed, according to literature procedure, starting from the commercially available 2,6-pyridinedicarbonitrile. Pyridine-2,6-bis(carboximidhydrazide) **2** is obtained in almost quantitative yield upon reaction with hydrazine monohydrate in ethanol at room temperature. Condensation with trifluoroacetic anhydride in diethylene glycol dimethyl ether and subsequent reaction with aqueous HCl at 90 °C afforded the 2,6-bis(1H-1,2,4-triazol-5-yl)pyridine tridentate ligand **3** in good yield.

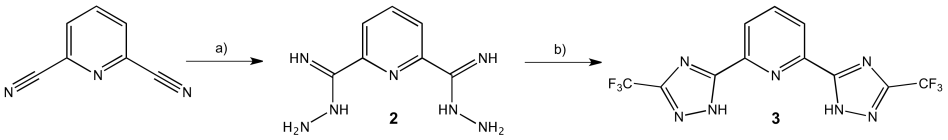


**Scheme 3.1** *Synthesis of the tridentate ligand* ***3****: a)* $NH_2NH_2{\cdot}H_2O$*, EtOH, r.t., 3 d, 98%; b)* $(CF_3CO)_2O$*, diethylene glycol dimethyl ether, r.t., 10 min → 1 h, reflux; then* $HCl_{aq}$*, 90 °C, 12 h, 74%.*

The straightforward coordination of **3** with $Pt(DMSO)_2Cl_2$ in DMF at 75 °C for 12 h afforded precursor **4** in 64% yield.

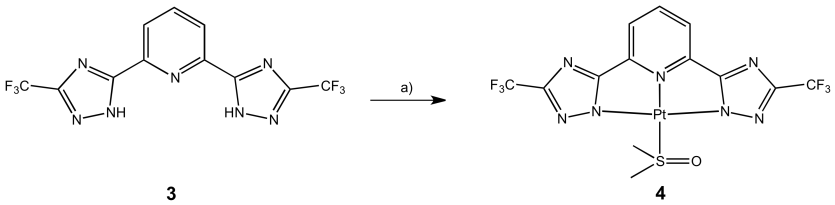


**Scheme 3.2** *Synthesis of the Pt-DMSO precursor* ***4****: a)* $Pt(DMSO)_2Cl_2$*, DMF, 75 °C, 12 h, 64%.*

Pyridine ancillary ligand bearing Boc-protected amino group was obtained *via* a 3-steps convergent synthesis (Scheme 3.3); reaction with N-hydroxysuccinimide (NHS), starting from commercially available isonicotinic

acid, afforded activated ester **5**. Condensation of **5** with mono-protected 1,2-bis(2-aminoethoxy)ethane gave functionalized pyridine ligand **7** in 43% yield.

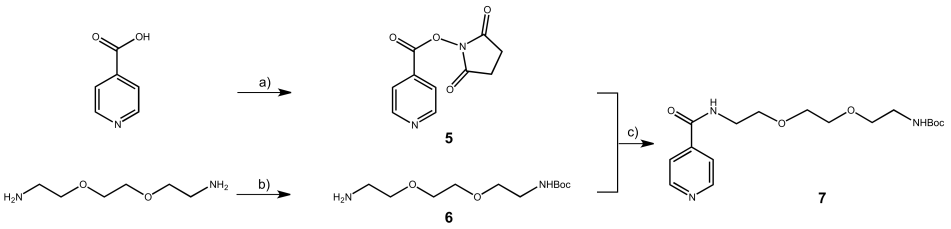


**Scheme 3.3** *Synthesis of Boc-protected pyridine ligand* **7***: a) NHS, N-(3-dimethylaminopropyl)-N'-ethylcarbodiimide hydrochloride, DMF, r.t., 12 h, quantitative; b) Di-tert-butyl carbonate, $CH_2Cl_2$, r.t., 12 h, 62%; c) $Et(iPr)_2N$, DMF, r.t. 12 h, 43%.*

Finally, coordination of Boc-protected pyridine ligand on the highly reactive precursor **4**, followed by deprotection under acid conditions, afforded luminescent complex **9** in 56% overall yield (Scheme 3.4). Low yield is due to troublesome purification.

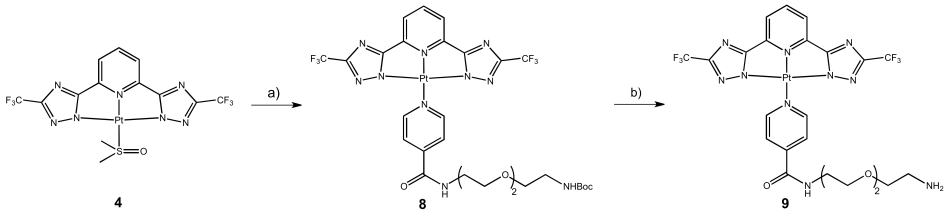


**Scheme 3.4** *Synthesis of the amino-functionalized complex* **9***: a)* **7***, $CH_3CN$, r.t., 12 h, 56%; b) trifluoroacetic acid, $CH_2Cl_2$, r.t., 2 h, quantitative.*

$^1$H and $^{19}$F NMR spectroscopy confirmed the success of the adopted synthetic protocol. Spectroscopic characterization of compound **9** displays the typical behaviour that characterizes amphiphilic square planar Pt(II) complexes. As shown in Fig. 3.15, when **9** is molecularly dissolved in a good solvent like 1,4-dioxane, a weak blue emission is detected, attributable to an excited state with mainly a triplet ligand centred ($^3$LC) character. Flash injection of the 1,4-dioxane solution of **9** (c = $10^{-3}$ M) in water (dioxane: water ratio 5: 95) leads to a dramatic change in both absorption and emission spectra; in particular, the rise of a strong orange phosphorescence ($\lambda_{em}$ = 610 nm) was detected.

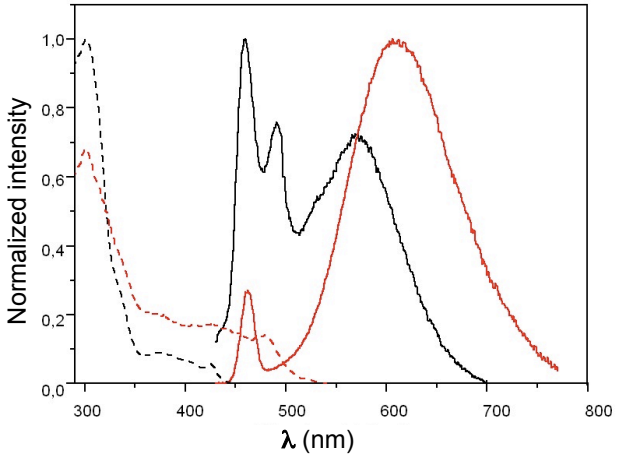


**Figure 3.15** *Excitation (dashed lines) and emission spectra (solid lines) of complex* ***9*** *in 1,4-dioxane (c = 10-4 M, black lines) and after flash-injection in water (c = 10-4 M, 95% water content, red lines).*

Previous investigations[84] through dynamic light scattering and SEM analyses revealed the formation of soft nanoparticles with a relatively narrow distribution. In these aggregates, induced by injection in a non-solvent like water, hydrophilic TEG chains are expected to point towards the highly polar medium and be solvated by water molecules, while hydrophobic effect forces the metal centres to tightly pack in the inner core of the assembly *via* establishment of metallophilic interactions.

Preliminary studies of cytotoxicity and cell internalization were performed on complex **8** with protected amino group, being closest to the final system, where the anchoring site is part of the polymer backbone in the PAA hydrogel. Cell viability was evaluated through MTT assay based on the reduction of yellow tetrazolium MTT [(3-(4, 5-dimethylthiazolyl-2)-2,5-diphenyltetrazolium bromide)] by metabolically active cells; quantification of formed intracellular purple formazan by spectrophotometric means provides a reliable way to determine cell proliferation. (Details about internalization and viability studies are reported in the Experimental Section). Compound **8**, dissolved in a minimum amount of DMSO, was diluted in phosphate buffer saline (PBS) to obtain a 30 μM solution (final DMSO content below 1%). HeLa cells were cultured in 2D and incubated at 37 °C with the complex solution; confocal laser scanning microscopy (CLSM) confirmed the internalization of the luminescent

compound and displayed a progressively increasing yellow emission coming from cellular compartments upon excitation at 400 nm (Figure 3.16).

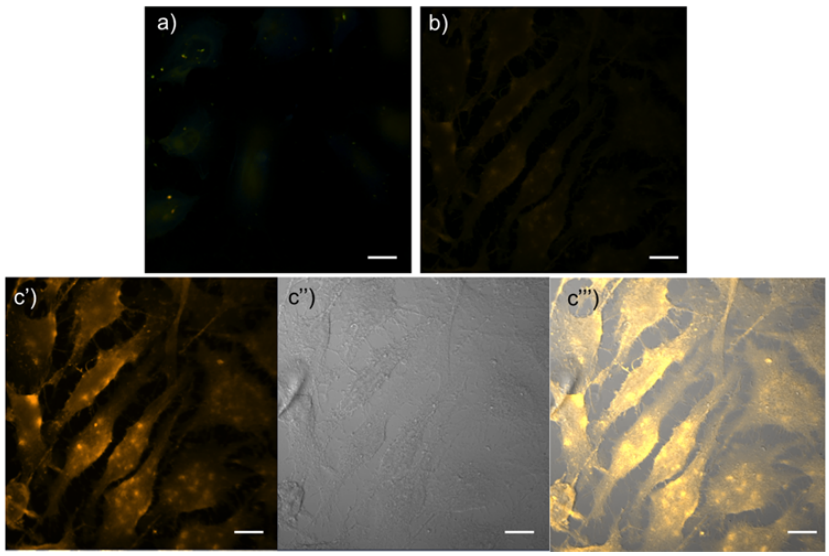


**Figure 3.16** *Confocal microscopy images showing the internalization of* ***8*** *in HeLa cells incubated with 30 μM solution after 15 minutes (a); 1 h (b); 2 h (c). Incubation after 2 h is displayed in true colour (c'), brightfield (c'') and overlay (c'''). Scale bar is 5 μm. Excitation at 400 nm.*

After 1 h of incubation, most of the cells started to show clear signs of unhealthy apoptotic state, like shrinkage and membrane blebbing, proving the high cytotoxicity of complex **8**. MTT assay allowed the quantification of HeLa viability upon treatment with complex solutions at 2 different concentrations (150 μM and 300 μM). For the lower concentration, HeLa viability was found to be 34% after 1 h of incubation and 25% after 3 h, whereas the viability of non-treated cells was respectively 100% and 89%. Clearly, uptake and resulting cell apoptosis were found to be even more pronounced for the concentrated solution, where HeLa viability resulted in 15% after 3 h (Figure 3.17).

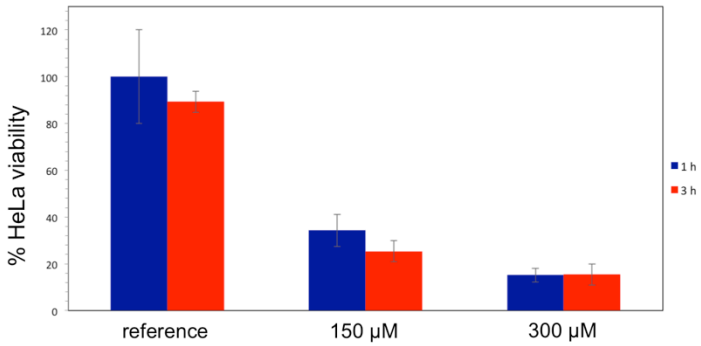


**Figure 3.17** *MTT graph showing HeLa viability for non-treated cells and for cells incubated with 150 µM and 300 µM solutions of complex* ***8*** *after 1 h (blue bars) and 3 h (red bars).*

Interestingly, confocal images collected after incubation in cell culture medium showed that the replacement of PBS as incubating medium failed to evidence any complex internalization (Figure 3.18). Missed uptake, even for longer incubation times, can be most likely explained with the establishment of interactions with the proteins present in the culture medium, resulting in a sequestration of the complex.

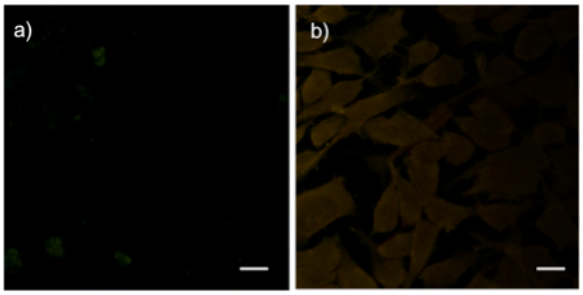


**Figure 3.18** *Confocal microscopy images of HeLa cells incubated with 30 µM solution in culture medium after 1 h (a) and 4 h (b). Scale bar is 5 µm. Excitation at 400 nm.*

Results about the cytotoxicity of the complex, when the latter is free in solution, are in line with the observations made for the aforementioned Ir(III) compound in analogous conditions and reinforce the need for a robust anchoring to the hydrogel.

### 3.2.2 Preparation of the hybrid Pt-PAA hydrogel

Preliminary tests on the cytotoxicity of compound **8** upon cell uptake highlighted as a necessary requirement the covalent grafting of the complex to the polymeric backbone of the hydrogel. Non-covalent strategies, sometimes adopted in the preparation of luminescent hydrogels, suffer, as major drawback, for stability issues. Leaking of luminescent probes, incorporated through labile bonds (i.e. electrostatic interactions[85] or physical encapsulation[86]), often causes a diminishing of the emission intensity over time and potential cytotoxicity issues. To achieve the covalent grafting of compound **9** to the polymeric backbone of the hydrogel, standard aza-Michael poly-addition protocol was adopted. Preliminary stability tests in the strong basic conditions required for the hydrogel formation were performed, to check the feasibility of the proposed approach. Thus, 140 μL of PEHA were added to a solution of 5 mg of complex **9** in 2 mL of MeOD; the intensely yellow colour of the initial solution immediately turned to pale yellow. $^{1}H$ and $^{19}F$ NMR confirmed the degradation of the complex, probably due to the coordination of the aliphatic amine, which partially replaces the pyridine ancillary ligand. Comparison between $^{19}F$ NMR spectra of the complex before and after the addition of PEHA (Figure 3.19), in particular, evidenced the appearance of additional peaks indicating a drastic change in the coordination environment of the metal centre with the formation of several species.

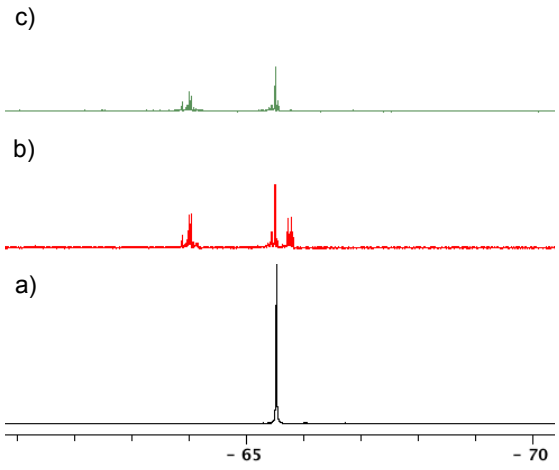


**Figure 3.19** *$^{19}F$ NMR spectra in MeOD (376 MHz) of complex **9** (a) and upon addition of PEHA after 5 minutes (b) and 3 h (c).*

Considering the instability of the complex under the basic conditions required for gelation, a different approach was investigated. The new strategy foresees the covalent anchoring of the amino-functionalized pyridine ligand to the polymer backbone, followed by coordination of the highly reactive Pt(II)-DMSO precursor on the pre-formed hydrogel scaffold. Thus, deprotection of ligand **7** in acid conditions afforded compound **10** (Scheme 3.5), suitable to act as co-monomer in the aza-Michael poly-addition.

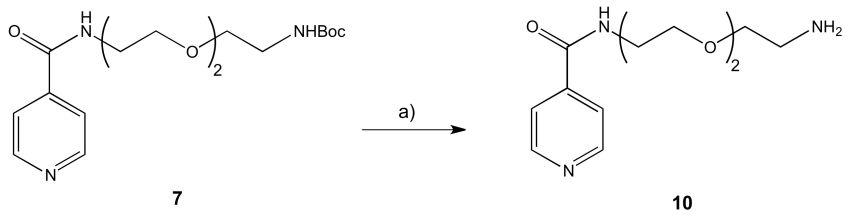


7 10

**Scheme 3.5** *Synthesis of the amino-functionalized ligand **10**: a) HCl 3 M, $CH_2Cl_2$, r.t., 3 h, 75%.*

Pyridine-decorated hydrogel was prepared by dissolving ligand **10** a 1:1 $H_2O$: MeOH solution; after dilution with water until a final volume of 1.5 mL, the solution was added to the pre-weighted solid components (MBA and GABA). A proper amount of PEHA was added and the mixture was stirred at 37 °C. Within a few minutes, complete dissolution of the reagents was observed; after 2.5 h, gelation of the clear solution was confirmed *via* 'inverted vial' test. The success of the covalent grafting was proved by $^1$H NMR spectroscopy; no aromatic signals were observed in the supernatant solution after several washing cycles with $D_2O$. Washed gel was incubated for 12 h with a stoichiometric amount of precursor **4** dissolved in 1 mL of MeOH. Repeated washing cycles with MeOD revealed no release of the complex over time. The resulting orange gel displays a bright yellow-orange luminescence under UV irradiation in the dry state, while almost no emission was detected in the water-equilibrated sample. Photophysical investigation evidenced an emission characterized by a broad featureless band centred at 592 nm ($\lambda_{exc}$ = 400 nm), suggesting the presence of Pt···Pt interactions in the solid scaffold. Emission spectra in solid-state, indeed, appear much closer to the one recorded in aqueous media than the one of molecularly dissolved complex (Figure 3.20).

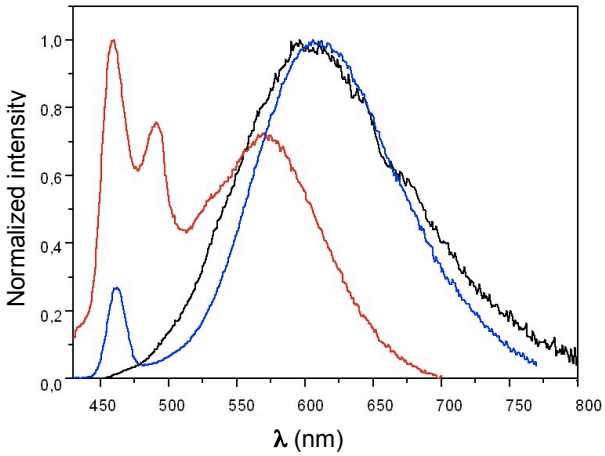


**Figure 3.20** *Comparison between the emission spectra of the dry hydrogel (black line) and of complex* ***9*** *in 1,4-dioxane (c = 10-4 M, red line) and after flash-injection in water (c = 10-4 M, 95% water content, blue line). Excitation at 400 nm.*

Complete exchange between MeOH, used for the incubation of the Pt(II)-DMSO precursor, and $H_2O$ is required to study the biocompatibility of the obtained scaffold with cells. Substitution of the embedded solvent can be simply achieved by soaking the hydrogel in $H_2O$ over multiple cycles.

### 3.2.3 *In vitro* investigation of Pt-PAA hydrogel

The efficacy of the obtained hybrid hydrogel to support cell proliferation was investigated with HeLa cells. Sterilized Pt(II)-PAA hydrogel was washed with $H_2O$ and PBS and finally equilibrated with culture medium overnight; after removal of the culture medium, cells were seeded and incubated at 37 °C for 2 h. Confocal microscopy imaging revealed the good biocompatibility of the hybrid scaffold; after several hours of incubation, indeed, seeded cells appear healthy and well-adherent to the hydrogel. This observation confirms PAA-based hydrogels as excellent 3D platforms for cell growth and proliferation; furthermore, considering the high cytotoxicity of the free complex, the lack of apoptotic symptoms from seeded cells provides an additional evidence of the robustness of the adopted strategy. In this case MTT assay couldn't provide a quantification of cell viability because of the strong background emission coming from the scaffold. Hybrid hydrogel, indeed, displays a bright yellow

luminescence upon excitation at 400 nm; unfortunately, as displayed in Fig. 3.21, observed luminescence comes exclusively from the 3D scaffold and not from cell compartments of seeded HeLa.

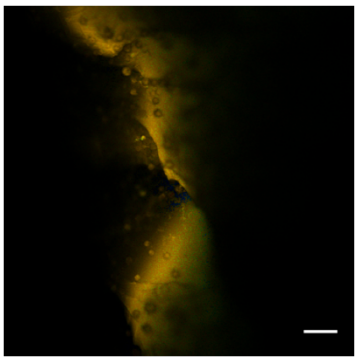

**Figure 3.21** *Confocal microscopy image of Pt(II)-PAA hydrogel with growing HeLa cells. Scale bar is 10 μm. Excitation at 400 nm.*

This result seems to suggest that for Pt(II)-PAA hydrogel, unlike Ir(III)-PAA, covalent grafting to the polymeric backbone prevents any intercalation of the luminescent probe into the cell membrane. A likely explanation relies on the aggregated state observed in the hydrogel scaffold. Even if the establishment of metallophilic interactions was a necessary requirement for achieving the desired responsiveness, formed aggregates could have hampered the intercalation into the cell membrane being too strong for being disrupted.

### 3.2.4 Pt(II) complexes for mechanochromic materials

Unique photoluminescent properties of Pt(II) complexes upon changes of their aggregation state can be also exploited in the preparation of mechanochromic materials. Historically, for this kind of systems, mechanochromism has been extensively studied in the bulk state, where the simple grinding of the powder in a mortar led to a dramatic colour change due to the shortening of Pt···Pt distances. More recently, different polymeric films doped with square planar Pt(II) complexes[62,63,64] have been used as memory devices and sensors with a easily detectable optical read-out. This new trend highlights how the incorporation into a polymer matrix is a necessary requirement for exploiting

Pt(II) complexes features for practical applications. So far, all examples reported in the literature foresee the simple dispersion of complexes into the matrix to achieve a material whose responsiveness to mechanical stimuli can be elicited exclusively through compression or scraping. In these cases the mechanical solicitation promotes stronger metallophilic interactions leading to a bathochromically shifted emission. By contrast, we investigated the possibility to reverse the conventional responsiveness in a material where pre-existing Pt···Pt interactions can be disrupted upon stretching, leading to a blueshifted emission. Thus, properly functionalized Pt(II) complexes were covalently incorporated in different polymer matrices and the luminescence of the resulting material was tested under tensile stress. In particular, 4 polymer scaffolds displaying completely different mechanical properties were studied: a rigid poly(4-vinylpyiridine) (P4VP), an elastomeric poly(dimethylsiloxane) (PDMS), a linear poly(norbornene) and acrylamide-based hydrogels.

### 3.2.5 Poly(4-vinylpyridine)

Because of the presence of pendant pyridine groups suitable for coordinating to the metal centre, P4VP appears particularly promising for the incorporation of Pt(II) complexes. Thus, coordination of the highly reactive Pt(II)-DMSO precursor through the simple mixing between a solution of pristine P4VP and a solution of compound **4** ensures the robust anchoring of the luminescent complex to the polymeric backbone. Highly emissive polymeric films with different concentrations were obtained by solution casting of the resulting mixture into a mould. (Details about samples preparation are reported in the Experimental Section). Slow evaporation of the solvent led to yellow films, which display a yellow-green luminescence upon UV irradiation. Unfortunately the extreme rigidity of the matrix prevented mechanical testing under tensile stress; therefore, responsiveness of the obtained films under compressive loading was investigated. Fig. 3.22 displays the comparison between emission spectra of the **Pt-P4VP** films as casted, after washing with $CH_3CN$ and after mechanical grinding with a pestle. Exposure to $CH_3CN$ induced a redshift of the emission band of 20 nm, in agreement with the behaviour reported for solvatochromic studies of similar systems.[63] On the other hand, mechanical grinding causes a blueshift of the emission maximum of about 45 nm, together with a change in the band shape from a broad featureless band to a more structured profile. These observations seem to

suggest that, in contrast with the conventional behaviour, compressive stress induces a disruption of the few Pt···Pt interactions present in the pristine **Pt-P4VP** films. Because of their limited extent, these changes in the emission profile cannot be appreciated with naked eye.

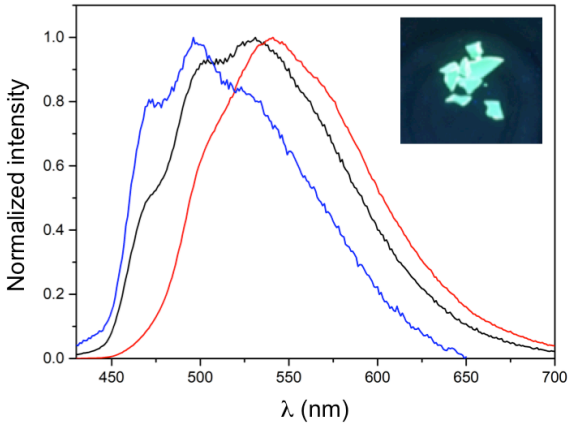


**Figure 3.22** *Emission spectra of the as-casted green-emissive **Pt-P4VP** film (black line), after washing with $CH_3CN$ (red line) and after grinding (blue line) (excitation at 400 nm); in the inset, photograph of the film upon UV irradiation at 364 nm.*

In an attempt to decrease the rigidity of the polymer matrix, poly(4-vinylpyridine-*co*-butylmethacrylate) (P4VP-*co*-BMA) films were prepared and tested in analogous conditions. Also in this case, because of the non-stretchability of the resulting yellow-emissive films **Pt-P4VP-*co*-BMA**, mechanical tests under compressive loading were performed. Emission of the as-casted film, displaying a broad featureless band centred at 560 nm, suggests stronger aggregation in respect to **Pt-P4VP** film. Furthermore, washing with $CH_3CN$, in this case, induces an unconventional blueshift of 15 nm, while mechanical grinding leads to an emission profile totally similar to the one observed for grinded **Pt-P4VP** films (Figure 3.23).

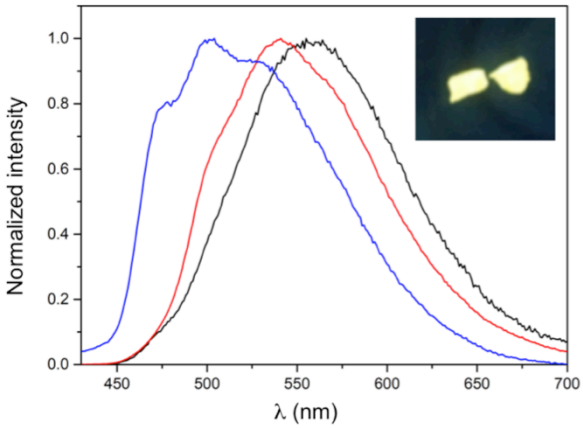


**Figure 3.23** *Emission spectra of the as-casted yellow-emissive* ***Pt-P4VP-co-BMA*** *film (black line), after washing with $CH_3CN$ (red line) and after grinding (blue line) (excitation at 400 nm); in the inset, photograph of the film upon UV irradiation at 364 nm.*

These results show, on the one hand, that P4VP and P4VP-*co*-BMA provide a convenient scaffold for an easy and robust incorporation of Pt(II) complexes to achieve highly emissive films; on the other hand, however, selected matrices fail to evidence any practical mechanochromic application upon stretching because of their extreme rigidity.

### 3.2.6 Poly(dimethylsiloxane)

Since the matrices taken into account so far resulted not suitable for the application of a tensile stress, an elastomeric matrix was investigated. The poly(dimethylsiloxane) (PDMS) used, Sylgard 184, is a two-part (Base and Curing Agent, typically mixed in a 10:1 ratio) silicone elastomer comprising vinyl terminated poly(dimethylsiloxane), poly(methylhydrosiloxane-co-dimethylsiloxane) copolymer and a platinum catalyst. The covalent incorporation of a molecule of interest into the polymer network can be achieved through the introduction of an alkene functionalization suitable for hydrosilylation protocol. Therefore the adopted strategy foresees the synthesis of a Pt(II) complex bearing a terminal double bond on the pyridine ancillary ligand (Figure 3.24). The amphiphilic character of compound **11**, which can be exploited for inducing strong aggregation in aqueous media, is guaranteed by the presence of a triethylene glycol (TEG) chain as spacer.

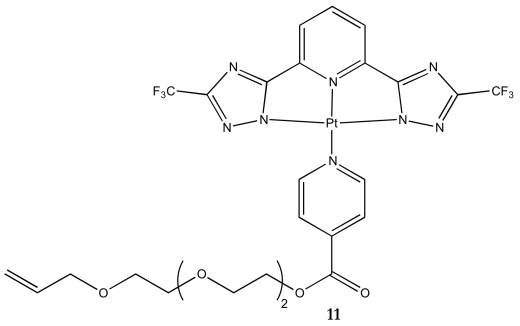


**Figure 3.24** *Chemical structure of the designed target molecule **11**.*

Thus, the basic idea relies on the covalent incorporation of micellar-like aggregates[46] into PDMS, based on the amphiphilic nature of compound **11**. In aqueous media hydrophobic Pt(py-$CF_3$-trz) moieties are expected to pack together, while TEG chains point towards the solvent and expose the anchoring sites, which thus become available for hydrosilylation. Stretching of the resulting material is expected to induce the disruption of metallophilic interactions, with a consequent blueshift of the emission. Alkene-functionalized Pt(II) complex **11** was obtained *via* a 4-steps convergent synthesis (Scheme 3.6). Nucleophilic substitution of commercially available triethylene glycol on allyl bromide under basic conditions afforded mono-alkene triethylene glycol **12**. Functionalized pyridine ligand **13** was obtained under mild conditions upon condensation between isonicotinic acid-activated ester **5** and compound **12**.

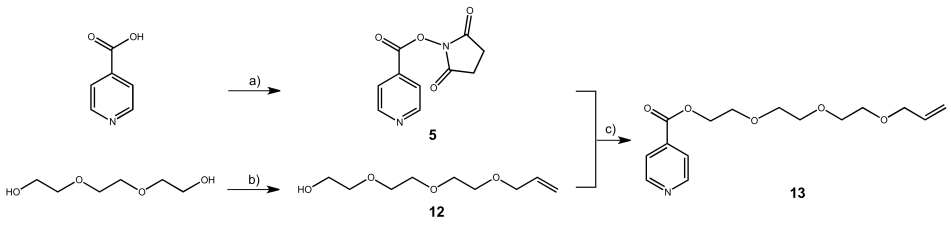


**Scheme 3.6** *Synthesis of alkene-functionalized pyridine ligand **13**: a) NHS, N-(3-dimethylaminopropyl)-N'-ethylcarbodiimide hydrochloride, DMF, r.t., 12 h, quantitative; b) allyl bromide, NaH, DMF, r.t., 12 h, 71%; c) Et(iPr)$_2$N, DMF, r.t., 12 h, 63%.*

Finally, substitution of the labile DMSO-ligand with functionalized ancillary ligand **13** was achieved by simple mixing of the two components in $CH_3CN$ solution at room temperature (Scheme 3.7).

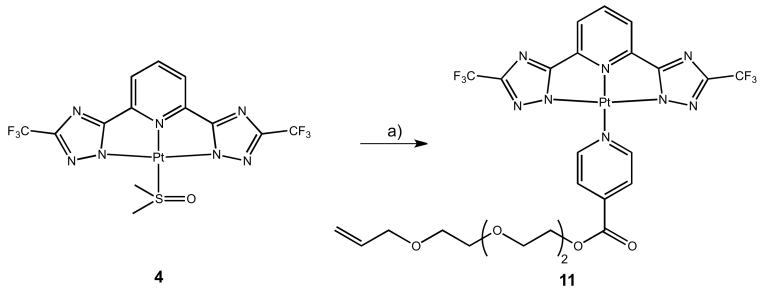


**Scheme 3.7** *Synthesis of the alkene-functionalized complex **11**: a) **13**, $CH_3CN$, r.t., 12 h, 61%.*

Purification *via* column chromatography afforded complex **11** as a yellow solid in 61% yield. $^1H$ and $^{19}F$ NMR confirmed the success of the adopted synthetic strategy. Photophysical characterization of compound **11** displays the typical behaviour of amphiphilic square planar Pt(II) complexes. Thus, when molecularly dissolved in good solvents like 1,4-dioxane or $CH_2Cl_2$, emission spectrum presents a weak structured band attributable to an excited state with mainly a triplet ligand centred ($^3$LC) character. Flash injection in water leads to the rise of a strong orange phosphorescence ($\lambda_{em}$ = 605 nm), due to the formation of micellar-like aggregates. Alkene-decorated complex **11** was employed as co-monomer in the preparation of PDMS specimens; the presence of a vinyl-terminated substituent on the ancillary ligand ensures the covalent incorporation in the polymeric backbone *via* hydrosilylation protocol. To achieve the desired responsiveness upon mechanical stretching, PDMS-embedding of complex **11** has to be performed in the form of stable micellar-like aggregates. Therefore different procedures for the preparation of luminescent PDMS films were investigated, to overcome issues related to the poor homogeneity of the resulting mixture or the stability of Pt(II) aggregates. (Details about samples preparation are reported in the Experimental Section). Flash injection of a 1,4-dioxane solution in $H_2O$ (dioxane: $H_2O$ ratio 5: 95) resulted in the formation of an orange-emitting suspension and the stability of aggregates was preserved even after incorporation into the PDMS matrix. Finally, photophysical properties of the resulting **Pt-PDMS** films upon tensile stress were investigated. Specimens containing complex **11** at different concentrations were uniaxially stretched and emission spectra were recorded at progressively increasing applied force. In all cases, no maxima variation was observed. Fig. 3.25 is representative of the general behaviour observed for all tested specimens. Since the only visible effect is the λ-independent decrease in emission due to the thinning of polymer films upon elongation, we can

conclude that the disruption of the Pt(II) aggregates *via* mechanical solicitation was not possible.

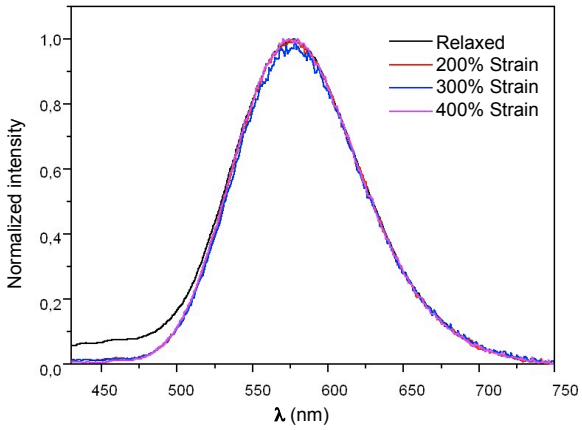


**Figure 3.25** *Emission spectra of* ***Pt-PDMS*** *specimen (0.5% w/w, Table S3.1, entry III) upon progressive elongation.*

Furthermore, despite the extreme elasticity of the matrix, specimens were stretched to a maximum elongation of 400% before rupture; this observation suggests that the incorporation of Pt(II) complexes affects the mechanical properties of the pristine PDMS.

### 3.2.7 Acrylamide-based hydrogels

In order to maximize the channelling of applied mechanical forces for promoting the disruption of Pt(II) aggregates, we decided to move towards a system in which micellar-like assemblies act as unique cross-linkers into the polymer backbone. The choice of the matrix was inspired by a similar system, reported in literature,[87] where acrylate-functionalized Pluronic F127 micelles have been used as multifunctional cross-links for the preparation of super tough and highly resilient nanomicelle hydrogels. The tendency of resulting F127 diacrylate (F127DA) to spontaneously self-assemble in water afforded nanomicelles with vinyl groups on surface (Figure 3.26); their copolymerization with acrylamide (AAm) monomers leads to the formation of a hydrogel where micelles act as unique cross-linkers.

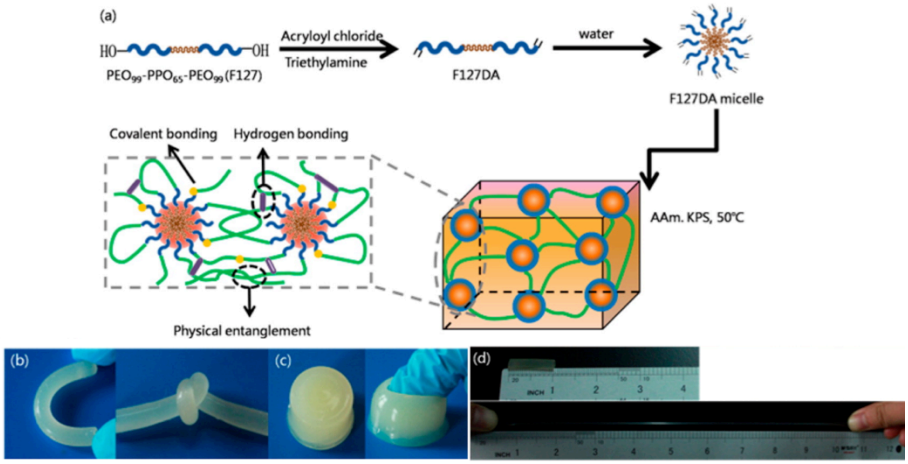


**Figure 3.26** *a) Schematic illustration of the synthesis hydrogels with F127 micelles as macro-cross-linkers; (b–d) photographs showing that hydrogels could withstand (b) bending, knotting, (c) compression, and (d) ultra-stretching.*[85]

Our approach is based on the use of an amphiphilic Pt(II) complex bearing an acrylate moiety, whose tendency to self-assemble in aqueous media can be exploited to achieve an analogous elastic hydrogel. The advantage of this strategy relies on the absence of any additional cross-linker, in contrast with the previously reported approach, where pristine Sylgard 184 already displays a high degree of reticulation. This implies that tensile forces applied to the resulting material are expected to act necessarily on Pt(II) aggregates. Synthesis of complex **14** was performed, according to the standard procedure, through a convergent approach. Reaction between triethylene glycol and acryloyl chloride under basic conditions afforded compound **15**, whose condensation with isonicotinic acid-activated ester **5** gave functionalized pyridine ligand **16** under mild conditions (Scheme 3.8).

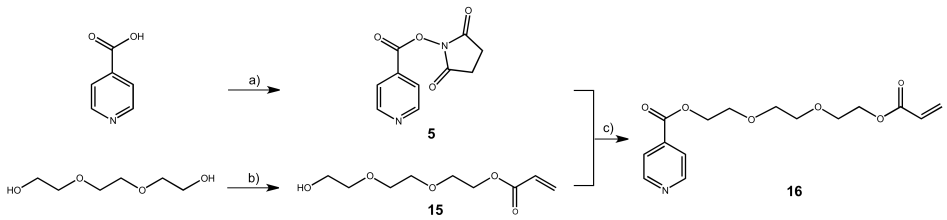

**Scheme 3.8** *Synthesis of acrylate-functionalized pyridine ligand* ***16****: a) NHS, N-(3-dimethylaminopropyl)-N'-ethylcarbodiimide hydrochloride, DMF, r.t., 12 h, quantitative; b) acryloyl chloride,* $Et_3N$*,* $CH_2Cl_2$*, r.t., 12 h, 68%; c)* $Et(iPr)_2N$*, DMF, r.t., 12 h, 58%.*

Amphiphilic complex **14** was obtained *via* coordination of **16** to precursor **4** in $CH_3CN$ solution (Scheme 3.9).

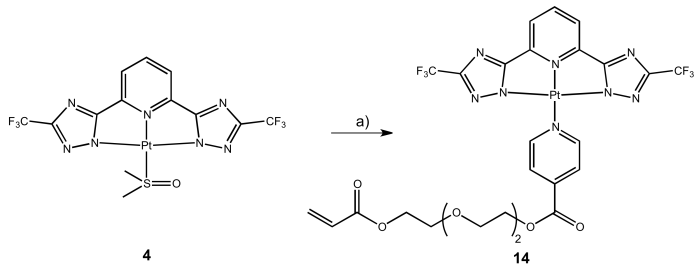

**Scheme 3.9** *Synthesis of the acrylate-functionalized complex* ***14****: a)* ***16****,* $CH_3CN$*, r.t., 12 h, 63%.*

As a reference, acrylamide-based hydrogels with F127DA were prepared following the reported procedure.[85] Gelation was achieved through a one-step sequential radical polymerization; to a degassed water solution of AAm and F127DA, 0.1 mol% (with respect to AAm) of initiator potassium persulfate (KPS) was added and the mixture was heated at 70 °C. After 10 minutes, gelation of the clear solution was confirmed *via* 'inverted vial' test; obtained hydrogels display optical transparency and extreme elasticity. Following the same procedure, the formation of AAm-based hydrogels cross-linked with micellar-like aggregates of complex **14** was investigated. (Details about gelation conditions are reported in the Experimental Section). AAm monomer and thermal initiator were added to the orange-emitting suspension obtained by flash-injection of a 1,4-dioxane solution of **14** in water. Heating the mixture at 70 °C resulted in an immediate disruption of Pt(II) aggregates, leading to a weak green luminescence. Further attempts to achieve gelation at lower temperatures gave similar results. In order to avoid thermal activation, KPS

was replaced with Irgacure 2959, highly efficient at promoting UV curing of acrylate-based systems in aqueous media. Starting from suspensions of Pt(II) aggregates in water at different concentrations, AAm monomer and photoinitiator were added. In this case, disruption of aggregates was not observed but irradiation at 280 nm failed to evidence any gelation of the system, irrespectively of the amount of cross-linker. For this reason, we investigated the use of additional cross-linkers together with complex **14** in order to achieve the desired curing. The use of F127DA and MBA as cross-linkers led, in both cases, to gelation; nevertheless, the presence of F127DA induced immediate disruption of the micelles, while MBA afforded an extremely soft material unable to stand tensile stresses. In conclusion, the use of micellar-like aggregates based on amphiphilic Pt(II) complexes as macro-cross-linkers for the polymerization of acrylamide monomers resulted ineffective at inducing a real curing of the system.

### 3.2.8 Poly(norbornene)

Despite the use of micellar-like aggregates as cross-linking units in solid matrices appeared the most promising strategy to guarantee an efficient channelling of applied mechanical forces, investigated PDMS and acrylamide-based hydrogel failed to evidence respectively any emission change upon stretching or any effective reticulation. Thus, we decided to study a simpler approach which relies on the use of a linear polymer backbone bearing pendant Pt(II) complexes. The choice of the polymeric scaffold was inspired by an interesting system reported in literature[88] where a low $T_g$ co-polymer from norbornene and photochromic ruthenium monomers is described; resulting polymeric films undergo a macroscopic deformation triggered by the molecular rearrangement of isomerizable units upon laser irradiation. Thus, a poly(norbornene) co-polymer with pendant Pt(II) complexes was investigated; in this case, for high functionalization degrees, Pt···Pt interactions are expected between neighbouring metal centres along the polymer backbone as schematized in Fig. 3.27.

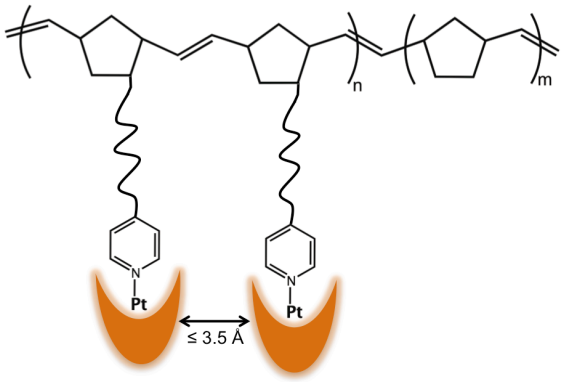


**Figure 3.27** *Sketch of the target poly(norbornene) co-polymer with pendant Pt(II) complexes.*

Introduction of a norbornene moiety on the pyridine ligand afforded Pt(II) complex **17** suitable for acting as co-monomer during the ring opening metathesis polymerization (ROMP). Synthesis of the functionalized ancillary ligand **19** was quite straightforward (Scheme 3.10); chlorination of commercially available norbornene carboxylic acid (mixture of *endo*- and *exo*-) with oxalic acid afforded reactive acyl chloride **18**, which was directly condensed with 4-pyridinepropanol to give ligand **19** as a colourless/light yellow oil.

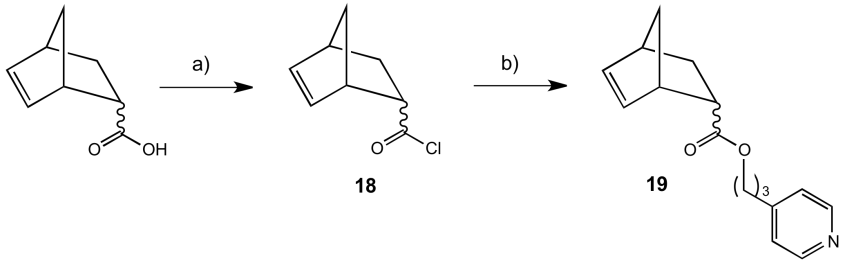


**Scheme 3.10** *Synthesis of norbornene-functionalized pyridine ligand **19**: a) oxalic acid, r.t., 2 h, quantitative; b) 4-pyridinepropanol, $CH_2Cl_2$, $Et_3N$, r.t., 12 h, 88%.*

Finally, substitution of the labile DMSO-ligand with functionalized ancillary ligand **19** was achieved by simple mixing of the two components in DMF solution at room temperature (Scheme 3.11).

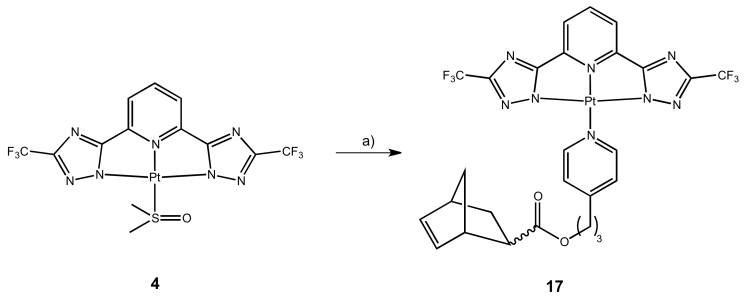


**Scheme 3.11** *Synthesis of the norbornene-functionalized complex* ***17****: a)* ***19****, DMF, r.t., 12 h, 69%.*

Complex **17** was used as co-monomer together with plain norbornene in ROMP activated by first generation Grubbs catalyst (**17**: NB ratios between 1: 60 and 1: 25). The two monomers were dissolved in $CH_2Cl_2$, the resulting solution was degassed before the addition of the catalyst and stirred at room temperature for 24 h. The polymer was precipitated in MeOH, dried under vacuum and solution casted to achieve highly emissive films **Pt-*p*NB**. As a reference, simple poly(norbornene) films were prepared following the same procedure. Polymer specimens with pendant Pt(II) complexes display an intense orange luminescence ($\lambda_{max}$ = 607 nm), which suggests the presence of Pt···Pt interactions between neighbouring metal centres (Figure 3.28).

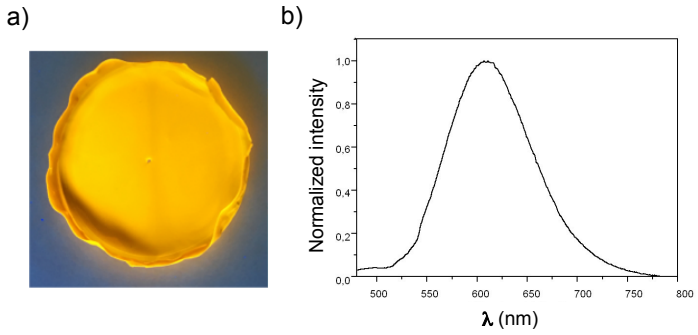


**Figure 3.28** *a) Photograph of the orange* **Pt-*p*NB** *under UV irradiation (365 nm) and b) normalized emission spectrum ($\lambda_{exc}$ = 420 nm).*

Also in this case, the addition of the complex was found to strongly affect the mechanical properties of the material; indeed, while plain poly(norbornene)

appears elastic, the decorated co-polymer results more rigid and thus unable to stand tensile stress.

## 3.3 Conclusions

In conclusion unique photophysical properties of square planar Pt(II) complexes upon aggregation were investigated with the aim to exploit them for two different applications. In the first case, an hybrid PAA-based hydrogel bearing covalently incorporated Pt(II) complexes was studied as 3D platform for cell growth and proliferation. Furthermore, the presence of luminescent probes could provide a real-time visualization of live cells without the need for additional staining. Synthetic approach for the preparation of the hybrid material was adapted from a previously reported system[81] based on the use of luminescent Ir(III) complexes as switchable chromophores. Thus, we investigated the possibility to move from an *OFF/ON* responsiveness to a finer modulation of the emission; in this perspective, the use of Pt(II) complexes, whose luminescence is strongly affected by even slight variations of their environment, represents a sound alternative. Owing to the instability of Pt(II) complexes under the strong basic conditions required for the formation of PAA hydrogels, the initial synthetic strategy was modified; the new strategy, involving the coordination of a highly reactive precursor to the pre-formed 3D scaffold, afforded the desired luminescent hydrogel. Finally, the efficacy of the obtained material to support cell proliferation was investigated with HeLa cells; confocal microscopy revealed that, while the original biocompatibility was retained even after decoration with emissive probes, no luminescence was detected from cell compartments. A likely explanation for the lack of intercalation of the luminescent probe into the cell membrane relies on the aggregated state observed in the hydrogel scaffold, where established metallophilic interactions could be too strong for being disrupted.
As second approach, we studied the possibility to covalently incorporate Pt(II) complexes into polymers for the realization of mechanochromic materials responsive upon tensile stresses. In this perspective, 4 different matrices were taken into account. In particular, P4VP and P4VP-*co*-BMA were initially investigated since the presence of pendant pyridines provides suitable coordinating groups for the metal centres. Photophysical characterization on **Pt-P4VP** and **Pt-P4VP-*co*-BMA** films evidenced some slight variation in the

emission profile upon mechanical grinding, but the rigidity of the material precluded its stretchability. Thus, an elastomeric PDMS matrix was employed; incorporation of properly functionalized Pt(II) complexes in the aggregated state led to highly luminescent and elastic films. Emission spectra recorded at progressively increasing strain failed to evidence any maxima variation. Micellar-like aggregates were also used as macro-cross-linkers in the radical polymerization of acrylamide monomers but resulted ineffective at promoting a proper curing of the material. Eventually, a linear poly(norbornene) with pendant Pt(II) complexes was prepared; high degrees of functionalization ensured the establishment of lateral Pt···Pt interactions between neighbouring metal centres. Unfortunately, the covalent incorporation of luminescent probes strongly affected the mechanical properties of the polymer, leading to a sizable increase of its rigidity with respect to plain poly(norbornene). Overall, the failure of all these approaches calls for an in depth analysis of the influence of the Pt(II) complex on polymers mechanical properties.

## 3.4 Acknowledgements

Special thanks to Prof. Luisa De Cola and all her group, in particular Giuseppe Alonci and Dr. Alessandro Aliprandi, from the Institut de Science et d'Ingégnerie Supramoléculaire (ISIS), Strasbourg, France.

## 3.5 Experimental Section

**Pyridine-2,6-bis(carboximidhydrazide) (2)**
Hydrazine monohydrate (8 mL, 0.16 mol) was added to a suspension of 2,6-pyridinedicarbonitrile (1.0 g, 7.74 mmol) in 20 mL of EtOH. The mixture was stirred at room temperature for 3 days. The slightly yellowish precipitate was filtered, washed with EtOH and dried under vacuum to give product **2** in 98% yield (1.466 g, 7.59 mmol).
**$^1$H NMR** (DMSO-$d_6$, 400 MHz): δ (ppm) = 7.8 (d, 2H, J=8.2 Hz, Ar**H**), 7.65 (t, 1H, J=8.2 Hz, Ar**H**), 6.04 (s, 4H, N**H$_2$**), 5.27 (s, 4H, N**H**).
**ESI-MS:** *m/z* = 194.3 $[M+H]^+$.

**2,6-bis(3-(trifluoromethyl)-1H-1,2,4-triazol-5-yl)pyridine ligand (3)**
Compound **2** (1.4 g, 7.25 mmol) was dispersed in 15 mL of diethylene glycol dimethyl ether and sonicated to obtain a fine suspension. Trifluoroacetic anhydride (2.217 mL, 15.95 mmol) was slowly added and the resulting mixture was stirred at room temperature for 10 minutes and then heated at reflux for 1 h. After cooling to room temperature, $H_2O$ (40 mL) and HCl 37% (1.25 mL) were added and the mixture was heated at 90 °C for 12 h. After cooling to room temperature the white precipitate was filtered, washed with $H_2O$ and petroleum ether and dried under vacuum to afford product **3** as a white solid in 74% yield (1.872 g, 5.37 mmol).
**$^1$H NMR** (Acetone-$d_6$, 400 MHz): δ (ppm) = 8.38 (m, 3H, Ar**H**).
**$^{19}$F{$^1$H} NMR** (Acetone-$d_6$, 376 MHz): δ (ppm) = - 65.8 (s, 3H, C**F$_3$**).
**ESI-MS:** *m/z* = 372.1 $[M+Na]^+$.

**Pt(II)-DMSO precursor (4)**
$Pt(DMSO)_2Cl_2$ (0.25 g, 0.59 mmol), synthesized as reported in literature,[89] was added to a solution of ligand **3** (0.207 g, 0.59 mmol) in 4 mL of DMF; the solution was heated at 75 °C for 12 h. After cooling to room temperature, volatiles were removed in vacuo. The crude was purified by centrifugation in $CH_2Cl_2$ and MeOH to afford Pt(II)-DMSO precursor **4** as a red solid in 64% yield (0.236 g, 0.38 mmol).
**$^1$H NMR** (MeOD, 400 MHz): δ (ppm) = 8.26 (t, 1H, J=7.9 Hz, Ar**H**), 7.89 (d, 2H, J=7.9 Hz, Ar**H**), 2.71 (s, 6H, C**H$_3$**).
**$^{19}$F{$^1$H} NMR** (MeOD, 376 MHz): δ (ppm) = - 65.66 (s, 3H, C**F$_3$**).
**HR-ESI-ToF-MS:** *m/z* = $[M+Na]^+$ calculated: 643.0034; found: 643.0071.

**Isonicotinic acid-activated ester (5)**

N-hydroxysuccinimide (0.514 g, 4.47 mmol) and N-(3-dimethylaminopropyl)-N′-ethylcarbodiimide hydrochloride (0.856 g, 4.47 mmol) were added to an ice-cold solution of isonicotinic acid (0.500 g, 4.06 mmol) in 7 mL of dry DMF and the mixture was stirred at room temperature for 12 h. The solution was poured in AcOEt (15 mL) and the organic phase was washed with $H_2O$, $NaHCO_{3\ aq}$, brine and eventually $H_2O$. The solvent was evaporated under reduced pressure to give compound **5** as a white crystalline solid in quantitative yield (0.893 g, 4.06 mmol).

**$^1$H NMR** ($CDCl_3$, 400 MHz): δ (ppm) = 8.91 (dd, 2H, $J_o$=6.1 Hz, $J_m$=4.4 Hz, Ar**H**), 7.97 (dd, 2H, $J_o$=6.1 Hz, $J_m$=4.4 Hz, Ar**H**), 2.96 (s, 4H, -C**H$_2$**-).

**ESI-MS:** *m/z* = 221.2 $[M+H]^+$.

**Mono-Boc protected 1,2-bis(2-aminoethoxy)ethane (6)**

A solution of di-*tert*-butyl carbonate (0.329 g, 1.51 mmol) in 3 mL of dry $CH_2Cl_2$ was added drop-wise over 1 h to an ice-cold solution of 1,2-bis(2-aminoethoxy)ethane (0.200 mL, 1.37 mmol) in 2 mL of dry $CH_2Cl_2$. The mixture was stirred at room temperature for 12 h. The organic phase was washed with $H_2O$, brine and $H_2O$ and the solvent was removed under reduced pressure. Purification *via* flash column chromatography (gradient from hexane/AcOEt 1:1 to hexane/AcOEt 3:7) afforded compound **6** as a colourless oil in 62% yield (0.211 g, 0.85 mmol).

**$^1$H NMR** ($CDCl_3$, 400 MHz): δ (ppm) = 3.64 (m, 4H, -OC**H$_2$**-), 3.56 (m, 4H, -OC**H$_2$**$CH_2$O-), 3.34 (m, 2H, C**H$_2$**$NH_2$), 2.91 (m, 2H, -C**H$_2$**NH-), 1.47 (s, 9H, **$^t$Bu**).

**ESI-MS:** *m/z* = 249.3 $[M+H]^+$.

**Boc-protected pyridine ligand (7)**

Mono-Boc protected 1,2-bis(2-aminoethoxy)ethane **6** (0.210 g, 0.85 mmol) was added to a solution of isonicotinic acid-activated ester **5** (0.156 g, 0.71 mmol) in 6 mL of dry DMF, followed by $Et(iPr)_2N$ (0.117 mL, 0.67 mmol). The mixture was stirred at room temperature for 12 h. Volatiles were removed under vacuum and the crude was recovered with $CH_2Cl_2$ and washed with $NaHCO_{3\ aq}$ and $H_2O$. The solvent was evaporated under reduced pressure and the crude was purified by flash column chromatography (gradient from $CH_2Cl_2$/MeOH 98:2 to $CH_2Cl_2$/MeOH 95:5) to give compound **7** as a slightly yellow oil in 43% yield (0.108 g, 0.31 mmol).

**$^1$H NMR** (MeOD, 400 MHz): δ (ppm) = 8.71 (d, 2H, J=6.0 Hz, Ar**H**), 7.81 (d, 2H, J=6.0 Hz, Ar**H**), 3.72-3.6 (m, 8H, -OC**H$_2$**-), 3.33 (m, 2H, -C**H$_2$**NHBoc-), 3.23 (m, 2H, -C**H$_2$**NH-), 1.44 (s, 9H, **$^t$Bu**).

**ESI-MS:** *m/z* = 354.3 $[M+H]^+$.

**Boc-protected Pt(II) complex (8)**
Pt(II)-DMSO precursor **4** (0.191 g, 0.31 mmol) was added to a solution of Boc-protected pyridine ligand **7** (0.100 g, 0.28 mmol) in 5 mL of $CH_3CN$. The solution was stirred at room temperature for 12 h. Volatiles were removed under vacuum and the crude was purified by flash column chromatography (gradient from CyHex/AcOEt 4:6 to CyHex/AcOEt 2:8) to give complex **8** as a yellow solid in 56% yield (0.140 g, 0.16 mmol).
**$^1$H NMR** (MeOD, 400 MHz): δ (ppm) = 8.62 (d, 2H, J=5.9 Hz, Ar**H**), 7.67 (t, 1H, J=7.8 Hz, Ar**H**), 7.23 (d, 2H, J=5.9 Hz, Ar**H**), 6.91 (d, 2H, J=7.8 Hz, Ar**H**), 3.78-3.67 (m, 8H, -OC**H$_2$**-), 3.58 (t, 2H, J=5.7 Hz, -C**H$_2$**NHBoc-), 3.28 (t, 2H, J=5.7 Hz, -C**H$_2$**NH-), 1.47 (s, 9H, **$^t$Bu**).
**$^{19}$F{$^1$H} NMR** (MeOD, 376 MHz): δ (ppm) = - 65.53 (s, 3H, C**F$_3$**).

**Amino-functionalized Pt(II) complex (9)**
Boc-protected Pt(II) complex **8** (0.08 g, 0.087 mmol) was added to an ice-cold solution of trifluoroacetic acid (6 mL, 78 mmol, 15% v/v) in 40 mL of $CH_2Cl_2$. The solution was stirred at room temperature for 2 h. Volatiles were removed under vacuum, the crude was recovered with $CH_2Cl_2$ and washed with $NaOH_{aq}$ to give complex **9** as a yellow solid in quantitative yield (0.069 g, 0.087 mmol).
**$^1$H NMR** (MeOD, 400 MHz): δ (ppm) = 8.95 (d, 2H, J=5.9 Hz, Ar**H**), 7.82 (t, 1H, J=7.8 Hz, Ar**H**), 7.47 (d, 2H, J=5.9 Hz, Ar**H**), 7.14 (d, 2H, J=7.8 Hz, Ar**H**), 3.78-3.66 (m, 8H, -OC**H$_2$**-), 3.58 (t, 2H, J=5.7 Hz, -C**H$_2$**$NH_2$), 3.28 (t, 2H, J=5.7 Hz, -C**H$_2$**NH-).
**$^{19}$F{$^1$H} NMR** (MeOD, 376 MHz): δ (ppm) = - 65.54 (s, 3H, C**F$_3$**).

**In vitro cell culture**
Cervical cancer cells HeLa were purchased from ATCC and used between P6 and P15. Cells were cultured in high glucose Dulbecco's Modified Eagle Medium (DMEM) with 1% Penicillin-Streptomycin, 1% L-Glutamine 200 mM and 10% Fetal Bovine Serum (FBS). Cells were kept in 75 $cm^2$ culture flasks (Corning Inc., NY, USA) at 37 °C with a controlled atmosphere of 5% $CO_2$ and were grown until reaching 80 to 85% of confluence. Eventually, they were washed with Phosphate Buffer Solution (PBS) and treated with trypsin to detach them from surface. Approximately 50 000 cells were reseeded on the

monolayer glass cover slip inside a 96-well plate culture dish; fresh culture medium was gently added and cells were grown for 12 h.

**Internalization studies with Boc-protected Pt(II) complex 8 in PBS**

The culture media was removed and 2 mL of a solution of complex **8** (30 μM in less than 1% DMSO containing PBS) were gently added onto the cells. After incubation at 37 °C for a variable time (15 min, 1 h, 2 h), the incubating medium was removed, the cell layer was gently washed with PBS (x 3) and fixed with a 4% paraformaldehyde solution for 10 min. Finally, cells were visualized with CLSM.

**Internalization studies with Boc-protected Pt(II) complex 8 in culture medium**

The culture media was removed and 2 mL of a solution of complex **8** (30 μM in less than 1% DMSO containing culture medium) were gently added onto the cells. After incubation at 37 °C for a variable time (15', 1 h, 4 h), the incubating medium was removed, the cell layer was gently washed with PBS (x 3) and 2 mL of fresh culture medium were added. Finally, cells were visualized with CLSM.

**Cell viability with Boc-protected Pt(II) complex 8**

Cell viability was assessed using MTT cell proliferation assay. Briefly, yellow tetrazolium MTT (3-(4, 5-dimethylthiazolyl-2)-2, 5-diphenyltetrazolium bromide) is reduced by metabolically active cells, in part by the action of dehydrogenase enzymes, to generate reducing equivalents such as NADH and NADPH (Figure 3.29). The resulting intracellular purple formazan can be solubilized and quantified by spectrophotometric means.

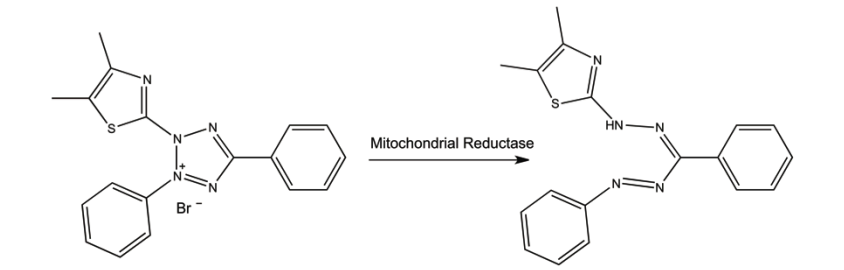


**Figure 3.29** *Reduction of yellow tetrazole MTT into purple Formazan in living cells.*

Experimentally, HeLa cells were seeded onto a glass bottom petri dish and grown for 24 h in DMEM. Then, the culture medium was removed and 2 ml of DMEM solution containing the Pt(II) complex were gently added onto the cells. After incubation for 3 h at 37 °C, the staining medium was removed and replaced by fresh medium. Eventually, cells were recovered and visualized immediately with CLSM without washing.

**Preparation of Pt(II)-PAA hydrogels**

MBA (0.200 g, 1.3 mmol) and GABA (0.05 g, 0.49 mmol) were weighted in a 5-mL glass vial. A 1:1 $H_2O$: MeOH solution of amino-functionalized pyridine ligand **10** (0.013 g, 0.052 mmol, 4% mol) was diluted with water until a final volume of 1.5 mL and added to the solid components. PEHA (0.08 mL, 0.31 mmol) was added and the mixture was stirred at 37 °C. Within a few minutes, complete dissolution of the reagents was observed; after 2.5 h, gelation of the clear solution was confirmed *via* 'inverted vial' test. The resulting hydrogel was washed with $D_2O$ (x 3) and the supernatant solution was analysed *via* $^1H$ NMR spectroscopy to check the eventual release of **10**. Incubation with 1 mL of MeOH solution of precursor **4** for 12 h, followed by 3 cycles of washing with MeOD afforded the orange-emissive Pt(II)-PAA hydrogel. Photophysical characterization was performed on dried hydrogel.

**In vitro cell culture on Pt(II)-PAA hydrogel**

Embedded MeOH, used for the incorporation of Pt(II)-DMSO precursor **4**, was replaced with $H_2O$ *via* 3-cycles of incubation for 12 h. Hydrogel samples were cut in slices (1 cm ∅ x 0.5 mm thickness) and sterilized by immersion in a 70% v/v ethanol in nanopure water for 20 min. Then, the ethanol-water mixture was discarded, hydrogels were washed with $H_2O$ (3 x 1 h), PBS (3 x 1 h) and finally equilibrated in culture medium at 37 °C for 12 h. After removal of the culture medium, approximately from 10 000 to 20 000 HeLa cells, detached from the culture flask by trypsination, were reseeded onto the hydrogel scaffold and incubated at 37 °C for 2 h. Eventually, fresh culture medium was gently added and cells were visualized with CLSM.

**P4VP and P4VP-*co*-BMA films**

Polymer films with different concentrations of Pt(II)-DMSO precursor **4** were prepared according to the following procedure. A solution of P4VP in $CHCl_3$ or of P4VP-*co*-BMA in DMF was added to a solution of Pt(II)-DMSO precursor **4** in $CH_3CN$; the resulting mixture was stirred at room temperature for 2 h and then

poured into a mould. Slow evaporation of the solvent afforded emissive polymer films. Before mechanical testing, samples were washed with $CH_3CN$ to remove eventual non-coordinated Pt(II)-DMSO precursor **4**. The homogeneity of the resulting solution appears related to the concentration of Pt(II) complexes. For low degrees of functionalization the solution remains clear, while at concentrations higher than 15-20% w/w the immediate formation of a precipitate is observed.

| | Conc (% w/w) | Castability |
|---|---|---|
| **I** | **5** | ✓ |
| **II** | **10** | ✓ |
| **III** | **15** | ✓ |
| **IV** | **20** | ✓ |
| **V** | **> 20** | ✗ |

**Table S3.1** *P4VP specimens with Pt(II)-DMSO precursor; castable homogeneous solutions are indicated with (✓), while non-castable suspensions are indicated with (✗).*

| | Conc (% w/w) | Castability |
|---|---|---|
| **I** | **5** | ✓ |
| **II** | **10** | ✓ |
| **III** | **15** | ✓ |
| **IV** | **20** | ✗ |
| **V** | **> 20** | ✗ |

**Table S3.2** *P4VP-co-BMA specimens with Pt(II)-DMSO precursor; castable homogeneous solutions are indicated with (✓), while non-castable suspensions are indicated with (✗).*

**Mono-alkene functionalized triethylene glycol (12)**
NaH (0.069 g, 1.7 mmol, 60% dispersion in oil) was added to an ice-cold solution of triethylene glycol (0.926 mL, 6.94 mmol) in 3 mL of dry DMF. After 10 min allyl bromide (0.150 mL, 1.7 mmol) was slowly added and the mixture was stirred at room temperature for 12 h. Volatiles were removed in vacuo and the crude was purified *via* flash column chromatography ($CHCl_3$/MeOH 98:2) to afford product **12** as a colourless oil in 71% yield (0.229 g, 1.2 mmol).
**$^1$H NMR** ($CDCl_3$, 400 MHz): δ (ppm) = 5.94 (m, 1H, C**H**=$CH_2$), 5.25 (m, 2H, CH=C**H$_2$**), 4.05 (dt, 2H, $^1$J=5.6 Hz, $^2$J=1.3 Hz, C**H$_2$**CH=$CH_2$), 3.77-3.73 (m, 2H, C**H$_2$**OH), 3.71-3.68 (m, 6H, -OC**H$_2$**-), 3.65-3.62 (m, 4H, -OC**H$_2$**-).
**ESI-MS:** *m/z* = 191.2 $[M+H]^+$.

**Alkene-functionalized pyridine ligand (13)**
Mono-alkene functionalized triethylene glycol **12** (0.152 g, 0.8 mmol) dissolved in 2 mL of dry DMF was added to a solution of isonicotinic acid-activated ester **5** (0.147 g, 0.67 mmol) in 5 mL of dry DMF, followed by $Et(iPr)_2N$ (0.139 mL, 0.8 mmol). The mixture was stirred at room temperature for 12 h. Volatiles were removed in vacuo and the crude was purified *via* flash column chromatography (gradient from $CH_2Cl_2$/MeOH 98:2 to $CH_2Cl_2$/MeOH 95:5) to afford product **13** as a colourless oil in 63% yield (0.125 g, 0.42 mmol).
**$^1$H NMR** (MeOD, 400 MHz): δ (ppm) = 8.76 (dd, 2H, $J_o$=6.1 Hz, $J_m$=1.7 Hz, Ar**H**), 7.98 (dd, 2H, $J_o$=6.1 Hz, $J_m$=1.7 Hz, Ar**H**), 5.92 (m, 1H, C**H**=$CH_2$), 5.22 (m, 2H, CH=C**H$_2$**), 4.54 (m, 2H, C**H$_2$**O(CO)), 4.04 (m, 2H, C**H$_2$**CH=$CH_2$), 3.72-3.68 (m, 6H, -OC**H$_2$**-), 3.65-3.59 (m, 4H, -OC**H$_2$**-).
**ESI-MS:** *m/z* = 296.6 $[M+H]^+$.

**Alkene-functionalized Pt(II) complex (11)**
Pt(II)-DMSO precursor **4** (0.232 g, 0.37 mmol) was added to a solution of alkene-functionalized pyridine ligand **13** (0.100 g, 0.34 mmol) in 5 mL of $CH_3CN$. The solution was stirred at room temperature for 12 h. Volatiles were removed under vacuum and the crude was purified by flash column chromatography (gradient from CyHex/AcOEt 4:6 to CyHex/AcOEt 3:7) to give complex **11** as a yellow solid in 61% yield (0.174 g, 0.21 mmol).
**$^1$H NMR** ($CD_2Cl_2$, 400 MHz): δ (ppm) = 9.75 (d, 2H, J=6.8 Hz, Ar**H**), 8.09 (dd, 2H, $J_o$=6.8 Hz, $J_m$=1.3 Hz, Ar**H**), 8.02 (t, 1H, J=7.9 Hz, Ar**H**), 7.69 (d, 2H, J=7.9 Hz, Ar**H**), 5.95 (m, 1H, C**H**=$CH_2$), 5.32 (m, 2H, CH=C**H$_2$**), 5.20 (m, 2H, C**H$_2$**O(CO)), 4.02 (m, 2H, C**H$_2$**CH=$CH_2$), 3.71-3.69 (m, 6H, -OC**H$_2$**-), 3.67-3.63 (m, 4H, -OC**H$_2$**-).

**$^{19}F\{^{1}H\}$ NMR** ($CD_2Cl_2$, 376 MHz): δ (ppm) = - 64.55 (s, 3H, C**F**$_3$).

**PDMS Samples preparation**

Sylgard 184 Base (1.0 g) and a suspension of complex **11** were homogenized with vortex in a 15 mL Falcon tube. Sylgard 184 Curing Agent (0.1 g) was added and the tube was extensively shacked with a vortex. The mixture was degassed under vacuum and poured onto a PTFE plate. After a second degassing the sample was cured at room temperature for 48 h. Once cured the film was pealed away and cut into stripes for mechanical testing.

Several procedures have been investigated (Table S3.3) to obtain a stable dispersion of micellar-like aggregates in aqueous media suitable for being homogenised with the polymer matrix. The major problems encountered are related to the lack of homogeneity for the resulting films or the poor stability of the Pt(II) aggregates.

| | **Procedure** | **Before mixing with PDMS** | **After mixing with PDMS** |
|---|---|---|---|
| **I** | Dissolve in THF, dilute with $H_2O$ (1:10) and inject in $H_2O$ | Orange phosphorescence ($\lambda_{em}$ = 605 nm) | Green-yellow phosphorescence ($\lambda_{em}$ = 550 nm) |
| **II** | Dissolve in a THF: $H_2O$ mixture (4:6) and inject in $H_2O$ | Orange phosphorescence ($\lambda_{em}$ = 605 nm) | Green-yellow phosphorescence ($\lambda_{em}$ = 550 nm) |
| **III** | Dissolve in dioxane and inject in $H_2O$ (dioxane: $H_2O$ 5: 95) | Orange phosphorescence ($\lambda_{em}$ = 605 nm) | Yellow-orange phosphorescence ($\lambda_{em}$ = 580 nm) |

**Table S3.3** *PDMS specimens with complex **11**.*

Once optimized the experimental conditions to obtain stable aggregates into the polymeric matrix (entry III, Table S3.3), specimens with concentration ranging from 0.1% to 1% w/w of complex **11** were prepared.

**Mono-acrylate functionalized triethylene glycol (15)**

$Et_3N$ (0.517 mL, 3.71 mmol) was added to an ice-cold solution of triethylene glycol (1.98 mL, 14.8 mmol) in 5 mL of dry $CH_2Cl_2$. A solution of acryloyl chloride (0.300 mL, 3.71 mmol) in 5 mL of dry $CH_2Cl_2$ was added drop-wise over 1 h and the mixture was stirred at room temperature for 12 h. The organic phase was washed with $H_2O$ and the solvent was evaporated under reduced pressure. The crude was purified *via* flash column chromatography

($CHCl_3$/MeOH 98:2) to afford product **15** as a colourless oil in 68% yield (0.515 g, 2.52 mmol).
**$^1$H NMR** ($CDCl_3$, 400 MHz): δ (ppm) = 6.45 (m, 1H, $\mathbf{H_{cis}}$HC=CH), 6.18 (m, 1H, (CO)C**H**=$CH_2$), 5.86 (m, 1H, $\mathbf{H_{trans}}$HC=CH), 4.35 (m, 2H, C$\mathbf{H_2}$O(CO)), 3.79-3.74 (m, 4H, -OC$\mathbf{H_2}$-), 3.71-3.69 (m, 4H, -OC$\mathbf{H_2}$-), 3.63 (t, 2H, J=4.2 Hz, C$\mathbf{H_2}$OH).
**ESI-MS:** *m/z* = 205.4 $[M+H]^+$.

**Acrylate-functionalized pyridine ligand (16)**
Mono-acrylate functionalized triethylene glycol **15** (0.149 g, 0.73 mmol) dissolved in 2 mL of dry DMF was added to a solution of isonicotinic acid-activated ester **5** (0.134 g, 0.61 mmol) in 4 mL of dry DMF, followed by $Et(iPr)_2N$ (0.106 mL, 0.61 mmol). The mixture was stirred at room temperature for 12 h. Volatiles were removed in vacuo and the crude was purified *via* flash column chromatography (gradient from $CH_2Cl_2$/MeOH 98:2 to $CH_2Cl_2$/MeOH 95:5) to afford product **16** as a colourless oil in 58% yield (0.109 g, 0.35 mmol).
**$^1$H NMR** ($CDCl_3$, 400 MHz): δ (ppm) = 8.80 (dd, 2H, $J_o$=6.0 Hz, $J_m$=1.6 Hz, Ar**H**), 7.89 (dd, 2H, $J_o$=6.0 Hz, $J_m$=1.6 Hz, Ar**H**), 6.44 (dd, 1H, $J_{trans}$=17.3 Hz, $J_{gem}$=1.5 Hz, $\mathbf{H_{cis}}$HC=CH), 6.16 (dd, 1H, $J_{trans}$=17.3 Hz, $J_{cis}$=10.4 Hz, (CO)C**H**=$CH_2$), 5.85 (dd, 1H, $J_{cis}$=10.4 Hz, $J_{gem}$=1.5 Hz, $\mathbf{H_{trans}}$HC=CH), 4.53 (m, 2H, C$\mathbf{H_2}$O(CO)Ar), 4.33 (m, 2H, C$\mathbf{H_2}$O(CO)CH=$CH_2$), 3.88-3.85 (m, 2H, -OC$\mathbf{H_2}$-), 3.78-3.75 (m, 2H, -OC$\mathbf{H_2}$-), 3.73-3.70 (m, 4H, -OC$\mathbf{H_2}$-).
**ESI-MS:** *m/z* = 310.4 $[M+H]^+$.

**Acrylate-functionalized Pt(II) complex (14)**
Pt(II)-DMSO precursor **4** (0.221 g, 0.36 mmol) was added to a solution of acrylate-functionalized pyridine ligand **16** (0.100 g, 0.32 mmol) in 5 mL of $CH_3CN$. The solution was stirred at room temperature for 12 h. Volatiles were removed under vacuum and the crude was purified by flash column chromatography (gradient from CyHex/AcOEt 4:6 to CyHex/AcOEt 3:7). Precipitation from MeOH afforded complex **14** as a yellow solid in 63% yield (0.172 g, 0.20 mmol).
**$^1$H NMR** ($CD_2Cl_2$, 400 MHz): δ (ppm) = 9.89 (d, 2H, J=6.8 Hz, Ar**H**), 8.21 (dd, 2H, $J_o$=6.8 Hz, $J_m$=1.4 Hz, Ar**H**), 8.11 (t, 1H, J=7.8 Hz, Ar**H**), 7.84 (d, 2H, J=7.8 Hz, Ar**H**), 6.42 (dd, 1H, $J_{trans}$=17.3 Hz, $J_{gem}$=1.5 Hz, $\mathbf{H_{cis}}$HC=CH), 6.17 (dd, 1H, $J_{trans}$=17.3 Hz, $J_{cis}$=10.4 Hz, (CO)C**H**=$CH_2$), 5.86 (dd, 1H, $J_{cis}$=10.4 Hz, $J_{gem}$=1.5 Hz, $\mathbf{H_{trans}}$HC=CH), 4.61 (m, 2H, C$\mathbf{H_2}$O(CO)Ar), 4.32 (m, 2H, C$\mathbf{H_2}$O(CO)CH=$CH_2$), 3.92-3.89 (m, 2H, -OC$\mathbf{H_2}$-), 3.77-3.69 (m, 6H, -OC$\mathbf{H_2}$-).

**$^{19}F\{^{1}H\}$ NMR** ($CD_2Cl_2$, 376 MHz): δ (ppm) = - 64.52 (s, 3H, C**F**$_3$).

**Pluronic F127DA**

F127DA was synthesized according to a well-established literature procedure.[90] F127 (2 g, 0.159 mol) and $Et_3N$ (0.221 mL, 1.59 mol) were dissolved in 20 mL of dry $CH_2Cl_2$; acryloyl chloride (0.128 mL, 1.59 mol) was added drop-wise and the mixture was stirred at room temperature for 24 h. The solution was poured in anhydrous diethyl ether and the resulting precipitate was filtered and dried under vacuum. Acrylation degree was determined to be more than 90% by $^{1}H$ NMR in $CDCl_3$ and calculated by the ratio of acryl protons of F127DA (δ = 5.8-6.4) to methyl protons in poly(propyleneoxide) groups (δ = 1.1).

**Nano-micellar hydrogels with F127DA**

Hydrogels were prepared *via* one-step sequential free-radical polymerization. AAm (5 mol/L) and F127DA ($6{\cdot}10^{-3}$ mol/L) were dissolved in water; after bubbling under a nitrogen atmosphere for 30 min, 0.1 mol% (with respect to AAm) of KPS were added and the mixture was heated at 70 °C. After 10 min gelation was confirmed *via* 'inverted vial' test. Obtained hydrogels appear optically transparent and extremely elastic.

**AAm-based hydrogels with complex 14**

In a 5-mL glass vial, a 1,4-dioxane solution of complex **14** was flash-injected in water; then AAm (5 mol/L) was added. After degassing, 0.1 mol% (with respect to AAm) of initiator were added and the mixture was irradiated under UV lamp (280 nm) for 15 min. Results are schematized in Table S3.4.

| | AAm | Complex 14 | F127DA | MBA | Outcome |
|---|---|---|---|---|---|
| **I** | 5 mol/L | $6{\cdot}10^{-3}$ mol/L | / | / | No gelation |
| **II** | 5 mol/L | $1{\cdot}10^{-2}$ mol/L | / | / | No gelation |
| **III** | 5 mol/L | $6{\cdot}10^{-2}$ mol/L | / | / | No gelation |
| **IV** | 5 mol/L | $6{\cdot}10^{-3}$ mol/L | $6{\cdot}10^{-3}$ mol/L | / | Aggregates disruption |
| **V** | 5 mol/L | $6{\cdot}10^{-3}$ mol/L | $6{\cdot}10^{-4}$ mol/L | / | Aggregates disruption |
| **VI** | 5 mol/L | $6{\cdot}10^{-3}$ mol/L | / | $6{\cdot}10^{-3}$ mol/L | Soft hydrogel |
| **VII** | 5 mol/L | $6{\cdot}10^{-3}$ mol/L | / | $6{\cdot}10^{-2}$ mol/L | Soft hydrogel |

**Table S3.4** *AAm-based hydrogels with complex **14**.*

**Norbornene-functionalized pyridine ligand (19)**

Norbornene carboxylic acid (mixture of *endo*- and *exo*-) (1.0 g, 7.26 mmol) was dissolved in 5 mL of oxalyl chloride under nitrogen flux and the solution was stirred at room temperature for 2 h. Volatiles were removed under vacuum and the acyl chloride intermediate **18** was directly re-dissolved in dry $CH_2Cl_2$. The solution of **18** was added drop-wise to an ice-cold solution of 4-pyridinepropanol (0.939 mL, 7.26 mmol) and $Et_3N$ (1.009 mL, 7.26 mmol). The mixture was stirred at room temperature for 12 h. The solvent was removed under reduced pressure, the crude was recovered with $CH_2Cl_2$, washed with HCl 1 M, brine and $H_2O$ and dried. Product **19** was obtained as a colourless oil in 88% yield (1.733 g, 6.39 mmol).

**$^1$H NMR** ($CDCl_3$, 400 MHz): δ (ppm) = 8.63 (m, 2H, Ar**H**), 7.27 (m, 2H, Ar**H**), 6.23 (m, 1H, C**H**=C(CO)), 4.47 (m, 2H, C**H$_2$**O(CO)), 2.96 (m, 2H, -C**H$_2$**Ar), 2.45 (m, 2H, C**H$_{NB}$**), 1.94-1.81 (m, 2H, -C**H$_2$**$CH_2$Ar), 1.62-1.39 (m, 6H, C**H$_{2NB}$**).

**ESI-MS:** *m/z* = 258.5 $[M+H]^+$.

**Norbornene-functionalized Pt(II) complex (17)**

Pt(II)-DMSO precursor **4** (0.171 g, 0.22 mmol) was added to a solution of norbornene-functionalized pyridine ligand **19** (0.05 g, 0.19 mmol) in 3 mL of DMF. The solution was stirred at room temperature for 12 h. Volatiles were removed under vacuum and the crude was purified by flash column chromatography (CyHex/AcOEt 2:8) to afford complex **17** as a yellow solid in 69% yield (0.105 g, 0.13 mmol).

**$^1$H NMR** ($CD_2Cl_2$, 400 MHz): δ (ppm) = 9.35 (d, 2H, J=6.6 Hz, Ar**H**), 7.92 (t, 1H, J=7.9 Hz, Ar**H**), 7.54 (d, 2H, J=7.9 Hz, Ar**H**), 7.39 (d, 2H, J=6.6 Hz, Ar**H**), 6.31 (m, 1H, C**H**=C(CO)), 4.52 (m, 2H, C**H$_2$**O(CO)), 2.98 (m, 2H, -C**H$_2$**Ar), 2.47 (m, 2H, C**H$_{NB}$**), 2.11-1.99 (m, 2H, -C**H$_2$**$CH_2$Ar), 1.74-1.42 (m, 6H, C**H$_{2NB}$**).

**$^{19}$F{$^1$H} NMR** ($CD_2Cl_2$, 376 MHz): δ (ppm) = - 64.53 (s, 3H, C**F$_3$**).

**Poly(norbornene) samples preparation**

Complex **17** and norbornene with different ratios (Table S3.5) were dissolved in degassed $CH_2Cl_2$ to obtain a 0.1 M solution. The solution was added drop-wise to a rapidly stirred and degassed $CH_2Cl_2$ solution containing first generation Grubbs'catalyst (1 mg/mL). The mixture was stirred at room temperature for 24 h, then ethyl vinyl ether was added and the mixture was stirred for an additional 30 min. The solution was concentrated under reduced pressure and then added drop-wise to MeOH. The precipitated polymer was dried under

vacuum at 50 °C. Polymer films were prepared by solution casting from $CH_2Cl_2$ in a PTFE mould.

| | **Pt : NB ratio** | **Outcome** |
|---|---|---|
| **I** | 1 : 60 | Orange emitting and rigid film |
| **II** | 1 : 40 | Orange emitting and rigid film |
| **III** | 1 : 25 | Orange emitting and rigid film |
| **IV** | 0 : 100 | Elastic film |

**Table S3.5** *Poly(norbornene) films with complex **17**.*

## 3.6 References

[1] V. Balzani, G. Bergamini, S. Campagna, F. Puntoriero, *Photochemistry and Photophysics of Coordination Compound*, **2007**, Springer, Berlin, Heidelberg.

[2] a) A. Barbieri, G. Accorsi, N. Armaroli, *Chem. Comm*. **2008**, 2185-2193; b) D. V. Scaltrito, D. W. Thompson, J. A. O'Callaghan, G. J. Meyer, *Coord. Chem. Rev*. **2000**, *208*, 243-266; c) A. Laviecombot, M. Cantuel, Y. Leydet, G. Jonusauskas, D. Bassani, N. McClenaghan, *Coord. Chem. Rev*. **2008**, *252*, 2572-2584; d) D. R. McMillin, J. R. Kirchoff, K. V. Goodwin, *Coord. Chem. Rev*. **1985**, *64*, 83-92.

[3] a) M. Mauro, E. Q. Procopio, Y. Sun, C. -H. Chien, D. Donghi, M. Panigati, P. Mercandelli, P. Mussini, G. D'Alfonso, L. De Cola, *Adv. Funct. Mater*. **2009**, *19*, 2607-2614; b) P. T. Chou, Y. Chi, *Chem. Eur. J*. **2007**, *13*, 380-395.

[4] S. Di Bella, *Chem. Soc. Rev*. **2001**, *30*, 355-366.

[5] a) M. S. Lowry, J. I. Goldsmith, J. D. Slinker, R. Rohl, R. A. Pascal, G. G. Malliaras, S. Bernhard, *Chem. Mater*. **2005**, *17*, 5712-5719; b) S. Rau, D. Walther, J. G. Vos, *Dalton Trans*. **2007**, 915-919; c) R. Reithmeier, C. Bruckmeier, B. Rieger, *Catalysts* **2012**, *2*, 544-571.

[6] a) M. Staffilani, E. Höss, U. Giesen, E. Schneider, F. Hartl, H. -P. Josel, L. De Cola, *Inorg. Chem*. **2003**, *42*, 7789-7798; b) M. M. Richter, *Chem. Rev*. **2004**, *104*, 3003-3036.

[7] A. Y. Tam, V. W. Yam, *Chem. Soc. Rev*. **2013**, *42*, 1540-1567.

[8] A. Ruggi, F. W. B. van Leeuwen, A. H. Velders, *Coord. Chem. Rev*. **2011**, *255*, 2542-2554.

[9] V. Fernandez-Moreira, F. L. Thorp-Greenwood, M. P. Coogan, *Chem. Comm*. **2010**, *46*, 186-202.

[10] a) H. Yersin, *Highly efficient OLEDs with Phosphorescent Materials*, **2008**, Wiley ed.; b) R. H. Crabtree, D. M. P. Mingos, *Comprehensive organometallic chemistry III: Applications I: main group compounds in organic synthesis*, **2007**, Elsevier ed.; c) C. Cebrian, M. Mauro, D. Kourkoulos, P. Mercandelli, D. Hertel, K. Meerholz, C. A. Strassert, L. De Cola, *Adv. Mater*. **2013**, *25*, 437-442; d) M. Mauro, C. H. Yang, C. Y. Shin, M. Panigati, C. H. Chang, G. D'Alfonso, L. De Cola, *Adv.*

*Mater*. **2012**, *24*, 2054-2058; e) M. Mydlak, M. Mauro, F. Polo, M. Felicetti, J. Leonhardt, G. Diener, L. De Cola, C. A. Strassert, *Chem. Mater*. **2011**, *23*, 3659-3667; f) R. D. Costa, E. Ortì, H. J. Bolink, F. Monti, G. Accorsi, N. Armaroli, *Angew. Chem. Int. Ed.* **2012**, *51*, 8178-8211; g) T. Hu, L. He, L. Duan, Y. Qiu, *J. Mater. Chem*. **2012**, *22*, 4206-4215.

[11] a) B. E. Hardin, H. J. Snaith, M. D. McGehee, *Nat. Photon*. **2012**, *6*, 162-169; b) A. Orbelli Biroli, F. Tessore, M. Pizzotti, C. Biaggi, R. Ugo, S. Caramori, A. Aliprandi, C. A. Bignozzi, F. De Angelis, G. Giorgi, E. Licandro, E. Longhi, *J. Phys. Chem. C* **2011**, *115*, 23170-23182; c) M. Mba, M. D'Acunzo, P. Salice, T. Carofiglio, M. Maggini, S. Caramori, A. Campana, A. Aliprandi, R. Argazzi, S. Carli, C. A. Bignozzi, *J. Phys. Chem. C* **2013**, *117*, 19885-19896.

[12] a) I. Eryazici, C. N. Moorefield, G. R. Newkome, *Chem. Rev*. **2008**, *108*, 1834-1895; b) W. Paw, S. D. Cummings, M. A. Mansour, W. B. Connick, D. K. Geiger, R. Eisenberg, *Coord. Chem. Rev*. **1998**, *171*, 125-150; c) J. A. G. Williams, S. Develay, D. L. Rochester, L. Murphy, *Coord. Chem. Rev*. **2008**, *252*, 2596-2611.

[13] J. S. Griffith, L. E. Orgel, *Quarterly Reviews, Chemical Society* **1957**, *11*, 381-393.

[14] a) A. Dedieu, R. Hoffmann, *J. Am. Chem. Soc*. **1978**, 2074-2079; b) V. M. Miskowski, V. H. Houlding, *Inorg. Chem*. **1991**, *30*, 4446-4452.

[15] a) I. M. Sluch, A. J. Miranda, O. Elbjeirami, M. A. Omary, L. M. Slaughter, *Inorg. Chem*. **2012**, *51*, 10728-10746; b) D. Kim, J. -L. Brédas, *J. Am. Chem. Soc*. **2009**, *131*, 11371-11380; c) M. Kato, C. Kosuge, K. Morii, J. S. Ahn, H. Kitagawa, T. Mitani, M. Matsushita, T. Kato, S. Yano, M. Kimura, *Inorg. Chem*. **1999**, *38*, 1638-1641; d) G. Arena, G. Calogero, S. Campagna, L. M. Scolaro, V. Ricevuto, R. Romeo, *Inorg. Chem*. **1998**, *37*, 2763-2769.

[16] M. Mauro, A. Aliprandi, D. Septiadi, N. S. Kehr, L. De Cola, *Chem. Soc. Rev*. **2014**, *43*, 4144-4166.

[17] a) J. A. Gareth Williams, S. Develay, D. L. Rochester, L. Murphy, *Coord. Chem. Rev*. **2008**, *252*, 2596-2611; b) G. S. Tong, C. M. Che, *Chem. Eur. J*. **2009**, *15*, 7225-7237.

[18] D. R. McMillin, J. J. Moore, *Coord. Chem. Rev*. **2002**, *229*, 113-121.

[19] a) C. -M. Che, K. -T. Wan, L. -Y. He, C. -K. Poon, V. W. -W. Yam, *J. Chem. Soc. Chem. Commun*. **1989**, *14*, 943-944; b) M. H. Wilson, L. P. Ledwaba, J. S. Field, D. R. McMillin, *Dalton Trans.* **2005**, 2754-2759.

[20] a) C. -W. Chan, L. -K. Cheng, C. -M. Che, *Coord. Chem. Rev*. **1994**, 132, 87-97; b) M. Hissler, W. B. Connick, D. K. Geiger, J. E. McGarrah, D. Lipa, R. J. Lachicotte, R. Eisenberg, *Inorg. Chem*. **2000**, *39,* 447-457; c) C. E. Whittle, J. A. Weinstein, M. W. George, K. S. Schanze, *Inorg. Chem*. **2001**, *40*, 4053-4062; d) V. W. -W. Yam, R. P. -L. Tang, K. M. -C. Wong, K. -K. Cheung, *Organometallics* **2001**, *20*, 4476-4482; e) Q. -Z. Yang, L. -Z. Wu, Z. -X. Wu, L. -P. Zhang, C. -H. Tung, *Inorg. Chem*. **2002**, *41,* 5653-5655; f) I. E. Pomestchenko, C. R. Luman, M. Hissler, R. Ziessel, F. N. Castellano, *Inorg. Chem*. **2003**, *42*, 1394-1396; g) F. Hua, S. Kinayyigit, J. R. Cable, F. N. Castellano, *Inorg. Chem*. **2003**, *44*, 471-473; h) F. Hua, S. Kinayyigit, J. R. Cable, F. N. Castellano, *Inorg. Chem*. **2006**, *45*, 4304-4306; i) X. -J. Liu, J. -K. Feng, J. Meng, Q. -J. Pan, A. -M. Ren, X. Zhou, H. -X. Zhang, *Eur. J. Inorg. Chem*. **2005**, 1856-1866.

[21] R. C. Evans, P. Douglas, C. J. Winscom, *Coord. Chem. Rev*. **2006**, *250*, 2093-2126.

[22] For a recent example see: S. P. Argent, H. Adams, T. Riis-Johannessen, J. C. Jeffery, L. P. Harding, W. Clegg, R. W. Harrington, M. D. Ward, *Dalton Trans.* **2006**, *42*, 4996-5013.

[23] a) S. -Y. Chang, J. Kavitha, S. -W. Li, C. -S. Hsu, Y. Chi, Y. -S. Yeh, P. -T. Chou, G. -H. Lee, A. J. Carty, Y. -T. Tao, C. -H. Chien, *Inorg. Chem*. **2006**, *45*, 137-146; b) S. -Y. Chang, J. Kavitha, J. -Y. Hung, Y. Chi, Y. -M. Cheng, E. Y. Li, P. -T. Chou, G. -H. Lee, A. J. Carty, *Inorg. Chem*. **2007**, *46*, 7064-7074.

[24] C. -H. Yang, S. -W. Li, Y. Chi, Y. -M. Cheng, Y. -S. Yeh, P. -T. Chou, G. -H. Lee, C. -H. Wang, C. -F. Shu, *Inorg. Chem*. **2005**, *44*, 7770-7780.

[25] P. Pyykko, *Chem. Rev*. **1997**, *97*, 597–636.

[26] a) F. Scherbaum, A. Grohmann, B. Huber, C. Krüger, H. Schmidbaur, *Angew. Chem. Int. Ed*. **1988**, *27*, 1544-1546; b) P. Pyykko, M. Straka, *Phys. Chem. Chem. Phys*. **2000**, *2*, 2489-2493.

[27] S. Sculfort, P. Braunstein, *Chem. Soc. Rev*. **1995**, *24*, 391-400.

[28] a) C. Yu, K. H. Chan, K. M. Wong, V. W. -W. Yam, *Proc. Natl. Acad. Sci. U.S.A.* **2006**, *103*, 19652-19657; b) J. Moussa, K. M. -C. Wong, L. M. Chamoreau, H. Amouri, V. W. -W. Yam, *Dalton Trans*. **2007**, 3526-3530; c) T. Cardolaccia, Y. Li, K. S. Schanze, *J. Am. Chem. Soc*. **2008**, *130*, 2535-2545; d) M. Y. Yuen, V. A. Roy, W. Lu, S. C. Kui, G. S. Tong, M. H. So, S. S. Chui, M. Muccini, J. Q. Ning, S. J. Xu, C. M. Che, *Angew. Chem. Int. Ed.* **2008**, *47*, 9895-9899; e) W. Lu, Y. Chen, V. A. Roy, S. S. Chui, C. M. Che, *Angew. Chem. Int. Ed*. **2009**, *48*, 7621-7625.

[29] a) For a very recent example see: S. Y. -L. Leung, W. H. Lam, V. W. -W. Yam, *Proc. Natl. Acad. Sci. U.S.A*. **2013**, *11*, 7986–7991; b) V. W. -W. Yam, K. M. -C. Wong, N. Zhu, *J. Am. Chem. Soc*. **2002**, *124*, 6506–6507.

[30] a) For a recent example see: X. Zhang, B. Cao, E. J. Valente, T. K. Hollis, *Organometallics* **2013**, *32*, 752–761; b) Y. Tanaka, K. M. -C. Wong, V. W. -W. Yam, *Chem. Sci*. **2012**, *3*, 1185–1191; c) L. -Y. Zhang, L. -J. Xu, X. Zhang, J. -Y. Wang, J. Li, Z. N. Chen, *Inorg. Chem*. **2013**, *52*, 5167–5175.

[31] a) C. A. Strassert, C. -H. Chien, M. D. Galvez Lopez, D. Kourkoulos, D. Hertel, K. Meerholz, L. De Cola, *Angew. Chem., Int. Ed*. **2011**, *50*, 946–950; b) S. Y. -L. Leung, V. W. -W. Yam, *Chem. Sci*. **2013**, *4*, 4228–4234.

[32] a) M. C. -L. Yeung, V. W. -W. Yam, *Chem. Sci*. **2013**, *4*, 2928–2935; b) V. W. -W. Yam, K. H. -Y. Chan, K. M. -C. Wong, N. Zhu, *Chem. Eur. J.* **2005**, *11*, 4535–4543.

[33] C. -M. Che, C. -F. Chow, M. -Y. Yuen, V. A. L. Roy, W. Lu, Y. Chen, S. S. -Y. Chui, N. Zhu, *Chem. Sci*. **2011**, *2*, 216–222.

[34] Y. Sun, K. Ye, H. Zhang, J. Zhang, L. Zhao, B. Li, G. Yang, B. Yang, Y. Wang, S. -W. Lai, C. -M. Che, *Angew. Chem. Int. Ed*. **2006**, *118*, 5738–5741.

[35] W. Zhang, W. Jin, T. Fukushima, N. Ishii, T. Aida, *Angew. Chem., Int. Ed*. **2009**, *48*, 4747–4750.

[36] V. N. Kozhevnikov, B. Donnio, D. W. Bruce, *Angew. Chem., Int. Ed*. **2008**, *47*, 6286–6289.

[37] a) Y. Li, E. S. -H. Lam, A. Y. -Y. Tam, K. M. -C. Wong, W. H. Lam, L. Wu, V. W. -W. Yam, *Chem. Eur. J.* **2013**, *19*, 9987–9994; b) N. K. Allampally, C. A. Strassert, L. De Cola, *Dalton Trans*. **2012**, *41*, 13132–13137.

[38] a) F. Camerel, R. Ziessel, B. Donnio, C. Bourgogne, D. Guillon, M. Schmutz, C. Iacovita, J. -P. Bucher, *Angew. Chem. Int. Ed.* **2006**, *119*, 2713-2716; b) M. Chen, C. Wei, X. Wu, M. Khan, N. Huang, G. Zhang, L. Li, *Chem. Eur. J*. **2015**, *21*, 4213-4217.

[39] a) W. Lu, S. S. Chui, K. M. Ng, C. M. Che, *Angew. Chem. Int. Ed*. **2008**, *47*, 4568-4572; b) Y. Guo, L. Xu, H. Liu, Y. Li, C. M. Che, Y. Li, *Adv. Mater*. **2015**, *27*, 985-1013.

[40] a) Y. -J. Tian, E. W. Mejier, F. Wang, *Chem. Commun*. **2013**, *49*, 9197-9199; b) A. Aliprandi, M. Mauro, L. De Cola, *Nature Chem*. **2016**, *8*, 10-15.

[41] a) A. Y.-Y. Tam, K. M. -C. Wong, V. W. -W. Yam, *J. Am. Chem. Soc*. **2009**, *131*, 6253-6260; b) V. W. Yam, Y. Hu, K. H. Chan, C. Y. Chung, *Chem. Commun*. **2009**, 6216-6218.

[42] K. M. -C. Wong, M. M. -Y. Chan, V. W. -W. Yam, *Adv. Mater*. **2014**, *26*, 5558-5568.

[43] K. H. Chan, J. W. Lam, K. M. Wong, B. Z. Tang, V. W. -W. Yam, *Chem. Eur. J.* **2009**, *15*, 2328-2334.

[44] C. Yu, K. H. Chan, K. M. Wong, V. W. -W. Yam, *Chem. Eur. J*. **2008**, *14*, 4577-4584.

[45] C. Y. Chung, V. W. Yam, *Chem. Eur. J*. **2014**, *20*, 13016-13027.

[46] C. Po, A. Y. Tam, K. M. Wong, V. W. Yam, *J. Am. Chem. Soc*. **2011**, *133*, 12136-12143.

[47] C. Po, A. Y. -Y. Tam, V. W. -W. Yam, *Chem. Sci*. **2014**, *5*, 2688-2695.

[48] C. Po, V. W. -W. Yam, *Chem. Sci*. **2014**, *5*, 4868-4872.

[49] Y. Chen, C. -M. Che, W. Lu, *Chem. Commun*. **2015**, *51*, 5371-5374.

[50] a) S. Y. -L. Leung, V. W. –W. Yam, *Chem. Sci*. **2013**, *4*, 4228-4234; b) S. Y. -L. Leung, W. H. Lam, V. W. –W. Yam, *Proc. Natl. Acad. Sci. U.S.A*. **2013**, *110*, 7986-7991.

[51] C. Po, Z. Ke, A. Y. Tam, H. F. Chow, V. W. Yam, *Chem. Eur. J*. **2013**, *19*, 15735-15744.

[52] Y. Mao, K. Liu, L. Meng, L. Chen, L. Chen, T. Yi, *Soft Matter* **2014**, *10*, 7615-7622.

[53] N. K. Allampally, C. G. Daniliuc, C. A. Strassert, L. De Cola, *Inorg. Chem*. **2015**, *54*, 1588-1596.

[54] C. A. Strassert, C. H. Chien, M. D. Galvez Lopez, D. Kourkoulos, D. Hertel, K. Meerholz, L. De Cola, *Angew. Chem. Int. Ed.* **2011**, *50*, 946-950.

[55] N. K. Allampally, C. A. Strassert, L. De Cola, *Dalton Trans*. **2012**, *41*, 13132-13137.

[56] N. K. Allampally, M. Bredol, C. A. Strassert, L. De Cola, *Chem. Eur. J*. **2014**, *20*, 16863-16868.

[57] a) M. L. Muro, C. A. Daws, F. N. Castellano, *Chem. Commun*. **2008**, 6134-6136; b) J. S. Field, C. D. Grimmer, O. Q. Munro, B. P. Waldron, *Dalton Trans*. **2010**, *39*, 1558-1567; c) T. J. Wadas, Q. M. Wang, Y. J. Kim, C, Flaschenreim, T. N. Blanton, R. Eisenberg, *J. Am. Chem. Soc*. **2004**, *126*, 16841-16849.

[58] Y. Sagara, T. Kato, *Nat. Chem*. **2009**, *1*, 605-610.

[59] J. Ni, Y. -G. Wang, H. -H. Wang, L. Xu, Y. -Q. Zhao, Y. -Z. Pana, J. -J. Zhang, *Dalton Trans*. **2014**, *43*, 352-360.

[60] N. Kitani, N. Kuwamura, T. Tsukuda, N. Yoshinari, T. Konno, *Chem. Commun*. **2014**, *50*, 13529-13532.

[61] L. -M. Huang, G. -M. Tu, Y. Chi, W. -Y. Hung, Y.-C. Song, M. -R. Tseng, P. -T. Chou, G. -H. Lee, K. -T. Wong, S. -H. Cheng, W. -S. Tsai, *J. Mater. Chem. C* **2013**, *1*, 7582-7592.

[62] M. Krikorian, S. Liu, T. M. Swager, *J. Am. Chem. Soc.* **2014**, *136*, 2952−2955.

[63] J. R. Kumpfer, S. D. Taylor, W. B. Connick, S. J. Rowan *J. Mater. Chem.* **2012**, *22*, 14196-14204.

[64] X. Zhang, J. -Y. Wang, J. Ni, L. -Y. Zhang, Z. -N. Chen, *Inorg. Chem.* **2012**, *51*, 5569−5579.

[65] S. J. Choi, J. Kuwabara, Y. Nishimura, T. Arai, T. Kanbara, *Chem. Lett.* **2012**, *41*, 65-67.

[66] M. Mauro, A. Aliprandi, D. Septiadi, N. S. Kehr, L. De Cola, *Chem. Soc. Rev.* **2014**, *43*, 4144-4166.

[67] a) S. W. Botchway, M. Charnley, J. W. Haycock, A. W. Parker, D. L. Rochester, J. A. Weinstein, J. A. G. Williams, *Proc. Natl. Acad. Sci. U.S.A.* **2008**, *105*, 16071-16076; b) E. Baggaley, S. W. Botchay, J. W. Haycock, H. Morris, I. V. Sazanovich, J. A. G. Williams, J. A. Weinstein, *Chem. Sci.* **2014**, *5*, 879-886.

[68] C. Y. -S. Chung, S. P. -Y. Li, M. -W. Louie, K. K. -W. Lo, W. -W. Yam, *Chem. Sci.* **2013**, *4*, 2453-2462.

[69] S. Liu, H. Sun, Y. Ma, S. Ye, X. Liu, X. Zhou, X. Mou, L. Wang, Q. Zhao, W. Huang, *J. Mater. Chem.* **2012**, *22*, 22167-22173.

[70] T. Zou, C. -N. Lok, Y. M. E. Funga, C. -M. Che, *Chem. Commun.* **2013**, *49*, 5423-5425.

[71] a) D. J. Maltman, S. A. Przyborski, *Biochem. Soc. Trans.* **2010**, *38*, 1072-1075; b) E. Cukierman, D. E. Bassi, *Semin. Cancer Biol.* **2010**, *20*, 139-145; c) E. Santos, R. M. Hernández, J. L. Pedraz, G. Orive, *Trends Biotechnol.* **2012**, *30*, 331-341.

[72] a) D. Seliktar, *Science (New York, N.Y.)* **2012**, *336*, 1124-1128; b) D. Buenger, F. Topuz, J. Groll, *Prog. Polym. Sci.* **2012**, *37*, 1678-1719.

[73] O. Wichterle, D. Lím, *Nature* **1960**, *185*, 117-118.

[74] a) J. A. Rowley, G. Madlambayan, D. J. Mooney, *Biomaterials* **1999**, *20*, 45-53; b) M. W. Tibbitt, K. S. Anseth, *Biotechnol. Bioeng.* **2009**, *103*, 655-663.

[75] a) H. Geckil, F. Xu, X. Zhang, S. Moon, U. Demirci, *Nanomedicine* **2010**, *5*, 469-484; b) J. A. Hunt, R. Chen, T. van Veen, N. Bryan, *J. Mat. Chem. B* **2014**, *2*, 5319-5338.

[76] F. Danusso, P. Ferruti, *Polymer* **1970**, *11*, 88-113.

[77] P. Ferruti, *J. Polym. Sci. Part A: Polym. Chem.* **2013**, 51, 2319–2353.

[78] E. Ranucci, G. Spagnoli, P. Ferruti, D. Sgouras, R. Duncan, *J. Biomater. Sci. Polym. Ed.* **1991**, *2*, 303-315.

[79] N. Mauro, A. Manfredi, E. Ranucci, P. Procacci, M. Laus, D. Antonioli, C. Mantovani, V. Magnaghi, P. Ferruti, *Macromol. Biosci.* **2013**, *13*, 332-347.

[80] Y. Sun, Z. Deng, Y. Tian, C. Lin, *J. Appl. Polym. Sci.* **2013**, *127*, 40-48.

[81] F. Fiorini's PhD thesis *"Soft hybrid materials for cell growth and proliferation"*, **2016**.

[82] C. -W. Chang, Y. Hwang, D. Brafman, T. Hagan, C. Phung, S. Varghese, *Biomaterials* **2013**, *34*, 912-921.

[83] S. Sinn, F. Biedermann, L. De Cola, *Chem. Eur. J.* **2017**, *23*, 1965–1971.

[84] A. Aliprandi, M. Mauro, L. De Cola, *Nat. Chem.* **2016**, *8*, 10-15.

[85] S. Marpu, Z. Hu, M. A. Omary, *Langmuir* **2010**, *26*, 15523-15531.

[86] C. Chang, J. Peng, L. Zhang, D. -W. Pang, *J. Mater. Chem.* **2009**, *19*, 7771-7776.

[87] Y. Sun, G. Gao, G. Du, Y. Cheng, J. Fu, *ACS Macro Lett.* **2014**, *3*, 495-500.

[88] Y. J. Shadrick, I. M. Paris, J. J. Rack, *Adv. Mater.* **2011**, *23*, 4312-4317.

[89] J. H. Price, A. N. Williamson, R. F. Schramm, B. B. Wayland, *Inorg. Chem.* **1972**, *11*, 1280–1284.

[90] S. -Y. Lee, G. Tae, *J. Control. Release* **2007**, *119*(3), 313-319.

# Materials and Methods

## Materials

All commercial reagents were used as received. Unless otherwise stated, reactions were conducted in flame-dried glassware under an atmosphere of argon using anhydrous solvents (either freshly distilled or passed through activated alumina columns). Silica column chromatography was performed using silica gel 60 (Fluka 230-400 mesh ASTM), or silica gel 60 (MERCK 70-230 mesh).

## Methods

**• NMR Measurements**

$^{1}H$ NMR spectra were obtained using a Bruker AVANCE 300 (300 MHz) or a Bruker AVANCE 400 (400 MHz) spectrometer at 25 °C. All chemical shifts (δ) were reported in ppm relative to the proton resonances resulting from the incomplete deuteration of the NMR solvents. $^{13}C$ NMR spectra were obtained using a Bruker AVANCE 300 (75 MHz) or a Bruker AVANCE 400 (100 MHz) spectrometer. All chemical shifts (δ) were reported in ppm relative to the carbon resonances of the NMR solvents. $^{31}P$ NMR spectra were obtained using a Bruker AVANCE 400 (162 MHz) spectrometer. All chemical shifts (δ) were recorded in ppm relative to external 85% $H_3PO_4$ at 0.00 ppm. $^{19}F$ NMR spectra were obtained using a Bruker AVANCE 400 (376 MHz) spectrometer. All chemical shifts (δ) were recorded in ppm relative to external $CCl_3F$ at 0.00 ppm.

**• MS Measurements**

Electrospray ionization ESI-MS experiments were performed on a Waters ZMD spectrometer equipped with an electrospray interface. MALDI was performed on an AB SCIEX MALDI TOF-TOF 4800 Plus (matrix: α–cyano-4-hydroxycinnamic acid).

• **UV-Vis Measurements**

UV-Vis spectra were collected using a Thermo Scientific Evolution 260 Bio spectrophotometer equipped with a Peltier water-cooled cell changer device, using matched quartz cells of 1 cm path length.

• **Fluorescence measurements**

Steady-state emission measurements were performed on a HORIBA Jobin-Yvon IBH FL-322 Fluorolog 3 spectrometer equipped with a 450 W xenon arc lamp as exciting source and two monochromators (2.1 nm/mm dispersion; 1200 grooves/mm) for incident and emitted light in a 90° arrangement, a TBX-04 single photon-counting detector for the UV-Vis range and a Hamamatsu R2658P photomultiplier for NIR region. Excitation spectra were corrected for source intensity and for detector spectral response and emission grating by standard correction curves.

• **Fluorescence microscopy**

HeLa cells, both grown onto Pt-PAA in glass bottom petri dishes or in 2D directly onto glass bottom dishes, were visualized as they were. Imaging was performed using Zeiss LSM 710 confocal microscope set up with 10-63x magnification objective, numerical aperture (NA) 1.3 of Zeiss LCI Plan-NEOFLUAR water immersion objective lens (Zeiss GmbH, Germany). The samples were excited by continuous wave laser at 400 nm, collecting the emission from 420 to 700 nm. For viability experiments, the samples were stained with MTT reagent and absorbance was recorded at 570 nm. All image processing was performed by using ZEN software (Zeiss GmbH, Germany).

• **XPS Measurements**

XPS experiments were carried out in a UHV apparatus with a base pressure in the $10^{-10}$ mbar range. Monochromatized Al Kα radiation was used for XPS measurements (1486.6 eV, 100 W). The detector was a SPECS PHOIBOS 150 hemispherical analyser mounting a 1D-DLD detector, the angle between the analyser axis and the X-ray source was 54.44°. The XPS spectra were measured with fixed pass energy of 100 eV. The binding energy (BE) scale was calibrated setting the C*1s* signal of the substrate at 284.5 eV.

• **Transport measurements**

Transport measurements were performed in 4-point probes configuration using a 2601 Keithley SMU to supply current and a 2182A Keithley nanovoltmeter for voltage reading. The instrumentation was interfaced with a Quantum Design

PPMS in order to perform measurements at cryogenics temperatures (down to 2.5 K) and in presence of magnetic fields (up to 7 T). The reported characterization has been carried out subsequently in each of the three devices obtained on the STO substrates for each kind of OSV revealing similar qualitative behaviour.

• **DIC measurements**

DIC measurements were carried out using a Nikon D3200 camera with AF-S Nikkor 18-105 mm 1: 3.5-5.6 G ED objective. Data analysis was performed with an open source, subset-based 2D-DIC MATLAB software Ncorr. Comparing different pictures taken during the test, the DIC technique tracks the relative displacements of material points between a reference (typically, the undeformed) state and a current (typically, the deformed) one. The adopted software uses a non-linear optimization algorithm to find the best matching, for a given tolerance, between the reference and the current images. The strain field is derived from the displacement field using the large deformation theory; in particular, the Green-Lagrange deformation tensor is evaluated in each picture's point in an established region of interest, which is the part of the sample not influenced by boundary effects. The dimensionless nature of this technique ensures that measures are not influenced by the length scale; thus, measured displacements must be scaled from pixels to physical units. Collected strain data about films' expansion were processed by removing any negative value and retaining only values between the tenth and ninetieth percentile.

# Abbreviations

| | |
|---|---|
| **AAm** | Acrylamide |
| **AcOEt** | Ethyl acetate |
| **CD** | Circular dichroism |
| **CLSM** | Confocal laser scanning microscopy |
| **CyHex** | Cyclohexane |
| **DBDP** | Diethyl 12-bromododecylphosphonate |
| **DCM** | Dichlorometane |
| **DIC** | Digital image correlation |
| **DMEM** | Dulbecco's Modified Eagle Medium |
| **DMF** | Dimethylformamide |
| **DMSO** | Dimethylsulfoxide |
| **GABA** | γ-amino butirric acid |
| **LFT** | Ligand field theory |
| **LMMCT** | Ligand-to-metal-metal charge transfer |
| **$LnPc_2$/ $TbPc_2$** | Lanthanide/terbium bis-phthalocyaninate |
| **LSMO** | Lanthanum strontium manganite |
| **MALDI-TOF** | Matrix-assisted laser desorption ionization-time of flight |
| **MBA** | Methylene bis-acrylamide |
| **MC** | Merocyanine |
| **MMLCT** | Metal-metal-to-ligand charge transfer |
| **MR** | Magnetoresistance |
| **MTT** | [(3-(4,5-dimethylthiazolyl-2)-2,5-diphenyltetrazolium bromide)] |
| **MW** | Microwave |
| **NaPy** | 2,7-diamido-1,8-naphthyridine |
| **NBS** | N-bromosuccinimide |
| **NHS** | N-hydroxysuccinimide |
| **OSV** | Organic spin valve |
| **P4VP** | Poly(4-vinylpyridine) |
| **PAA** | Poly(amido amine) |
| **PBS** | Phosphate buffer saline |
| **PCC** | Pyridinium chlorochromate |
| **PDMS** | Poly(dimethylsiloxane) |
| **PEHA** | Pentaethylenehexamine |
| **PLQY** | Photoluminescence quantum yield |
| **PMA / PMMA** | Poly(methacrylate)/ poly(methyl methacrylate) |
| **PMB** | *P*-methoxybenzyl |
| **PTFE** | Poly(tetrafluoro ethylene) |

| | |
|---|---|
| **PU** | Polyurethane |
| **py-$CF_3$-trz** | 2,6-bis(3-trifluoromethyl)-1H-1,2,4-triazol-5-yl)pyridine |
| **QxCav** | Tetraquinoxaline cavitand |
| **ROMP** | Ring-opening metathesis polymerization |
| **SAM** | Self-assembled monolayer |
| **SMM** | Single Molecule Magnet |
| **SP** | Spiropyran |
| **SWCNT** | Single-wall carbon nanotube |
| **TBDMS** | *tert*-butyl dimethyl silyl |
| **TEG** | Triethylene glycol |
| **TFA** | Trifluoroacetic acid |
| **THF** | Tetrahydrofuran |
| **TMC** | Transition metal complex |
| **UHV** | Ultra-high vacuum |
| **UPy** | 2-ureido-4[1H]-pyrimidinone |
| **XAS** | X-ray absorption spectroscopy |
| **XMCD** | X-ray magnetic circular dichroism |
| **XNLD** | X-ray natural linear dichroism |
| **XPS** | X-ray photoelectron spectroscopy |

# *Acknowledgments*

*Arrivata alla fine di questo percorso di dottorato e di questa tesi, non mi rimane che ringraziare tutti coloro che hanno reso, più o meno consapevolmente, questi tre anni fantastici.*

*Un grazie particolare va ad Enrico, per avermi accolto nel suo gruppo e avermi dato la possibilità di intraprendere un percorso che, tornando indietro, rifarei mille volte. In questi anni di dottorato è stato una guida preziosa, non semplicemente con i suoi consigli ma fornendo quotidianamente un esempio di passione e dedizione per il suo lavoro…il che è molto più importante.*

*Grazie a Roberta, per la sua costante disponibilità e gentilezza che la rendono una vera colonna portante del laboratorio.*

*Grazie a tutto il gruppo, presente e passato…mentre scrivo queste righe mi tornano in mente tutti i momenti fantastici trascorsi insieme e mi rendo conto che difficilmente sarò in grado di esprimere adeguatamente quello che sento.*

*Una menzione d'onore va ovviamente ai miei compagni del 187, innanzitutto Fede e Ale, che mi hanno insegnato tanto, forse più di quanto loro stessi immaginino. Per questo vi perdono per tutti i lunedì mattina in cui mi sono dovuta sorbire il dettagliatissimo resoconto della giornata di campionato. Come non ricordare Burlax, che con i suoi immancabili palloni da 1 L ha sempre fatto sfigurare le nostre misere sintesi sulla scala dei pochi milligrammi. Infine Ilaria, che ha condiviso con me questo ultimo, glorioso periodo di supremazia femminile al 187, fatto di risate e insostituibili pause tè…finalmente abbiamo potuto tenere accesa la stufetta quanto volevamo, per contrastare il gelido microclima che misteriosamente avvolge il laboratorio anche in piena estate.*

*Grazie anche a tutti i ragazzi del 213/210…benché si trovino dalla parte "sbagliata" del tunnel. In particolare Francesca, per aver preso parte al "circolo del tè" con pettegolezzi annessi; Anjali, per la sua dolcezza e per aver portato una sana ventata di Oriente nel nostro gruppo; Jonathan, per essere il tedesco meno tedesco che si possa immaginare; Alessia, per la sua spontaneità; e ancora Arek, Andreas, Tahnee e tutti gli altri.*

*Thanks to Prof. De Cola for giving me the amazing opportunity to spend six months in her group. During my period of 'Strasbourg life' I met wonderful people, which made*

*me feel at home in a way I never thought. I couldn't have wished for better friends and colleagues. In particular I have to thank Mike, for his help and his kindness; Giuseppe, for being a great partner in the lab and a great pilot…I will remember forever the magic flight over a magic city like Strasbourg; Leana, Eko, Alessandro and Simone, for their precious advices; Mariel, Charles, John, Matteo, Brian and Remi for all the funny and crazy nights!*

*Guardando indietro sento di dover ringraziare anche tutte le persone che ho avuto la fortuna di conoscere durante i miei anni da studentessa, i miei compagni di corso e i professori, perché, di sicuro, se alla fine sono arrivata ad amare la chimica fino a questo punto è anche merito loro.*

*Non rimane che ringraziare le persone care al di fuori dell'università…le mie amiche di sempre, Jessica, Greta e Nicole, per essere una presenza costante e insostituibile nella mia vita.*

*Grazie a mamma e papà, per avermi sempre sostenuta con la loro pazienza e i loro sacrifici in questo lungo cammino, per avermi spesso domandato del mio lavoro pur senza capirne la risposta…ora l'ho messa giù, nero su bianco, in questa tesi. Un grazie speciale al mio Lory, per il sostegno informatico e per l'appoggio che solo un fratello sa dare.*

*Grazie alle mie nonne, che con dolcezza e tenacia rappresentano per me un punto di riferimento e un modello.*

*Grazie infine al mio vero pilastro, Raffaele, l'unico in grado di infondermi serenità e fiducia anche nei momenti più difficili; è tutto merito tuo e del tuo starmi vicino, sempre.*

*Martina*

# *The author*

*Born in Parma, Italy on July 5th, 1990*

| | |
|---|---|
| *July 2009* | ***High School Diploma***<br>*Liceo Classico "G. D. Romagnosi", Parma, Italy* |
| *October 2012* | ***Bachelor in Chemistry***<br>*University of Parma, Italy*<br>*Supervisor: G. Pelosi* |
| *October 2014* | ***Master in Chemistry***<br>*University of Parma, Italy*<br>*Supervisor: E. Dalcanale* |
| *November 2014 – November 2017* | ***Doctoral Research***<br>*University of Parma, Italy*<br>*Supervisor: E. Dalcanale* |
| *January – June 2017* | ***Research Exchange***<br>*Institut de Science et d'Ingegnérie Supramoléculaire (ISIS), Strasbourg, France*<br>*Supervisor: L. De Cola* |